MSc. Dissertation

A DETAILED PETROGRAPHIC AND OXYGEN ISOTOPE STUDY OF METAMORPHIC ROCKS AND ARCHEAN BASEMENT COMPLEX GNEISSES FROM THE VREDEFORT DOME, SOUTH AFRICA

Mandy La Grange
University of Cape Town
South Africa

2004

ABSTRACT

Metamorphism observed in the Vredefort structure increases in grade on a regional scale from lower greenschist facies in the outer perimeter of the Potchefstroom syncline, through upper greenschist and amphibolite grades within rocks of the Witwatersrand Supergroup and Dominion Group in the collar of the Vredefort dome, to granulite grades in the core of the dome. In the collar, two metamorphic assemblages have been identified, one representing a peak metamorphic event pre-impact in age and constrained to temperatures >420-620°C at 3.0-4.0 kbar, and a younger retrograde event, constrained to 500-540 ± 15°C, which overprints the latter assemblage and overgrows pseudotachylite in a small number of samples. Oxygen isotope data obtained for the dome indicate that the collar rocks have been exposed to significant fluid/rock interaction which has resulted in the resetting of oxygen isotopes to $\delta^{18}O$ values depleted by approximately 2-4°/$_{oo}$ relative to Witwatersrand quartzites, now displaying values ranging from 6-8°/$_{oo}$. Samples in extreme close proximity (less than 100m) to igneous intrusions within the collar are depleted even further to values as low as 1.4 and 4.6°/$_{oo}$. $\delta^{18}O$ values for lower grade metapelitic units from the Southeastern (SE) quadrant of the dome are depleted even more to values ranging from 4-6°/$_{oo}$, this suggests that the fluid flow associated with the oxygen isotope resetting event occurred on a regional scale across the dome. In contrast to the collar rocks, $\delta^{18}O$ values obtained for the core of the dome, including both gneisses and metapelitic lithologies, do not appear to display any significant resetting of their oxygen isotopes. Gneisses from both the OGG and ILG exhibit $\delta^{18}O$ values in the range 8-10°/$_{oo}$ and do not display any significant perturbation across the Vredefort discontinuity, however, temperatures calculated from mineral separate data indicate that the OGG-ILG transition zone may represent a zone of increased heat, and related fluid flow. The $\delta^{18}O$ values acquired for the granulite grade metapelitic units found within the ILG range from 10-12°/$_{oo}$ and are typical of what we would expect for restitic and migmatitic lithologies. Temperature estimates for the core calculated from mineral separate data range from 600-1000°C, which is comparable with temperatures obtained for the post-shock metamorphism experienced by these rocks (Gibson, 2002). We conclude that rocks in both the collar and the core of the dome experienced a major oxygen isotope resetting due to the influx of hydrothermal meteoric fluids associated with impact, but that the effect of this final resetting displays differently in the collar compared with the core due to their different pre-impact thermal and metamorphic histories. The rocks in the core of the dome are also likely to have been less permeable to fluid/rock interaction during and immediately after the impact event.

CONTENTS

ACKNOWLEDGEMENTS

I would like to thank all those that have assisted me throughout my Masters. Those whom I would specifically like to thank include: Gary Stevens, for continually believing in me and providing me with his scientific expertise, funding (through the NSCR), facilities, time in the field, patience and inspiration. Chris Harris for his expertise in stable isotopes, helping me run my samples on the oxygen isotope line and helping me get settled into UCT. In the UCT Geology department; Fayrooz Rawoot for helping me run my samples on the oxygen isotope line, Fran Pocock for running XRF analyses on my samples, Ivan Wilson and Ernest Stout for their assistance in various aspects of my sample processing, Dave Reid for helping retrieve some of my 'lost samples' and Anton le Roux in his assistance with administrative aspects. In the Wits University Geology Department; Roger Gibson and Uwe Reimold for their contribution of samples from and in-depth knowledge of the Vredefort structure and time in the field, and Spike McCarthy for allowing me some office space in the department for a short period of time. Rand Afrikaans University for the use of the microprobe. University of Stellenbosch Geology Department for the use of their microscopes and other facilites. My friend Gareth Pile for the extended use of his computer whilst living in the UK, without which I would never have managed to complete my thesis. And lastly, my Family for continually providing me with the love and support to complete what has proved to be a long and arduous task at times.

CHAPTER 1
INTRODUCTION

The Vredefort dome is a circular shaped geological feature ~70-80 km in diameter and situated ~120km South West of Johannesburg. It is strategically located at the centre of the economically important gold- and uranium-rich Witwatersrand Basin (Fig. 1.1) and McCarthy *et al.* (1990) have suggested that the presence of the Vredefort structure is one of the crucial reasons for the gold deposits of the Witwatersrand Basin having been preserved over such a long and complex geological history.

The dome consists of a central core of uplifted Archean basement rocks surrounded by overturned Archean to Palaeoproterozoic strata termed the 'collar rocks' and displays a regional-scale increase in grade of metamorphism towards the centre of the structure (Bischoff 1988). It is commonly accepted as the deeply eroded remnant of an impact crater and is believed to have brought on edge a unique deep crustal section of the Kaapvaal craton.

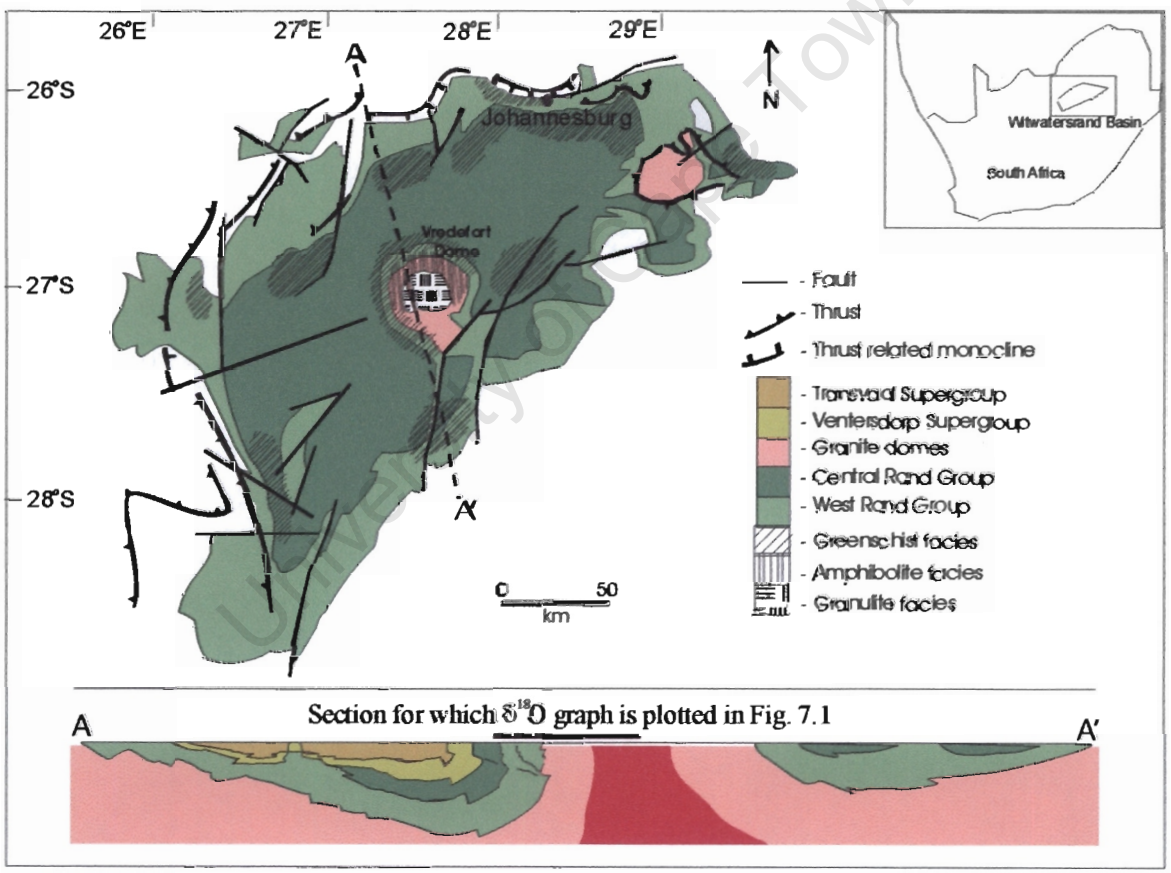

Figure 1.1: Diagram of the Witwatersrand Basin illustrating the distribution and metamorphic grade of rocks within it and the central location of the Vredefort dome, including a horizontal profile from A to A' (modified from Frimmel, 1994).

In consideration of our current understanding of the metamorphism of the Vredefort dome, the aim of this study is to provide further petrographical analysis in an attempt to present greater clarity on the metamorphic histories observed within both the core and the collar of the dome.

New Oxygen isotope data is presented for the dome, including analyses of fifty-four samples spanning both core and collar rocks in the Northwestern (NW) quadrant of the dome and eight metapelitic samples from the Southwestern (SW) quadrant of the dome. Samples taken from the NW quadrant of the dome focussed on an approximately 16 km transect which follows a similar path to the sampling transect of Hart *et al.* (1990a) in the core and extended into Dominion Group and Witwatersrand Supergroup rocks in the collar.

Oxygen isotope research can provide invaluable information on the history of a suite of rocks, especially on the influence of fluid phases and the impact of fluid/rock interaction over time. It allows us the opportunity to correlate resettings with episodes of fluid flow and in certain cases identify the source of the interacting fluids. It also provides an alternative geothermometry technique, which may be used for rocks of igneous origin, which do not have the mineralogy required by conventional mineral geothermometers. This is particularly useful with respect to the core of the Vredefort dome which is dominated by trondhjemite, tonalite and granitoid gneisses. For the first time we will be able to produce temperature estimates for this suite of rocks and make comparison with temperatures calculated for peak and post-shock metamorphism in the granulite-grade supracrustals found within the Inlandsee Leucogranofels (ILG).

Therefore, the aim of this project is to provide further information for an already comprehensive database recorded for the dome, specifically along a transect believed to represent a vertical section of crust brought on edge. Both the metamorphism and the oxygen isotope data will be considered in terms of their relationship to the impact event and our current understanding of the processes involved in impact cratering, specifically at Vredefort.

CHAPTER 2
GEOLOGICAL CONTEXT OF THIS STUDY

2.1 GEOLOGICAL SETTING OF THE VREDEFORT STRUCTURE

The Vredefort structure consists of a crystalline Archean basement core surrounded by an uplifted and overturned sequence of Precambrian strata, which is largely covered by Karoo sediments (Bisschoff, 1988) (Fig. 2.1.1). Exposure occurs predominantly in the NW quadrant, where the circular nature of the structure is easily observed.

In the NW quadrant, the Archean basement core consists primarily of gneissic trondjhemites, tonalites and granitoids with xenoliths of mafic and ultramafic granulites and a sequence of metasediments. The crystalline rocks have been categorized into two terranes, based on apparent petrological and geochemical differences as well as metamorphic grade, namely the amphibolite-grade Outer Granite Gneiss (OGG) terrane and the granulite-grade, inner, Inlandsee Leucogranofels (ILG) terrane (Fig 2.1.1) (Stepto, 1990). Metasediments found in the ILG terrane are commonly known as the Steynskraal Formation, due to the significant outcrops located on Steynskraal farm. Stepto (1990) delineated the basement core into three concentric zones, with the Steynskraal formation separating the OGG and the ILG, however, the more widely accepted view is that the Steynskraal metapelites are a group of xenolithic metasedimentary rocks caught up in the ILG.

The nature of the contact between the ILG and OGG has proved to be a debatable issue, with researchers initially proposing that it is a gradational transition between two genetically related igneous bodies (Stepto, 1979: Hart *et al.*, 1981). Hart *et al.* (1990a, b), then suggested that it is instead a sharp contact between basement rocks of different ages. They support this proposal with evidence in the form of geological mapping and with radiogenic whole rock geochronology data which suggests the age of formation of the ILG is ~3.5 Ga and the OGG ~3.0 Ga (Table 2.1.1). Hart *et al.* (1990a) postulate that the ILG is lower crust which has been juxtaposed against the upper crust (OGG), and that the transition zone represents a pre-2.0 Ga intracrustal thrust zone or a mid-crustal tectonic discontinuity which was reactivated during the 2.02 Ga Vredefort impact event (Table 2.1.1) (Kamo *et al.*, 1996, Spray *et al.*, 1995). Lana *et al.* (2003) find no such evidence for a tectonic boundary between these two basement lithologies. From lithological and structural mapping they observe the ILG and OGG to share a common polyphase tectonic history which culminated in high-grade metamorphism and melting at 3.1 Ga.

At the centre of the structure ultramafic rocks have been identified from a borehole core (Beta-1). Merkle & Wallmach (1997) suggest a magmatic origin for these peridotites and consider them to be cumulate rocks related to the Bushveld magmatic event. Hart *et al.* (1990a, 1999), in contrast, consider them to represent upper mantle which has rebounded to crustal levels following the impact event and propose that approximately 36 km of crust is exposed in the Vredefort dome. Henkel & Reimold (1998), however, propose that approximately 25km of crust is exposed in this section.

In the SE quadrant of the dome, the Archean basement is heterogenous and consists of a variety of gneisses and greenstones (Colliston *et al.*, 1987) which have been shown to be petrographically and structurally different from those exposed in the NW

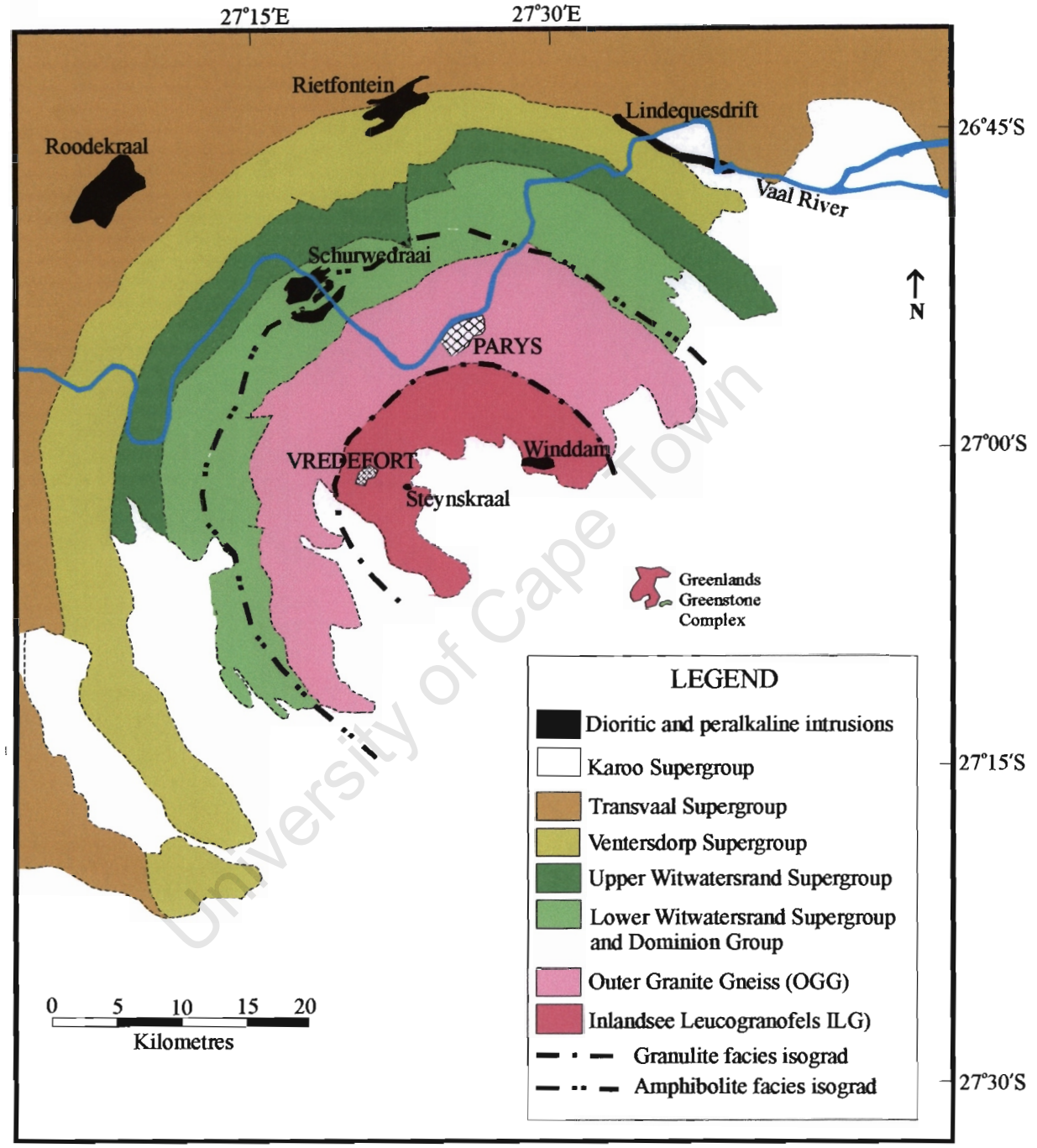

Figure 2.1.1: Map of the Vredefort dome (after Bischoff, 1988), including metamorphic facies isograds after Gibson & Wallmach (1995).

quadrant. Much of what is known about this portion of the structure has been obtained from two (sub)outcropping complexes, namely the Broodkop Migmatite complex (Colliston *et al.*, 1987) and the Greenlands greenstone complex (Minnitt & Reimold, 1994) (Fig 2.1.1).

Impact event	$^{40}Ar/^{39}Ar$*[1]	2,054 ± 11Ma	
	$^{40}Ar/^{39}Ar$*[1] (granophyre)	2,006 ± 16Ma	
	$^{40}Ar/^{39}Ar$*[2]	2,018 ± 14Ma	
	U/Pb*[3] (zircon)	2,023 ± 4Ma	
	U/Pb*[4] (zircon)	2,017 ± 5Ma	
OGG	Rb-Sr		
	Th-Pb	3,000 ± 30Ma	R_0= 0.7019
	Pb-Pb	3,060 ± 50Ma	
		3,080 ± 5Ma	
'Vredefort discontinuity'	Sm-Nd*[5]	2,471 ± 52Ma	R_0= 0.5088
Leucogranofels	Sm-Nd*6	2,836 ± 34Ma	R_0= 0.5087
	Rb-Sr	2,830 ± 30Ma	R_0= 0.7044
	Th-Pb	3,540 ± 70Ma	
Mafic and ultramafic xenoliths (ILG)	Th-Pb	3,540 ± 70Ma	
	Rb-Sr	3,488 ± 30Ma	R_0= 0.7006
	U-Pb*[6]	2,670 ± 4Ma	

Table 2.1.1: Table of age data obtained for components of the Vredefort basement. Data from: *[1] Allsopp *et al.* (1991), Spray *et al.* (1995), *[3] Kamo *et al.* (1996), *[4] Gibson *et al.* (1997), *[5]Hart *et al.* (1990a), *[6] Menuge (1982), *[6] Moser *et al.* (1997, 2001), all other data from Hart *et al.* (1981).

In the NW quadrant the unconformable core-collar contact reveals rocks of the OGG in contact with discontinuous metavolcanics and metasediments of the Dominion Group, followed outwards by supracrustals of the Witwatersrand, Ventersdorp and Transvaal Supergroups, which dip steeply (70-80°) towards the centre of the structure. Here, the stratigraphic sequence forms an almost complete stratigraphic section as observed in the Witwatersrand Basin, only exhibiting higher grades of metamorphism (Fig. 2.1.2), but in the SE quadrant only three outcrops of Orange Grove Subgroup ferruginous shales and orthoquartzites of the Lower Witwatersrand Supergroup are exposed on the eastern side of the Greenlands greenstone complex. These represent the best outcrop of collar rocks in the Southeastern perimeter of the dome and are significantly structurally atypical compared with the collar rocks in the NW quadrant, since they dip at shallow angles (30-40°) (Bisschoff, 2000) towards the Southeast, away from the core and strike oblique to the projected rim of the core (Du Toit, 1954).

To date, three hypotheses exist regarding the origin of the structure. These include an exogenic, catastrophic, shock event resulting from meteorite impact, as well as two endogenic models; one of which is based on catastrophism and the other on purely tectonic

reasoning. However, the most popular and widely accepted hypothesis is that the Vredefort dome is a deeply eroded remnant of an impact crater.

The first endogenic model to be put forth was that of a catastrophic internal process by Nicolayson (1972). He proposed that the shock deformation features observed in the structure may be the result of a "deep-seated CO_2-rich gas explosion" (Nicolayson & Ferguson, 1990). This model also has a tectonic/magmatic diapirism aspect to it to account for the updoming of the basement core.

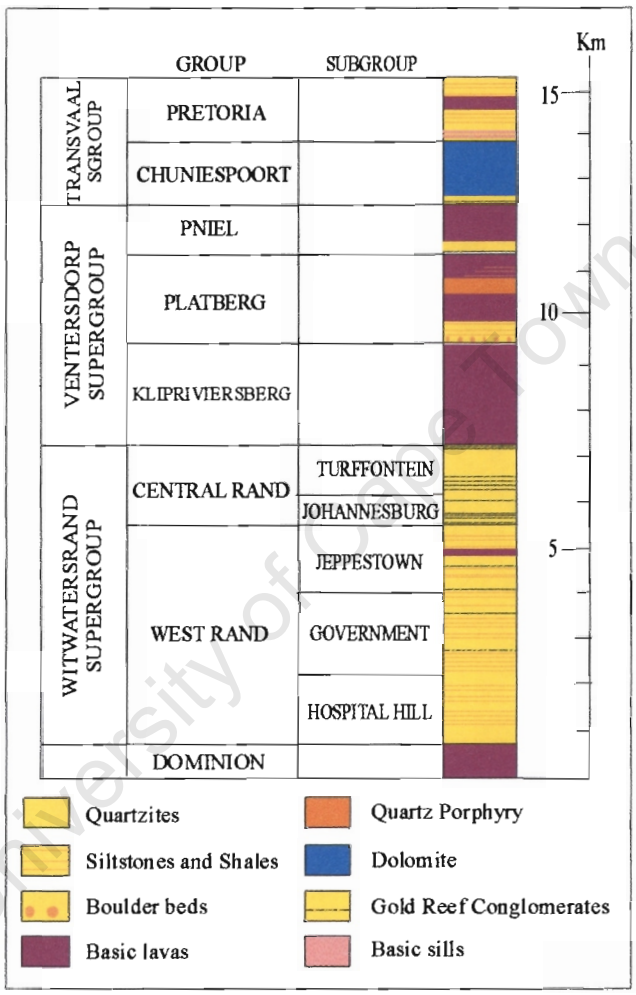

Figure 2.1.2: Stratigraphic column of the Witwatersrand, Ventersdorp and Transvaal Supergroups and Dominion Group constituting the fill of the Witwatersrand Basin, and as observed in the Northwestern quadrant of the Vredefort Dome (After Fletcher & Reimold, 1989).

Slawson (1976) then put forth his 'crust-on-edge' model (Fig. 2.1.3), suggesting that the central granitic portion of the structure had been extruded from depth, as a sub-solidus outflowing of granitic basement material through diapiric mechanisms. This model is based on the "bulls-eye" pattern of Rb/Sr and K/Rb ratios obtained for the basement core, where in general, the Rb/Sr ratios decrease towards the centre of the structure whilst K/Rb ratios increase radially inwards. These trends support the postulation of a vertically differentiated crust (Zartman & Wasserburg, 1969), with the rocks at the centre of the core being

representative of a greater crustal depth than those at the perimeter. Further evidence in support of a diapiric model for the emplacement of the basement core was focussed on the core-collar contact, where Slawson (1976) suggested that the granites had "neither engulfed nor baked the sediments, thus indicating a sub-solidus extrusion".

This 'crust-on-edge' model received support from detailed studies based on radiogenic crustal profiles through the basement (Hart *et al.*, 1981, 1990a), and the restriction of assemblages of the highest metamorphic grades to the innermost unit, the Inlandsee Leucogranofels (ILG) terrane (Stepto, 1990). Hart *et al.* (1981, 1990a,b) propose that the Vredefort structure provides a unique 'window' into the deep Archean geology of the Kaapvaal Craton. They suggest that an ~36 km section through the crust has been uplifted and turned 'on-edge' to expose a section of increasing crustal depth on the surface, towards the centre of the structure. Indeed, they propose that the 14 km of granitoid basement from the core-collar contact to the centre of the dome, is representative of a 14km vertical section through the upper and lower crust, and suggest that the variations in both major and trace elements across the basement are consistent with the 'crust-on-edge' model. The major and trace element profiles of Hart *et al.* (1990b) are important for consideration with respect to this study and are discussed in detail later in the chapter.

Colliston (1990) proposed an entirely tectonic model to describe the formation of the structure. It involves the initiation of a deep crustal shear zone being formed at the crust-mantle interface. Such a Northeast-trending and Southeast-dipping shear zone could propagate through the lower and middle crust to produce folding and, ultimately, faulting and, hence, result in crustal thickening to the Northwest to produce an asymmetrical domal feature (Fig. 2.1.4). Although Colliston (1990) provides suggestions for the explanation of shock features, the field evidence to support such a theory is based largely on preliminary structural studies which indicate foliations in the lower Witwatersrand Supergroup rocks and a shear zone at the basement-Dominion Group contact.

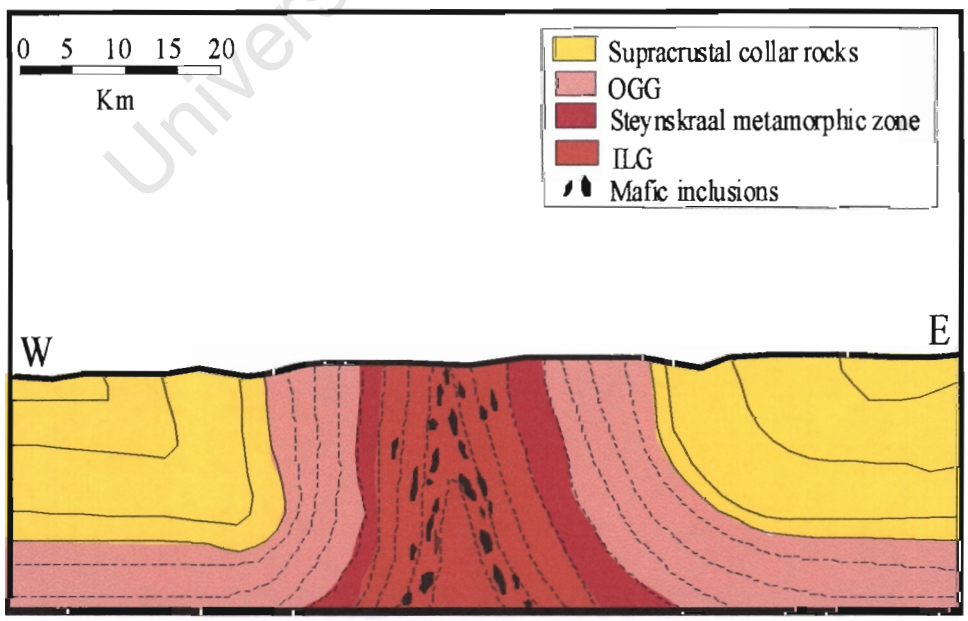

Figure 2.1.3: Schematic diagram of the Vredefort structure as suggested by Slawson's (1976) 'crust-on-edge' model (after Hart *et al.*, 1981; Stepto, 1990).

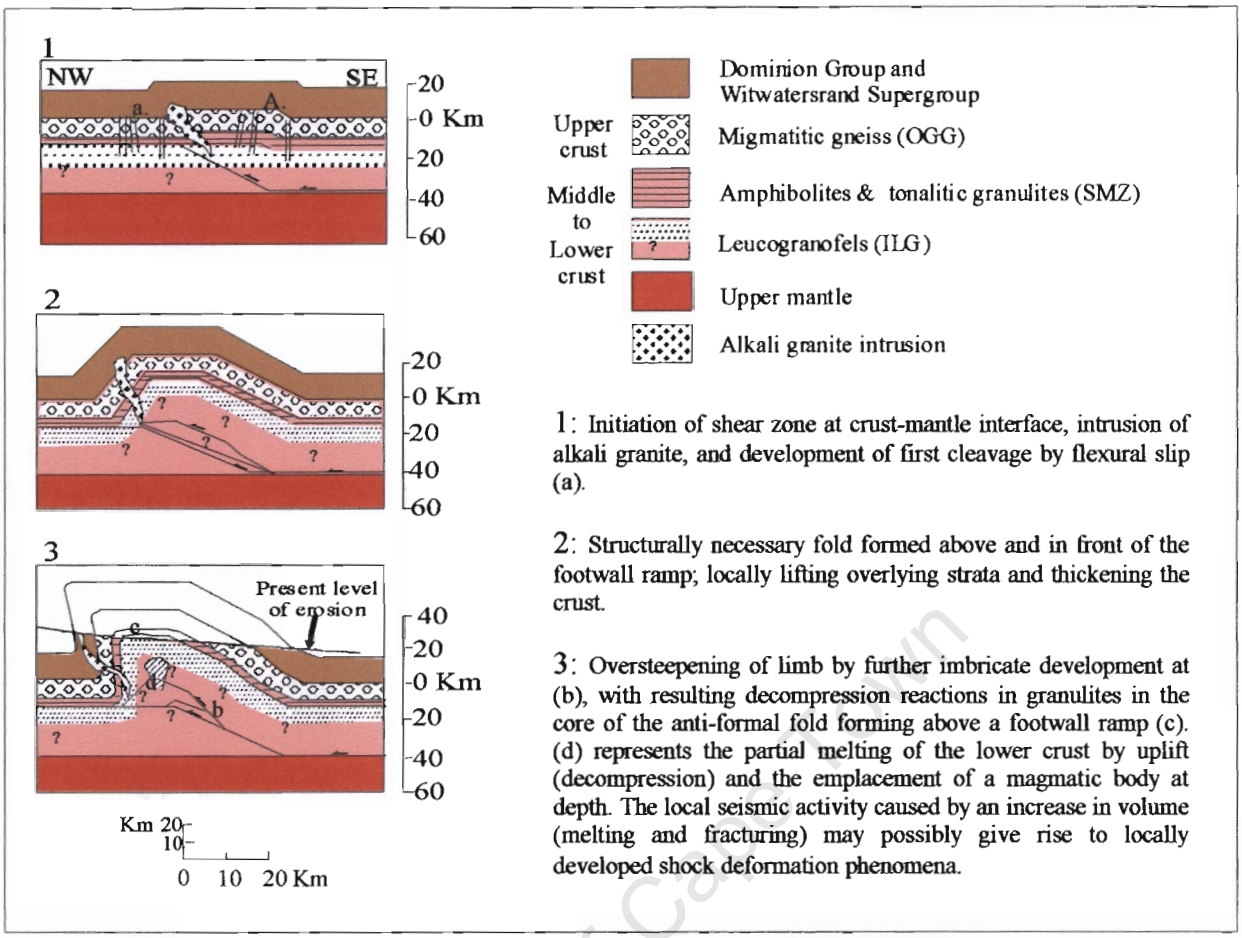

Figure 2.1.4: Schematic illustration of the tectonic model proposed by Colliston (1990) for the origin of the Vredefort structure (Adapted from Colliston, 1990).

After almost a century of detailed geological research, the most widely accepted hypothesis of origin remains that of an impact structure. Shand (1916), Nel (1927) and Hall & Molengraaff (1925) were the first researchers to speculate on a catastrophic origin for the structure after having highlighted the dynamic deformation features observed in the rocks of the Vredefort Dome. Daly (1947) was the first to suggest that extraterrestrial processes may have produced the Vredefort 'cryptoexplosion' structure, but it was Deitz (1960, 1961) and Hargraves (1961) who became the first ardent supporters of an impact origin for the Vredefort structure. Since then, many researchers have endeavoured to produce conclusive evidence in support of this theory and, to date, the hypothesis that the Vredefort structure is a deeply eroded remnant of an impact crater (Fig. 2.1.5) is predominantly supported by the following rock deformation features:

- The abundance of pseudotachylite (Bisschoff, 1962; Fletcher & Reimold, 1989; Killick & Reimold, 1990; Reimold, 1991)
- The presence of abundant shatter cones within the rocks of the collar strata (Deitz, 1961; Hargraves, 1961)
- Sub-planar microdeformation features in quartz (Grieve *et al.*, 1990; Reimold, 1990)
- Coesite and stishovite (high pressure polymorphs of quartz) within pseudotachylite veins (Martini , 1978, 1991).
- The Vredefort Granophyre, which has been interpreted on the grounds of its geochemical composition to be a meteorite impact-melt rock (Koeberl *et al.*, 1996).

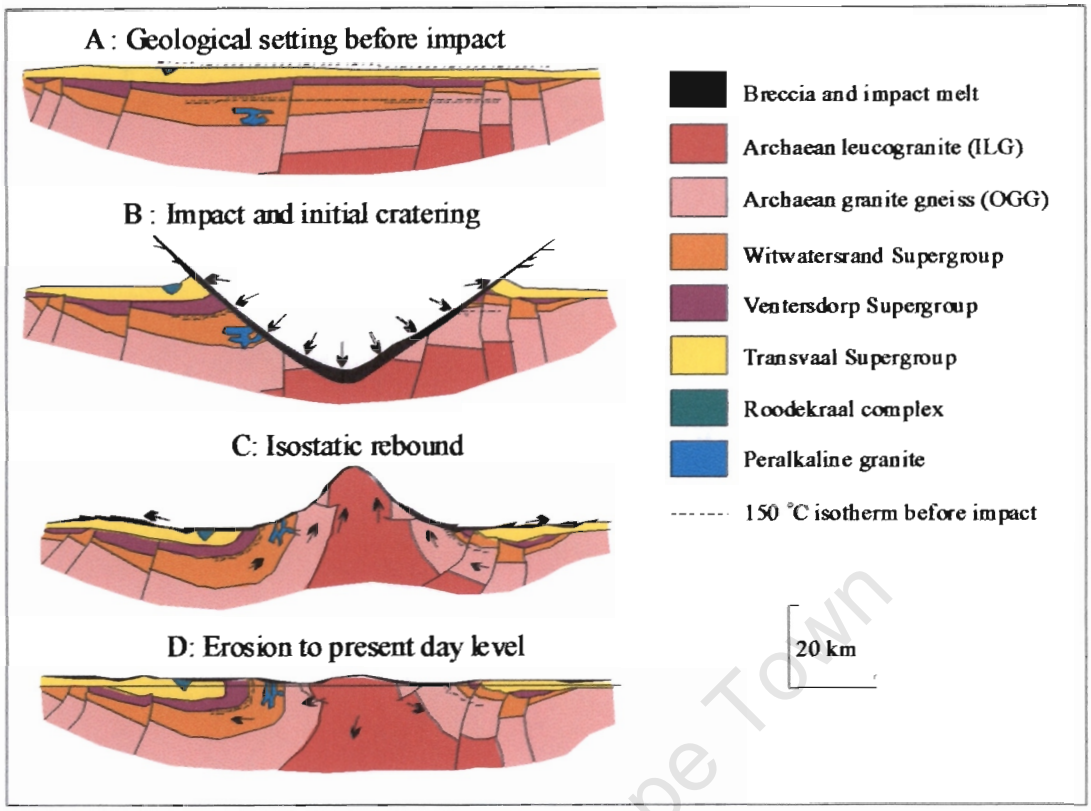

Figure 2.1.5: Model depicting the evolution of the Vredefort structure as a result of impact cratering (after Martini, 1992). Arrows indicate direction of motion of the crust due to impact in B and isostatic rebound in C.

2.2 STRUCTURE

2.2.1 Folding and Faulting

Macrostructural features, predominantly in the form of folding and faulting, are important components of the Vredefort dome. The most obvious effects of extreme folding are seen in the collar rocks in the NW quadrant of the dome. Detailed structural studies within the collar and rim syncline strata (Hall & Molengraaff, 1925; Nel, 1927; Manton, 1965; Simpson, 1978; Lilly, 1980; Brink, 1986) emphasize the ubiquitous occurrence of major thrust faults which define a concentric shape surrounding the central basement rocks. Manton (1965) had shown that the strike length of the collar rocks has been shortened by faulting and Lilly (1980) explained the fault pattern as a result of centripetal motion of the collar rocks along bounding concentric faults. In the Northwestern and Northern parts of the collar, concentrically aligned granophyre dykes are present and are presumed to have intruded along fault structures, which Lilly (1980) identified as wrench faults for which he assumed the fault planes to be vertical. He showed that over most of the collar the maximum principal stresses were tangential during faulting, and that a 'collapsing collar' could generate such a stress field.

Simpson (1978) pointed out structures in the rim synclinorium which are symmetrical about the exposed collar rocks, including strike-slip faults and normal faults which are

concentric and/or radiate outwards from the collar. She describes these faults as dipping and downthrown towards the core and suggests that they are the result of the maximal principal stresses associated with the overturning of the collar strata acting upwards and outwards. Folding on a local and regional scale also mimics this concentric shape (Fig. 2.2.1.1) and is discussed in detail by McCarthy *et al.* (1986).

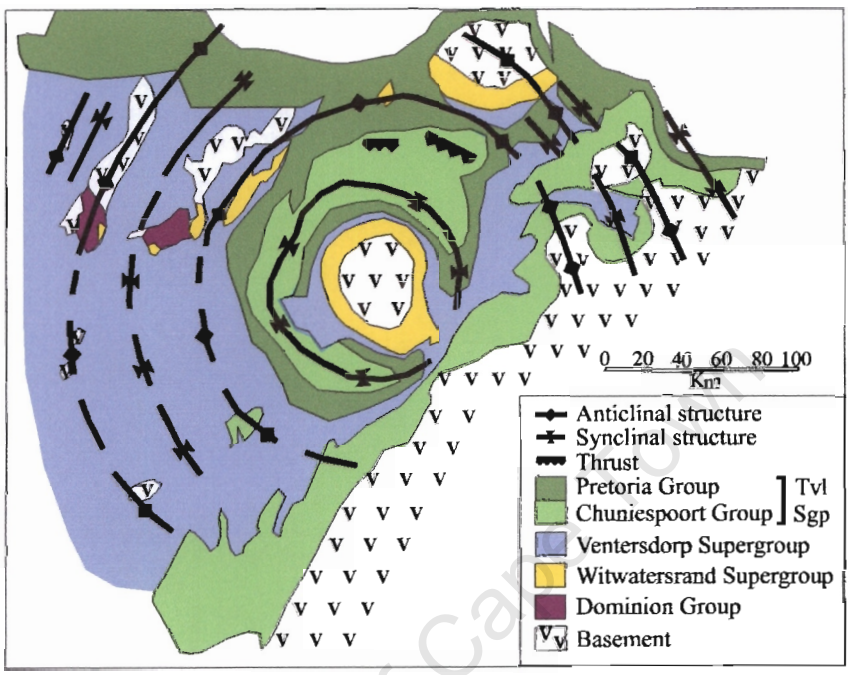

Figure 2.2.1.1: The fold pattern associated with the Potchefstroom (innermost) and Rim Synclinorium, which concentrically surrounds the Vredefort dome (after McCarthy *et al.*, 1990).

Although most of the macrostructural deformation in the collar is related to the Vredefort event, some of it can be attributed to the reactivation of pre-Vredefort structures. Roering *et al.* (1990) have identified pre-Vredefort deformation structures within the Witwatersrand Basin which should be considered in terms of the deformation structures observed within the Vredefort dome. These include several periods of extension and contraction, namely (1) a pre- and syn-early Ventersdorp (2.7 Ga) thrusting event, (2) middle Ventersdorp normal faulting, (3) middle Ventersdorp thrust faulting and (4) post-Transvaal tectonic activity prior to the Vredefort event.

The first group of structures include deformation events resulting in the foliation observed in granite-greenstone remnants within the basement core (prior to 3.1 Ga), compressional folding and faulting of Dominion Group rocks prior to Witwatersrand sedimentation, and a single pre- to syn-Klipriviersberg contractional event. During the latter event the Upper West Rand Group Witwatersrand strata experienced folding and thrust faulting. The middle Ventersdorp normal faulting event (2) is an extensional event which has been well documented in the literature throughout the Witwatersrand Basin (Winter, 1964; Olivier, 1965; Brink, 1986; Engelbrecht, 1986; Tucker & Viljoen, 1986; Tweedie, 1986; Vermaakt, 1987; Van Coller, 1987). Event (3) is characterised by Northerly-verging thrust faults and is exceptionally important in terms of the Vredefort Dome because some of the contractional faulting so clearly evident in the overturned collar rocks may well be related to this ~2.5 Ga compressional event, and would thus predate the Vredefort event. The post-

Transvaal tectonic activity (4) is significant with respect to the strain history of the rocks surrounding the Vredefort structure because of their relationship to both the emplacement of the Bushveld Igneous complex and the Vredefort impact event.

Beukes (1983) showed that at the time of the deposition of the Transvaal Supergroup a shallow water carbonate platform existed over most of the Kaapvaal Craton. These data showed that the Bushveld Igneous Complex was not emplaced in the middle of the Transvaal basin and that there was no expression or influence of the Vredefort structure at that time. Post Transvaal compressional, extensional and lateral displacement deformations have been identified, but their order of occurrence and relationship to the emplacement of the Bushveld Igneous Complex (2.05 Ga) is uncertain. One important implication drawn from such deformation structures is that an East-directed, horizontal, compressional stress field was in existence prior to the formation of the Vredefort structure.

In the core of the structure the earliest deformation features identified in the basement granitoid gneisses and associated metasedimentary xenoliths are related to pre-Dominion Group Archean deformation. Three main phases of ductile deformation have been observed with D1 features largely transposed by D2 and D3 deformation, with the latter two events overlapping peak metamorphism (Lana *et al.*, 2003). Structures which define D1 deformation include an S1 gneissic foliation which is locally preserved on a centimeter- to meter-scale in the subhorizontal S1/S2 fabric, and the pervasive sub-horizontal gneissic fabric (S2) observed in most of the migmatitic basement., These were subsequently folded by a NW-trending subvertical S3 fabric (Colliston *et al.*, 1987; Colliston & Reimold, 1990; Minnet *et al.*, 1994; Lana *et al.*, 2003) which itself exhibits late-D3 extensional shear bands (Fig 2.2.1.2) Stepto (1990).

Figure 2.2.1.2: D3 extensional shearing observed in the migmatised Outer Granite Gneisses at Leeuwkop Hill quarry.

2.2.2 Shock Deformation Features

The spectacular rock deformation features observed in the Vredefort structure are the structural features which predominantly fuelled the theory of origin by bolide impact. Evidence of dynamic rock deformation is pervasive in the form of shatter cones, planar

features in quartz grains, the occurrence of voluminous pseudotachylite, the Vredefort granophyre and the occurrence of the high-pressure SiO_2 polymorphs, coesite and stishovite. In particular, the Vredefort structure is the type locality for pseudotachylite (Figs. 2.2.2.1 and 2.2.2.2) and is world renowned for its shatter cones (Fig. 2.2.2.3).

Pseudotachylite

Shand (1916) coined the word 'pseudotachylite' to describe a breccia rock consisting of a dark, fine-grained matrix supporting clasts of the surrounding country rocks. Presently it is widely regarded to be a fault breccia formed 'as a friction melt as a consequence of co-seismic slip in brittle and brittle-ductile transition regimes of the upper crust' (Maglaughlin & Spray, 1992). Tectonically formed pseudotachylite veins seldom exceed a width of more than 30 cm. In contrast, enormous volumes of pseudotachylite have been identified in large impact structures, namely the Sudbury structure (Dressler, 1984; Thompson & Spray, 1996), the Roter-Kamm impact crater (Reimold & Miller, 1989), and the Vredefort structure (Fig 2.2.2.1 & 2). Reimold (1993b) suggested a distinction between these two types of pseudotachylite under the premise that the large-scale pseudotachylites observed in impact structures might not be friction melts and recommend the term 'pseudotachylite breccia' for the latter.

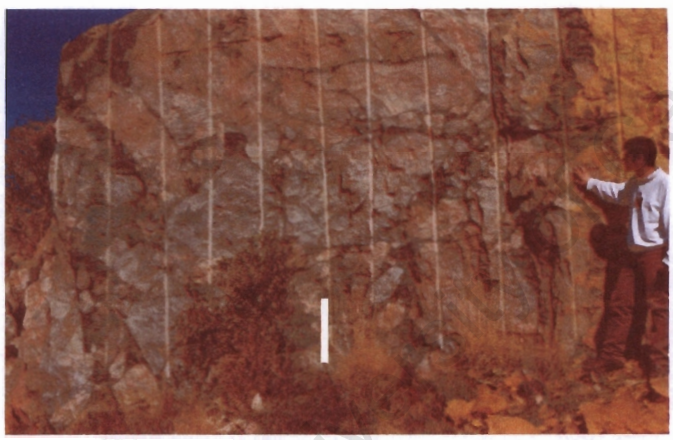

Figure 2.2.2.1: Photograph (~3m x 3m) detailing massive clast-laden pseudotachylite in the Leeuwkop quarry, Vredefort.

Figure 2.2.2.2: Massive pseudotachylite breccia observed in the Leeuwkop granite quarry in the well exposed NW quadrant of the Vredefort dome. Width of photograph ~10m and height ~20m.

Bisschoff (1962), Fletcher & Reimold (1989), Killick & Reimold (1990), Martini (1991), Reimold (1991) and Reimold & Colliston (1994) provide detailed summaries of the Vredefort pseudotachylite breccia. To date, there has been a tendency for Researchers to distinguish pseudotachylites of endogenic origin (frictional melts) and impact-related origin (shock generated) (Reimold, 1995; Spray, 1998). For those of impact origin, there is a further distinction between at least two generations of pseudotachylite. A-type (Martini,

1992) or S-type (Spray, 1998) are believed to be formed during shock compression within the crater floor and can therefore contain high pressure polymorphs such as coesite and stishovite. The second generation of impact-related pseudotachylites, B-type (Martini, 1992) or E-type (Spray, 1998) postdate the former generation and are a product of the collapse of the transient crater and decompression melting. Most recently, Kenkmann *et al.* (2000) showed that frictional melting may occur during shock compression.

Field observations, $^{40}Ar/^{39}Ar$ dating and Rb/Sr dating of Vredefort pseudotachylite breccia (Reimold *et al.*, 1987, 1988, 1990; Fletcher & Reimold, 1989; Killick & Reimold, 1990) initially favoured several phases of pseudotachylite development, specifically prior to 2.0 Ga, at 2.0 Ga and from 1.1–1.4 Ga. However, from the most recently obtained geochronological data (Spray *et al.*, 1995; Kamo *et al.*, 1996) it appears that most of the Vredefort pseudotachylitic breccia was formed during the Vredefort event. This contemporaniety with the impact event does not, however, provide further clarification whether the bulk of the Vredefort pseudotachylite was formed by compression and/or decompression melting or by the tectonic process of frictional melting.

Multiple generations of pseudotachylite have also been identified from within the Witwatersrand Basin (Killick & Reimold, 1990). Most of these are associated with South-dipping bedding faults tangential to the dome or within N-S trending normal faults. Killick & Roering (1998) observed these faults to have a normal dip-slip movement sense, which is consistent with inward collapse of the impact crater, however, further research is required to describe the relationship between these pseudotachylite occurrences and pseudotachylite from the Vredefort dome.

Shatter cones

Shatter cones of the Vredefort structure (Fig. 2.2.2.3) are most abundant in the Witwatersrand Supergroup rocks of the collar strata. They have also been observed in the komatiitic basalts of the Greenlands Greenstone complex, but are very rarely seen in the basement gneisses. Hargraves (1961) reported the first findings of shatter cones in the Vredefort structure, shortly after the presence of shatter cones had been reported as unambiguous evidence for the occurrence of impact structures (Deitz, 1961). However, although shatter cones are observed to be associated with a large number of proven impact structures, there is no *bona fide* recognition criteria for these deformation features as components of impact cratering yet.

Manton (1965), Albat (1988) and Albat & Mayer (1989) postulate that the apex orientation of a 'master cone' (the stereographic composite representation of a number of cones) will point towards the centre of an impact structure. In contrast, Nicolayson & Reimold (1987) pointed out that the formation of the Vredefort shatter cones can be related to multiple sets of closely spaced, curviplanar joints, termed multiply-striated joint sets (MSJS), and that the measured poles of striations of the shatter cones always cluster around intersections of joint traces, or along the joints. Furthermore, these authors showed that after rotation of the host rocks back to the horizontal, the shatter cones in the collar are not always oriented towards the centre of the dome. In addition to this, Reimold & Colliston (1994) found evidence of MSJS cross-cutting older pseudotachylitic breccia, implying these pseudotachylites were formed prior to the Vredefort event. Simpson (1978, 1981) reported the superimposition of shatter cones on a fault gouge which has been related to the upturning of the collar rocks, thus one of these features cannot be related to the shock

event. Only one of these observations must hold true, and since no evidence supporting other mechanisms for the formation of these shatter cones has come to light, their interpretation as deformation features related to an impact event, seems most plausible.

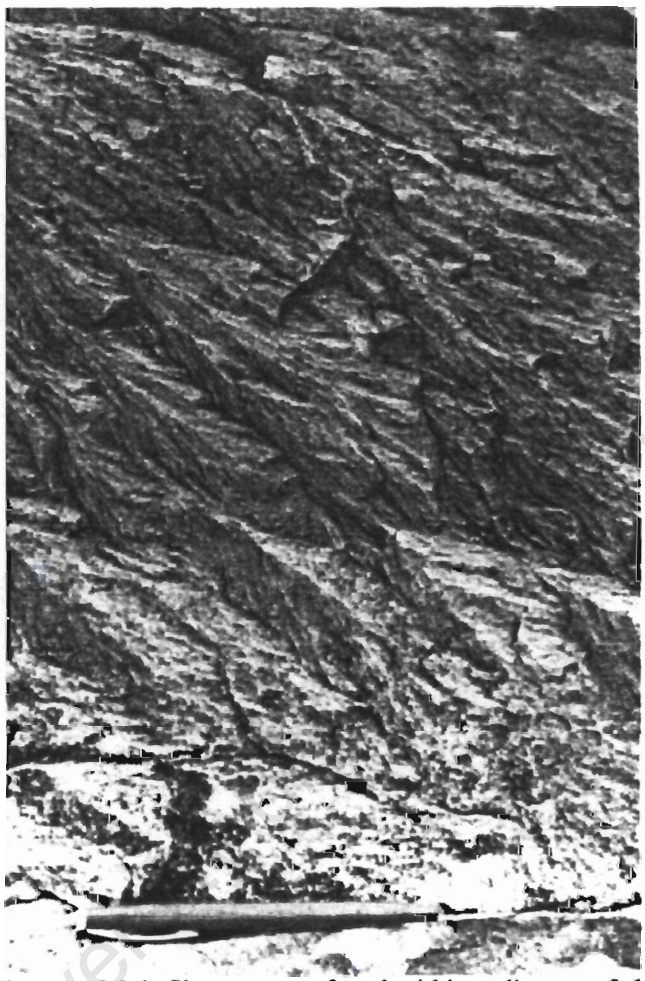

Figure 2.2.2.3: Shatter cones found within sediments of the Witwatersrand Supergroup in the Vredefort structure. See pen (~12 cm) in foreground for scale (from Reimold *et al.*, 1989).

Planar microdeformations in quartz

The discovery of planar microdeformations in Vredefort quartz grains (Fig. 2.2.2.4 and 2.2.2.5) was initially widely accepted as direct evidence for an impact origin (Carter, 1968). Since then much research in this field (Grieve *et al.*, 1990; Reimold, 1990; Leroux *et al.*, 1994) has shown that the (sub)planar microdeformations observed in Vredefort quartz are anomalous as impact indicators when compared to *bona fide* shock-produced planar deformation features (PDFs), as defined by Alexopoulus (1988).

Grieve *et al.* (1990) and Leroux *et al.* (1994) provide an explanation for this anomaly, by suggesting that most of the original shock defects in the rocks of the ILG terrane have been overprinted by an intense post-shock annealing event. The observation of such an annealing event also explains why the concentration of PDFs in quartz reach a maximum in the vicinity of the OGG-ILG transition zone (Reimold, 1990; Hart *et al.*, 1991), instead of increasing incrementally towards the centre of the dome.

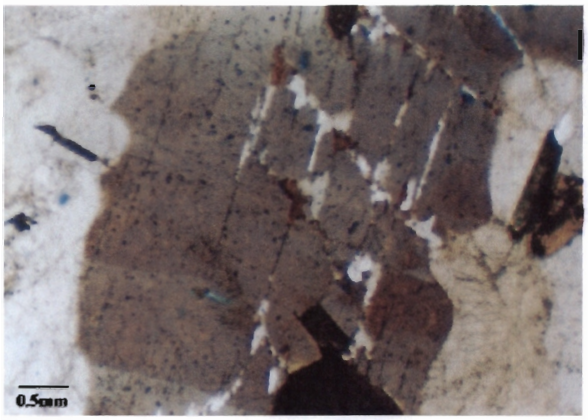

Figure 2.2.2.4: Planar deformation features (PDFs) observed in quartz under cross polarized light in sample 432. Note how quartz recrystallisation has occurred along the PDFs, which is typically how they are observed in most of the samples from the basement core.

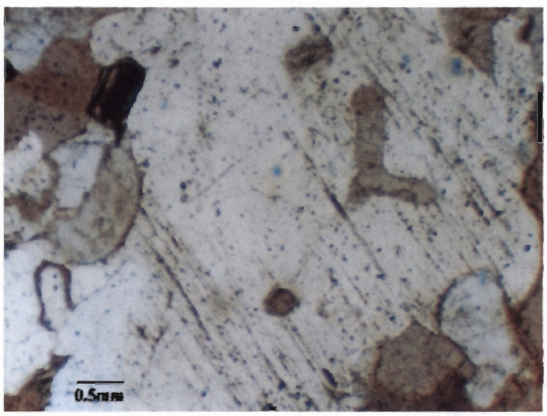

Figure 2.2.2.5: Photograph of PDFs observed in quartz in sample 432.

Vredefort granophyre

The Vredefort Granophyre occurs as vertical tangential dykes along the core-collar boundary and as vertical dykes trending NW-SE and NE-SW in the basement core. It is a regionally homogenous rock type and has an unusual chemical composition (~67% SiO_2, ~13% Al_2O_3, ~7% Fe_2O_3, ~3.5% MgO, ~ 3% CaO and ~2.5% each of K_2O and Na_2O). French & Neilson (1990) postulate that this composition can be produced by the impact melting and mixing (homogenization) of four rock types which constitute the lower part of the Vredefort stratigraphy, namely the Ventersdorp lavas (30-80%), Witwatersrand shales (5-20%) and quartzites (20%) and a granite component which varies inversely with basalt (5-25%). They provide further motivation for the granophyre being an impact melt rock based on its relationship to pseudotachylites. The granophyre is cross-cut by younger, undeformed, fracture-related pseudotachylite veins, but also cross-cuts older pseudotachylites. This implies the granophyre was formed at or immediately post-impact. These authors continue to support the hypothesis of an impact origin for the granophyre, even though they detected no enrichment in siderophile elements (e.g. Ir) derived from an extraterrestrial source. Clasts found within the granophyre include quartzite, siltstone, shale and granite. No characteristic shock deformation features have been observed in these clasts, although they do exhibit thermal alteration textures (Reimold, 1991). Therriault *et al.* (1997) argue against the granophyre being an impact melt rock based on the lack of shock metamorphic effects in the component clasts, and because of the strict structural control on its emplacement. Since then, however, Reimold *et al.* (2002) have found evidence of siderophile elements in the granophyre and Koeberl *et al.* (1996) have found a meteoritic component using Re-Os isotopes. The granophyre has thus been confirmed as an impact melt rock on the basis of this meteoritic Os, a small amount of which is observed in all Vredefort granophyre analysed.

O' Neil *et al.* (1987) produced limited $\delta^{18}O$ data for the granophyre, which yielded $\delta^{18}O$ values (7.3-7.9‰) similar to those obtained for the OGG (7.6-8.3‰) and the ILG (7.8-10.0‰). The upper range of $\delta^{18}O$ values for mafic rocks is 6-7‰ (Faure, 1986), therefore

one would expect the granophyre to have a relatively depleted isotopic signature relative to the granites due to a large proportion (80% basalt) of mafic material being the dominant component. Thus it seems the granophyre may have experienced an isotopic resetting associated with that of the surrounding granites, resulting in the observed enriched values.

Coesite and stishovite

Martini (1978) described the presence of the high pressure SiO_2 polymorphs, coesite and stishovite from pseudotachylite veins in the Vredefort structure. The positive identification of these minerals by McHone & Nieman (1988) was made using neutron-magnetic resonance techniques. Coesite has been observed in high grade metamorphic rocks, but stishovite has only been found associated with impact structures, since it is believed to be formed only under pressures of 80 kbar or more (Akaogi & Navrotsky, 1984). Thus, Martini (1991) proposed an impact model to account for the presence of these minerals in the Vredefort structure.

2.3 GEOPHYSICS

Geophysical techniques were initially implemented in the Vredefort structure by Maree (1945) in an attempt to further delineate the extent and nature of the structure, which is largely covered by Phanerozoic Karoo Supergroup sediments. It was found that the structure is, indeed, asymmetric. Since then detailed gravity, aeromagnetic, reflection and refraction seismic studies have been carried out over the Vredefort dome (Corner *et al.*, 1990; Green & Chetty, 1990; Antoine *et al.*, 1990; Stepto, 1990; Durrheim, 1991). The polygonal geometry of the core-collar contact is the most striking feature observed on gravity and magnetic images (Fig. 2.3.1). The basement rocks are characterized by a central circular gravity high (Fig. 2.3.2) which Corner *et al.* (1990) attributed to a core with a density typical of a diorite. Other explanations for this central positive Bouguer gravity anomaly include the presence of a deep-seated underlying pluton, a sheet intrusion (Green & Chetty, 1990) and even uplifted mantle material (Hart *et al.*, 1990b). The latter is based on the reported findings of ultramafic rocks in a borehole from the centre of the basement core, and such an observation clearly supports the 'crust-on-edge' model. The work of Stepto (1990) involving detailed gravity modelling of the basement also allows for the 'crust-on-edge' model to account for the observed gravity high. However, comprehensive modelling of the gravity field across the entire Witwatersrand Basin and the Vredefort Dome by Henkel & Reimold (1996a, b), rules out earlier suggestions that dense mantle material could have contributed to the observed gravity signature.

Another important geophysical feature within the basement rocks is a horse-shoe shaped negative magnetic anomaly which roughly defines the contact between the OGG and the ILG. It is in the area which Stepto (1990) terms the Steynskraal Metamorphic zone (SMZ), and the high magnetic remnance in this area has been attributed to elongated, single-domain magnetite particles found along PDFs in quartz grains (Cloete *et al.*, 1999; Hart *et al.*, 2000).

The Vredefort structure is situated at the intersection of two regional structural axes, namely a NNE-trending axis of crustal downwarp and the NW-trending Vredefort axis. A gravity low in the Southeastern parts of the structure which extends to Edenville indicates the presence of relatively shallow basement and an opening of the structure to the Southeast (Corner & Wilsher, 1989), and is regarded as part of the fundamental geanticline

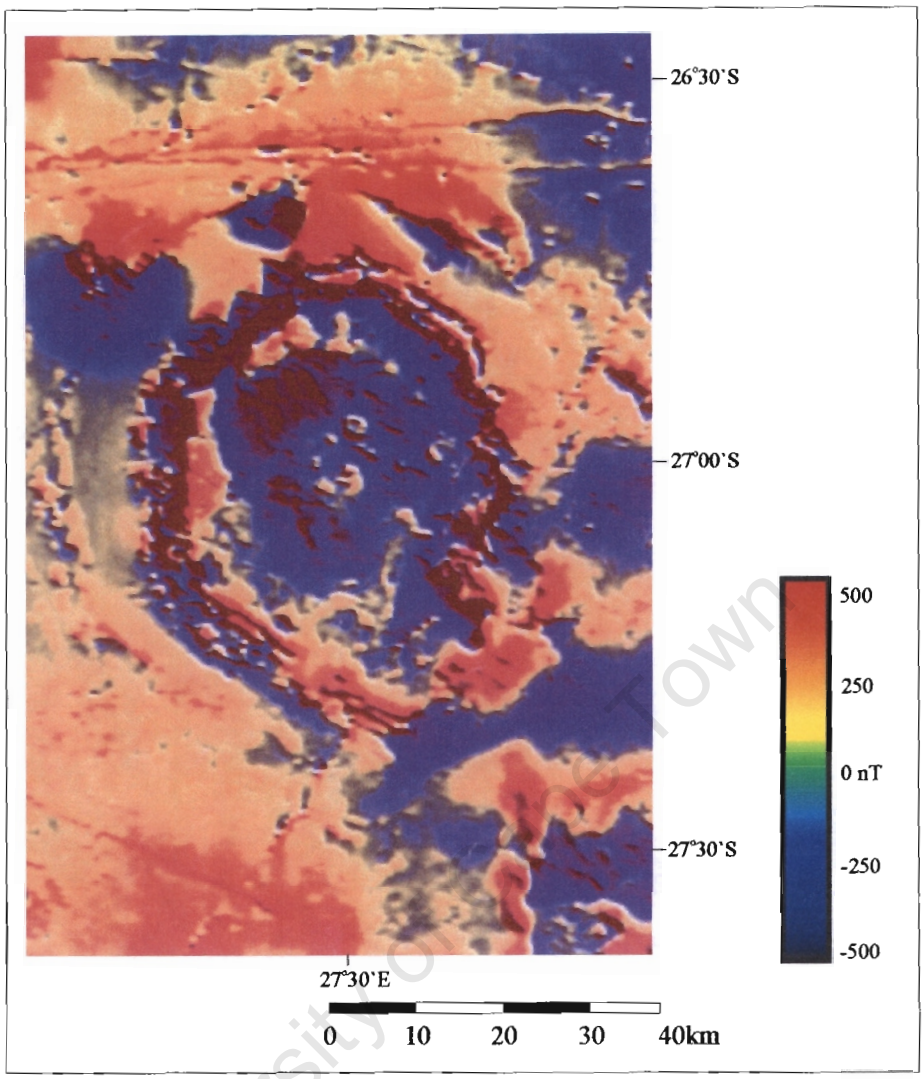

Figure 2.3.1: Magnetic map of the Vredefort structure (courtesey of R. J. Hart) illustrating its open-ended polygonal shape.

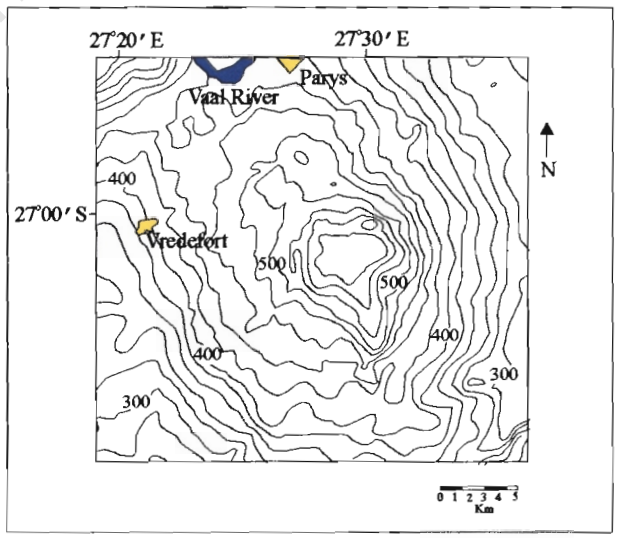

Figure 2.3.2: Bouguer gravity map of the central parts of the Vredefort dome (from Corner *et al.* 1990).

termed the Vredefort axis. The latter is an apex of crustal upwarp which extends along the crest of the Bethlehem gravity high, Northwest across the Vredefort structure and bisects the Potchefstroom Gap. The Witwatersrand Basin is roughly symmetrical about the Vredefort axis. The NNE-trending regional axis includes the Johannesburg Dome, the Trompsberg Complex and bisects the Bushveld Igneous Complex, and Corner & Wilsher (1989) suggest that the long axis of the Witwatersrand Basin lies on this lineament. Corner *et al.* (1990) propose that the central positioning of the Vredefort structure in relation to these axes strongly supports a tectonic control for its formation. The gravity and magnetic research of Henkel & Reimold (1996a, b) indicates that the structural uplift in the region of the Vredfort Dome is in the order of 13 km, and they continue to give support to an impact process for the structure.

2.4 INTRUSIONS

The Vredefort structure is intruded by numerous igneous bodies, which are discussed in detail by Bisschoff (1988) and Stepto (1990). The oldest intrusions in the collar rocks are epidiorite sills and dykes which intrude into the Witwatersrand and Ventersdorp Supergroups and were emplaced before the main episode of impact-related faulting since the sills are displaced by faulting.

Younger basic rocks also intrude the latter two Sequences as well as the Transvaal Supergroup and include dykes of dolerite, norite and orthopyroxenite, as well as the Losberg complex in the Potchefstroom synclinorium (Bisschoff, 1988). These can be correlated with mafic rocks of the Bushveld Igneous Complex and are thus pre-uplift in age.

Several intrusions occur in the Northwestern sector of the collar and include the Rietfontein, Roodekraal and Lindequesdrif complexes, as well as the nepheline syenite Schurwedraai body (Fig. 2.1.1). The Roodekraal and Lindequesdrif complexes are predominantly dioritic and andesitic in composition, whilst the Rietfontein body consists of a hypersolvus peralkaline granite that intrudes into a layered mafic pluton, which includes minor amounts of wehrlite, olivine diorite and troctolite. Subsolvus granitic dykes occur along the Vaal River in this vicinity and a few small wehrlite bodies are intrusive into the Central Rand Group quartzites on Koedoesfontein farm.

All of the intrusions display shatter cones and are cross-cut by pseudotachylite. The timing of their emplacement is therefore important when considering the internal evolution of the structure, since it appears that they were emplaced prior to the shock event.

Stepto (1990) observed the emplacement of most of the above-mentioned mafic and ultramafic intrusions in the core of the Vredefort dome. He subdivided the intrusions observed in the core into six categories:

1) an amphibole-orthopyroxene rock suite, which is restricted to the Steynskraal metamorphic sequence, and appears to be derived from partial melting of Archean basement which remained a closed system during metamorphism. According to Sutton & Watson (1951) it is suggested that these intrusions were emplaced prior to the peak metamorphic event at 3.1 Ga.
2) Peridotite pipes and dykes, which are observed in the ILG.
3) Metapyroxenites which predominantly intrude in the Steynskraal area and are composed of green hornblende + granular magnetite + ilmenite.

4) A tholeitic suite which includes pod-like bodies of bronzite dolerites, norite and melanorite in the Steynskraal formation and the OGG and which are considered as pre-uplift in age.
5) The Winddam wehrlite (Fig. 2.1.1) which is comparable to the wehrlite bodies in the collar, but in contrast to these is the only intrusive body which is not cross-cut by pseudotachylite. It is composed of equigranular augite + olivine + accessory plagioclase, orthopyroxene and hornblende.
6) The Vredefort granophyre which has previously been discussed.

The Central Anatectic Granite is a small, undeformed biotite granite (Fig. 2.4.1) located less than 1 km from the Inlandsee Lake. It appears to have a gradational contact with the surrounding ILG rocks and as a result, Hart *et al.* (1991) propose that it could be a product of partial melting of the ILG. (Gibson *et al.*, 1997b) have dated it at 2017 ± 5Ma from SHRIMP zircon dating, and, based on petrographic evidence, suggest that it was crystallised after the impact event. Gibson (2002) has identified it as a melt pod which has been extracted from a pelitic protolith at the time of impact.

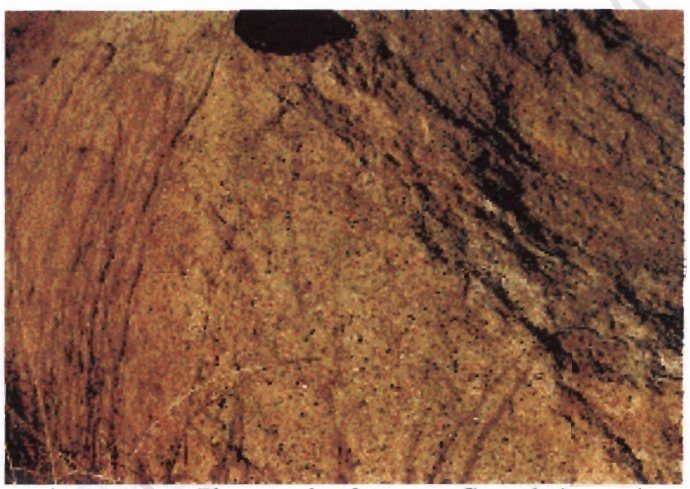

Figure 2.4.1: Photograph of *in situ* Central Anatectic Granite, note the abundant large black grains which are biotite. See camera lens cap for scale.

2.5 METAMORPHISM

The metamorphic rocks of the Vredefort dome are difficult to understand because of the polyphase thermal history they exhibit. Yet, because of the potential magnitude of their contribution to the understanding of the formation of the structure, and the metamorphism observed throughout the Witwatersrand Basin, much research has been focused on the metamorphic history of the rocks of the Vredefort dome.

To date, the metamorphism of the rocks of the Vredefort structure is understood to increase in grade radially in towards the centre of the dome (Fig. 2.1.1). Based on petrographic observation, Hall & Mollengraaf (1925) and Nel (1927) documented this increase in grade from greenschist facies in the Upper Witwatersrand metasediments of the middle collar to amphibolite grade within the lower West Rand Group of the inner collar, through mid- to upper-amphibolite grades which predominate throughout the OGG, up to granulite facies

grades within the Steynskraal metapelites of the ILG. Hall & Molengraaf (1925) concluded that the metamorphism was two-fold, with a regional event having been overprinted by a younger thermal event. They postulated the regional metamorphism to be a function of lithostatic loading as the overlying sediments and volcanics of the Dominion Group and Witwatersrand, Ventersdorp and Transvaal Supergroups were laid down onto the Archean granitic basement, whilst the thermal event was attributed to a "younger body of intrusive rocks". Nel (1927) was convinced that the metamorphism was a result of thermal metamorphism in the contact aureole of an extensive, yet largely concealed younger granitic intrusion.

Bisschoff (1982) later identified four main periods of metamorphism, the first was Archean in age and restricted to the basement core. Thereafter he proposed a regional low-grade event related to crustal loading in both the core and collar rocks, followed by a thermal, 'static' metamorphic event which was restricted to the central parts of the dome (inner collar and basement). He concluded that the thermal metamorphism increases in grade towards the centre of the dome, except where there are local increases in grade towards the granitic plutons within the collar, for which he predicted pressure-temperature (P-T) conditions for the metamorphism to be in the order of 650°C at 4-5 kbar (Bisschoff, 1969). Schreyer (1983) obtained peak metamorphic temperatures ranging from 550-600°C for the collar rocks. The Steynskraal metapelites were shown to exhibit evidence for temperatures of ~700°C at 5 kbar, based on the Fe/Mg distribution between cordierite and garnet in the prograde divariant reaction:

garnet 1 + quartz = orthopyroxene + cordierite + garnet 2 (Schreyer, 1983).

Granulite grade mafic xenoliths from the centre of the core suggest temperatures in excess of 900°C based on the observation of inverted pigeonites (Schreyer & Abrahams, 1978).

Bisschoff (1982) pointed out that the small granitic plutons alone could not have produced the large-scale metamorphism observed throughout the structure and, therefore, considered the presence of some "hotspot" beneath the surface at the centre of the structure. He suggested the presence of a basic pluton in the area of Maree's (1944) gravity anomaly, or the presence of deep crustal material having been brought close to the surface in accordance with Slawson's (1976) 'crust-on-edge' model. The theory of a 'hidden' central magmatic body as a source for the regional scale metamorphism was also supported by Schreyer (1983), Stepto (1990) and Grieve *et al.* (1990), however, it has been shown that there is no evidence for the existence of any such magmatic bodies, large enough to have induced the extent of regional metamorphism observed (Henkel & Reimold, 1996a, b).

In light of the above, Martini (1992) proposed that the 'static' metamorphism was due to continental crustal extension in a stress-free environment. Only recently has Gibson (1993) shown that the collar rocks which these previous researchers had termed hornfelses, indeed exhibit two syn-metamorphic mineral fabrics, thus questioning their contact metamorphic origin as presupposed by all of the aforementioned researchers. He considered these rocks to be the product of a dynamothermal metamorphic event which affected the entire Witwatersrand Basin. The findings of Gibson & Wallmach (1995) corroborate the idea of a dynamothermal history. Gibson & Wallmach (1995) looked at Hospital Hill and Government Reef Group metasediments within the Vredefort collar and identified two principle metamorphic assemblages, namely an M1a peak metamorphic assemblage and a lower grade M1b metamorphic assemblage. These authors constrain the timing of the two metamorphic events according to their relationship to the pseudotachylite-bearing brittle fracture deformation cleavage, believed to have been produced during impact. The M1a

assemblages are cross-cut by this cleavage which also offsets porphyroblasts belonging to the M1a assemblages, whereas M1b cordierite overgrows this cleavage. Thus the M1a peak metamorphic event is envisaged to be pre-impact in age, and M1b to be a post-impact event. The observed metamorphic assemblages and calculated pressures and temperatures of formation of these rocks are detailed in Table 2.5.1, and are important for consideration relative to the collar rocks sampled in this study. Gibson *et al.* (1998) provide further P-T constraints for the post-impact static metamorphism from the recrystallised assemblages observed in pseudotachylite breccias which cross-cut pre-impact metamorphic assemblages (Table 2.5.1).

Metamorphic event	**Bulk composition of metapelites**	**Metamorphic mineral assemblage**	**Calculated P-T conditions**
M1a	Mg + Al-rich (X_{Fe} ~ 0.4-0.5)	And + Crd + Bt ± Ms ± Mn-rich Grt	3.5 kbar, 550°C
	Fe-rich (X_{Fe} > 0.65)	And + St + Bt ± Grt OR Grt + Bt + Chl Note : No prograde Crd Some evidence for replacement of Grt by And + St Relationship between And + St undetermined	4.5 kbar, 570-600°C (phase stability) 500-525°C (Grt-Bt, Grt-Crd thermometry)
	Intermediate (X_{Fe} ~ 0.55-0.65)	Crd + And + Bt Note : And variably replaced by St by reaction : And + Bt → St + Ms Absence of Ms due to : Crd + Ms → St + Bt + Qtz	
M1b	Fe-rich compositions	Poikilitic Crd porphyroblasts which overgrow M1a paragenesis, associated with fine-grained Bt aggregates. Also as coronae between M1a St porphyroblasts and matrix Bt	Coarse grain size Crd = unlikely T<~500°C For X_{Fe} = 0.7 in H_2O depleted system, St → Crd stable at PT < 3.5 kbar, 530°C.
	*Recrystallised pseudotachylite assemblage cross cutting lower greenschist grade pre-impact metamorphic assemblages in Central Rand & Upper West Rand metapelites	Bt + Chl ± Ms	T<~400°C due to stability of Bt in this assemblage
	*Recrystallised pseudotachylite assemblage cross cutting lower amphibolite grade pre-impact metamorphic assemblages in Lower West Rand metapelites	Crd + Bt (which also overprints the M1a assemblage in the host rocks), or more rarely Grt + Bt or Bt ± Ms	T~500°C (Grt-Bt thermometry) 2.1-3.3 kbar (THERMOCALC)

Table 2.5.1: Summary of the metamorphic mineral assemblages identified in the rocks of the collar of the Vredefort dome by Gibson & Wallmach (1995) and * Gibson *et al.* (1998) and their P-T calculations for these assemblages. Mineral abbreviations after Kretz (1983).

Based on their observations Gibson & Wallmach (1995) derived an anticlockwise P-T path from which they suggested that the collar rocks were subject to a high geothermal gradient (~40°C/km), mid-amphibolite facies metamorphic event concomitant with thickening of the overlying crust, and estimated peak metamorphic temperatures of 570-600°C at 4.0–4.5 kbar. They concluded that the latter observations provide strong support for a syn-Bushveld (2.06 Ga) timing for the peak metamorphism, and suggest that this metamorphism may be related to the wide-scale greenschist facies metamorphism observed in the Witwatersrand goldfields, followed by a decompression event linked to the Vredefort catastrophe. The $^{40}Ar/^{39}Ar$ age data obtained by Gibson *et al.* (2000) support the latter conclusion with the majority of apparent ages from biotite and serecite grains ranging between 2.1-2.0Ga.

An anticlockwise P-T path was also derived for the granulite-grade basement supracrustals by Stevens *et al.* (1997a), who, as a result of the similarities ascertained for the metamorphism in the collar and the core, suggested a link between the two. In consideration of the peak metamorphic temperatures attained for the metamorphism of the Witwatersrand goldfields (350°C ± 50°C at 2-3 kbar, Phillips, 1987) and the similarities in the P-T paths calculated for the collar and the core, Stevens *et al.* (1997a) postulated a basin-wide model for the observed peak metamorphism throughout the Witwatersrand Basin, related to crustal underplating during the magmatic Bushveld event.

Since then continued research has produced evidence which proves the single basin-wide metamorphic model to be unlikely. Hart *et al.* (1999) analysed zircon and monazite grains from granulites near the centre of the core, which produced a concordant age of 3107 ± 9 Ma. Since secondary zircon in mafic rocks and monazite in metasedimentary rocks commonly form during prograde metamorphism under amphibolite grade conditions, and retain their isotopic ages of crystallization, this age must be considered a good constraint on the age of the peak metamorphic event in the core rocks. These authors also dated brecciated and pseudotachylized dolerite dykes within the core, which produced U-Pb zircon ages of >2560 Ma. Since these dolerites exhibit no evidence of granulite facies metamorphism, their age of formation must provide a minimum age constraint on the core peak metamorphism. Notably this is older than Bushveld event, which has been dated to ~2056 Ma (Walraven *et al.*, 1990; Walraven and Hattingh, 1993; Walraven and Martini, 1995).

Furthermore, Stevens & Preston (1998) have produced evidence that metamorphic grades in West Rand Group shales from the southern quadrant of the dome are lower (T~300°C) than those observed in the goldfields. Thus the amphibolite facies metamorphism appears to be restricted to the NW section of the collar. This observation implies that the peak thermal metamorphism could not have extended throughout the Witwatersrand Basin, unless the rocks analysed by Stevens and Preston (1998) were not buried to the same depths as those in the NW collar during metamorphism. Such a scenario should not be disregarded because Colliston *et al.* (1989) provide evidence for significant pre-Ventersdorp deformation in the Witwatersrand Supergroup rocks within the dome (Fig. 2.1.5). Lana *et al.* (2003) have demonstrated that the present asymmetry of dips in the collar rocks can be reconciled by symmetric impact-induced rotation of an inclined pre-impact sequence of supracrustal rocks.

Table 2.5.2 summarises the mineral assemblages identified by various researchers, upon which their proposals regarding the metamorphism in the core, discussed above, are based.

The metapelites investigated by Stevens *et al.* (1997) are of particular importance due to their similarity to samples collected for this study, and are discussed in detail in Chapter four.

Metamorphic event	Mineral assemblages	Calculated PT	Method, Reference
Peak pre-impact metamorphism	Crd + Grt ± Opx ± Bt ± Sp ± L (metapelite)	7-8 kbar	Crust on edge model, Schreyer & Abraham (1978)
	Grt + Opx + Qtz ± Cpx (meta-ironstone)	>800-850°C	Ferropigeonite stability, Schreyer *et al.* (1978)
	Cpx + Hbl + Pl ± Opx ± Bt (metabasite)	>875°C	Hbl breakdown, Schreyer (1983)
	Grt-Crd-Opx migmatites and restites	5.0-5.5 kbar, 850->920°C	Bt melting relations + thermobarometry, Stevens *et al.* (1997)
Post-impact metamorphism	Opx + Crd symplectite	5 kbar, 700°C	Fe-Mg exchange thermometry, Schreyer & Abraham (1978)
	Spl + Opx (metapelite)	2-3 kbar, <900°C	Fluid inclusions, Schreyer (1983)
		<2 kbar, >700°C	Fluid inclusions, Fricke *et al.* (1990)
		2.0-2.5 kbar, >700°C	Quantitative thermobarometry, Stevens *et al.* (1997)
	Recrystallised pseudotachylite breccia veins: Opx + Pl + Kfs ± Crd ± Bt (Opx-Crd coronae rim pre-impact Grt)	~2.1-3.3 kbar 700°C - 900°C	Gibson *et al.* (1998)
	Spl + Crd between alkali feldspar laths	800-850°C	Fe-Mg exchange thermometry Gibson (2002)

Table 2.5.2: Summary of the metamorphic assemblages identified in the core of the Vredefort dome and their associated P-T estimates (after Reimold and Gibson, 1996 plus more recent data).

The dynamic metamorphic features have already been discussed in Chapter 2, but are highlighted again with respect to their apparent decline toward centre of the dome. Hart *et al.* (1991) suggest that density of the planar deformation features observed in quartz does not increase towards the centre of the structure, but rather reaches a maximum concentration in the vicinity of the OGG-ILG transition zone. Schreyer (1983) and Fricke *et al.* (1990) provided evidence, based on fluid inclusion and quartz recrystallisation studies, which indicate that the lack of planar elements in quartz grains from the central core granitoids is a function of the quartz having been completely recrystallised during the shock event. In contrast, the quartz grains from the OGG which preserve fluid inclusion- and recrystallised quartz-decorated planar features, are in fact the original Archean quartz grains. Martini (1992) considered the post-shock metamorphism to be responsible for the recrystallisation of the shock features, particularly in the conversion of stishovite and coesite in the central core region to fibrous quartz, which in turn is replaced by triple-junctioned mosaic quartz. He considered the post-shock metamorphism to have been generated by the combined pre-existing heat of the country rocks plus the added heat released by the shock wave.

More recently, Gibson *et al.* (1998) and Gibson (2002) have suggested that the post-shock metamorphism observed in both the collar and the core to be the combined result of an elevated regional geothermal gradient of ~25°C/km plus the thermal effects of impact in the

target rocks. They consider the high geothermal gradient to be related to the Bushveld magmatic event and suggest that directly after impact these rocks were buried at depths of 8-11 km (from geobarometric estimates of 2-3 kbar from the metamorphic paragenesis) and have since been brought to the surface due to erosion.

The fluid inclusion data is important to consider from a metamorphic perspective, because of the great effect fluids may have had in the metamorphic evolution of the rocks being studied. Fricke *et al.* (1990) ultimately suggested a relationship between the ubiquity of the fluid inclusions and the shock event because of their concentration along PDFs in quartz grains, but imply an initial mantle origin based on the high CO_2 content of the fluid inclusions. Using a combination of the fluid inclusion densities and P-T values from other work done on the rocks in which the fluid inclusions are found (Bisschoff, 1969; Schreyer and Abraham, 1978; Schenk, 1983), Fricke *et al.* (1990) concluded that the fluid inclusions observed along planar features were trapped during or soon after the impact event under static metamorphic conditions of 2-5 kbar.

2.6 ISOTOPE STUDIES

Hart *et al.* (1981) produced two radioelement profiles through the basement rocks of the NW quadrant of the Vredefort dome, one on the NW side and one on the NE side. They reported a depletion in Th and U in the central part of the core and a regular decrease in the concentration of Th and U from the perimeter towards the centre of the core, however, they also observed unusually high Th/U and K/U ratios for the felsic portion of the core (ILG) (Fig. 2.6.1) which they have interpreted to be lower crust. In the outer 8 km of the core, the distribution of radioelements and heat production, are consistent with an exponential depth function.

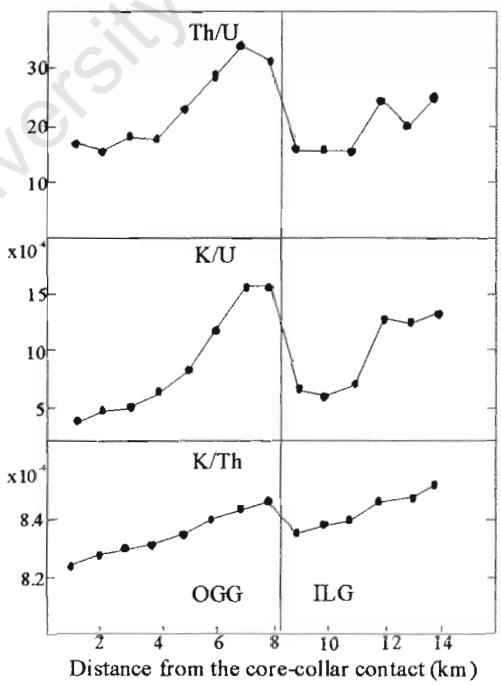

Figure 2.6.1: Averaged distribution Th/U, K/U and K/Th profiles across the Vredefort basement (from Hart *et al.*, 1990a).

Based on the 1981 radioelement profiles, Hart *et al.* (1990a) looked at a more comprehensive sample-set from the basement core. The results of the latter study include major and trace element profiles plotted as a function of distance from the core-collar contact (depth) (Figs. 2.6.2, 2.6.3) and rare earth element chondrite-normalized patterns (Fig. 2.6.4).

Based on the data collected, Hart *et al.* (1990a) identified three geochemical zones within the basement core, namely the OGG, a charnockite zone in the ILG and the lower ILG. They suggested that the OGG displays a bimodal character, with rocks in the upper 3-4 km (closest to the core-collar contact) exhibiting lower K/U and Th/U ratios, lower concentrations of Ba, Sr and Co, and higher K_2O/Na_2O ratios relative to the lower 3 km (closest to the OGG-ILG transition zone). In general, Hart *et al.* (1990a) described a decrease in SiO_2, K_2O and LILE elements (U, Th, Rb, Cs) and an increase in Al_2O_3, Na_2O, CaO, MgO, Fe_2O_3 and Co towards the Vredefort discontinuity. They then identified a 'sharp change' in major and trace element profiles at the Vredefort discontinuity, including a relative enrichment in SiO_2 and K_2O, and depletion in MgO, CaO, TiO_2 and Fe_2O_3 to the OGG, which they correlate with the change in lithology from OGG to charnockites and leucogranofels. They noted that the chemistry of the charnockite zone is determined by both charnockite and leucogranofels compositions, highlighting that the major and trace element chemistry of these two rock types is 'indistinguishable' bar a few exceptions. These exceptions include anomalously high concentrations of Ti_2O or Zr, and a relative enrichment in LREE compared to HREE in some charnockites found close to the Vredefort discontinuity (Fig. 2.6.4).

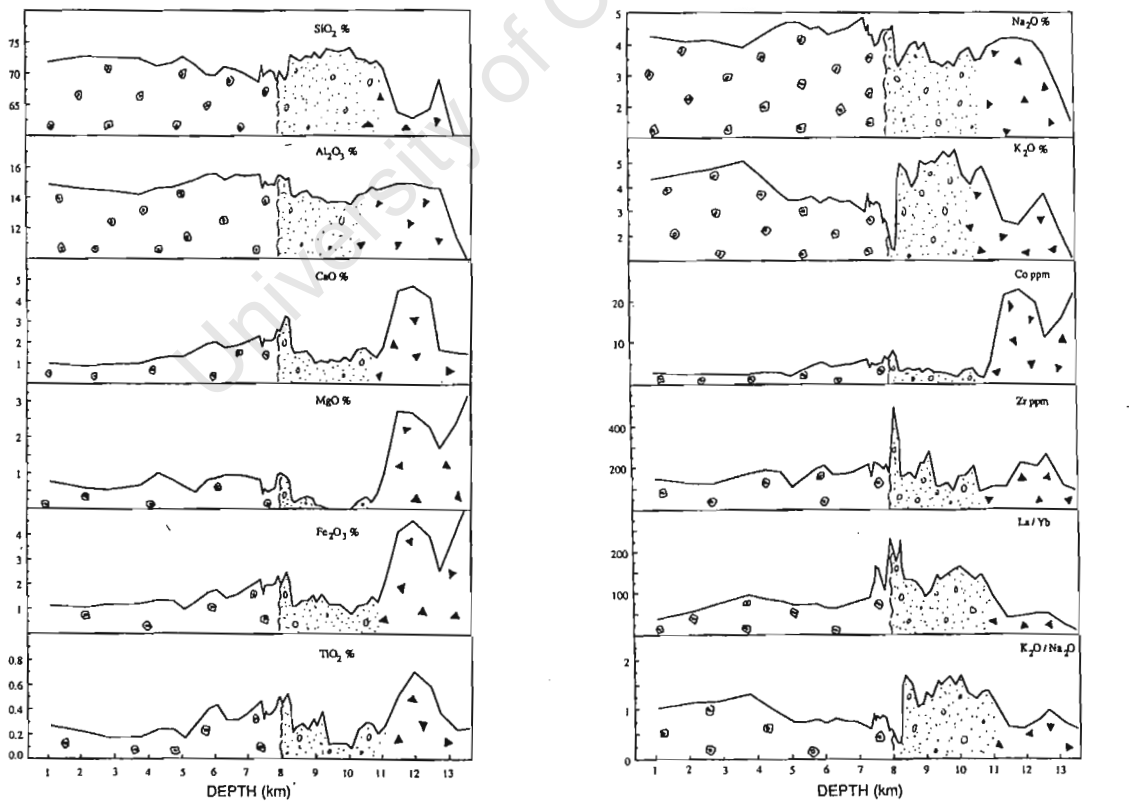

Figure 2.6.2: Major and Trace element concentration profiles taken along a single transect in the NW quadrant of the basement core. After Hart *et al.* (1990a). Where ⊙ = OGG, ⁘ = charnockite zone and ▲ = ILG.

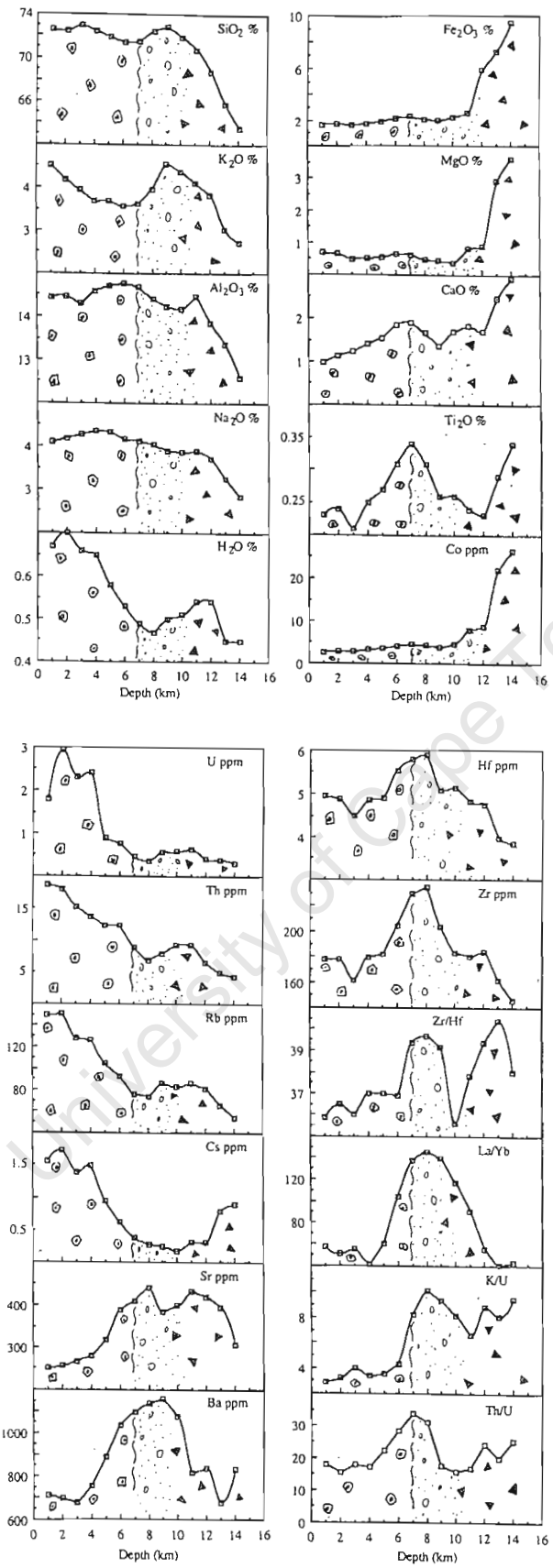

Figure 2.6.3: Profiles displaying the average distribution of some major and trace elements across the Vredefort dome. From Hart *et al.* (1990a).

Their division of the ILG into the charnockite zone and the lower ILG is a function of the inclusion of mafic xenoliths in the averaged element profiles in the lower ILG. Clearly, such an averaging process will reflect a significant change in major and trace element profiles, however, since the mafic rocks have been identified as xenoliths, one would expect the exclusion of these rocks from the chemical profiles to provide a more accurate basis upon which conclusions may be drawn regarding the nature of the gneissic core with 'increasing depth'. It is clearly evident that the large increase in Fe_2O_3, MgO and CaO and the decrease in SiO_2 and K_2O in the lower ILG are biased towards the mafic xenolith lithologies. This fact should be considered in terms of the geochemical profiles supporting the premise that the geochemistry across the core reflects an increase in depth within the crust.

The REE profiles of Hart *et al.* (1990a) succinctly display a difference in OGG and ILG compositions, with the ILG field being more fractionated and exhibiting a positive Eu anomaly compared to the flatter OGG field, which displays higher total REE concentrations and negative Eu anomalies for samples closest to the core-collar contact. An important observation is that the charnockite samples, although displaying noticeably different profiles to the OGG samples, plot within the OGG field and not the ILG field, the latter being the rocks with which the charnockite samples major and trace element chemistries were previously described as 'indistinguishable'.

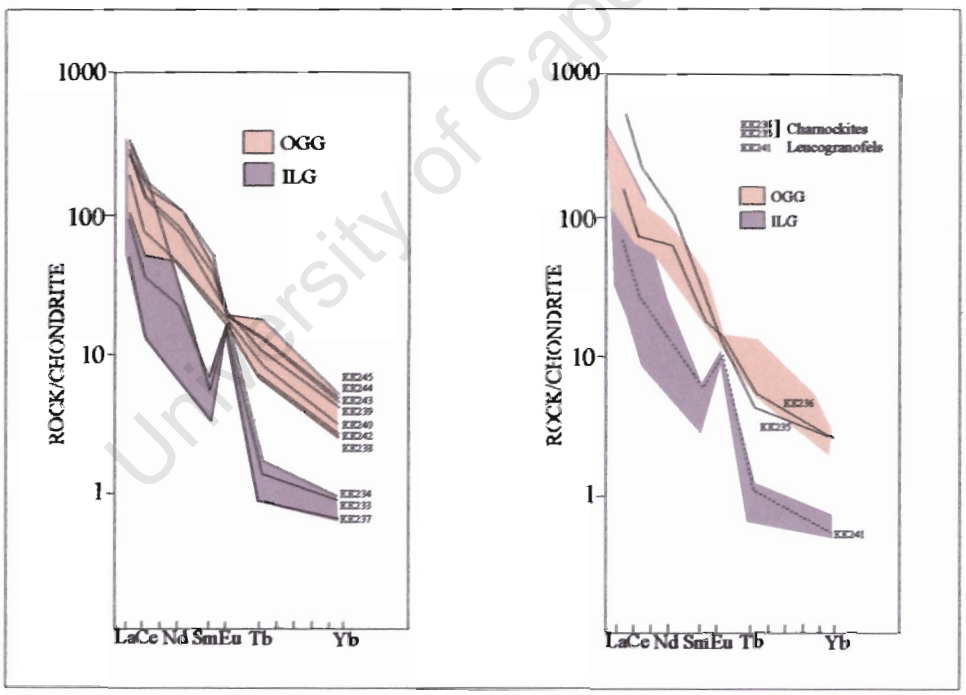

Figure 2.6.4: Chondrite-normalized REE plots from Hart *et al.* (1990a) illustrating the REE fields for the OGG and ILG and selected samples therein.

A stable isotope study was undertaken by O'Neil *et al.* (1987), the results of which are summarised in Table 2.6.1. From these results they concluded that both the OGG and the ILG yield $\delta^{18}O$ values typical for I-type granites, with the ILG having slightly higher values as a function of its marginally higher SiO_2 and K-feldspar abundances. They also observed that a transition zone between the OGG and ILG cannot be distinguished from the

$\delta^{18}O$ values, and that the rocks of the Lower Witwatersrand Supergroup from the Vredefort dome cover the same range of values as for these rock types in the vicinity of Johannesburg. Witwatersrand Supergroup quartzites have also been analysed in the Welkom, Klerksdorp, Evander and Carletonville goldfields (Harris & Watkins, 1990) (Table 2.6.2), and also exhibit $\delta^{18}O$ values in the range 8-11‰.

Sample	Locality	Rock type	$\delta^{18}O$(‰)
USA173	Inlandsee Pan	Carbonatized Peridotite	9.4
TL1	Inlandsee Pan	Recrystallised ILG	9.7
USA186	Rust en Vrede	ILG	10.0
USA183	Jagersvrede		8.3
USA31D	Lesutaskraal		7.9
HR32	Schietkop		7.8
USA31BI	Lesutaskraal	Charnockite in ILG	7.9
USA179	Otavi	OGG	7.6
USA180			8.3
USA31BP	Lesutoskraal	Pseudotachylite	8.1
USA184	Jagersvrede		8.0
USA178	Otavi		7.5
BG3	Holfontein	Vredefort granophyre	7.9
BG92	Rensburgdrif		7.3
USA13b	Witterand	Government quartzite	7.1
USA78			7.6
USA16			8.1
LU2III	Rensburgsdrif	Hospital Hill quartzite	9.4
LU2II			9.4
LUIII/1			10.5
USA41	Rietpoort		11.0
USA62	Johannesburg	Orange Grove quartzite	10.2
USA66A		Hospital Hill quartzite	8.2
USA68		Government quartzite	8.6

Table 2.6.1: $\delta^{18}O$ values (SMOW) obtained for a variety of rock types from the Vredefort dome and Johannesburg area (after O'Neil *et al.*, 1987).

Sample	Locality	$\delta^{18}O$(‰)
	Welkom Goldfield	
WG10	Free State Saaiplaats Gold Mine	8.6
WG22		8.7
WH28	Western Holdings Gold Mine	10.3
WH1		9.9
	Klerksdorp Goldfield	
MAF02	Hartebeesfontein Gold Mine	9.9
MAF08		10.1
	Evander Goldfield	
EV3	Winkelhaak Gold Mine	9.2
	Carletonville Goldfield	
CV8	Doornfontein Gold Mine	10.1

Table 2.6.2: $\delta^{18}O$ values (SMOW) for quartzites from the Witwatersrand Goldfields (from Harris & Watkins, 1990).

CHAPTER 3
PETROGRAPHY

3.1 SAMPLE COLLECTION

Samples constituting the sample-set for this study were selected in consideration of previous work done on the rocks of the Vredefort dome. In the Archean basement core, samples were collected along a NW-SE trending traverse, similar to that taken by Hart *et al.* (1981, 1990a) (Figs. 3.1.1-3). Samples, approximately 10 cm x 10 cm x 10 cm were taken approximately every 500 metres along this traverse, except in the vicinity of Hart *et al.*'s (1990) 'Vredefort discontinuity', where they were taken approximately every 50-100 metres (Fig. 3.1.3). The location of each of these samples was recorded using a GPS which allows for a 12 m radius of error. The HM suite of samples (Fig. 3.1.1) was collected by Dr. Gary Stevens from Helpmekaar farm and include granulite-grade metapelites from within the ILG.

In the collar of the structure the sample suite 412-426 was collected as a continuation of the NW-SE trending traverse taken in the core (Fig. 3.1.1) and, again, sample localities were recorded using a GPS. The remainder of the collar sample set was taken from samples collected earlier by Dr. Roger Gibson and extends from the Northern parts of the collar (CB1, VH23), to the Western parts (W1-19). The localities for these samples were recorded by Dr. Roger Gibson either onto aerial photographs or geological maps during collection.

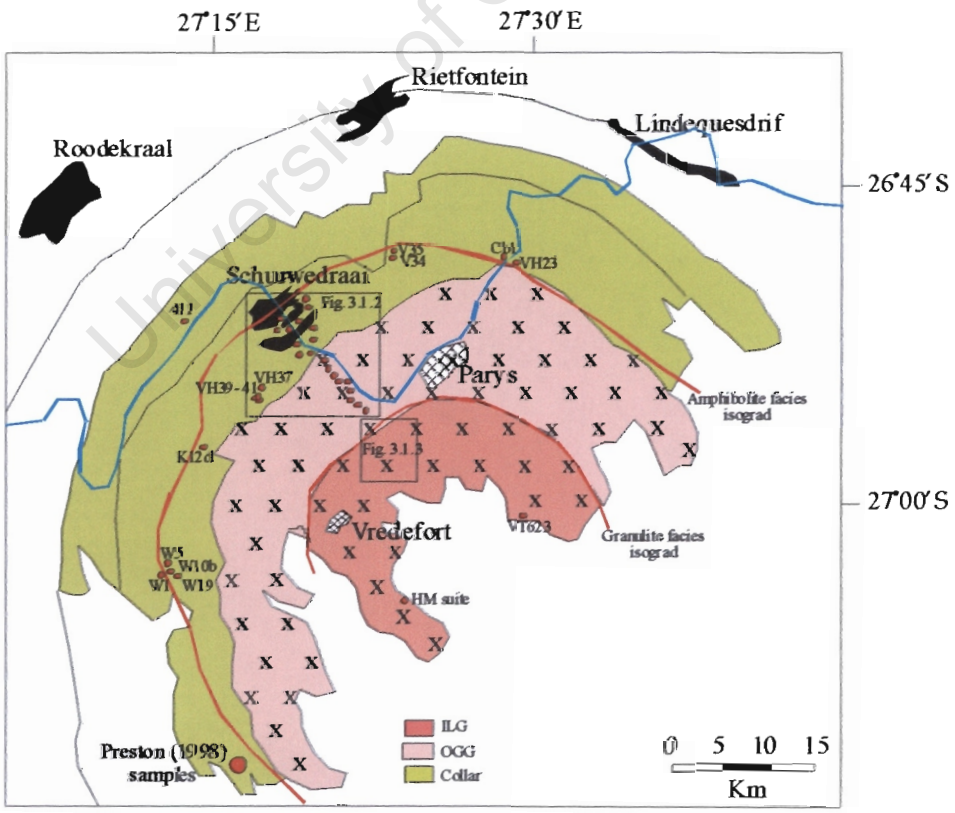

Figure 3.1.1: Map of the Vredefort dome displaying sample localities of the sample-set collected for this study. x – Archean basement core. Amphibolite and granulite facies isograds after Gibson & Wallmach (1995).

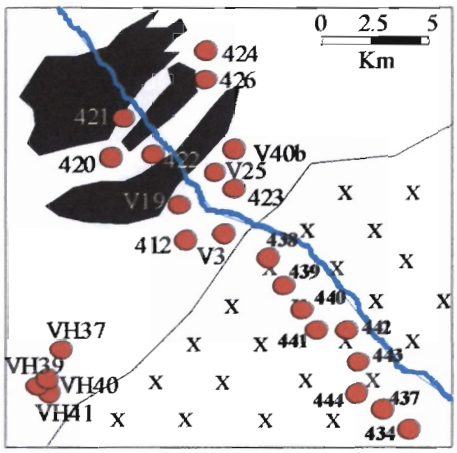

Figure 3.1.2: Magnified section of figure 3.1.1 illustrating the sample localities in the collar and outer core.

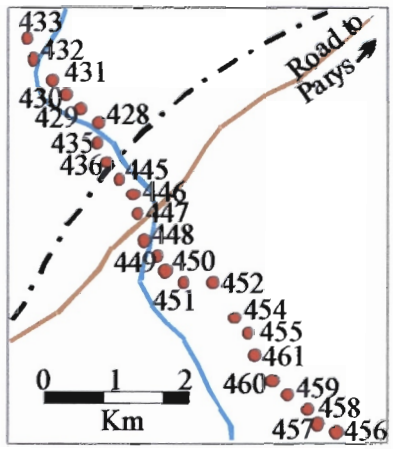

Figure 3.1.3: Magnified section of figure 3.1.1 illustrating the sample localities for the transect taken through the Archean basement core of the dome.

All of the samples were split using a hydraulic press. One half was used as a hand specimen from which thin sections were produced, whilst the other half was crushed further, using a jaw crusher and sieb mill, in turn, to produce the powders necessary for the application of various geochemical techniques.

Preston (1998) also donated some samples taken from boreholes in the West Rand Group shales in the SE portions of the structure for stable isotope analysis (Fig. 3.1.1). Stevens & Preston (1998) detail the petrography of these samples.

3.2 THE COLLAR ROCKS

Samples collected from the NW sector of the collar of the Vredefort dome include a variety of metapelites and a few metabasites from the lower West Rand Group and Dominion Group. They exhibit mineral compositions dependant on the initial bulk composition of their precursor rocks and the degree of metamorphism experienced. The metapelites typically include a number of the following minerals: quartz, feldspar, garnet, biotite, chlorite, muscovite, andalusite, cordierite, staurolite, hornblende, grunerite and opaque minerals, and the metabasites are composed of an array of quartz, feldspar, biotite, chlorite, garnet, actinolite, epidote, gedrite, hornblende and opaques. A brief description of each sample is given in Table 3.2.1.

Samples VH23, 411, V34, CB1, V25, V35, 420, 421 and 422 all contain amphibole minerals, including actinolite, gedrite, grunerite and hornblende, as well as epidote and garnet. Samples VH23 and 411 are amygdaloidal meta-lavas from the Dominion Group and Upper Witwatersrand Supergroup, respectively, and samples V34, V35 and CB1 are metamorphosed banded ironstone formations (BIFs) from the Government Reef Subgroup. Samples V25, and 420 to 422 are metamorphosed ferruginous Government Reef Subgroup shales.

In sample VH23, actinolite exhibits a decussate texture intergrown with granoblastic quartz, feldspar (plagioclase), chlorite and minor amounts of muscovite (Fig. 3.2.1).

Sample	Mineralogy	Description	Metamorphic Grade
VH23	Qtz + Fsp + Chl + Act + Opq ± Ms ± Ep	Act and Chl laths form a decussate texture in association with Qtz + Fsp	Greenschist
CB1	Grt + Gru + Qtz + Fsp + Ilm ± Bt ± Chl	Grt porphyroblasts and acicular Grun within a granoblastic matrix of Qtz, Fsp, Ilm and minor Bt and Chl	Lower Amphibolite
V34	Qtz + Opq + amphibole	Very fine grained	
V35	Grt + Gru + Hbl + Crd + Qtz + Fsp + Mag	Grt and amphibole porphyroblasts within a granoblastic Qtz + Fsp + Opq matrix, with original sedimentary layering preserved by opaque-rich layers	Amphibolite
424/426	Grt + Bt + Qtz + Fsp + Chl + Opq	Round Grt porphyroblasts within a Qtz-Bt-Chl-Fsp matrix rich in rounded Opq minerals	Upper Greenschist
420	amphibole + Qtz + Opq	Fine grained amphibole hornfels, very rich in Opq minerals	Upper Greenschist
422	Ep + amphibole + Qtz + Opq ± Grt ± Chl	Epidotite with a granoblastic texture including relict Grt porphyroblasts. Sedimentary bedding preserved by Opq minerals	Amphibolite
V40b	Grt + St + Crd + Bt + Chl + Qtz + Ms	Grt, St and Bt porphyroblasts in a Qtz-Ms-Bt-Chl matrix, plus massive and poikiloblastic Crd	Amphibolite
V25	Grt + Chl + Qtz + Fsp ± amphibole	Grt porphyroblasts in a Qtz-Fsp-Chl matrix exhibiting schistose fabric defined by Chl Includes Qtz vein with some amphibole grains and minor Grt inclusions	Amphibolite
V19	And + St + Bt + Chl + Qtz + Fsp + Opq	Poorly formed And + St in a Qtz-Fsp-Bt-Chl matrix	Amphibolite
412	Crd + And + Grt + Bt + Chl + Qtz ± Ms	Crd, Bt & Grt porphyroblasts in a Qtz-Bt-Chl matrix. Crd contains inclusions of all other minerals present	Amphibolite
423	And + Bt + Crd + Qtz + Ms ± St ± Chl	Euhedral And + Bt poikiloblasts in a Qtz-Ms matrix. And altered to Crd, St and Bt	Amphibolite
V3	Grt + Bt + Qtz + Fsp + Opq ± Chl	Rounded Grt in a Qtz-Fsp-Bt-Opq matrix	Upper Greenschist
411	Qtz + Ms + Fsp (Plag) + Chl ± Bt ± Ep + Opq	Fine grained granoblastic groundmass with decussate-textured Ms and Ep	Lower Greenschist
VH37	Qtz + Bt + Chl + Grt + Opq ± Ms	Grt, Bt poikiloblasts and Chl laths in a very fine-grained Qtz-Bt-Chl matrix	Upper Greenschist
VH39	Qtz + Ms + Bt + Grt + Crd + Opq ± Chl ± And	Ovoid Crd porphyroblasts in Qtz-Ms-Bt-Grt matrix. Crd contains inclusions of all other minerals present	Amphibolite
VH40	Qtz + Ms + Bt + Grt + Crd + Opq ± Chl ± And	Ovoid Crd porphyroblasts in Qtz-Ms-Bt-Grt matrix. Crd contains inclusions of all other minerals present	Amphibolite
VH41	Qtz + Ms + Bt + Grt + Crd + Opq ± Chl ± And	Ovoid Crd porphyroblasts in Qtz-Ms-Bt-Grt matrix. Crd contains inclusions of all other minerals present	Amphibolite
K12d	Qtz + Bt + Chl + Crd + Opq ± Ms	Crd porphyroblasts and Bt poikiloblasts in a Qtz-Bt-Chl-Ms matrix	Lower Amphibolite
W1	Qtz + Ms + Chl + Bt + Crd + And ± Grt	Qtz-Ms-Chl matrix with poikiloblastic Bt, ovoid Crd and euhedral And porphyroblasts	Amphibolite
W5	Bt + Grt + Crd +Ms + Qtz ± Chl	Euhedral Grt and poikiloblastic Bt in fine-grained Qtz-Bt-Chl matrix, + large Crd poikiloblasts containing inclusions of Grt & Bt	Upper Greenschist
W10	Bt + Grt + Crd +Ms + Qtz ± Chl	Euhedral Grt and poikiloblastic Bt in fine-grained Qtz-Bt-Chl matrix, + large Crd poikiloblasts containing inclusions of Grt & Bt	Upper Greenschist
W19	Qtz + Bt + Chl + Ms + Opq+ And + Plag	And + Plag porphyroblasts in a very fine-grained Qtz-Bt-Ms-Chl matrix	Amphibolite

Table 3.2.1: Mineralogy and metamorphic grade of the Collar rock samples. Mineral abbreviations after Kretz (1983) Opq – opaque minerals (Magnetite and Ilmenite).

Sample CB1 comprises garnet and grunerite, which appear to have grown simultaneously, in a quartz-feldspar-opaque-rich matrix (Fig. 3.2.2) and Sample V35 includes grunerite and hornblende, which are intimately associated, with hornblende replacing grunerite at the extremities of amphibole laths. Both amphibole phases overgrow and replace garnet, which is most abundant in oxide-rich layers (Fig. 3.2.3).

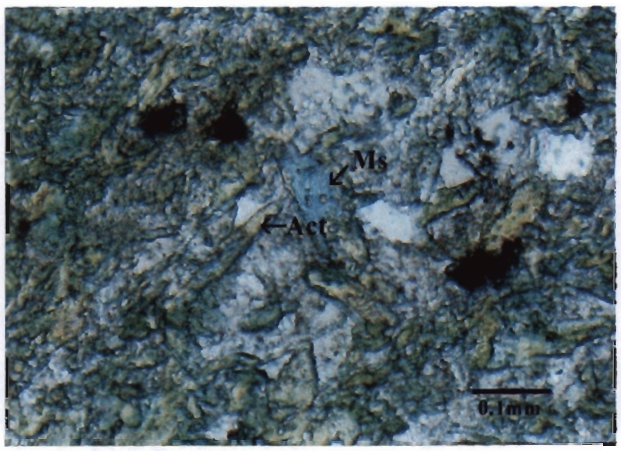

Figure 3.2.1: Photograph taken in plane polarised light illustrating the general mineralogy and texture observed in Sample VH23, a Dominion Group meta-lava.

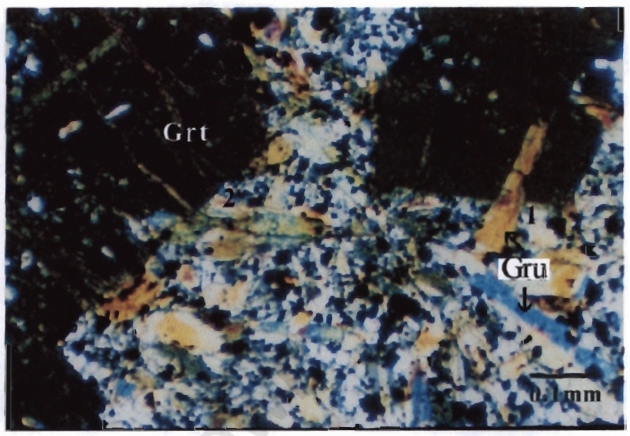

Figure 3.2.2: Photograph taken in cross polarised light exhibiting the cross-cutting relations between garnet and grunerite in sample CB1.

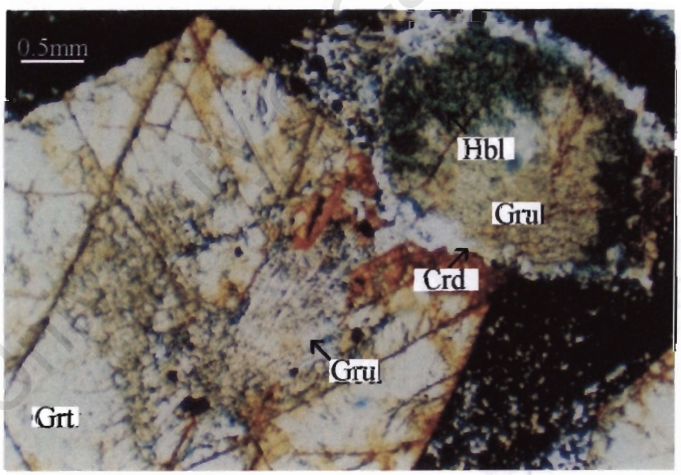

Figure 3.2.3: Grunerite and hornblende replacing garnet in sample V35.

Sample 422 is an epidotite rich in oxides, with minor orthoamphibole and garnet. The presence of abundant epidote indicates that the initial bulk composition of this sample was more aluminous and less magnesian in comparison to the samples containing only actinolite. All of the amphibole and epidote bearing rocks have increased iron and calcium contents, and decreased magnesium and alumina contents relative to the metapelitic assemblages. In the above samples garnet is largely euhedral in form, almandiferous in composition, and closely associated to the amphibole phases, either having grown simultaneously (CB1) or with amphiboles replacing garnet. Actinolite and grunerite form typically as laths and hornblende is less well-formed, displaying a more massive texture.

Sample 411, a meta-basite from the Central Rand Group, exhibits a lower greenschist facies assemblage comprising of quartz, feldspar, muscovite and chlorite (Fig. 3.2.4).

Sample V25 is a garnet-chlorite schist; the lack of muscovite and biotite in this assemblage indicate that the initial composition of its precursor must have been potassium deficient. It is a ferruginous metashale, the schistosity of which is defined by chlorite, which bends around the garnets. Poikiloblastic garnets exhibit two phases of growth and minor amounts of hornblende are associated with the garnets (Fig. 3.2.5). A portion of this sample contains a bedding-parallel vein comprising mainly quartz and feldspar, with minor amounts of garnet, hornblende, biotite and chlorite (Fig. 3.2.6). The vein appears to have formed as a result of the influx of a late-stage silica-rich fluid since it incorporates garnets from the original bulk rock and the contact between it and the bulk rock appears to be abrupt. In places it cross-cuts the schistose fabric of the bulk rock and engulfs garnets from it (Figs. 3.2.7 & 3.2.8).

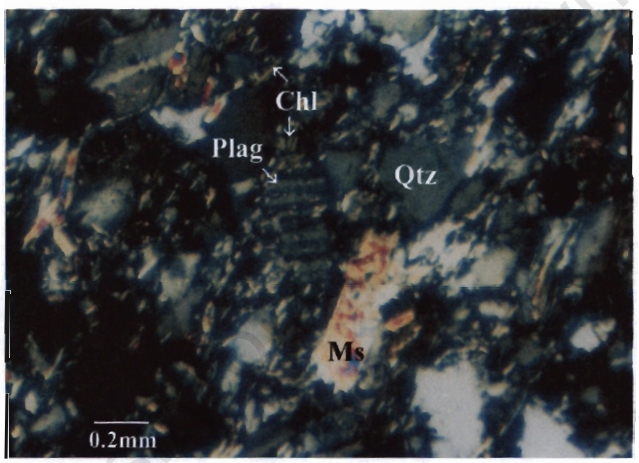

Figure 3.2.4: Photograph taken in cross polarised light of Sample 411, illustrating decussate Ms intergrown with Qtz, Fsp and Chl.

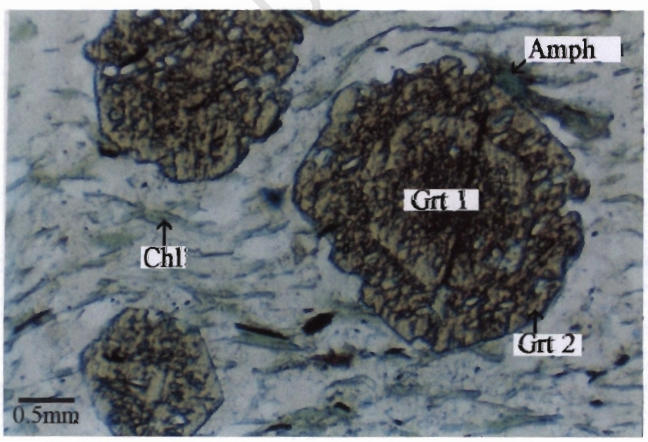

Figure 3.2.5: Sample V25, a Grt-Chl schist with minor amphibole, the fabric of which is defined by chlorite.

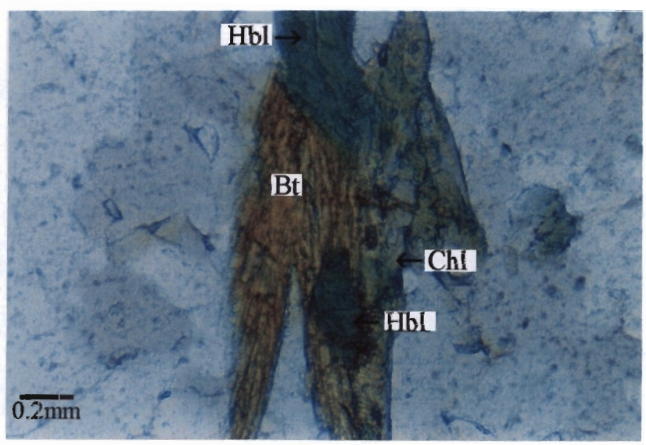

Figure 3.2.6: Vein within sample V25 dominated by quartz and feldspar containing minor garnet, hornblende, chlorite and biotite.

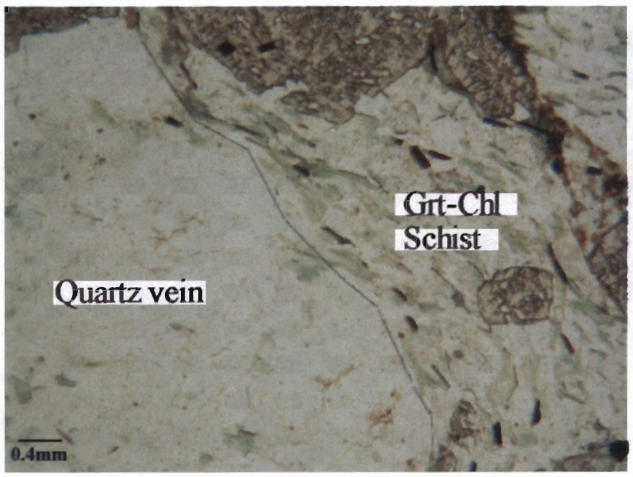

Figure 3.2.7: Photograph of the abrupt contact between the bulk rock and quartz vein running through Sample V25.

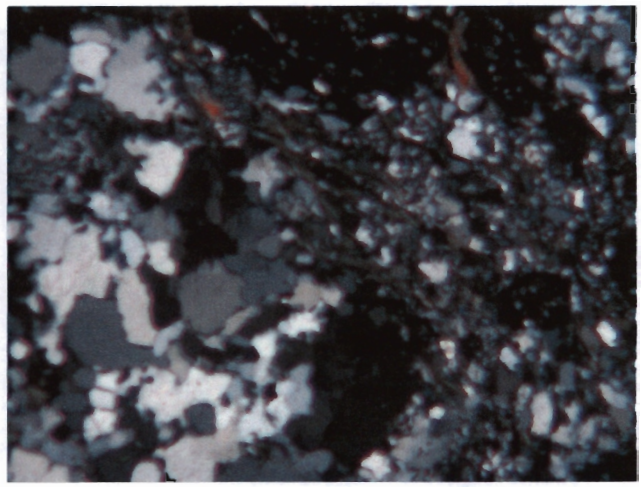

Figure 3.2.8: Figure 3.2.7 under cross polarised light. Note how the vein cross-cuts the schistose fabric of the bulk rock which implies it is bedding-parallel since schistosity runs oblique to the bedding, and the recrystallised nature of the quartz grains.

The rest of the collar samples are true metapelites, although slightly muscovite deficient, and include assemblages definitive of the grade of metamorphism experienced, as defined by the Barrovian zones of metamorphism (Chinner, 1965 & 1967; Atherton, 1977). Many of the metapelites have maintained their original sedimentary layering, although others have acquired metamorphic fabrics during metamorphism (Gibson, 1993).

Samples 424, 426, and V3 all contain quartz, biotite and garnet. The garnets in these samples are round and rich in quartz and chlorite inclusions, whilst biotite and chlorite are poorly formed. The Qtz-Chl-Bt matrix contains abundant round oxide phases which define the relict sedimentary layering preserved in each of these samples (Fig. 3.2.9).

The presence of andalusite, cordierite and/or staurolite distinguish the remainder of the samples, and these assemblages represent the highest grades of metamorphism attained within the collar. Sample W19 comprises euhedral andalusite and ovoid plagioclase within a very fine-grained Qtz-Bt-Ms-Chl matrix, which exhibits a well-formed crenulation cleavage (Fig. 3.2.10).

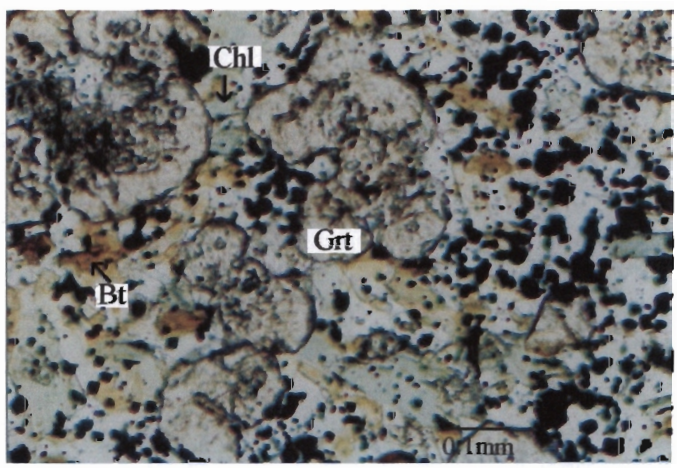

Figure 3.2.9: Round, inclusion-rich garnets embedded in an oxide-rich Qtz-Fsp-Bt-Chl matrix in Sample 424, typical of assemblages observed in Samples 424, 426 and V3.

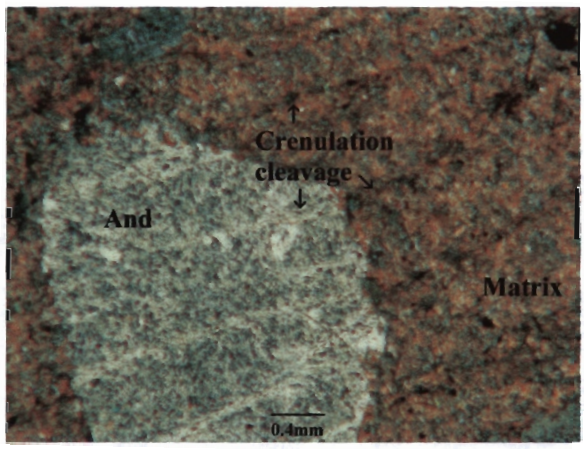

Figure 3.2.10: Photograph taken under cross polarized light exhibiting the crenulation cleavage in Sample W19.

Samples W5, W10 and VH37 contain garnet, biotite, cordierite, muscovite and chlorite. Samples W5 and W10 are relatively muscovite-rich compared with the majority of the metapelitic samples and contain garnet and biotite porphyroblasts and large cordierite grains which exhibit little crystal form (Figs. 3.2.11& 3.2.12). In sample VH37 the matrix is biotite-rich and includes garnet and biotite poikiloblasts, small poorly formed ovoid cordierite and acicular laths of chlorite (Fig. 3.2.13). In these samples the association between biotite and chlorite is complex with many of the biotite poikiloblasts exhibiting a 'criss-cross' texture where chlorite laths replace sections of the biotite grains (Fig. 3.2.14), and is likely to be the 'kink-banding' texture referred to by previous researchers (Hall & Molengraaff, 1925; Nel, 1927; Bisschoff, 1969, 1982). Samples 412, VH39 to VH41 and W1 all contain ovoid poikiloblastic cordierite rich in biotite, chlorite, quartz, muscovite and garnet inclusions. Each of these samples also contains andalusite within the cordierite porphyroblasts (Figs. 3.2.15-18) and are thus likely to represent the same precursor rock type as for samples W5, W10b and VH37 only metamorphosed to a slightly higher degree, assuming that the growth of andalusite is prograde.

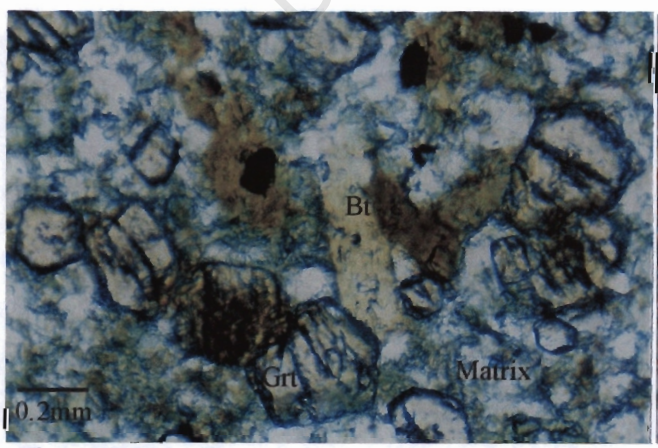

Figure 3.2.11: General character of garnet and biotite within the matrix of Sample W5.

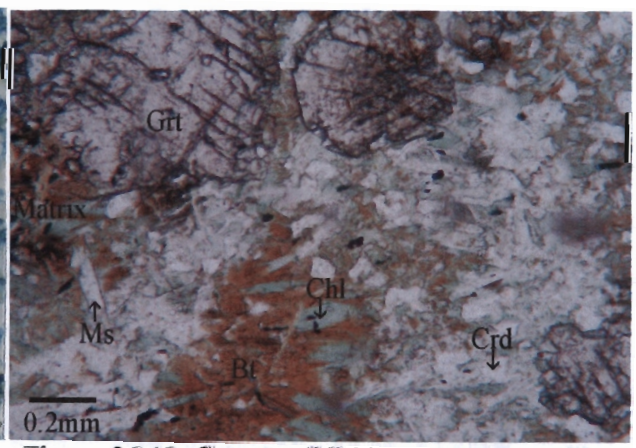

Figure 3.2.12: Garnet poikiloblasts in contact with a large cordierite grain, containing biotite and chlorite and intricately associated with muscovite in Sample W10b.

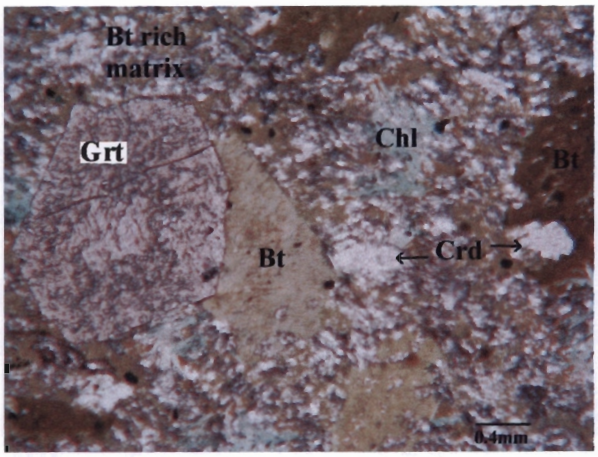

Figure 3.2.13: Mineralogy and textural relationships of the minerals comprising Sample VH37.

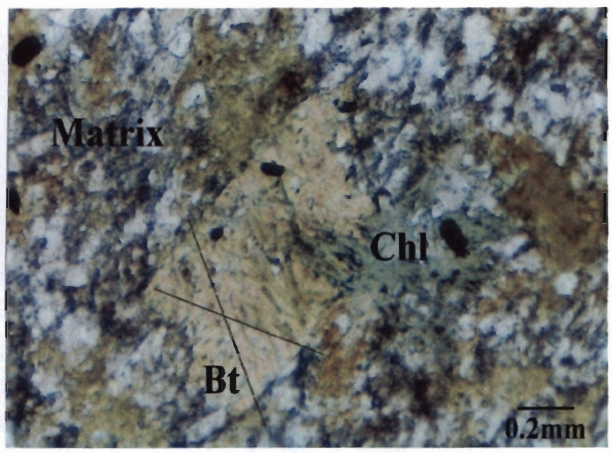

Figure 3.2.14: 'Kink-banding' texture observed in many biotites of the metapelites analysed.

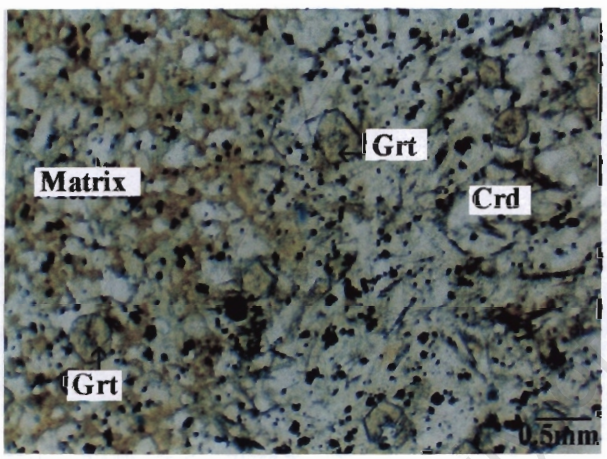

Figure 3.2.15: Typical texture of large cordierite poikiloblasts observed in Sample VH39, note garnet both in the matrix and as inclusions within cordierite.

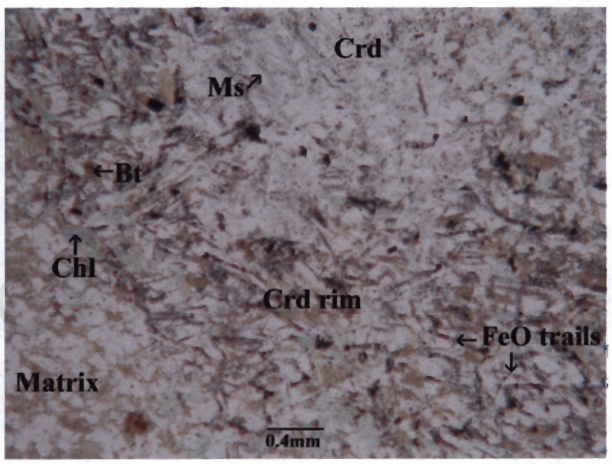

Figure 3.2.16: Cordierite grain, rich in muscovite as observed in Sample VH40, displaying a biotite, chlorite and FeO oxide-rich rim.

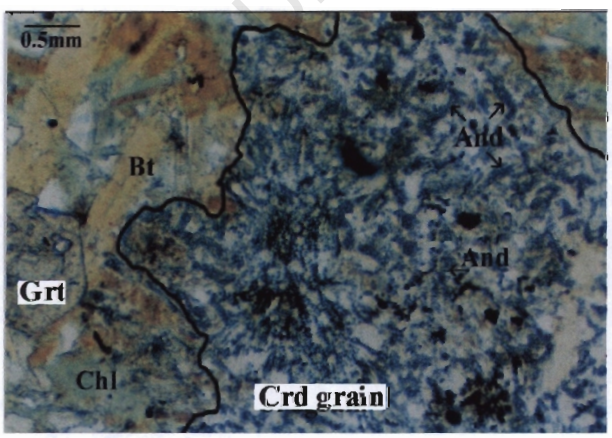

Figure 3.2.17: Relict cordierite grain, being altered to andalusite within the garnet-biotite-chlorite rich Sample 412.

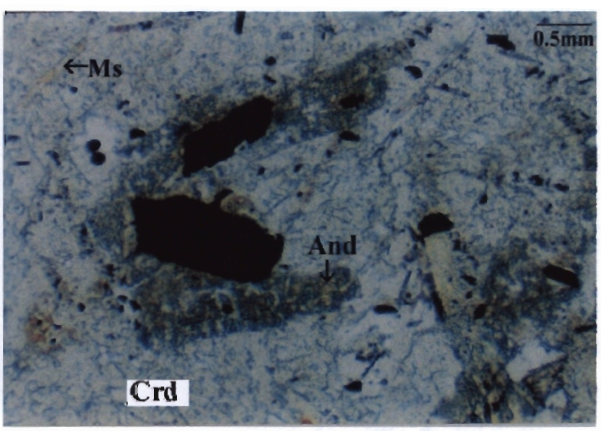

Figure 3.2.18: Andalusite grain found within a large cordierite porphyroblast in Sample 412.

Sample 423 includes biotite, chlorite, quartz, andalusite, cordierite and staurolite. Cordierite exhibits both a similar texture to that described in samples VH39-40 and W1 (cordierite 1, synonymous with M1a cordierite as identified by Gibson, 1996), and a different form where it appears to be replacing euhedral andalusite in the presence of biotite (cordierite 2, M1b (Gibson, 1996)). Andalusite predominates as well-formed euhedral porphyroblasts and biotite as poikiloblasts mostly exhibiting well-formed crystals, but in places (mostly in the presence of cordierite) having anhedral form. Staurolite is present as a minor component of the rock as poorly formed, small crystals within the matrix, closely associated with biotite, and in the rims of relict andalusite altered to cordierite (Figs. 3.2.19-21). The textural relationships between the minerals of this complex assemblage are discussed later when considering the degree of metamorphism exhibited by this assemblage.

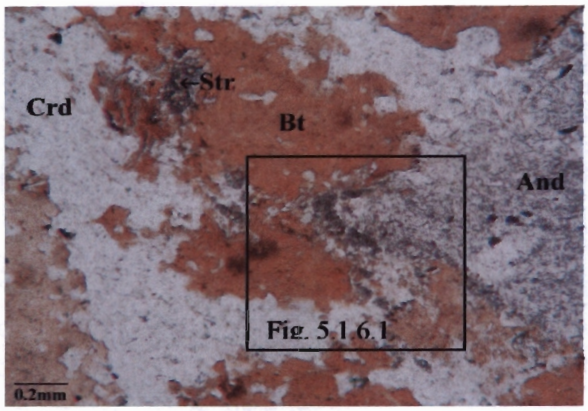

Figure 3.2.19: Photograph illustrating the general mineralogy of sample 423.

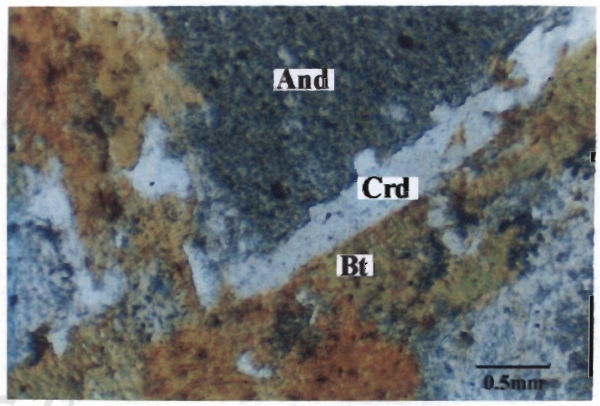

Figure 3.2.20: Sample 423, crd growing between bt and and.

Figure 3.2.21: Str at the rim of relict and which has been pseudomorphed by crd + ms in sample 423.

Sample V19 contains poorly formed staurolite and andalusite, which form part of a granoblastic assemblage including quartz, feldspar, biotite and chlorite. The relationship between andalusite and staurolite is difficult to discern, but since staurolite is observed to have andalusite growing around it in places, and the opposite is not observed, it seems likely that andalusite succeeds staurolite in such cases (Fig. 3.2.22). Staurolite is also associated with minor amounts of muscovite and biotite, the latter once again displaying a complex relationship with chlorite as discussed for Samples W5, W10b and VH37. Lastly, sample V40b exhibits an assemblage defined by large poikiloblasts of garnet, staurolite, biotite and cordierite. Cordierite, staurolite and biotite are intricately associated and all

grow around garnet (Fig. 3.2.23). In some areas staurolite is surrounded by cordierite, which appears to have grown at the expense of staurolite and biotite (Fig. 3.2.24) (Gibson & Wallmach, 1995; Gibson, 1996) and in other areas of the sample cordierite and staurolite appear to be the products of the reaction of muscovite and chlorite (Fig. 3.2.25 & 3.2.26). The matrix of this sample is muscovite-rich and once again biotite displays kink-banding defined by chlorite lath inclusions within biotite.

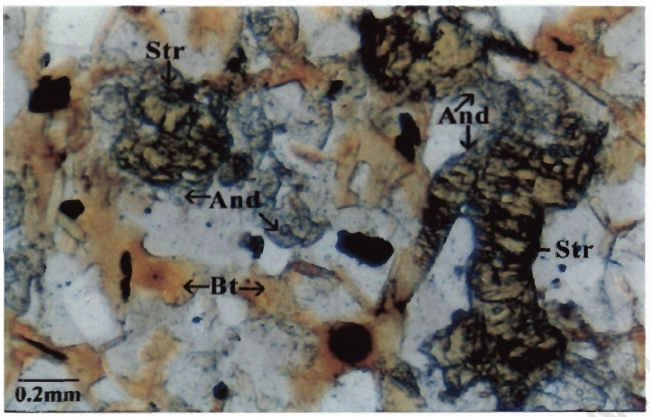

Figure 3.2.22: General mineralogy of Sample V19, note how andalusite grows around staurolite.

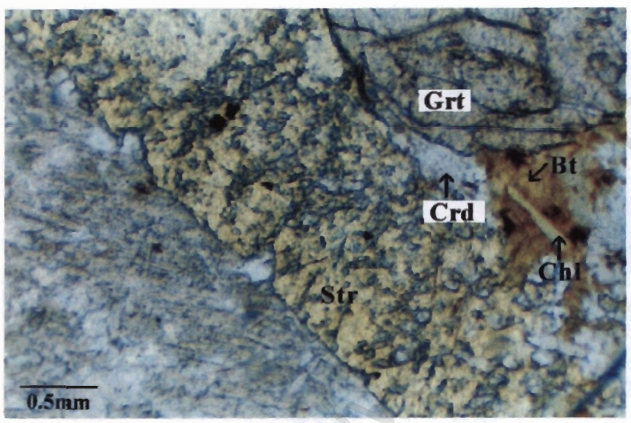

Figure 3.2.23: Grt porphyroblast and str and bt poikiloblasts in ms-rich matrix of Sample V40b. Note the presence of crd between bt and str.

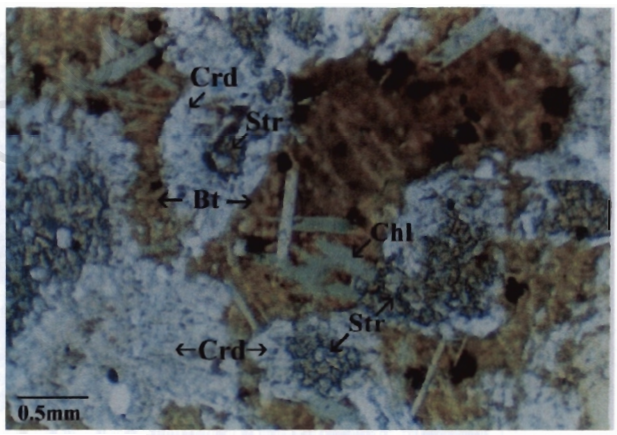

Figure 3.2.24: Photograph illustrating the intricate association of bt, str and crd in sample V40b. Note how crd appears to grow at the expense of str and bt.

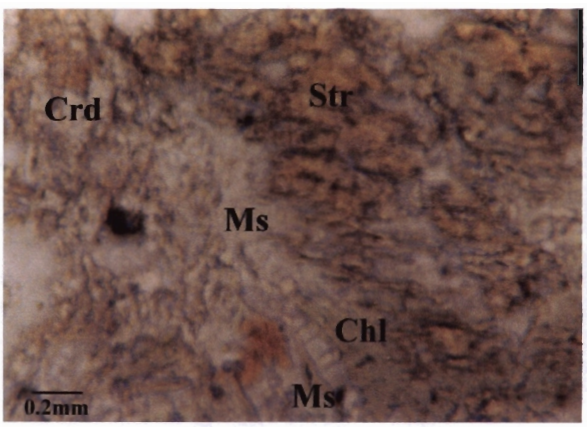

Figure 3.2.25: Sample V40b, photograph taken in plane polarised light illustrating the intricate association between str, crd, ms and chl.

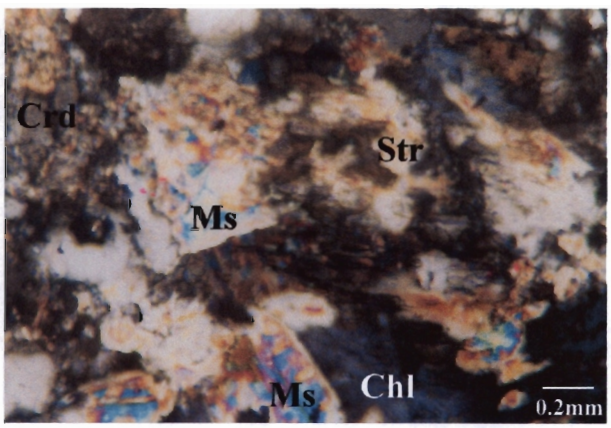

Figure 3.2.26: Sample V40b, photograph taken in cross polarised light illustrating the intricate association between str, crd, ms and chl.

3.3 ROCKS OF THE ARCHEAN BASEMENT COMPLEX FROM THE CORE

The Archean Basement Complex comprises both trondhjemitic, granitoid and tonalitic gneisses, and xenoliths of metapelitic supracrustal rocks within the gneisses. Table 3.3.1 summarises the petrography of all of the samples in this sample set, which will be discussed in greater detail below.

Sample	Locality	Lithology	Mineralogy	Description
438	OGG	FG Granite Gneiss	Qtz + Kfs + Plag + Bt ± Opq ± Ms ± Chl ± Opx	Qtz massively recrystallised. Very minor amount of Opx
439	OGG	FG Granodiorite	Qtz + Plag + Bt + Cpx ± Chl ± Ms ± Ep	Predominantly recrystallised Qtz Bt → Chl
440a	OGG	CG Granite Gneiss	Qtz + Fsp ± Bt ± Opq	Qtz completely recrystallised Fsp contains lath-like sericitization Bt → Chl and kink banded
440b	OGG	MG Granodiorite	Qtz + Fsp + Bt + Opx /Cpx /Amph ± Opq	Qtz completely recrystallised Fsp contains lath-like sericitization Bt → Chl and kink banded
441	OGG	CG Granite Gneiss	Qtz + Kfs + Plag + Bt ± Opx	Qtz massively recrystallised Kfs > Plag, Fsp sericitized Bt → Chl
442	OGG	CG Granite Gneiss	Qtz + Plag + Kfs + Bt + Opq ± Chl ± Ep	Qtz exhibits planar deformation features, including undulose extinction & recrystallised qtz (PDF) Fsp sericitized, Bt → Chl
443	OGG	CG Granite Gneiss	Qtz + Plag + Kfs + Bt + Opq ± Chl ± Ms	Qtz massively recrystallised Plag shows minor myrmekitic and antiperthitic textures, Fsp sericitized Bt slightly chloritized, kink banded
444	OGG	CG Granite Gneiss	Qtz + Kfs + Bt + Opq ± Chl ± Ms	2 phases of Qtz a) exhibits planar recrystallisation features (PDFs) & undulose extinction (ue) b) younger, massively recrystallised + Ms inclusions Fsp sericitized Increase in Bt content compared to 443, altered to Chl, kink banded
437	OGG	CG Granite Gneiss	Qtz + Plag + Fsp + Bt ± Chl ± Opq ± Ep	Qtz displays PDFs + ue Plag K-metasomatized, sericitized, shows minor graphic texture Bt → Chl
434	OGG	CG Granite Gneiss	Qtz + Plag + Fsp + Bt + Amph ± Chl ± Opq ± Ep	Same as for Sample 437 with increased mafic content
433	ILG	MG Granite	Qtz + Fsp + Plag + Bt ± Chl ± Opq ± Ms ± Px / Amph (yellow min.)	Qtz exhibits high concentration PDFs Fsp highly altered, sericitized, exhibits perthitic and graphic textures
432	OGG	MG Granodiorite	Qtz + Plag + Chl + Hbl ± Bt ± Opq	Qtz displays PDFs + ue Plag sericitized 2 phases biotite, older Bt →Chl
430	Dyke	Dolerite	Plag + Cpx + Qtz + Opq ± Bt ± Chl	Cpx being altered to Bt + Chl Cross-cut by pseudotachylite veins
431	OGG	CG Granite Gneiss	Qtz + Plag + Fsp + Bt ± Opq ± Ep	Qtz + Plag exhibit usual DMF Fsp show minor graphic & myrmekitic textures Bt slightly chloritized

Table 3.3.1: Mineralogy of samples collected from the basement complex of the core of the Vredefort dome. Mineral abbreviations after Kretz (1983). CG, MG, FG – coarse, medium & fine grained.

Sample	Locality	Lithology	Mineralogy	Description
428	ILG	MG Granite	Qtz + Plag + Kfs + Bt ± Chl ± Opq	Qtz + Fsp exhibit DMF Yellow mineral associated with Bt & Chl Lots of fluid inclusions (flincs) in all minerals
429a	ILG	FG Granite	Qtz + Plag + Fsp + Bt ± Chl ± Ep ± Opx	Plag K-metasomatized Qtz +Fsp display DMF Bt → Chl
429b	ILG	MG Granite	Qtz + Plag + Fsp + Bt ± Chl ± Ep ± Opx	Plag antiperthitic Increased Opx content compared to 429a
435	ILG	Charnockite	Plag + Cpx + Opx ± Bt ± Opq ± Qtz	Plag sericitized Opx altered to yellow mineral + Chl Cpx contains Opx lamellae All mafic minerals contain Qtz
436	ILG	Charnockite	Plag + Kfs + Opx (hypersthene) + Cpx ± Bt ± Opq ± Qtz	As for Sample 435 with decreased mafic content Bt kink-banded
445	ILG	F-MG Granite	Qtz + Plag + Fsp ± Bt ± Opq	Qtz exhibits ue Fsp sericitized but less so than other ILG samples Bt very fine grained
446	ILG	CG Granite	Plag + Kfs + Qtz + Bt ± Chl ± Opq ± Opx	Predominantly perthitic Kfs, sericitized Minor Opx + Bt, both altered to yellow mineral All minerals contain lots of flincs
447	ILG	M-CG Granite	Qtz + Plag + Kfs + Chl ± Bt ± Ep	Qtz displays PDFs + eu Fsp sericitized with some antiperthitic and myrmekitic textures Bt altered to Chl
448a	ILG	Charnockite	Plag + Qtz + Bt + Opx ± Opq	Qtz displays DMF + very fine grained recrystallisation Fsp antiperthitic and sericitized Opx altered to yellow mineral Bt associated with Opx + Opq
448b	ILG	MG Granite	Qtz + Plag + Kfs ± Chl	Qtz massively recrystallised, with a high concentration of PDFs Contains pseudotachylite which cross-cuts all other components
449	ILG	CG Granite	Qtz + Plag + Kfs ± Opx ± Ms ± Chl	Qtz + Plag exhibit DMF Plag K-metasomatized
450	ILG	M-CG Granite	Qtz + Kfs ± Plag ± Bt ± Chl ± Ms	Qtz displays PDFs + eu Fsp predominantly perthitic & myrmekitic, also sericitized Bt → Chl
451	ILG	CG Granite	Qtz + Plag ± Bt ± Chl ± Opq	High concentration pseudotachylite Bt kink-banded, altered to Chl + Opq
452	ILG	CG Granite	Qtz + Kfs + Plag +Chl ± Bt ± Ms ± Opq	Qtz exhibits a high concentration of PDFs Fsp sericitized, perthitic, myrmekitic
454a	ILG	CG Mafic Granulite	Opx (65%) + Cpx (15%) + Plag (15%)+ Microcline (3%) ± Qtz ± Bt (2%)	Pyroxenes euhedral and contain deformation twins

Table 3.3.1 (cont.): Mineralogy of samples collected from the basement complex of the core of the Vredefort dome. Mineral abbreviations after Kretz (1983). CG, MG, FG – coarse, medium & fine grained.

454b	ILG	MG Granite	Qtz + Plag + Fsp ± Bt ± Opq ± Ms ± Chl	Low concentration PDFs Fsp sericitized Bt very fine grained Pyroxenes altered to yellow mineral
455a	ILG	M-CG Granite	As for 454b with decreased Bt & increased Px content	Pyroxenes altered to Chl Contains pseudotachylite veins with recrystallised Qtz corona
455b	ILG	CG Granite	Qtz + Plag + Fsp ± Chl ± Bt ± Opq	Qtz shows PDFs + ue Fsp sericitized, antiperthitic, myrmekitic
461	ILG	CG Leucogranite	Qtz + Plag + Kfs	Qtz has low concentration of PDFs Fsp displays massive myrmekitic + perthitic textures
460	ILG	MG Granite	Qtz + Fsp + Plag ± Chl ± Bt ± Opq ± Ep	Qtz has low concentration of PDFs Fsp displays massive myrmekitic + perthitic textures
459	ILG	MG Leucogranite	Qtz + Fsp + Plag	As for 460 and 461
458	ILG	MG Granite	Qtz + Fsp + Plag ± Chl ± Bt ± Opq	Qtz displays PDFs Fsp slightly altered with some perthitic & myrmekitic textures
457	ILG	CG Granite	Qtz + Fsp + Plag ± Chl ± Ms ± Opq	Qtz grains show recrystallisation around the edges, display few PDFs Fsp perthitic, sericitized
456a	SMZ	Garnet-Cordierite restite	Qtz + Fsp + Bt matrix + Grt + Crd ± Chl ± (Crd-Opx symplectite) ± Sil	Grt large, euhedral, rich in Qtz inclusions (with symplectite corona) Fsp sericitized
456b	SMZ	Garnet-Cordierite restite	Qtz + Fsp + Bt matrix + Grt + Crd ± Chl ± (Crd-Opx symplectite) ± Sil	Grt large, euhedral, rich in Qtz inclusions (with symplectite corona) Fsp sericitized slightly finer grained than 456a
456c	ILG	CG Leucogranite	Qtz + Fsp ± Chl ± Ep ± Grt ± Sp	Qtz grains show recrystallisation around edges, show few PDFs Fsp perthitic, sericitized Contains spinel within garnet
VH14	SMZ	Garnet-Quartz restite	Qtz + Fsp + Bt matrix + Grt ± Chl ± (Crd-Opx symplectite) ± Sil ± Sp	Qtz grains highly recrystallised Crd-Opx symplectite around garnets and biotite, also Opx corona between Qtz and Fsp
VT652	SMZ	Garnet-Quartz restite	Qtz + Fsp + Bt matrix + Grt ± Chl ± (Crd-Opx symplectite)	As for VH14, symplectite coronas not as well developed
VT654	SMZ	Garnet-Quartz restite	Qtz + Fsp + Bt matrix + Sil + Grt ± Chl ± (Crd-Opx symplectite)	Grt highly altered Poorly formed pseudotachylite associated with all minerals Abundant large Sil in part of the rock
HM3	SMZ Helpmekaar	Cordierite restite	Crd + Fsp + Qtz + Bt ± Chl ± melt	Crd contains Qtz, Bt, Chl inclusions
HM4	Dyke	Dolerite	Plag + Cpx + Qtz + Opq ± Bt ± Chl	Cpx being altered to Bt + Chl Cross-cut by pseudotachylite veins
HM6	SMZ Helpmekaar	Garnet-Orthopyroxene migmatite	Qtz + Fsp + Bt + Grt + Opx ± Ep	Grt as for sample VH14 with symplectite coronas Qtz grains largely recrystallised Fsp highly sericitized
HM7	SMZ Helpmekaar	Garnet-Quartz restite	Qtz + Fsp + Bt matrix + Grt + Crd ± Chl ± Crd-Opx symplectite ± Sil, Ep	Fewer Grt and Bt than 456a Grt exhibits symplectite corona

Table 3.3.1 (cont.): Mineralogy of samples collected from the basement complex of the core of the Vredefort dome. Mineral abbreviations after Kretz (1983). CG, MG, FG – coarse, medium & fine grained.

HM10	SMZ Helpmekaar	Mafic granulite	Fsp + Plag + Opx + Cpx + Amph ± Qtz	
HM14	SMZ Helpmekaar	Cordierite restite	As for sample ± HM3 Sp	As for sample HM3, includes Sp
HM16	SMZ Helpmekaar	Garnet-cordierite-orthopyroxene migmatite	Grt + Crd + Opx + Qtz + Fsp + Bt + (Qtz + Fsp leucosome)	
H5		Garnet-quartz restite	As for sample 456a ± Chl	Displays Crd-Opx symplectite around Grt and Bt
VT623	metapelite	Crd restite	Crd + Fsp	Crd oikocryts recrystallised

Table 3.3.1 (cont.): Mineralogy of samples collected from the basement complex of the core of the Vredefort dome. Mineral abbreviations after Kretz (1983). CG, MG, FG – coarse, medium & fine grained.

The gneissic rocks of the core of the Vredefort structure have been categorized into two gneissic terranes, namely the OGG and the ILG. In outcrop, the migmatised OGG comprises a grey trondhjemitic component and a pink, coarse-grained granite gneiss with megacrysts of potassium feldspar (Fig. 3.3.1). In the field the relationship between these two rock types is complex, with no distinct intrusive contacts being evident between them, however, both rock types display the Archean age gneissic foliation described by Roering *et al.* (1990) and have experienced shearing which cross-cuts and displaces the gneissic foliation (Fig. 3.3.2). The trondhjemitic and granitoid gneisses of the OGG are coarse grained and typically contain quartz + k-feldspar + plagioclase + biotite ± opaques ± chlorite ± muscovite (Fig. 3.3.3). The trondhjemitic gneiss is medium-grained and comprises plagioclase + quartz + chlorite + biotite + opaques + k-feldspar ± hornblende (Figs. 3.3.4 & 3.3.5). At thin section scale the rocks of the OGG show recrystallisation textures associated with the impact event such as undulose extinction patterns, massive recrystallisation and planar recrystallisation features in quartz (Figs. 3.3.6 & 3.3.7) and kink-banding in biotite (Fig. 3.3.8). Large-scale sericitization (Fig. 3.3.9) and alteration are observed in feldspar, as well as perthitic and/or myrmekitic textures.

Figure 3.3.1: Outcrop of migmatitic OGG at Koppieskraal quarry, note the pink granite and grey trondhjemitic components.

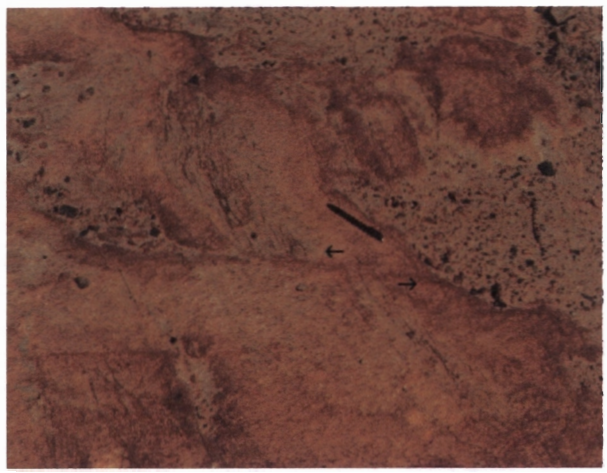

Fig. 3.3.2: Displacement (indicated by arrows) of the gneissic fabric in the OGG by younger shearing, as observed at Leeuwkop quarry.

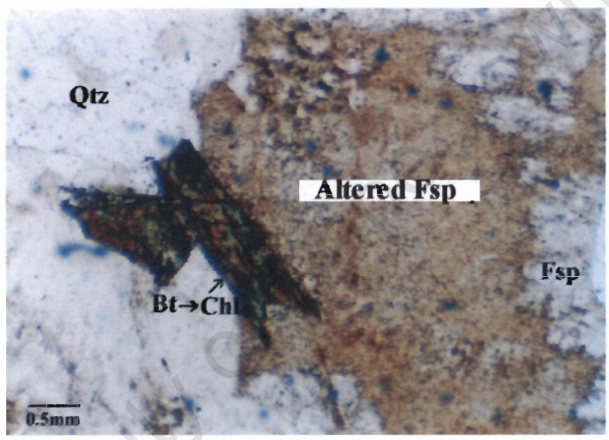

Figure 3.3.3: Thin section photograph of sample 442 illustrating the granitoid composition of OGG gneisses.

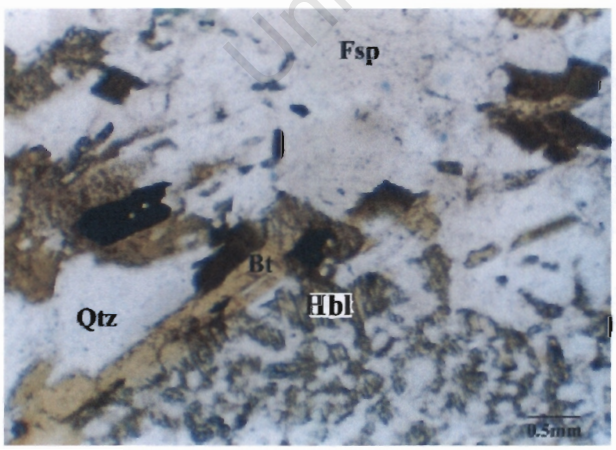

Figure 3.3.4: Thin section photograph of sample 440b displaying the typical mineral composition of the OGG trondhjemites, which contain ~20% amphibole.

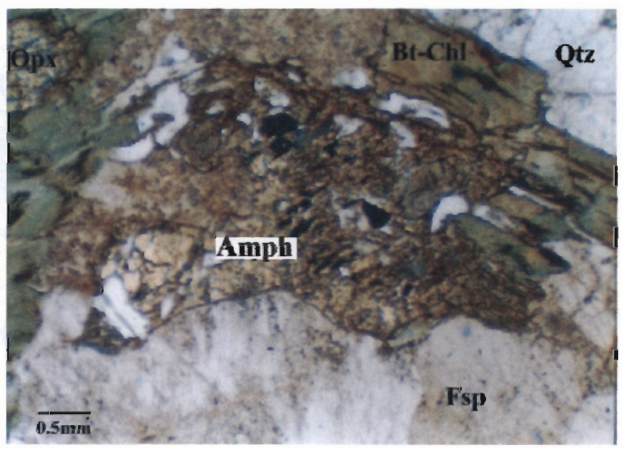

Figure 3.3.5: Thin section photograph of sample 432 displaying the typical mineral composition of the OGG trondhjemites, which contain ~20% amphibole.

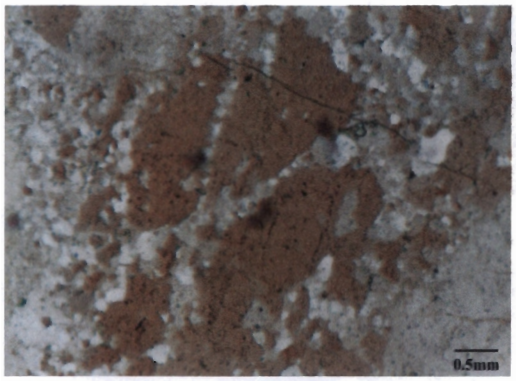

Figure 3.3.6: Photograph taken under partially cross polarized light displaying the recrystallisation of quartz in sample 448, which is observed throughout the basement granites.

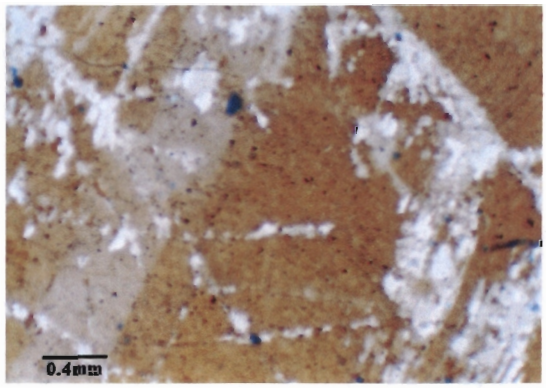

Figure 3.3.7: Recrystallised PDFs observed in quartz grains under cross polarized light, in sample 435. Note how quartz recrystallisation has occurred along the PDFs, which is typically how they are observed in most of the samples from the basement core.

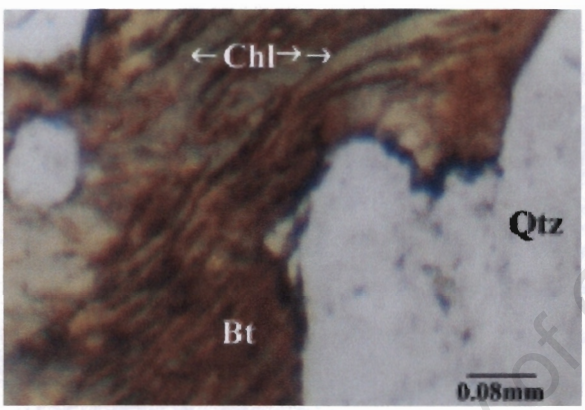

Figure 3.3.8: Chlorite replacing kink-banded biotite in sample 448a as observed throughout the granitoid sample set.

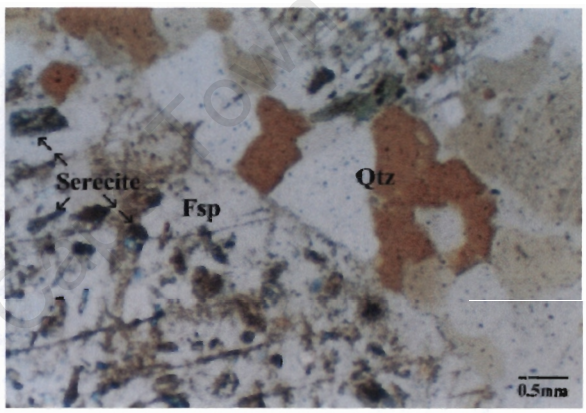

Figure 3.3.9: Photograph of sample 440a illustrating the sericitization of feldspar, a texture observed in most of the samples from the basement granitoids.

The gneisses of the ILG terrane are also coarse-grained, but are more leucocratic compared to those from the OGG terrane. The ILG gneisses are composed of quartz + perthitic plagioclase + k-feldspar ± biotite ± chlorite ± orthopyroxene (Fig. 3.3.10). In thin section these gneisses look very much like those from the OGG and display the same deformation features in each of the minerals as described for the OGG samples. Previous researchers (Hart *et al.*, 1981) suggest an increase in concentration of the planar deformation features along which quartz recrystallisation has occurred, towards what they have termed the 'Vredefort discontinuity', however, the samples analysed in this study seem to indicate variable concentration of quartz recrystallisation features throughout the OGG and the ILG.

The ILG terrane also includes some charnockites close to the boundary which separates the OGG and ILG. The charnockites are medium-grained dark brown rocks which are composed of plagioclase + orthopyroxene + clinopyroxene + orthoamphiboles ± quartz ± biotite ± opaques (Fig. 3.3.11).

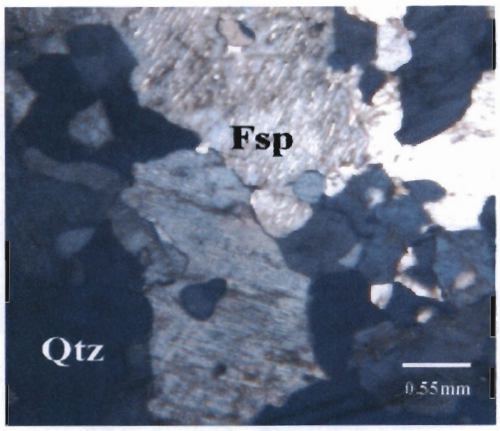

Figure 3.3.10: Thin section photograph taken under cross polarized light of sample 456c, displaying the typical perthitic texture of feldspar seen in many of the ILG gneisses.

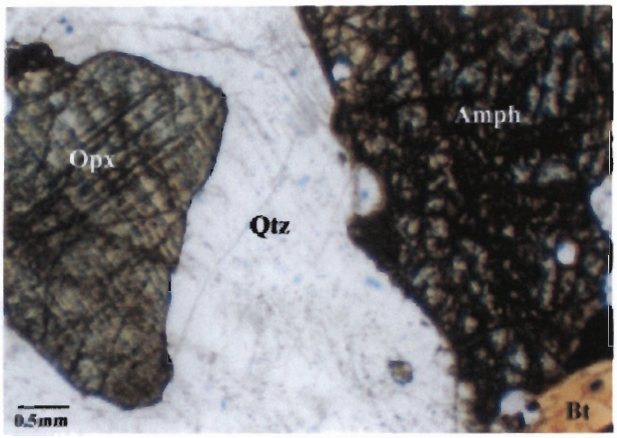

Figure 3.3.11: Photograph of the mafic-rich charnockite (sample 435) found within the ILG, which contain abundant ortho- and clinopyroxene, amphibole and biotite within a quartz-feldspar groundmass.

A number of xenolithic supracrustal rocks are caught up in the trondhjemites and tonalites of the ILG. These include mafic granulites and metapelitic units which include migmatites and restites. The mafic granulites are typically fine-grained orthogneisses and have compositions as for sample 454a (Table 3.3.1) which contains the minerals andesine, clinopyroxene, plagioclase, microcline and minor quartz, biotite, hornblende and magnetite (Figure 3.3.12) (Stepto, 1990).

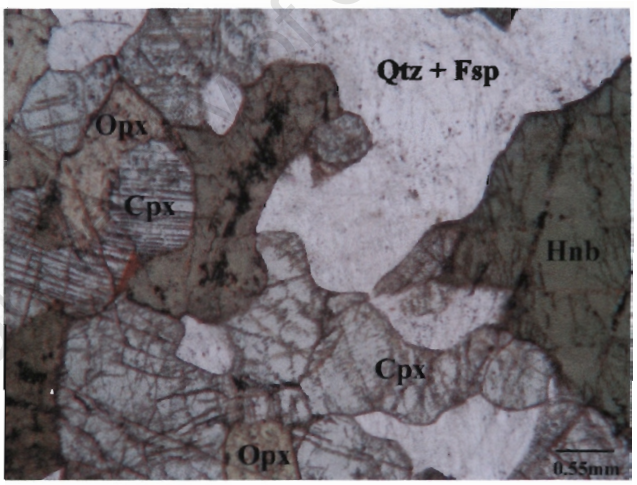

Figure 3.3.12: Sample 454a, mineral assemblage typical of the mafic granulites observed within the ILG.

Schreyer & Abraham (1978) and Stevens *et al.* (1997a) have produced detailed petrographic work on the Steynskraal type granulite-grade metapelites. They identified garnet-cordierite and garnet–cordierite-orthopyroxene migmatites, which comprise the latter minerals 'produced in conjunction with stromatic leucosomes of Qtz + Plag + Kfs' (Stevens *et al.*, 1997a), and suggest these formed as the product of biotite breakdown to create a H_2O-undersaturated melt plus a mafic residual crystalline component. Stevens *et al.* (1997a) also identified three types of restites, namely garnet-quartz, garnet-cordierite and cordierite restites, from which they suggest the melt phase observed in the migmatites was removed as a result of temperatures exceeding the maximum for Bt-melt co-existence.

Two retrograde assemblages were also described by Stevens *et al.* (1997a), these include the replacement of cordierite by Bt + Sil (referred to as the M2 assemblage) and a younger retrograde assemblage (M3) comprising cordierite-orthopyroxene symplectites surrounding and replacing garnet and a spinel (Sp) + Opx assemblage which overgrows and replaces the M2 assemblage. Gibson (2002) has since found that the latter M3 assemblage is more complex than initially described by Stevens *et al.* (1997a) and that the Crd-Opx symplectite coronas surrounding garnet are themselves surrounded by either a 'corona of blocky or columnar orthopyroxene, developed against matrix quartz, or by an Opx-Plag symplectite, developed either where garnet abuts feldspar or between the blocky Opx and the Crd-Opx symplectite' (Gibson, 2002). He also identifies an interstitial K-feldspar, 'moat-like' texture between Qtz and Fsp which is associated with the blocky orthopyroxene phase.

The samples collected in this study for the latter group of rocks exhibit all of the metamorphic assemblages described by Stevens *et al.* (1997a) and Gibson (2002) (Table 3.3.1, Figs. 3.3.13-17), therefore no further petrographic or geochemical work was done on these samples and most of the petrographic and geochemical data quoted for these rocks are taken from the previous studies.

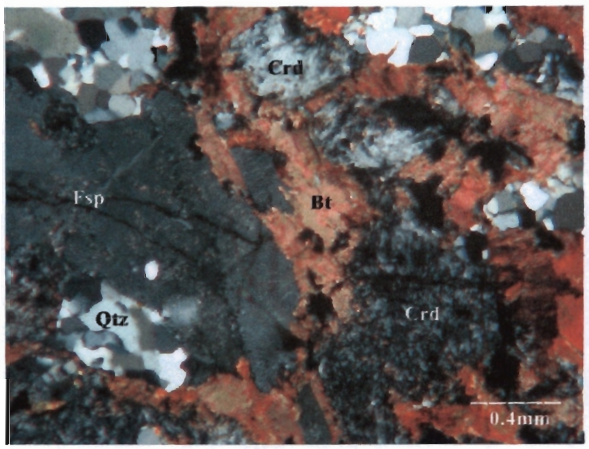

Figure 3.3.13: Photograph taken under cross polarised light displaying the typical mineral assemblage of a cordierite restite (sample HM3).

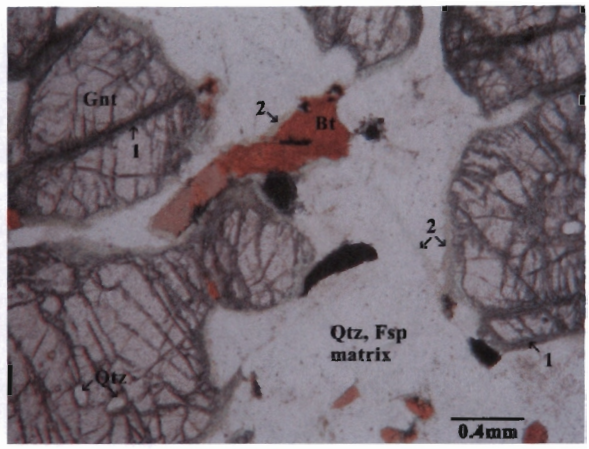

Figure 3.3.14: Photograph illustrating two phases of symplectite growth around garnet and biotite as observed in sample 456b. 1 – Crd-Opx symplectite 2 – Opx or Opx-Plag symplectite.

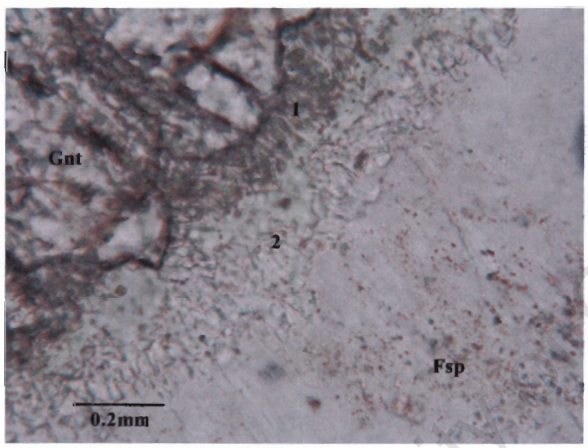

Figure 3.3.15: Close-up plane polarised photograph of two phases of symplectite growth observed in sample 456a. 1 – Crd-Opx symplectite 2 – Opx-Plag symplectite abutting Fsp.

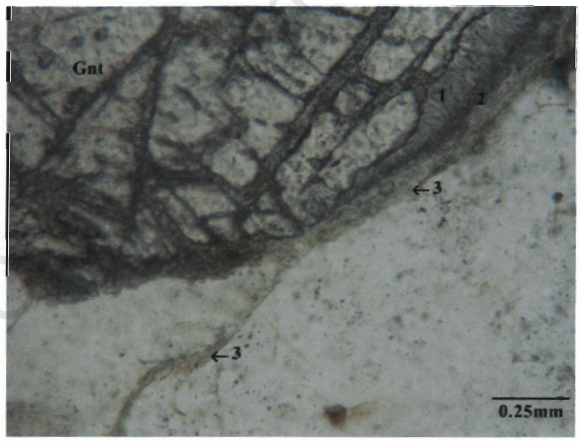

Figure 3.3.16: Photograph illustrating three phases of symplectite growth around garnet (1,2&3) and between matrix Qtz & Fsp (3) as observed in sample VH14. 1 – Crd-Opx symplectite 2 – blocky Opx 3 - Ksp symplectite which continues as a 'moat-like' feature where matrix minerals abut one another.

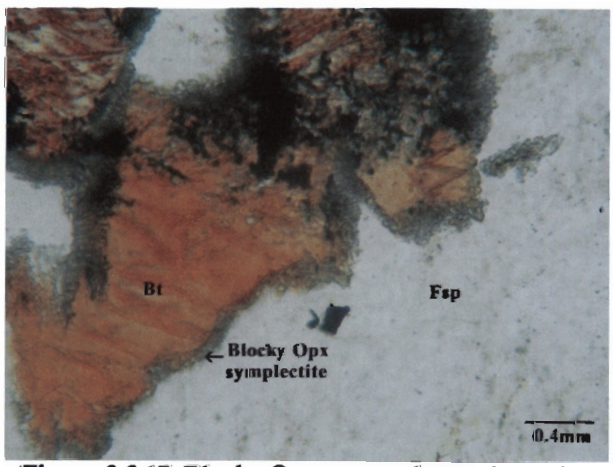

Figure 3.3.17: Blocky Opx corona observed growing around biotite in sample VH14 under plane polarized light. Also note kink banding texture in Bt. Black mineral is ilmenite.

CHAPTER 4
MINERAL CHEMISTRY

4.1 THE COLLAR ROCKS

Mineral compositions were determined for selected samples using the Camebax 355 microprobe at Rand Afrikaans University. The link exl2 EDS system is used for data processing which applies ZAF corrections against Smithsonian and Microanalysis Consultants standards. The microprobe was run at 15kV and 10nA on brass, and counting times for analyses varied from 40-60 seconds for the amphiboles, biotites, chlorites and cordierites, and up to 90 seconds for the garnets.

Figure 4.1.1 is an AFM plot of the garnet, biotite, chlorite, cordierite and amphibole mineral compositions analysed and exhibits the variation in mineral chemistry observed across the sample set. Mineral composition data are presented in Tables 4.1.1-7 and the results obtained for each mineral analysed are discussed below.

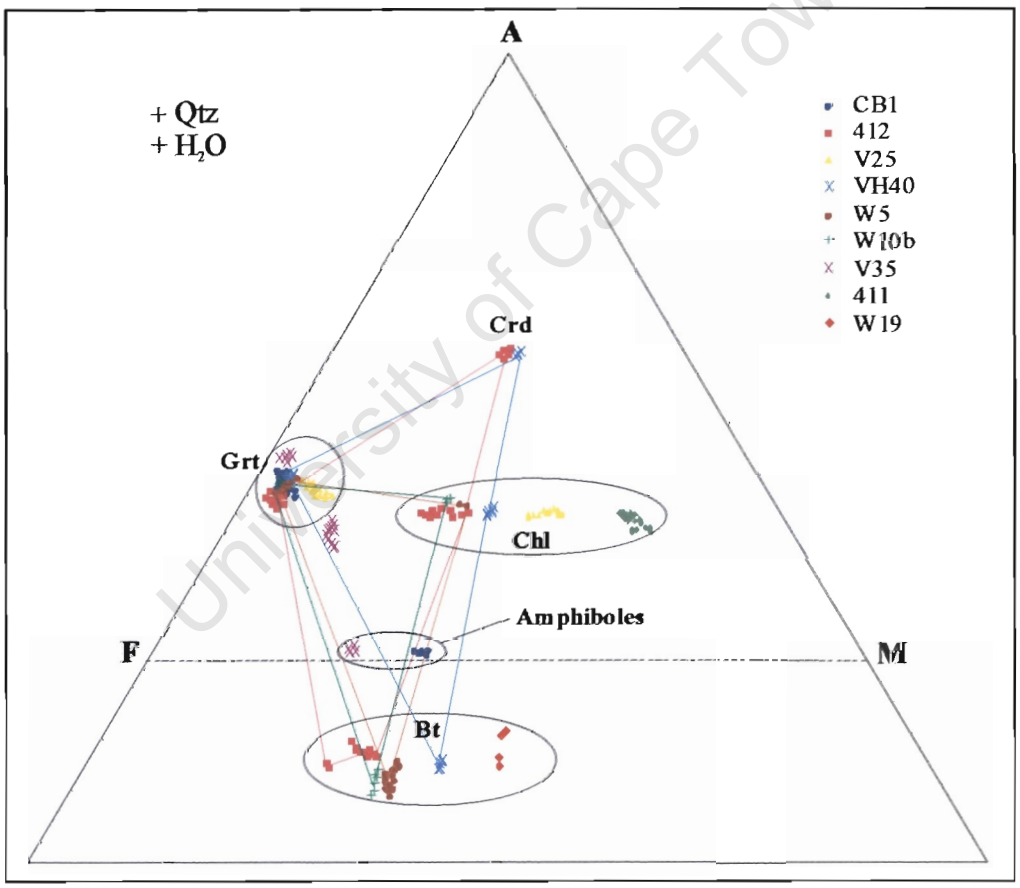

Figure 4.1.1: AFM diagram illustrating the mineral compositions of phases analysed for Samples CB1, 412, V25, 411, V35, VH40, W5, W10 and W19.

4.1.1 Garnet

Garnet is observed in a large proportion of the samples collected from the Vredefort collar and compositional data are presented for garnets in each of the samples 412, V25, VH40,

	CB1 Garnet 1					
Point	**1**	**2**	**3**	**4**	**5**	**7**
SiO_2	37.6	37.1	37.6	37.7	37.6	37.5
TiO_2	-	-	0.1	0.1	-	0.1
Al_2O_3	21.2	21.1	21.1	21	21.3	21
FeO	36.9	36.1	34.9	35.3	33.9	33.6
MnO	1.6	3.5	3	2.5	4.6	5
MgO	1.1	1.2	1.2	1.4	1	1
CaO	3.3	2.7	3.3	3.2	3.6	3.6
Cr_2O_3	0.1	0.1	-	-	0.1	-
Total	101.8	101.8	101.2	101.2	102.1	101.8
Si	6.008 } 6.01	5.957 } 6.00	6.027 } 6.03	6.038 } 6.04	5.993 } 6.00	6.001 } 6.00
Al^{2+}	-	0.043	-	-	0.007	-
Al^{3+}	3.994 } 4.01	3.951 } 4.00	3.988 } 4.00	3.965 } 4.00	3.993 } 4.01	3.962 } 4.00
Cr	0.013	0.013	-	-	0.013	-
Fe^{3+}	-	0.036	-	0.023	-	0.026
Ti	-	-	0.012	0.012	-	0.012
Mg	0.262 } 5.98	0.287 } 6.04	0.287 } 5.94	0.334 } 5.93	0.238 } 5.99	0.238 } 6.00
Fe^{2+}	4.931	4.812	4.679	4.706	4.519	4.471
Mn	0.217	0.476	0.407	0.339	0.621	0.678
Ca	0.565	0.465	0.567	0.549	0.615	0.617
X_{Fe}	0.950	0.944	0.942	0.934	0.950	0.949

	CB1 Garnet 1				Garnet 2
Point	**8**	**9**	**10**	**11**	**1**
SiO_2	37.6	37.2	37.1	37.6	37.3
TiO_2	-	-	-	-	-
Al_2O_3	21.2	20.7	20.9	21.3	21
FeO	35.3	34.7	35.4	36.1	36
MnO	2.5	2.9	2.1	1.9	1.9
MgO	1.3	1.3	1.4	1.6	1.4
CaO	3.5	3.5	3.5	3.2	3
Cr_2O_3	-	-	-	0.1	-
Total	101.4	100.3	100.4	101.8	100.6
Si	6.015 } 6.02	6.025 } 6.03	6.001 } 6.00	5.992 } 6.00	6.018 } 6.02
Al^{2+}	-	-	-	0.008	-
Al^{3+}	3.998 } 4.00	3.953 } 4.00	3.985 } 4.00	3.994 } 4.01	3.994 } 4.00
Cr	-	-	-	0.013	-
Fe^{3+}	0.002	0.047	0.015	-	0.006
Ti	-	-	-	-	-
Mg	0.310 } 5.97	0.314 } 5.97	0.337 } 6.01	0.380 } 5.99	0.337 } 5.97
Fe^{2+}	4.721	4.654	4.774	4.811	4.852
Mn	0.339	0.398	0.288	0.256	0.260
Ca	0.600	0.607	0.607	0.546	0.519
X_{Fe}	0.938	0.937	0.934	0.927	0.935

Table 4.1.1.1: Mineral composition data, number of ions on the basis of 24O and X_{Fe} values calculated for all garnet point analyses in sample CB1 garnets 1& 2. Rim - blue, Core - pink.

CB1 Garnet 3

Point	1		2		3		4		5		6		7	
SiO_2	37.2		37.8		37.7		37.8		37.7		36.7		37.5	
TiO_2	0.1		-		-		-		0.2		0.1		-	
Al_2O_3	20.9		21.1		21.1		21.2		21.2		20.5		21.2	
FeO	35.3		34.4		33.8		34.6		34.5		34.9		35.3	
MnO	2.5		3.7		4.2		4.2		3.4		3		2.8	
MgO	1.2		1.1		1.2		1.1		1.1		1.1		1.3	
CaO	3.3		3.7		3.5		3.5		3.3		2.7		3.2	
Cr_2O_3	0.1		-		0.1		-		-		0.1		0.1	
Total	100.6		101.8		101.6		102.4		101.4		99.1		101.4	
Si	6.008	6.01	6.031	6.03	6.024	6.02	6.009	6.01	6.028	6.03	6.025	6.03	6.005	6.01
Al^{2+}	-		-		-		-		-		-		-	
Al^{3+}	3.980	4.01	3.969	4.00	3.975	4.00	3.973	4.00	3.996	4.02	3.968	4.00	4.002	4.02
Cr	0.013		-		0.013		-		-		0.013		0.013	
Fe^{3+}	-		0.031		0.012		0.027		-		0.007		-	
Ti	0.012		-		-		-		0.024		0.012		-	
Mg	0.289	5.97	0.262	5.95	0.286	5.96	0.261	6.00	0.262	5.90	0.269	5.95	0.310	5.97
Fe^{2+}	4.768		4.559		4.505		4.573		4.613		4.785		4.728	
Mn	0.342		0.500		0.568		0.566		0.460		0.417		0.380	
Ca	0.571		0.633		0.599		0.596		0.565		0.475		0.549	
X_{Fe}	0.943		0.946		0.940		0.946		0.946		0.947		0.938	

CB1 Garnet 4

Point	1		2		3		4		5		6		7	
SiO_2	37.7		37.4		37.1		37.6		37.4		37.5		37.6	
TiO_2	-		-		-		-		-		-		-	
Al_2O_3	21.2		21.1		21		21		20.9		20.9		21.2	
FeO	36.4		35.4		34.1		32.9		32.9		34.4		36.5	
MnO	1.3		3		4.4		5.7		5.4		4.2		1.5	
MgO	1.3		1.4		1.1		0.9		0.9		1.1		1.4	
CaO	3.4		3.5		3.5		3.6		3.6		3.6		3.1	
Cr_2O_3	0.1		0.1		-		-		-		0.1		0.1	
Total	101.4		101.9		101.2		101.7		101.1		101.8		101.4	
Si	6.027	6.03	5.975	6.00	5.977	6.00	6.021	6.02	6.022	6.02	6.004	6.00	6.015	6.02
Al^{2+}	-		0.025		0.023		-		-		-		-	
Al^{3+}	3.995	4.01	3.949	4.00	3.966	4.00	3.964	4.00	3.968	4.00	3.945	4.00	3.999	4.01
Cr	0.013		0.013		-		-		-		0.013		0.013	
Fe^{3+}	-		0.038		0.034		0.036		0.032		0.042		-	
Ti	-		-		-		-		-		-		-	
Mg	0.310	5.93	0.333	6.03	0.264	6.03	0.215	5.98	0.216	5.97	0.262	6.01	0.334	5.95
Fe^{2+}	4.866		4.692		4.560		4.370		4.399		4.564		4.884	
Mn	0.176		0.406		0.600		0.773		0.737		0.570		0.203	
Ca	0.582		0.599		0.604		0.618		0.621		0.618		0.531	
X_{Fe}	0.940		0.934		0.945		0.953		0.953		0.946		0.936	

Table 4.1.1.2: Mineral composition data, number of ions on the basis of 24O and X_{Fe} values calculated for all garnet point analyses in sample CB1 garnets 3&4. Rim - blue, Core - pink.

	412 Garnet 1				412 Garnet 2		
Point	**2**	**4**	**5**	**6**	**1**	**2**	**3**
SiO_2	37.56	37.49	37.38	37.54	37.66	37.47	37.85
TiO_2	0.04	0.03	0.21	0.02	-	-	0.08
Al_2O_3	21.04	21.23	21.13	21.34	21.26	21.3	21.21
FeO	36.97	38.18	36.19	36.68	37.69	37.09	37.51
MnO	2.79	0.97	3.4	3.2	3.11	3.88	2.68
MgO	1.52	1.51	1.48	1.44	0.94	1.25	1.23
CaO	1.26	1.53	1.4	1.27	1.24	0.9	1.41
Cr_2O_3	-	-	-	-	-	-	-
Total	101.18	100.94	101.19	101.49	101.9	101.89	101.97
Si	6.038	6.030	6.009	6.017	6.034	6.006	6.043
	6.04	6.03	6.01	6.02	6.03	6.01	6.04
Al^{2+}	-	-	-	-	-	-	-
Al^{3+}	3.988	4.026	4.005	4.032	4.016	4.025	3.992
Cr	-	-	-	-	-	-	-
	4.00	4.03	4.03	4.03	4.02	4.03	4.00
Fe^{3+}	0.007	-	-	-	-	-	-
Ti	0.005	0.004	0.025	0.002	-	-	0.010
Mg	0.364	0.362	0.355	0.344	0.224	0.299	0.293
Fe^{2+}	4.964	5.136	4.866	4.917	5.050	4.972	5.009
	5.93	5.89	5.92	5.91	5.91	5.95	5.91
Mn	0.380	0.132	0.463	0.434	0.422	0.527	0.362
Ca	0.217	0.264	0.241	0.218	0.213	0.155	0.241
X_{Fe}	0.932	0.934	0.932	0.935	0.957	0.943	0.945

	412 Garnet 4				
Point	**1**	**2**	**4**	**5**	**6**
SiO_2	37.54	37.5	37.64	37.56	37.54
TiO_2	0.13	0.04	-	0.03	0.09
Al_2O_3	21.12	21.27	21.47	21.22	21.38
FeO	38.86	36.51	35.32	36.8	38.99
MnO	1.27	4.22	4.91	3.63	0.82
MgO	1.6	1.24	1.27	1.51	1.62
CaO	1.33	0.94	1.33	0.9	1.47
Cr_2O_3	-	-	-	0	0
Total	101.85	101.72	101.94	101.65	101.91
Si	6.006	6.015	6.012	6.019	5.994
	6.01	6.02	6.01	6.02	6.00
Al^{2+}	-	-	-	-	0.006
Al^{3+}	3.984	4.022	4.043	4.009	4.018
Cr	-	-	-	-	-
	4.00	4.02	4.04	4.01	4.03
Fe^{3+}	-	-	-	-	-
Ti	0.016	-	-	0.004	0.011
Mg	0.382	0.296	0.302	0.361	0.385
Fe^{2+}	5.200	4.897	4.718	4.932	5.206
	5.98	5.93	5.91	5.94	5.95
Mn	0.172	0.573	0.664	0.493	0.111
Ca	0.228	0.162	0.228	0.155	0.251
X_{Fe}	0.932	0.943	0.940	0.932	0.931

Table 4.1.1.3: Mineral composition data, number of ions on the basis of 24O and X_{Fe} values calculated for all garnet point analyses in sample 412 garnets 1, 2 & 4. Rim - blue, Core - pink.

	V25 Garnet 1			V25 Garnet 5	
Point	**2**	**3**	**6**	**1**	**2**
SiO_2	38.04	38.35	38.18	38.56	38.42
TiO_2	0.05	0.25	0.04	0.03	0.02
Al_2O_3	21.17	21.56	21.64	21.93	21.45
FeO	35.41	34.6	34.67	34.53	32.5
MnO	0.21	0.46	0.73	0.06	3.27
MgO	3.16	3.09	3.19	3.94	1.94
CaO	3.2	3.37	3.02	3.11	4.47
Cr_2O_3	0.02	0.11	0.21	-	0.04
Total	101.26	101.79	101.68	102.16	102.11
Si	6.024	6.021	6.007	6.006	6.047
Al^{2+}	-	-	-	-	-
	6.02	6.02	6.01	6.01	6.05
Al^{3+}	3.953	3.990	4.014	4.027	3.980
Cr	0.003	0.014	0.026	-	0.005
Fe^{3+}	0.038	-	-	-	0.013
Ti	0.006	0.030	0.005	0.004	0.002
	4.00	4.03	4.05	4.03	4.00
Mg	0.746	0.723	0.748	0.915	0.455
Fe^{2+}	4.652	4.543	4.562	4.498	4.265
Mn	0.028	0.061	0.097	0.008	0.436
Ca	0.543	0.567	0.509	0.519	0.754
	5.97	5.89	5.92	5.94	5.91
X_{Fe}	0.862	0.863	0.859	0.831	0.904

	V25 Garnet 3				
Point	**1**	**2**	**3**	**4**	**5**
SiO_2	38.63	38.49	36.94	38.67	38.71
TiO_2	0.05	0.05	0.08	0.08	0.11
Al_2O_3	21.63	21.58	20.76	21.68	21.58
FeO	34.16	32.91	32.96	33.79	34.2
MnO	0.55	2.33	2.67	0.45	0.09
MgO	3.42	2.37	2.67	3.68	3.87
CaO	3.58	4.56	3.77	3.29	3.41
Cr_2O_3	0.19	0.21	0.16	0.17	0.27
Total	102.21	102.5	100.01	101.81	102.24
Si	6.029	6.023	5.960	6.040	6.026
Al^{2+}	-	-	0.040	-	-
	6.03	6.02	6.00	6.04	6.03
Al^{3+}	3.980	3.981	3.909	3.992	3.961
Cr	0.023	0.026	0.020	0.021	0.033
Fe^{3+}	-	-	0.070	-	-
Ti	0.006	0.006	0.010	0.009	0.013
	4.01	4.01	4.00	4.02	4.01
Mg	0.795	0.553	0.642	0.857	0.898
Fe^{2+}	4.459	4.307	4.378	4.414	4.453
Mn	0.073	0.309	0.365	0.060	0.012
Ca	0.599	0.765	0.652	0.551	0.569
	5.93	5.93	6.04	5.88	5.93
X_{Fe}	0.849	0.886	0.872	0.837	0.832

Table 4.1.1.4: Mineral composition data, number of ions on the basis of 24O and X_{Fe} values calculated for all garnet point analyses in sample V25 garnets 1, 3 & 5. Rim - blue, Core - pink.

	V25 Garnet 4					
Point	**1**	**2**	**3**	**4**	**5**	**6**
SiO_2	38.55	38.41	38.42	38.11	38.5	38.64
TiO_2	0.06	0.1	0.21	0.07	0.22	0.04
Al_2O_3	21.5	21.76	21.5	21.24	21.49	21.64
FeO	35.02	34.26	32.93	32.32	33.84	34.5
MnO	0.91	1.75	2.82	4.18	0.65	0.21
MgO	2.86	2.93	2.16	1.61	3.47	3.81
CaO	3.45	3.52	4.45	4.52	3.61	3
Cr_2O_3	0.02	-	0.14	0.14	0.12	0.03
Total	102.37	102.73	102.63	102.19	101.9	101.87
Si	6.037	5.997	6.017	6.023	6.025	6.039
Al^{2+}	- } 6.04	0.003 } 6.00	- } 6.02	- } 6.02	- } 6.03	- } 6.04
Al^{3+}	3.969	4.002	3.969	3.957	3.965	3.987
Cr	0.002	-	0.017	0.017	0.015	0.004
Fe^{3+}	0.022 } 4.00	- } 4.01	- } 4.01	0.018 } 4.00	- } 4.01	0.004 } 4.00
Ti	0.007	0.012	0.025	0.008	0.026	0.005
Mg	0.668	0.682	0.504	0.379	0.809	0.887
Fe^{2+}	4.565	4.473	4.313	4.256	4.429	4.505
Mn	0.121 } 5.93	0.231 } 5.98	0.374 } 5.94	0.560 } 5.96	0.086 } 5.93	0.028 } 5.92
Ca	0.579	0.589	0.747	0.765	0.605	0.502
X_{Fe}	0.872	0.868	0.895	0.918	0.846	0.835

	V35 Gnt 1	V35 Garnet 2		
Point	**1**	**1**	**2**	**3**
SiO_2	37.52	37.52	37.46	37.7
TiO_2	0.04	0.06	0.07	-
Al_2O_3	21.42	21.57	21.3	21.13
FeO	31.64	29.22	28.62	28.26
MnO	6.08	7.57	8.17	8.04
MgO	0.56	0.79	0.59	0.67
CaO	5.37	5.85	5.74	5.79
Cr_2O_3	-	-	-	0.1
Total	102.63	102.58	101.95	101.69
Si	5.956	5.941	5.971	6.011
Al^{2+}	0.044 } 6.00	0.059 } 6.00	0.029 } 6.00	- } 6.01
Al^{3+}	3.965	3.968	3.973	3.972
Cr	-	-	-	0.013
Fe^{3+}	0.030 } 4.00	0.025 } 4.00	0.019 } 4.00	0.015 } 4.00
Ti	0.005	0.007	0.008	-
Mg	0.132	0.186	0.140	0.159
Fe^{2+}	4.171	3.844	3.796	3.753
Mn	0.818 } 6.03	1.015 } 6.04	1.103 } 6.02	1.086 } 5.99
Ca	0.913	0.993	0.980	0.989
X_{Fe}	0.969	0.954	0.964	0.959

Table 4.1.1.5: Mineral composition data, number of ions on the basis of 24O and X_{Fe} values calculated for all garnet point analyses in sample V25 garnet 4 and V35 garnets 1 & 2. Rim - blue, Core - pink.

	VH40 Garnet 4									
Point	**1**		**2**		**3**		**4**		**5**	
SiO_2	37.91		37.92		37.73		37.87		37.48	
TiO_2	-		0.2		0.21		0.21		-	
Al_2O_3	21.43		21.42		21.24		21.31		21.28	
FeO	33.12		33.22		33.35		33.59		32.96	
MnO	6.21		6.13		5.92		6.09		4.84	
MgO	1.65		1.66		1.7		1.45		1.4	
CaO	1.69		1.9		1.67		1.83		2.78	
Cr_2O_3	0.05		0.08		0.18		0.07		0.11	
Total	102.06		102.53		102		102.42		100.85	
Si	6.025	6.03	6.003	6.00	6.006	6.01	6.011	6.01	6.019	6.02
Al^{2+}	-		-		-		-		-	
Al^{3+}	4.015	4.02	3.998	4.03	3.986	4.03	3.988	4.02	4.029	4.04
Cr	0.006		0.010		0.023		0.009		0.014	
Fe^{3+}	-		-		-		-		-	
Ti	-		0.024		0.025		0.025		-	
Mg	0.391	5.92	0.392	5.93	0.403	5.93	0.343	5.93	0.335	5.90
Fe^{2+}	4.402		4.398		4.440		4.459		4.427	
Mn	0.836		0.822		0.798		0.819		0.658	
Ca	0.288		0.322		0.285		0.311		0.478	
X_{Fe}	0.918		0.918		0.917		0.929		0.930	

	VH40 Gnt 1		VH40 Garnet 5					
Point	**1**		**1**		**2**		**3**		**4**	
SiO_2	37.24		36.99		37.8		37.78		37.73	
TiO_2	-		-		-		0.01		-	
Al_2O_3	20.99		20.68		21.36		21.59		21.39	
FeO	32.51		32.43		32.55		33.09		34.39	
MnO	6.87		6.86		6.87		6.83		4.27	
MgO	1.48		1.44		1.57		1.61		1.36	
CaO	1.54		1.61		1.48		1.4		2.54	
Cr_2O_3	0.14		0.11		-		0.08		0.13	
Total	100.77		100.12		101.63		102.39		101.81	
Si	6.013	6.01	6.019	6.02	6.010	6.01	6.034	6.03	6.014	6.01
Al^{2+}	-		-		-		-		-	
Al^{3+}	3.996	4.01	3.967	4.00	3.979	4.01	4.020	4.02	4.020	4.04
Cr	0.018		0.014		0.019		-		0.016	
Fe^{3+}	-		0.019		-		-		-	
Ti	-		-		0.016		-		-	
Mg	0.356	5.95	0.349	5.97	0.372	5.95	0.374	5.90	0.323	5.92
Fe^{2+}	4.390		4.395		4.412		4.346		4.584	
Mn	0.940		0.946		0.886		0.929		0.577	
Ca	0.266		0.281		0.281		0.253		0.434	
X_{Fe}	0.925		0.926		0.922		0.921		0.934	

Table 4.1.1.6: Mineral composition data, number of ions on the basis of 24O and X_{Fe} values calculated for all garnet point analyses in sample VH40 garnets 1, 4 & 5. Rim - blue, Core - pink.

	W5 Garnet 1a							W5 Garnet 1b							W5 Garnet 2a						
Point	**1**		**2**		**3**			**1**		**2**					**1**		**2**				
SiO_2	37.43		37.57		37.54			37.41		37.58					37.85		37.42				
TiO_2	-		0.1		0.11			-		0.17					0.13		-				
Al_2O_3	21.5		21.17		20.99			21.32		21.41					21.33		21.56				
FeO	35		32.71		33.01			34.57		34.41					34.82		34.83				
MnO	4.5		4.71		4.67			4.23		4.14					4.04		4.14				
MgO	1.65		1.39		1.54			1.65		1.64					1.7		1.47				
CaO	1.67		4.1		3.21			1.94		2.61					2.25		2.9				
Cr_2O_3	0.09		0.12		0.22			0.22		0.14					0.1		0.12				
Total	101.84		101.87		101.29			101.34		102.1					102.22		102.44				
Si	5.976	6.00	5.984	6.00	6.010	6.01		5.993	6.00	5.974	6.00				6.007	6.01	5.946	6.00			
Al^{2+}	0.024		0.016		-			0.007		0.026					-		0.054				
Al^{3+}	4.023	4.03	3.959	4.00	3.961	4.00		4.020	4.05	3.987	4.03				3.991	4.02	3.985	4.00			
Cr	0.011		0.015		0.028			0.028		0.018					0.013		0.015				
Fe^{3+}	-		0.014		-			-		-					-		-				
Ti	-		0.012		0.013			-		0.020					0.016		-				
Mg	0.393	5.96	0.330	6.01	0.367	5.97		0.394	5.93	0.389	5.97				0.402	5.95	0.348	6.03			
Fe^{2+}	4.673		4.343		4.419			4.632		4.575					4.622		4.628				
Mn	0.609		0.635		0.633			0.574		0.557					0.543		0.557				
Ca	0.286		0.700		0.551			0.333		0.445					0.383		0.494				
X_{Fe}	0.923		0.929		0.923			0.922		0.922					0.920		0.930				

	W5 Garnet 3a				W5 Gnt 3b			W10b Garnet 2b							W10b Garnet 3						
Point	**1**		**2**		**1**			**2**		**3**					**1**		**2**				
SiO_2	37.24		37.8		37.61			37.13		37.11					37.57		37.7				
TiO_2	0.11		0.29		-			0.19		0.05					0.28		0.13				
Al_2O_3	21.31		20.62		21.62			21.12		21.21					21.3		21.59				
FeO	35.65		31.98		35.61			34.56		34.51					33.24		35.05				
MnO	3.93		5.35		4.2			5.47		5.65					6.59		3.07				
MgO	1.73		1.51		1.59			1.18		1.37					1.36		1.35				
CaO	1.87		5.01		1.66			1.84		1.91					2.34		3.51				
Cr_2O_3	-		0.14		-			0.03		0.21					0.06		0.13				
Total	101.84		102.7		102.29			101.52		102.02					102.74		102.53				
Si	5.956	6.00	5.986	6.00	5.980	6.00		5.973	6.00	5.946	6.00				5.963	6.00	5.968	6.00			
Al^{2+}	0.044		0.014		0.020			0.027		0.054					0.037		0.032				
Al^{3+}	3.974	4.00	3.835	4.00	4.033	4.03		3.978	4.01	3.952	4.00				3.949	4.00	3.997	4.03			
Cr	-		0.018		-			0.004		0.027					0.008		0.016				
Fe^{3+}	0.013		0.112		-			-		0.015					0.010		-				
Ti	0.013		0.035		-			0.023		0.006					0.033		0.015				
Mg	0.412	6.02	0.356	6.05	0.377	5.96		0.283	5.99	0.327	6.03				0.322	6.01	0.318	5.97			
Fe^{2+}	4.756		4.123		4.735			4.649		4.609					4.402		4.640				
Mn	0.532		0.718		0.566			0.745		0.767					0.886		0.412				
Ca	0.320		0.850		0.283			0.317		0.328					0.398		0.595				
X_{Fe}	0.920		0.920		0.926			0.943		0.934					0.932		0.936				

Table 4.1.1.7: Mineral composition data, number of ions on the basis of 24O and X_{Fe} values calculated for all garnet point analyses in sample W5 and W10b garnets . Rim - blue, Core - pink.

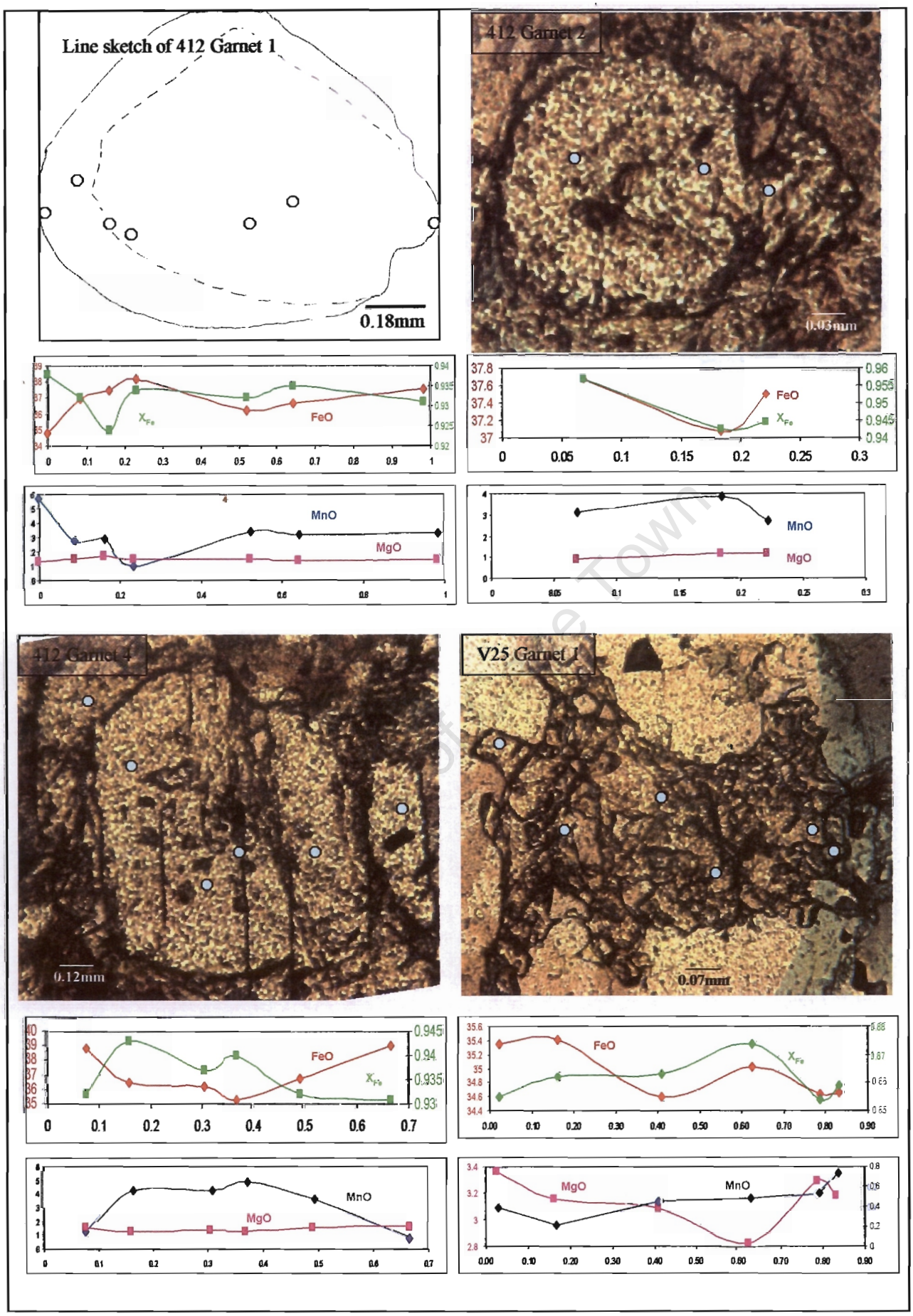

Figure 4.1.1.1: X_{Fe}, FeO, MgO and MnO profiles obtained by point analyses across garnets from samples 412 and V25. All X-axes in mm, Y-axes for FeO, MgO and MnO in wt %.

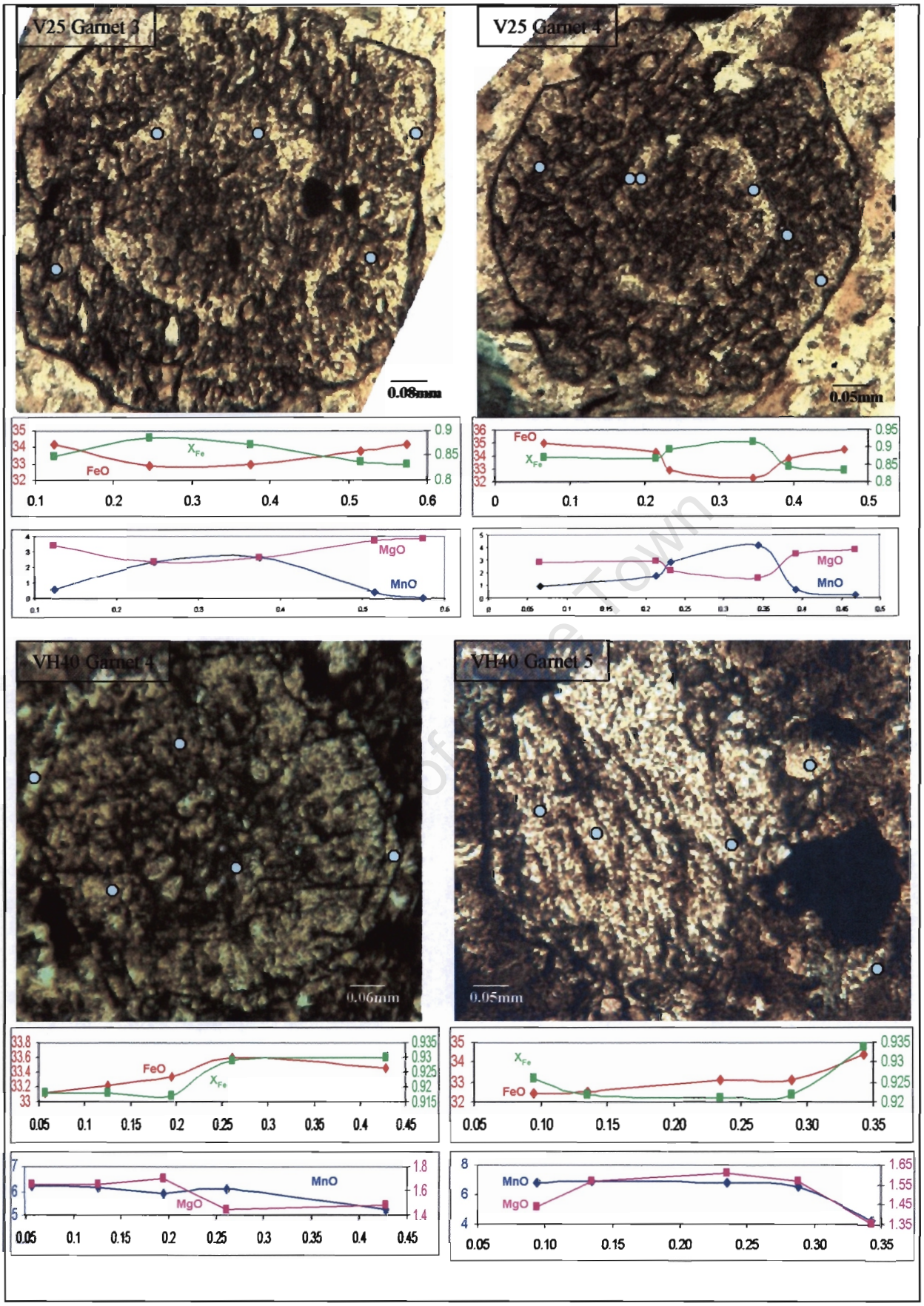

Figure 4.1.1.2: X_{Fe}, FeO, MgO and MnO profiles obtained by point analyses across garnets from samples V25 and VH40. All X-axes in mm, Y-axes for FeO, MgO and MnO in wt %.

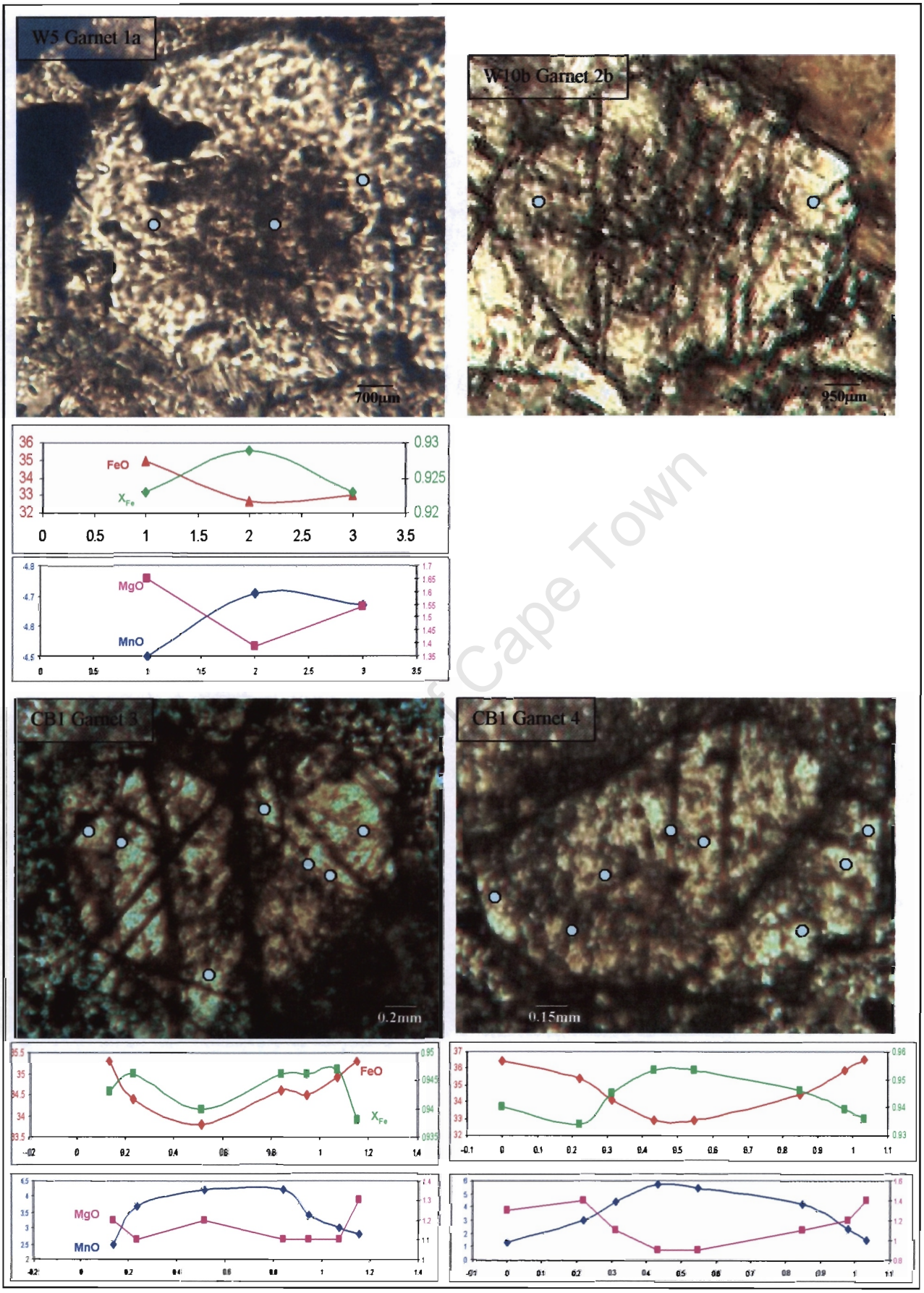

Figure 4.1.1.3: X_{Fe}, FeO, MgO and MnO profiles obtained by point analyses across garnets from samples W5, W10b and CB1. W5 and W10b X-axes in microns, CB1 X-axes in mm, Y-axes for FeO, MgO and MnO in wt %.

W5, W10b, CB1 and V35 (Tables 4.1.1.1-7). Point analyses were performed on each of the garnets analysed in order to identify compositional zoning, of which a small degree is observed in numerous of the grains analysed (Figs. 4.1.1.1-3). Values presented for core and rim compositions as highlighted in pink and blue, respectively, in Tables 4.1.1.1-7 are the data points most representative of the respective compositions across each grain which will be used for thermometry calculations.

All garnets analysed are almandiferous in composition and exhibit X_{Fe} values in the range 0.831-0.969 (Table 4.1.1.9).

Sample	Average X_{Fe}	
	Rim	Core
CB1	0.937	0.941
412	0.935	0.942
412 Grt 1	0.933	
V25	0.845	0.887
V25 Grt 1	0.861	
VH40	0.926	0.920
V35	0.962	
W5	0.923	0.926
W10	0.937	0.935

Table 4.1.1.8: Average X_{Fe} values for all garnets analysed in each of the collar samples.

The ferruginous meta-shale V25 contains garnets which have distinctly different compositions to garnets found in the metapelites. They exhibit the lowest X_{Fe} values, ranging from 0.831-0.918, are the most magnesian of all the garnets analysed and contain the least FeO and MnO compared to the garnets in the metapelites. Garnets found within sample V35 exhibit the highest X_{Fe} values but contain the lowest amounts of Mg and Fe relative to all garnets analysed (Fig. 4.1.1.4). Manganese content displays the opposite trend to iron content (relative to Mg) in the samples analysed (Fig. 4.1.1.5), with garnet in sample V35 containing the most Mn and those in sample V25 having the lowest Mn content. The rest of the samples garnets show a spread in Mn content, with sample VH40 garnet being slightly more enriched in Mn than garnet in samples W5 and W10, which themselves are slightly more enriched in Mn compared to the garnets from samples CB1 and 412.

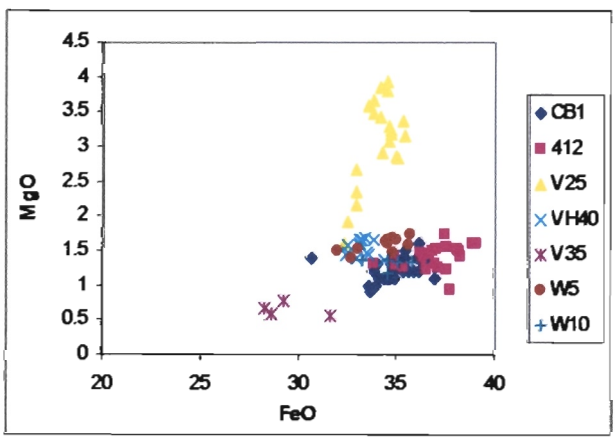

Figure 4.1.1.4: Plot of FeO vs. MgO (wt. %) for all garnets analysed in the sample set.

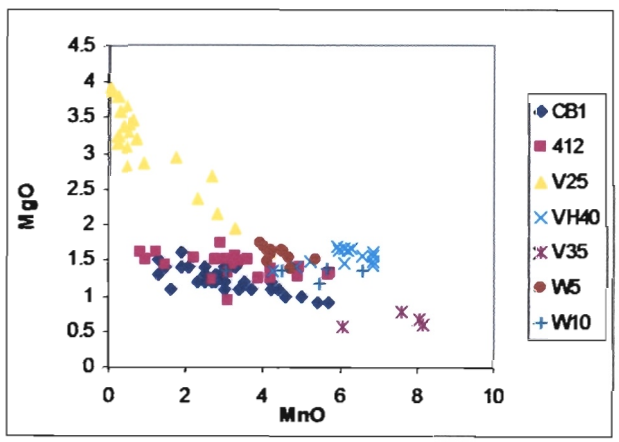

Figure 4.1.1.5: Plot of MnO vs. MgO (wt. %) for all garnets analysed in the sample set.

For garnets which exhibit compositional zoning, the majority display increasing Fe and Mg, and decreasing Mn and X_{Fe} from core to rim (Figs. 4.1.1.1-3), which is consistent with the findings of Gibson and Wallmach (1995). However, in sample VH40 Mg content remains relatively constant across the grains analysed (Fig. 4.1.1.3) and in sample 412 Garnet 1 displays a rather erratic change in composition across the grain but tending towards the opposite trend with Fe and Mg decreasing and Mn and X_{Fe} increasing from core to rim (Fig. 4.1.1.2).

Calcium content is relatively constant within garnets from each sample (Fig. 4.1.1.6) (approximately 2 wt % variation), other than for sample W5 which shows a wider spread. Garnets with the lowest Ca content are found in sample 412 and the highest in sample V35.

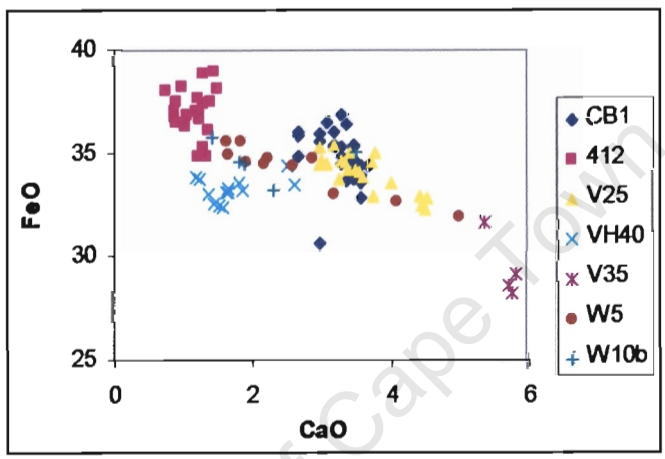

Figure 4.1.1.6: Plot of CaO vs. FeO (wt. %) for all garnets analysed in the sample set.

Compositional variation is also observed between garnets from the same sample. In Sample 412, garnet found as an inclusion within a cordierite poikiloblast (Grt 2) exhibits a more homogenous composition across the grain compared to other grains analysed from within the matrix which exhibit zonation. The garnet found within cordierite displays a slightly lower Mg content and X_{Fe} compared to other garnets (Figs. 4.1.1.7 & 4.1.1.8). This may be the result of garnet having been consumed in the production of cordierite, leaving behind the core of the reactant garnet, depleted in Mg due to cordierite's greater affinity for Mg, or due to cordierite isolating garnet from the matrix as they grew simultaneously. Neither of these minerals have been identified as retrograde, therefore, it is unlikely to be the result of retrograde FeMg exchange between cordierite garnet.

In sample V25, garnet found within a quartz vein (Grt 1) is skeletal and displays a homogenous composition similar to that of the rims observed in garnets found within the bulk rock, only slightly more Fe-rich. This suggests that garnet found within the vein was originally from the bulk rock and became engulfed by a late-stage fluid which passed through the rock, resulting in the formation of the vein and increasing the overall Fe-content within such garnets, assuming they had a higher affinity for Fe than the fluid passing through (Figs. 4.1.1.9 & 4.1.1.10).

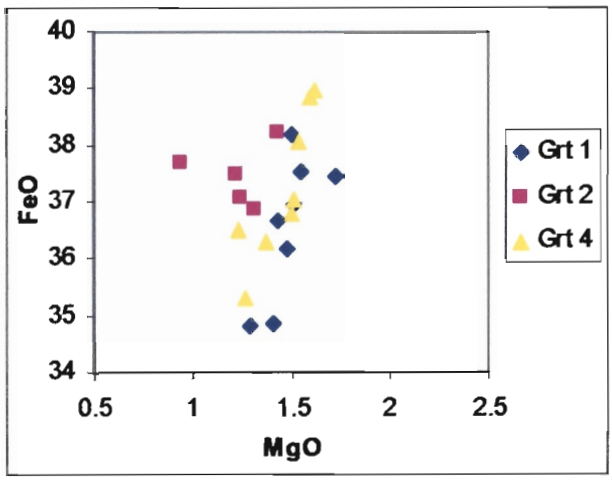

Figure 4.1.1.7: Binary plot of MgO vs. FeO by wt. % for sample 412, illustrating the slightly depleted Mg content for Grt 2 found within cordierite compared to Grt 1 and 4 from the host rock. Also note the smaller variance in both FeO and MnO for Grt 2 compared to Grt 1 and 4 which exhibit compositional zoning.

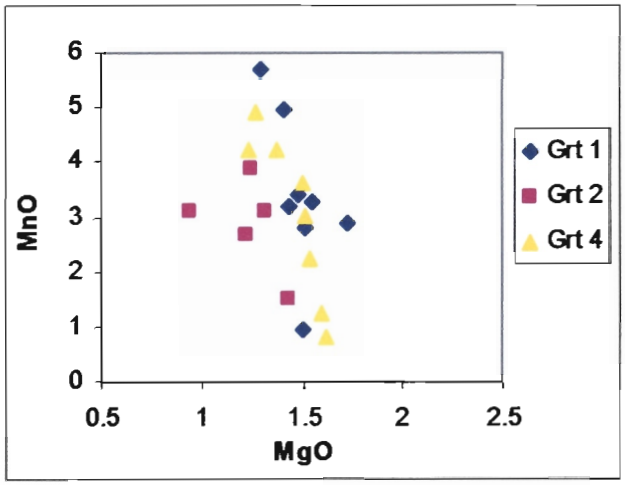

Figure 4.1.1.8: Binary plot of MgO vs. MnO by wt. % for sample 412, illustrating the slightly depleted Mg content for Grt 2 found within cordierite compared to Grt 1 and 4 from the host rock.

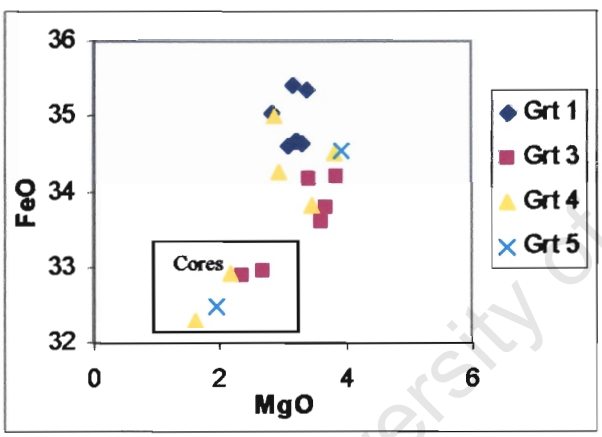

Figure 4.1.1.9: MgO vs. FeO (wt. %) for sample V25 illustrating the similar composition of garnet caught up in a quartz vein (Grt 1) to rim compositions of garnets found in the host rock (Grt 3, 4 and 5).

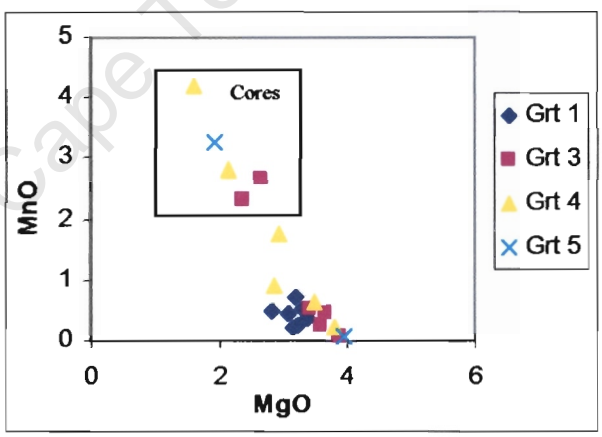

Figure 4.1.1.10: MgO vs. MnO (wt. %) for sample V25 illustrating the similar composition of garnet caught up in a quartz vein (Grt 1) to rim compositions of garnets found in the host rock (Grt 3, 4 and 5).

4.1.2 Biotite

Biotite was analysed in Samples 412, VH40, W5, W10 and W19 (Tables 4.1.2.1-3). X_{Fe} values calculated range from 0.490 – 0.706, with biotites from sample 412 being most Fe-rich and the biotites of Sample W19 the least Fe-rich (Table 4.1.2.4). Mg content follows an opposite trend to Fe content across the sample set, with the lowest Mg content seen in sample 412 biotites and increasing through biotite from samples W10b to W5 to VH40 to W19, which exhibit the highest Mg content (Fig 4.1.2.1). Potassium content is consistent throughout all biotites analysed, whilst Sodium content shows a slight spread across the sample set, ranging between 0 and 0.46 weight percentage Na_2O (Fig 4.1.2.2). Alumina content ranges from 19.2 to 20.8 weight percentage Al_2O_3 and Titanium content ranges from 1.4 – 2.2 weight percentage TiO_2, with biotite in sample W10 containing the most Ti and those in sample VH40 containing the least (Fig. 4.1.2.3).

	412											
	2.1		2.2		2.3		3.1		3.3		4.1	
SiO_2	35.13		35.48		34.73		34.86		35.05		34.55	
TiO_2	1.75		2.08		1.92		1.68		1.66		1.86	
Al_2O_3	20.46		20.47		19.86		20.03		20.39		19.21	
FeO	23.86		24.26		25.41		23.78		24.58		24.20	
MnO	0.13		0.00		0.04		0.01		0.04		0.00	
MgO	6.31		5.90		5.93		6.36		6.14		7.11	
CaO	0.00		0.00		0.00		0.00		0.00		0.00	
Na_2O	0.11		0.06		0.13		0.20		0.28		0.24	
K_2O	8.41		7.97		8.54		7.90		8.11		8.17	
Cr_2O_3	0.10		0.13		0.09		0.49		0.18		0.11	
Total	96.26		96.35		96.65		95.36		96.43		95.45	
Si	5.362	8.00	5.396	8.00	5.333	8.00	5.368	8.00	5.353	8.00	5.342	8.00
Al^{2+}	2.638		2.604		2.667		2.632		2.647		2.658	
Al^{3+}	1.044	5.74	1.066	5.73	0.928	5.78	1.005	5.72	1.024	5.76	0.844	5.83
Ti	0.201		0.238		0.222		0.195		0.191		0.216	
Fe	3.046		3.085		3.263		3.063		3.139		3.129	
Mn	0.017		0.000		0.005		0.001		0.005		0.000	
Mg	1.435		1.337		1.357		1.460		1.397		1.638	
Ca	0.000	1.67	0.000	1.56	0.000	1.71	0.000	1.61	0.000	1.66	0.000	1.68
Na	0.033		0.018		0.039		0.060		0.083		0.072	
K	1.638		1.546		1.673		1.552		1.580		1.612	
Cr	0.012		0.016		0.011		0.060		0.022		0.013	
X_{Fe}	0.680		0.698		0.706		0.677		0.692		0.656	

	412		VH40			W5				
	4.2		1.1		4.2	1.2		1.4		1.6	
SiO_2	34.93		35.50		34.93	34.34		35.27		34.91	
TiO_2	1.60		1.42		1.55	1.81		1.89		1.95	
Al_2O_3	19.56		19.75		20.08	19.48		19.72		20.22	
FeO	24.03		20.76		20.62	22.56		22.58		22.76	
MnO	0.04		0.16		0.00	0.04		0.13		0.24	
MgO	7.28		8.55		8.58	6.84		7.34		7.17	
CaO	0.00		0.00		0.00	0.00		0.00		0.00	
Na_2O	0.24		0.13		0.35	0.26		0.33		0.29	
K_2O	8.34		8.42		8.21	8.44		8.65		8.77	
Cr_2O_3	0.18		0.06		0.17	0.42		0.04		0.23	
Total	96.19		94.76		94.49	94.19		95.95		96.54	
Si	5.351	8.00	5.429	8.00	5.355	5.355	8.00	5.386	8.00	5.312	8.00
Al^{2+}	2.649		2.571		3.629	2.645		2.614		2.688	
Al^{3+}	0.884	5.81	0.989	5.78	-	0.936	5.69	0.936	5.72	0.939	5.72
Ti	0.184		0.163		0.179	0.212		0.217		0.223	
Fe	3.079		2.655		2.644	2.942		2.884		2.896	
Mn	0.005		0.021		0.000	0.005		0.017		0.031	
Mg	1.662		1.949		1.960	1.590		1.670		1.626	
Ca	0.000	1.70	0.000	1.68	0.000	0.000	1.76	0.000	1.78	0.000	1.79
Na	0.071		0.039		0.104	0.079		0.098		0.086	
K	1.630		1.643		1.606	1.679		1.685		1.703	
Cr	0.022		0.007		0.021	0.052		0.005		0.028	
X_{Fe}	0.649		0.577		0.574	0.649		0.633		0.640	

Table 4.1.2.1: Mineral composition data as wt. % oxide, number of ions on the basis of 22O and X_{Fe} values calculated for biotite grains analysed from samples 412, VH40 and W5.

	W5											
	2.1		**2.2**		**2.3**		**3.1**		**3.2**		**3.4**	
SiO_2	34.87		34.47		34.42		34.86		35.15		34.99	
TiO_2	1.69		1.73		2.02		1.85		1.73		1.89	
Al_2O_3	19.83		20.01		19.32		20.19		19.61		19.48	
FeO	22.71		21.87		22.92		22.68		22.85		22.42	
MnO	0.02		0.00		0.07		0.14		0.10		0.16	
MgO	7.38		7.49		6.99		7.57		7.31		7.23	
CaO	0.00		0.00		0.00		0.00		0.00		0.00	
Na_2O	0.33		0.40		0.31		0.31		0.32		0.45	
K_2O	8.61		8.43		8.56		8.86		8.80		8.92	
Cr_2O_3	0.41		0.34		0.14		0.27		0.22		0.17	
Total	95.86		94.73		94.75		96.73		96.08		95.70	
Si	5.340	8.00	5.320	8.00	5.347	8.00	5.295	8.00	5.376	8.00	5.373	8.00
Al^{2+}	2.660		2.680		2.653		2.705		2.624		2.627	
Al^{3+}	0.920		0.961		0.885		0.91		0.912		0.9	
Ti	0.195		0.201		0.236		0.211		0.199		0.218	
Fe	2.909	5.71	2.823	5.71	2.978	5.73	2.881	5.73	2.923	5.71	2.879	5.67
Mn	0.003		0.000		0.009		0.018		0.013		0.021	
Mg	1.684		1.723		1.618		1.714		1.666		1.655	
Ca	0.000		0.000		0.000		0.000		0.000		0.000	
Na	0.098	1.78	0.120	1.78	0.093	1.79	0.091	1.81	0.095	1.81	0.134	1.88
K	1.682		1.660		1.697		1.717		1.717		1.748	
Cr	0.050		0.041		0.017		0.032		0.027		0.021	
X_{Fe}	0.633		0.621		0.648		0.627		0.637		0.635	

	W10b											
	1.1		**1.2**		**2.2**		**2.4**		**3.1**		**3.2**	
SiO_2	35.03		34.82		34.69		34.35		34.98		34.96	
TiO_2	2.01		1.94		2.01		2.21		2.09		2.16	
Al_2O_3	20.75		20.46		20.19		19.87		19.94		20.35	
FeO	22.71		23.26		22.62		22.34		22.94		22.71	
MnO	0.00		0.18		0.04		0.00		0.04		0.00	
MgO	6.65		6.75		6.66		6.71		6.68		6.73	
CaO	0.00		0.00		0.00		0.00		0.00		0.00	
Na_2O	0.30		0.19		0.23		0.28		0.22		0.27	
K_2O	8.68		8.78		8.44		8.77		8.90		8.81	
Cr_2O_3	0.27		0.34		0.24		0.27		0.23		0.35	
Total	96.40		96.71		95.14		94.79		96.02		96.34	
Si	5.321	8.00	5.298	8.00	5.342	8.00	5.321	8.00	5.355	8.00	5.324	8.00
Al^{2+}	2.679		2.702		2.658		2.679		2.645		2.676	
Al^{3+}	1.037		0.968		1.007		0.949		0.954		0.977	
Ti	0.230		0.222		0.233		0.257		0.241		0.247	
Fe	2.885	5.66	2.960	5.70	2.913	5.69	2.894	5.65	2.937	5.66	2.892	5.64
Mn	0.000		0.023		0.005		0.000		0.005		0.000	
Mg	1.505		1.531		1.528		1.549		1.524		1.527	
Ca	0.000		0.000		0.000		0.000		0.000		0.000	
Na	0.088	1.77	0.056	1.76	0.069	1.73	0.084	1.82	0.065	1.80	0.080	1.79
K	1.682		1.704		1.658		1.733		1.738		1.712	
Cr	0.032		0.041		0.029		0.033		0.028		0.042	
X_{Fe}	0.657		0.659		0.656		0.651		0.658		0.654	

Table 4.1.2.2: Mineral composition data as wt. % oxide, number of ions on the basis of 22O and X_{Fe} values calculated for biotite grains analysed from samples W5 and W10.

	W19			
	1.1	2.1	2.2	3.1
SiO_2	37.34	36.33	36.26	35.97
TiO_2	1.61	1.87	1.93	1.87
Al_2O_3	21.28	19.64	20.06	19.54
FeO	17.49	18.36	18.65	18.16
MnO	0.00	0.00	0.00	0.18
MgO	10.21	10.27	10.38	10.07
CaO	0.00	0.00	0.00	0.00
Na_2O	0.11	0.00	0.16	0.00
K_2O	8.37	8.07	8.28	8.70
Cr_2O_3	0.22	0.41	0.50	0.30
Total	96.63	94.93	96.22	94.79
Si	5.466	5.456	5.390	5.437
Al^{2+}	2.534 (8.00)	2.544 (8.00)	2.610 (8.00)	2.563 (8.00)
Al^{3+}	1.139	0.933	0.906	0.919
Ti	0.177	0.211	0.216	0.213
Fe	2.141 (5.69)	2.306 (5.75)	2.319 (5.74)	2.295 (5.72)
Mn	0.000	0.000	0.000	0.023
Mg	2.228	2.298	2.300	2.268
Ca	0.000	0.000	0.000	0.000
Na	0.031 (1.59)	0.000 (1.55)	0.046 (1.62)	0.000 (1.68)
K	1.563	1.546	1.570	1.678
Cr	0.025	0.049	0.059	0.036
X_{Fe}	0.490	0.501	0.502	0.503

Table 4.1.2.3: Mineral composition data as wt. % oxide, number of ions on the basis of 22O and X_{Fe} values calculated for biotite grains analysed from sample W19.

In sample 412 two compositional types of biotite occur, with biotites from the matrix being less aluminous and more magnesian than the biotite inclusions within cordierite poikiloblasts (Fig. 4.1.2.4). This may be a consequence of biotite, similar to garnet, being consumed in the production of cordierite which has a higher affinity for Mg than Fe, or being isolated from the matrix by cordierite growing simultaneously to it. However, the higher Alumina content of the biotite found within cordierite porphyroblasts suggests that it is in fact retrograde biotite. For each of the other samples, the biotite porphyroblasts analysed are compositionally homogenous.

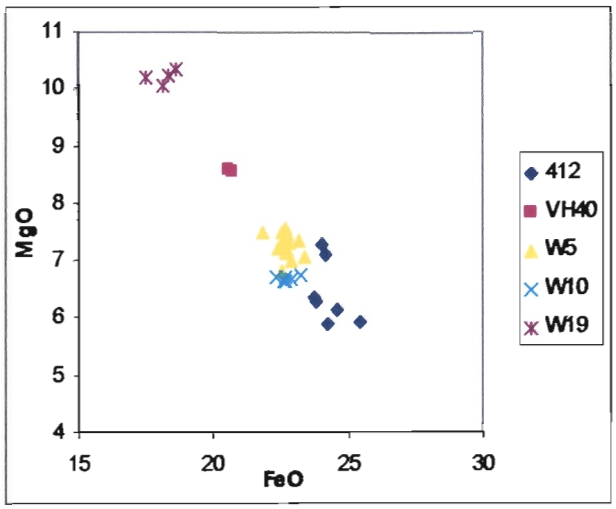

Figure 4.1.2.1: FeO vs. MgO by wt. % for all biotites analysed, illustrating opposite trends in Fe and Mg content across the sample set.

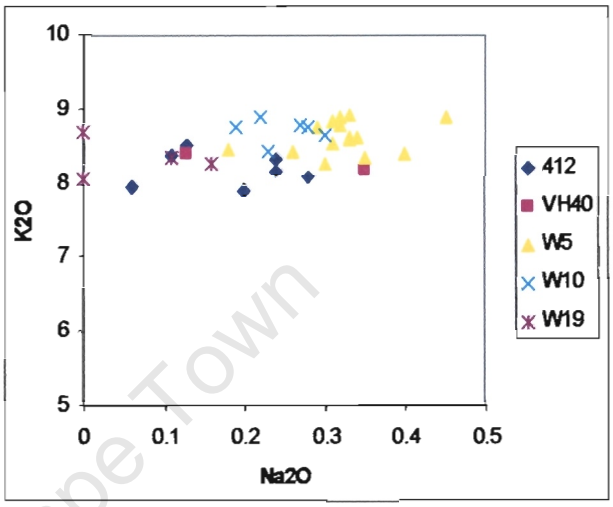

Figure 4.1.2.2: Na_2O vs. K_2O (wt. %) for all biotites analysed, illustrating the consistent K-content t and a slight spread in Na content throughout the sample set.

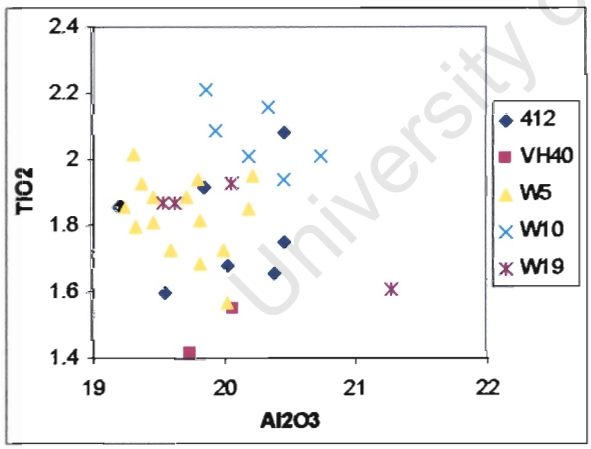

Figure 4.1.2.3: Al_2O_3 vs. TiO2 (wt. %) binary diagram for all biotites analysed.

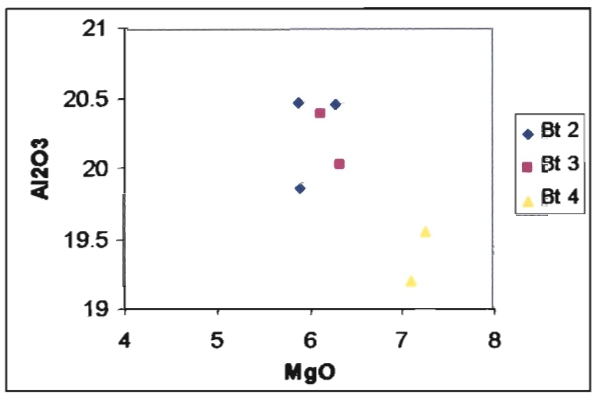

Figure 4.1.2.4: MgO vs. Al_2O_3 (wt. %) binary diagram demonstrating the difference in Al and Mg content in Bt found within Crd (Bt 2&3) compared to Bt found in the matrix (Bt 4) of sample 412.

Sample	X_{Fe}
412	0.679
VH40	0.576
W5	0.636
W10	0.656
W19	0.499

Table 4.1.2.4: Average X_{Fe} values calculated for all biotites analysed.

4.1.3 Retrograde Chlorite

Chlorite appears in many of the rocks of the Vredefort collar and is often intricately associated with biotite, garnet and/or amphibole phases. In the meta-basite sample 411 and meta-shale sample V25 chlorite is compositionally distinct to chlorite analysed in the metapelitic samples 412, VH40, W5 and W10. Chlorite analysed from samples 411 and V25 are more Mg-rich and plot towards the clinochlore end-member of the series, whilst the rest are of the medium magnesian variety typical of pelites, but plot slightly nearer to the chamosite end-member of the series (Fig. 4.1.3.1) X_{Fe} values decrease from 0.662-0.246 in the order 412>W10>W5>VH40>V25>411 (Tables 4.1.3.1-3) and all chlorites analysed have low Mn content.

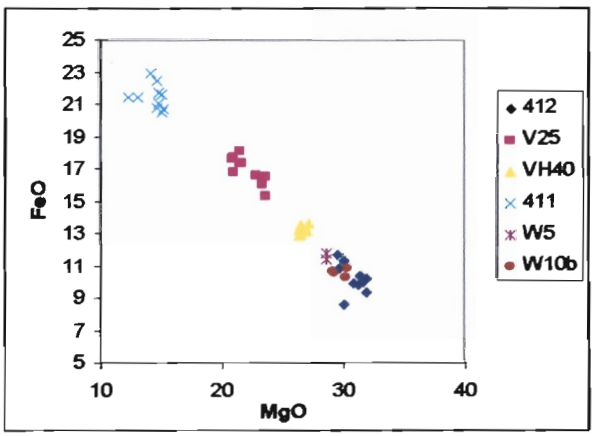

Figure 4.1.3.1: Graph illustrating variation in Fe and Mg content across chlorites of the sample set.

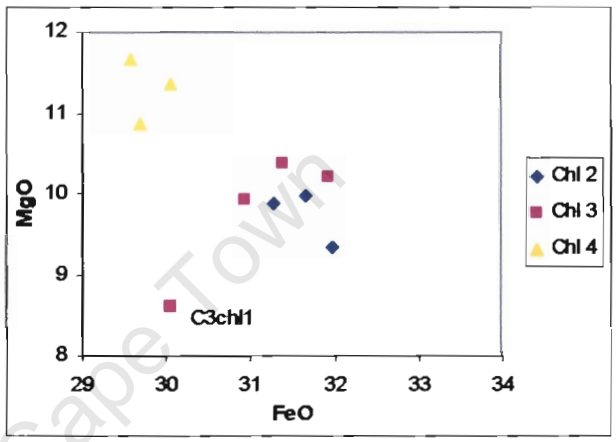

Figure 4.1.3.2: FeO vs. MgO (wt. %) binary diagram of chlorites in sample 412. Chl found as inclusions within Crd (2 & 3) are relatively depleted in MgO and enriched in FeO compared to Chl within the host rock.

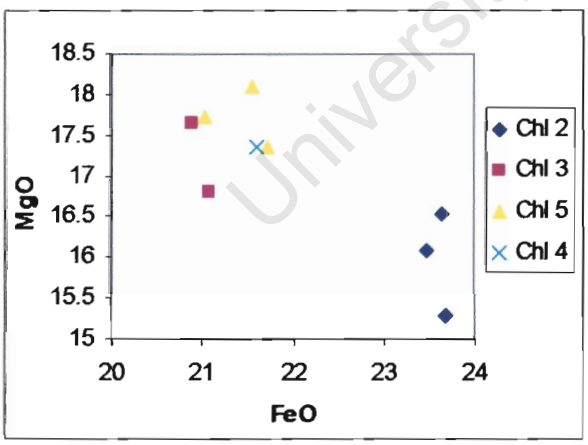

Figure 4.1.3.3: Binary diagram illustrating the difference in MgO and FeO content between chlorite found as an inclusion in cordierite (Chl 2) and chlorite observed in the matrix (Chl 3, 4, 5) of sample V25.

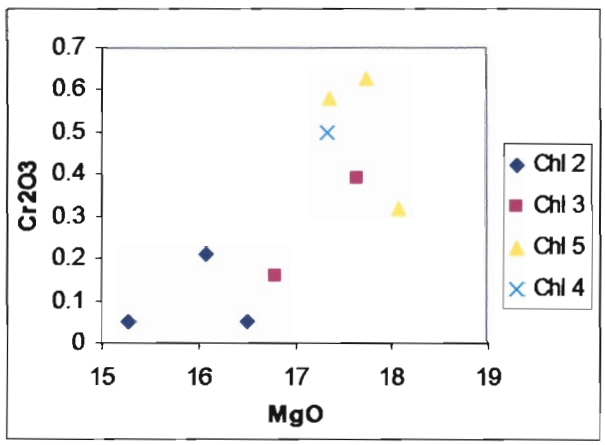

Figure 4.1.3.4: Binary diagram illustrating the difference in MgO and Cr_2O_3 content between chlorite found as an inclusion in cordierite (Chl 2) and chlorite observed in the matrix (Chl 3, 4, 5) of sample V25.

For samples 411, VH40, W5 and W10, all chlorites analysed are relatively homogeneous in composition within each of the samples and appear to have formed as a single retrograde phase. In Sample 412, however, chlorites found in the matrix are more magnesian than chlorites located within cordierite poikiloblasts, which have a greater Fe content (Fig.

	412													
	2.1		**2.2**		**2.4**		**3**		**3.1**		**3.2**		**3.3**	
SiO_2	23.87		23.30		23.81		26.76		24.46		23.96		24.56	
TiO_2	0.20		0.18		0.00		0.74		0.13		0.20		0.22	
Al_2O_3	23.69		22.38		22.52		21.60		23.51		23.35		23.71	
Cr_2O_3	0.07		0.05		0.06		0.12		0.19		0.23		0.20	
FeO	31.68		31.98		31.29		30.07		31.39		31.94		30.94	
MnO	0.06		0.10		0.06		0.00		0.05		0.18		0.04	
MgO	9.98		9.34		9.88		8.61		10.37		10.22		9.93	
CaO	0.02		0.01		0.07		0.00		0.07		0.02		0.00	
Na_2O	0.09		0.00		0.17		0.02		0.00		0.04		0.00	
K_2O	0.00		0.02		0.04		2.21		0.04		0.06		0.00	
Total	89.65		87.38		87.90		90.14		90.21		90.21		89.60	
Si	5.081	8.00	5.126	8.00	5.179	8.00	5.660	8.00	5.159	8.00	5.083	8.00	5.197	8.00
Al^{2+}	2.919		2.874		2.821		2.340		2.841		2.917		2.803	
Al^{3+}	3.026	11.93	2.930	11.94	2.954	11.97	3.046	11.82	3.004	11.89	2.923	11.96	3.112	11.79
Ti	0.032		0.030		0.000		0.118		0.021		0.032		0.035	
Cr	0.012		0.009		0.010		0.020		0.032		0.039		0.033	
Fe	5.640		5.884		5.692		5.319		5.537		5.667		5.475	
Mn	0.011		0.019		0.011		0.000		0.009		0.032		0.007	
Mg	3.166		3.062		3.203		2.714		3.259		3.231		3.131	
Ca	0.005		0.002		0.016		0.000		0.016		0.005		0.000	
Na	0.037		0.000		0.072		0.008		0.000		0.016		0.000	
K	0.000		0.006		0.011		0.596		0.011		0.016		0.000	
OH		16.07		16.06		16.03		16.18		16.11		16.04		16.21
X_{Fe}	0.640		0.658		0.640		0.662		0.629		0.637		0.636	

	412						V25							
	4.1		**4.2**		**4.3**		**1.2**		**2.1**		**2.2**		**2.3**	
SiO_2	23.90		25.73		23.64		25.67		25.17		26.49		25.39	
TiO_2	0.14		0.11		0.11		0.01		0.19		0.08		0.17	
Al_2O_3	24.13		23.74		23.34		23.82		22.44		23.20		22.69	
Cr_2O_3	0.18		0.20		0.19		0.10		0.05		0.05		0.21	
FeO	30.07		29.58		29.71		22.90		23.69		23.65		23.47	
MnO	0.02		0.00		0.18		0.00		0.07		0.10		0.18	
MgO	11.36		11.67		10.87		16.62		15.29		16.53		16.09	
CaO	0.00		0.10		0.05		0.00		0.17		0.09		0.08	
Na_2O	0.00		0.09		0.00		0.00		0.00		0.00		0.02	
K_2O	0.00		0.19		0.09		0.06		0.02		0.00		0.00	
Total	89.80		91.42		88.18		89.19		87.09		90.18		88.28	
Si	5.032	8.00	5.286	8.00	5.082	8.00	5.225	8.00	5.290	8.00	5.345	8.00	5.255	8.00
Al^{2+}	2.968		2.714		2.918		2.775		2.710		2.655		2.745	
Al^{3+}	3.021	11.94	3.036	11.85	2.997	11.94	2.941	11.91	2.850	11.90	2.863	11.88	2.792	11.94
Ti	0.022		0.017		0.018		0.002		0.030		0.012		0.026	
Cr	0.030		0.032		0.032		0.016		0.008		0.008		0.034	
Fe	5.295		5.082		5.341		3.898		4.164		3.991		4.063	
Mn	0.004		0.000		0.033		0.000		0.012		0.017		0.032	
Mg	3.564		3.573		3.482		5.042		4.789		4.970		4.963	
Ca	0.000		0.022		0.012		0.000		0.038		0.019		0.018	
Na	0.000		0.036		0.000		0.000		0.000		0.000		0.008	
K	0.000		0.050		0.025		0.016		0.005		0.000		0.000	
OH		16.06		16.15		16.06		16.09		16.10		16.12		16.06
X_{Fe}	0.598		0.587		0.605		0.436		0.465		0.445		0.450	

Table 4.1.3.1: Mineral composition data as wt. % oxide, number of ions on the basis of 28O where (OH) is given as 16 and X_{Fe} values calculated for chlorites analysed in samples 412 and V25.

	V25						VH40
	3.1	**3.2**	**4.1**	**5.1**	**5.2**	**5.3**	**2.1**
SiO_2	26.11	26.69	25.88	26.23	26.98	25.64	24.84
TiO_2	0.15	0.00	0.20	0.08	0.20	0.15	0.23
Al_2O_3	22.39	23.96	22.69	22.31	22.43	22.98	23.08
Cr_2O_3	0.39	0.16	0.50	0.58	0.32	0.63	0.00
FeO	20.91	21.08	21.61	21.73	21.57	21.05	26.54
MnO	0.03	0.17	0.09	0.00	0.00	0.00	0.15
MgO	17.65	16.80	17.35	17.36	18.09	17.74	13.60
CaO	0.10	0.36	0.15	0.19	0.11	0.07	0.00
Na_2O	0.00	0.00	0.00	0.00	0.00	0.00	0.00
K_2O	0.00	0.01	0.03	0.00	0.00	0.02	0.05
Total	87.72	89.22	88.51	88.47	89.70	88.28	88.50
Si	5.359	5.371	5.291	5.362	5.418	5.239	5.211
Al^{2+}	2.641	2.629	2.709	2.638	2.582	2.761	2.789
	8.00	8.00	8.00	8.00	8.00	8.00	8.00
Al^{3+}	2.777	3.055	2.760	2.739	2.720	2.775	2.919
Ti	0.023	0.000	0.031	0.012	0.030	0.023	0.036
Cr	0.063	0.025	0.081	0.094	0.051	0.102	0.000
Fe	3.589	3.548	3.695	3.715	3.623	3.597	4.657
Mn	0.005	0.029	0.016	0.000	0.000	0.000	0.027
Mg	5.399	5.038	5.286	5.289	5.414	5.403	4.252
Ca	0.022	0.078	0.033	0.042	0.024	0.015	0.000
Na	0.000	0.000	0.000	0.000	0.000	0.000	0.000
K	0.000	0.003	0.008	0.000	0.000	0.005	0.013
	11.88	11.78	11.91	11.89	11.86	11.92	11.90
OH	16.12	16.22	16.09	16.11	16.14	16.08	16.10
X_{Fe}	0.399	0.413	0.411	0.413	0.401	0.400	0.523

	VH40					411	
	2.2	**2.3**	**2.4**	**5.2**	**5.4**	**1.1**	**1.2**
SiO_2	24.47	24.13	24.03	24.72	24.34	29.65	29.85
TiO_2	0.17	0.00	0.09	0.09	0.04	0.00	0.17
Al_2O_3	22.74	22.66	22.78	23.35	22.60	21.46	19.93
Cr_2O_3	0.20	0.02	0.15	0.06	0.18	0.02	0.00
FeO	26.40	26.49	26.58	27.30	27.06	14.24	15.11
MnO	0.02	0.12	0.26	0.21	0.23	0.26	0.00
MgO	13.24	12.88	13.04	13.61	13.17	23.00	21.62
CaO	0.00	0.02	0.14	0.06	0.00	0.05	0.25
Na_2O	0.00	0.00	0.00	0.00	0.00	0.00	0.00
K_2O	0.11	0.11	0.04	0.01	0.02	0.00	0.00
Total	87.36	86.43	87.12	89.41	87.64	88.68	86.94
Si	5.209	5.201	5.147	5.154	5.187	5.776	5.956
Al^{2+}	2.791	2.799	2.853	2.846	2.813	2.224	2.044
	8.00	8.00	8.00	8.00	8.00	8.00	8.00
Al^{3+}	2.915	2.959	2.900	2.893	2.865	2.705	2.644
Ti	0.027	0.000	0.014	0.014	0.006	0.000	0.026
Cr	0.034	0.003	0.025	0.010	0.030	0.003	0.000
Fe	4.700	4.775	4.762	4.760	4.823	2.320	2.522
Mn	0.004	0.022	0.047	0.037	0.042	0.043	0.000
Mg	4.200	4.138	4.163	4.229	4.183	6.677	6.429
Ca	0.000	0.005	0.032	0.013	0.000	0.010	0.053
Na	0.000	0.000	0.000	0.000	0.000	0.000	0.000
K	0.030	0.030	0.011	0.003	0.005	0.000	0.000
	11.91	11.93	11.95	11.96	11.95	11.76	11.67
OH	16.09	16.07	16.05	16.04	16.05	16.24	16.33
X_{Fe}	0.528	0.536	0.534	0.530	0.536	0.258	0.282

Table 4.1.3.2: Mineral composition data as wt. % oxide, number of ions on the basis of 28O where (OH) is given as 16 and X_{Fe} values calculated for chlorites analysed in samples V25 (cont.), VH40 and 411.

	411						
	1.3	**2**	**2.1**	**2.2**	**3.1**	**3.2**	**3.3**
SiO_2	28.01	27.70	32.74	34.71	28.48	27.80	28.04
TiO_2	0.03	0.04	0.00	0.19	0.00	0.00	0.00
Al_2O_3	22.42	22.14	19.28	18.79	22.78	23.19	23.44
Cr_2O_3	0.64	0.55	1.00	0.28	0.00	0.15	0.00
FeO	14.83	14.83	13.13	12.42	14.76	15.29	15.17
MnO	0.16	0.19	0.09	0.09	0.28	0.02	0.15
MgO	21.05	21.73	21.44	21.42	22.45	20.73	20.49
CaO	0.07	0.06	0.38	0.56	0.07	0.09	0.02
Na_2O	0.00	0.00	0.00	0.00	0.00	0.00	0.00
K_2O	0.00	0.00	0.06	0.26	0.02	0.03	0.04
Total	87.22	87.23	88.12	88.71	88.84	87.30	87.34
Si	5.584	5.529	6.357	6.638	5.562	5.536	5.571
Al^{2+}	2.416 } 8.00	2.471 } 8.00	1.643 } 8.00	1.362 } 8.00	2.438 } 8.00	2.464 } 8.00	2.429 } 8.00
Al^{3+}	2.853	2.739	2.770	2.874	2.807	2.980	3.061
Ti	0.004	0.006	0.000	0.027	0.000	0.000	0.000
Cr	0.101	0.087	0.153	0.042	0.000	0.024	0.000
Fe	2.472	2.476	2.132	1.986	2.411	2.547	2.521
Mn	0.027 } 11.73	0.032 } 11.82	0.015 } 11.37	0.015 } 11.23	0.046 } 11.82	0.003 } 11.73	0.025 } 11.69
Mg	6.254	6.464	6.204	6.105	6.534	6.152	6.067
Ca	0.015	0.013	0.079	0.115	0.015	0.019	0.004
Na	0.000	0.000	0.000	0.000	0.000	0.000	0.000
K	0.000	0.000	0.015	0.063	0.005	0.008	0.010
OH	16.27	16.18	16.63	16.77	16.18	16.27	16.31
X_{Fe}	0.283	0.277	0.256	0.246	0.270	0.293	0.294

	411	W5		W10b			
	4.3	**1.1**	**1.2**	**1.1**	**1.2**	**2.1**	**2.2**
SiO_2	27.49	24.05	23.42	23.51	23.65	23.73	24.22
TiO_2	0.00	0.04	0.18	0.11	0.14	0.12	0.05
Al_2O_3	22.33	24.08	23.36	23.18	22.96	23.74	23.64
Cr_2O_3	0.38	0.22	0.31	0.27	0.24	0.34	0.26
FeO	14.78	28.67	28.63	29.34	30.26	29.25	30.37
MnO	0.25	0.19	0.12	0.21	0.10	0.19	0.20
MgO	20.81	11.82	11.39	10.59	10.33	10.68	10.88
CaO	0.10	0.03	0.09	0.02	0.05	0.06	0.03
Na_2O	0.00	0.00	0.00	0.00	0.00	0.00	0.00
K_2O	0.00	0.07	0.06	0.01	0.07	0.05	0.01
Total	86.14	89.16	87.57	87.23	87.80	88.14	89.67
Si	5.553	5.069	5.047	5.102	5.122	5.085	5.120
Al^{2+}	2.447 } 8.00	2.931 } 8.00	2.953 } 8.00	2.898 } 8.00	2.878 } 8.00	2.915 } 8.00	2.880 } 8.00
Al^{3+}	2.871	3.053	2.981	3.033	2.984	3.083	3.012
Ti	0.000	0.006	0.029	0.018	0.023	0.019	0.008
Cr	0.061	0.037	0.053	0.046	0.041	0.058	0.043
Fe	2.497	5.054	5.159	5.325	5.481	5.242	5.369
Mn	0.043 } 11.76	0.034 } 11.92	0.022 } 11.94	0.039 } 11.89	0.018 } 11.91	0.034 } 11.87	0.036 } 11.91
Mg	6.265	3.713	3.658	3.425	3.334	3.411	3.428
Ca	0.022	0.007	0.021	0.005	0.012	0.014	0.007
Na	0.000	0.000	0.000	0.000	0.000	0.000	0.000
K	0.000	0.019	0.016	0.003	0.019	0.014	0.003
OH	16.24	16.08	16.06	16.11	16.09	16.13	16.09
X_{Fe}	0.285	0.576	0.585	0.609	0.622	0.606	0.610

Table 4.1.3.3: Mineral composition data as wt. % oxide, number of ions on the basis of 28O where (OH) is given as 16 and X_{Fe} values calculated for chlorites analysed in samples 411 (cont.), W5 and W10b.

4.1.3.2). Chlorites analysed in sample V25 also exhibit two distinct compositions, with those located in the bulk rock matrix having higher Mg and Chromium (Cr) contents and lower FeO content compared to those located within the quartz vein (Fig. 4.1.3.3). This may be due to the Si-rich fluid having a higher affinity for Mg and Cr, such that garnet from the matrix which became engulfed in it exchanged Mg and Cr for Fe with it.

4.1.4 Cordierite

Cordierite was analysed in samples 412 and VH40 (Table 4.1.4), due to the small number of analyses it is difficult to make definitive statements regarding variations observed, however, it is apparent that cordierite in sample VH40 is slightly more magnesian and less ferrous than that in sample 412.

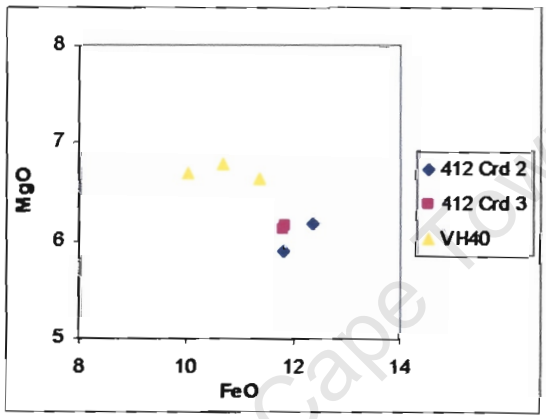

Figure 4.1.4: Diagram illustrating the difference in composition of cordierite in samples 412 & VH40.

	412								VH40			
	2		2.1		3.1		3.2		3.1		3.3	
SiO_2	47.88		47.18		48.07		47.89		48.36		48.41	
TiO_2	0.04		0.00		0.00		0.12		0.39		0.00	
Al_2O_3	33.18		33.33		32.75		33.36		33.33		33.55	
FeO	12.34		11.80		11.83		11.79		10.69		10.01	
MnO	0.22		0.33		0.08		0.15		0.25		0.43	
MgO	6.16		5.89		6.15		6.11		6.78		6.68	
CaO	0.06		0.07		0.05		0.06		0.00		0.12	
Na_2O	0.48		0.37		0.38		0.49		0.28		0.23	
K_2O	0.02		0.00		0.00		0.00		0.00		0.03	
Total	100.38		98.98		99.31		100.01		100.07		99.46	
Si	4.931	6.00	4.924	6.00	4.989	6.00	4.939	6.00	4.952	6.00	4.973	6.00
Al^{2+}	1.07		1.08		1.01		1.06		1.05		1.03	
Al^{3+}	2.960	3.00	3.025	3.03	2.996	3.00	2.995	3.00	2.976	3.01	3.036	3.04
Ti	0.003		0.000		0.000		0.009		0.030		0.000	
Fe^{3+}	0.037		0.000		0.004		0.000		0.000		0.000	
Fe^{2+}	1.026	1.99	1.030	1.98	1.023	1.98	1.017	1.97	0.916	1.97	0.860	1.92
Mn	0.019		0.029		0.007		0.013		0.022		0.037	
Mg	0.946		0.916		0.951		0.939		1.035		1.023	
Ca	0.007	0.11	0.008	0.08	0.006	0.08	0.007	0.10	0.000	0.06	0.013	0.06
Na	0.096		0.075		0.076		0.098		0.056		0.046	
K	0.003		0.000		0.000		0.000		0.000		0.004	
X_{Fe}	0.520		0.529		0.518		0.520		0.469		0.457	

Table 4.1.4: Cordierite mineral composition data, number of ions on the basis of 18O (ignoring H_2O) and X_{Fe}.

4.1.5 Amphiboles

A relatively small number of amphibole grains were analysed in samples CB1, V25, 420 and V35, for which mineral composition data are provided in Tables 4.1.5.1-3. From the binary diagrams plotting Si, Al, Fe, Mg, Ca and Na content (Figs. 4.1.5.1-3), we see that two types of amphibole predominate in the sample set, namely a magnesio-grunerite variety and a ferro-tschermakite hornblende, and that there are a few grains with intermediate compositions between these, tending towards gedrite-anthophyllite compositions. Sample CB1 contains only magnesio-grunerite, which in the vicinity of pseudotachylite appears to have been enriched in alumina and slightly depleted in silica, iron and magnesium, thus suggesting alteration towards a ferro-anthophyllite type of amphibole. The two amphiboles analysed from sample 420 have compositions intermediate between ferro-gedrite and ferro-anthophyllite, exhibiting MgO and FeO content typical for gedrite, but low Al content more typical of anthophyllite (Figs. 4.1.5.1 &2). Thus, it would seem these amphiboles have experienced significant (Mg, Fe) ⇆ Al substitutions. All of the amphiboles in both sample CB1 and 420 have very low Ca content (Fig. 4.1.5.3), which excludes the possibility that they are gedrites as initially thought upon inspection at the thin section scale. Sample V35 also comprises both magnesio-grunerite and ferro-tschermakitic hornblende as for sample CB1, but exhibit lower Mg and Fe content in relation to the amphiboles analysed in all the other samples (Fig. 4.1.5.2). The tschermakites of sample V35 also have slightly lower Al, Si and higher Na content compared to the tschermakites of sample V25. The ferruginous meta-shale, sample V25 also contains gedrite.

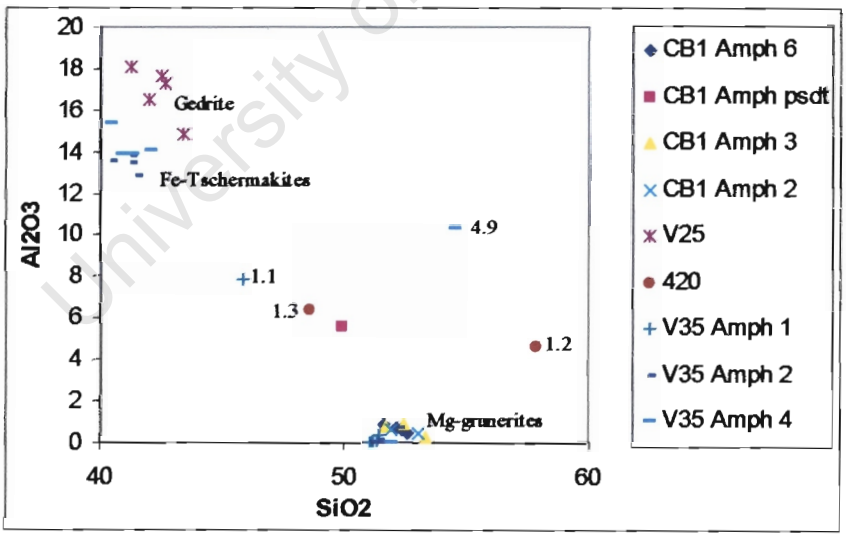

Figure 4.1.5.1: Binary plot illustrating the variation in amphibole Al_2O_3 content across the samples analysed.

	CB1						
	2.2 (Mg-grun)	**2.3** (Mg-grun)	**3.1** (Mg-grun)	**3.2** (Mg-grun)	**3.4** (Mg-grun)	**6.1** (Mg-grun)	**6.3** (Mg-grun)
SiO_2	53.04	51.95	53.32	51.72	52.43	52.54	51.65
TiO_2	0.00	0.03	0.00	0.05	0.13	0.04	0.02
Al_2O_3	0.44	0.59	0.27	0.78	0.84	0.49	0.88
FeO	32.48	33.11	32.51	32.93	32.48	33.76	33.39
MnO	0.35	0.42	0.30	0.48	0.32	0.37	0.26
MgO	12.20	11.76	11.89	11.56	11.35	11.99	11.02
CaO	0.29	0.50	0.22	0.38	0.35	0.22	0.46
Na_2O	0.20	0.00	0.00	0.16	0.04	0.00	0.00
K_2O	0.06	0.00	0.00	0.00	0.04	0.00	0.04
Total	99.05	98.35	98.56	98.07	98.02	99.40	97.75
Si	7.970	7.908	8.038	7.890	7.962	7.920	7.920
Al^{2+}	0.030 (8.00)	0.092 (8.00)	0.000 (8.04)	0.110 (8.00)	0.038 (8.00)	0.080 (8.00)	0.080 (8.00)
Al^{3+}	0.048	0.014	0.048	0.030	0.112	0.007	0.079
Ti	0.000	0.003	0.000	0.006	0.015	0.005	0.002
Fe	4.082	4.215	4.099	4.201	4.125	4.256	4.282
Mn	0.045	0.054	0.038	0.062	0.041	0.047	0.034
Mg	2.732 (7.02)	2.668 (7.04)	2.671 (6.89)	2.628 (7.04)	2.569 (6.94)	2.694 (7.04)	2.519 (7.00)
Ca	0.047	0.082	0.036	0.062	0.057	0.036	0.076
Na	0.058	0.000	0.000	0.047	0.012	0.000	0.000
K	0.012	0.000	0.000	0.000	0.008	0.000	0.008
X_{Fe}	0.599	0.6124	0.6054	0.6152	0.6163	0.6124	0.6297

	CB1				420	
	6.4 (Mg-grun)	**6.5** (Mg-grun)	**6.6** (Mg-grun)	**psdt** (Fe-anth)	**1.2** (Fe-ged)	**1.3** (Fe-anth)
SiO_2	52.58	52.37	52.15	49.95	48.59	57.86
TiO_2	0.00	0.00	0.03	0.04	0.06	0.12
Al_2O_3	0.42	0.64	0.69	5.57	6.35	4.59
FeO	33.09	33.02	33.43	31.57	31.85	26.36
MnO	0.41	0.35	0.40	0.21	0.68	0.49
MgO	11.78	12.07	11.85	10.15	10.26	8.30
CaO	0.30	0.41	0.22	0.39	0.35	0.73
Na_2O	0.02	0.03	0.00	0.08	0.33	0.19
K_2O	0.05	0.06	0.00	0.30	0.05	0.06
Total	98.63	98.96	98.77	98.26	98.52	98.69
Si	7.968	7.895	7.904	7.547	7.363	8.325
Al^{2+}	0.032 (8.000)	0.105 (8.000)	0.096 (8.000)	0.453 (8.000)	0.637 (8.000)	0.000 (8.325)
Al^{3+}	0.043	0.009	0.027	0.539	0.497	0.779
Ti	0.000	0.000	0.003	0.005	0.007	0.013
Fe	4.194	4.163	4.238	3.989	4.036	3.172
Mn	0.053	0.045	0.051	0.027	0.087 (7.001)	0.060
Mg	2.660 (7.01)	2.712 (7.02)	2.677 (7.03)	2.285 (6.99)	2.317	1.780 (5.98)
Ca	0.049	0.066	0.036	0.063	0.057	0.113
Na	0.006	0.009	0.000	0.023	0.097 (0.107)	0.053
K	0.010	0.012	0.000	0.058	0.010	0.011
X_{Fe}	0.6118	0.6056	0.6129	0.6358	0.6353	0.6406

Table 4.1.5.1: Mineral composition data (wt. % oxide), number of ions on the basis of 24 (O, OH) and X_{Fe} values calculated for amphiboles analysed in samples CB1and 420.

	V35						
	2.11 (Fe-tsch)	4.1 (Fe-tsch)	4.4 (Fe-tsch)	4.5 (Mg-grun)	4.6 (Fe-tsch)	4.7 (Fe-tsch)	4.9 (Hnb)
SiO_2	40.48	41.32	40.86	51.90	40.47	42.04	54.51
TiO_2	0.00	0.02	0.03	0.00	0.03	0.05	0.05
Al_2O_3	13.58	13.90	13.90	0.00	15.35	14.09	10.34
FeO	27.47	27.38	26.95	37.49	26.70	26.23	21.35
MnO	0.24	0.39	0.30	0.98	0.29	0.35	0.32
MgO	3.63	3.65	3.69	8.48	3.45	3.62	2.68
CaO	10.59	10.23	10.54	0.48	10.61	10.18	8.05
Na_2O	1.52	1.46	1.53	0.07	1.68	1.64	0.96
K_2O	0.49	0.50	0.49	0.03	0.55	0.52	0.36
Total	98.00	98.85	98.30	99.44	99.12	98.73	98.62
Si	6.346	6.392	6.362	7.996	6.233	6.463	7.869
Al^{2+}	1.654 (8.00)	1.608 (8.00)	1.638 (8.00)	0.000 (8.00)	1.767 (8.00)	1.537 (8.00)	0.131 (8.00)
Al^{3+}	0.856	0.927	0.913	0.000	1.020	1.017	1.629
Ti	0.000	0.002	0.004	0.000	0.003	0.006	0.005
Fe	3.602 (5.34)	3.542 (5.36)	3.509 (5.32)	4.830	3.439 (5.29)	3.372 (5.27)	2.577 (4.83)
Mn	0.032	0.051	0.040	0.128 (7.01)	0.038	0.046	0.039
Mg	0.848	0.841	0.856	1.947	0.792	0.829	0.577
Ca	1.779	1.696	1.758	0.079	1.751	1.677	1.245
Na	0.462 (2.34)	0.438 (2.23)	0.462 (2.32)	0.021	0.502 (2.36)	0.489 (2.27)	0.269 (1.58)
K	0.098	0.099	0.097	0.006	0.108	0.102	0.066
X_{Fe}	0.8094	0.808	0.8039	0.7127	0.8128	0.8026	0.8172

	V25				
	1.1 (Al-tsch)	2.1 (Al-tsch)	2.2 (Fe-ged)	2.4 (Fe-ged)	4.1 (Al-tsch)
SiO_2	42.55	41.26	42.68	43.43	41.98
TiO_2	0.19	0.36	0.00	0.06	0.35
Al_2O_3	17.60	18.12	17.25	14.89	16.52
FeO	18.49	20.21	27.01	27.48	17.43
MnO	0.00	0.07	0.24	0.29	0.13
MgO	7.37	6.19	10.02	10.11	7.83
CaO	10.57	10.13	0.54	0.52	11.08
Na_2O	0.84	1.16	1.59	1.39	1.00
K_2O	0.23	0.18	0.00	0.00	0.18
Total	97.83	97.69	99.33	98.17	96.50
Si	6.304	6.184	6.306	6.506	6.276
Al^{2+}	1.696 (8.00)	1.816 (8.00)	1.694 (8.00)	1.494 (8.00)	1.724 (8.00)
Al^{3+}	1.378	1.386	1.311	1.136	1.188
Ti	0.021	0.041	0.000	0.007	0.039
Fe	2.291 (5.32)	2.533 (5.35)	3.337 (6.97)	3.443 (6.96)	2.179 (5.17)
Mn	0.000	0.009	0.030	0.037	0.016
Mg	1.627	1.383	2.206	2.257	1.745
Ca	1.678	1.627	0.085	0.083	1.775
Na	0.241 (1.96)	0.337 (2.00)	0.455 (0.46)	0.404 (0.40)	0.290 (2.10)
K	0.043	0.034	0.000	0.000	0.034
X_{Fe}	0.5847	0.6469	0.602	0.604	0.5554

Table 4.1.5.3: Mineral composition data (wt % oxide), number of ions on the basis of 24 (O, OH) and X_{Fe} values calculated for amphiboles analysed in samples V35 and V25.

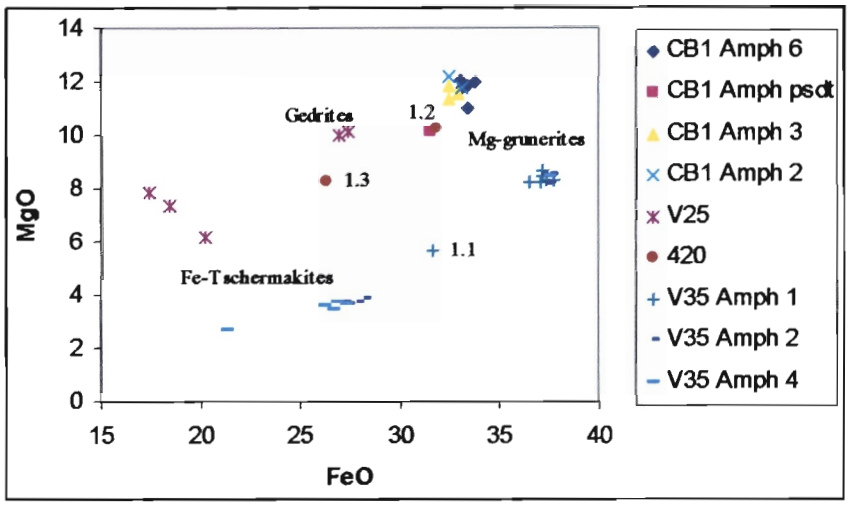

Figure 4.1.5.2: Binary plot illustrating the variation in amphibole FeO and MgO content across the samples analysed.

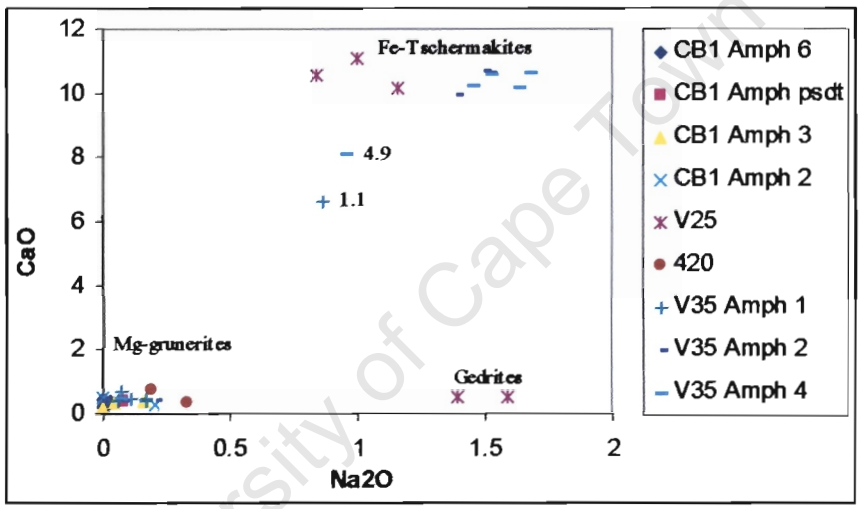

Figure 4.1.5.3: Binary plot illustrating the variation in amphibole Na_2O and CaO content across the samples analysed.

4.2 THE ARCHEAN BASEMENT COMPLEX ROCKS

Twenty one samples (10 x 10 x 10 cm) from the core of the dome were analysed using XRF, including fourteen granitoid samples (OGG and ILG), two charnockites (435, 436), one mafic granulite (454a), two garnet restites (456a, b), one migmatite (HM6) and one cordierite restite, VT623 (Table 4.2.1). The samples were prepared from 2g of sample powder which was dried at 110°C for four hours and then roasted at 850-1000°C overnight. A mixture of 0.7g of the sample and 6g of LiT-LiM flux in the proportion 57:43 with LiBr as a releasing agent, which had been dried at 450°C overnight, was then used to produce the claisse-fluxy fusion discs according to the method of Claisse (1989). The disks were analysed using the Phillips PW1480 wavelength dispersive XRF spectrometer in the Department of Geological Sciences at the University of Cape Town. The spectrometer uses a dual target Mo/Sc X-ray tube and all measurements are made with the tube at 50kV and 50mA. Analytical conditions for major element determinations are described by Willis (1999).

Fusion disks made up with 100% Johnson Matthey Specpure SiO_2 were used as blanks for all elements except Si, for which fusion disks made of Johnson Matthey Specpure Fe_2O_3 and $CaCO_3$ were used. Intensity data were collected using Phillips X40 software on a Pentium Celeron 333mHz PC. Data reduction was done off-line using internally developed software. All peaks were corrected for background, and spectral overlap corrections were made for Br on Al, Cr on Mn, Al and Ca on Mg and Mg on Ca and Na. Table 4.2.1 summarizes bulk rock compositions for all samples collected from the core of the structure.

	OGG						ILG				
Sample	438	441	443	437	432	431	433	429a	428	445	447
SiO_2	73.50	73.20	72.30	71.58	69.73	68.19	74.79	75.12	70.62	71.43	74.58
TiO_2	0.33	0.14	0.17	0.29	0.41	0.49	0.10	0.14	0.19	0.26	0.17
Al_2O_3	14.09	14.13	14.92	14.57	15.27	15.66	13.66	13.70	15.50	14.98	13.19
Fe_2O_3	2.10	1.31	1.72	2.64	2.94	3.46	1.20	1.63	1.90	2.02	1.88
MnO	0.04	0.02	0.02	0.02	0.03	0.02	0.02	0.02	0.03	0.02	0.02
MgO	0.27	0.27	0.38	0.58	0.97	0.83	0.15	0.31	0.66	0.60	0.43
Na_2O	3.95	3.35	4.76	4.54	4.84	4.58	3.56	4.12	4.07	3.83	3.57
CaO	1.01	0.81	1.67	1.81	2.73	2.36	1.06	1.63	2.37	1.97	1.51
K_2O	4.73	6.10	3.00	3.17	2.00	3.44	4.77	3.06	3.83	4.06	3.22
P_2O_5	0.08	0.09	0.06	0.12	0.18	0.23	0.02	0.03	0.10	0.08	0.05
NiO	0.00	0.00	0.00	0.00	0.00	0.00	0.00	0.00	0.00	0.00	0.00
Cr_2O_3	0.00	0.00	0.01	0.00	0.00	0.00	0.00	0.00	0.00	0.00	0.00
SO_3	-0.06	-0.07	-0.06	-0.06	-0.05	-0.05	-0.06	-0.06	-0.06	-0.06	-0.06
H_20-	0.09	0.08	0.09	0.08	0.09	0.10	0.10	0.12	0.13	0.09	0.10
LOI	0.50	0.51	0.41	0.62	0.58	0.57	0.37	0.40	0.79	0.43	0.44
Total	100.61	99.94	99.45	99.96	99.72	99.89	99.73	100.20	100.14	99.70	99.10

	ILG									
Sample	450	461	457	435	436		456a	456b	HM6	VT623
SiO_2	67.17	72.76	72.86	60.60	57.94	49.43	60.02	60.39	63.95	81.42
TiO_2	0.44	0.21	0.20	0.83	0.95	0.68	0.68	0.63	0.55	0.29
Al_2O_3	15.95	14.55	14.23	16.52	17.13	11.34	14.75	14.92	14.92	11.39
Fe_2O_3	3.48	1.84	1.54	6.22	6.97	11.79	14.79	14.68	8.07	2.17
MnO	0.04	0.03	0.03	0.08	0.09	0.21	0.23	0.22	0.30	0.03
MgO	0.94	0.51	0.27	2.17	2.84	9.63	5.32	5.14	4.75	0.62
Na_2O	5.50	4.41	4.32	4.90	5.08	2.70	1.02	1.41	2.36	0.70
CaO	3.09	1.62	1.12	5.16	5.93	11.12	1.02	1.14	1.01	0.10
K_2O	1.48	3.52	4.02	1.01	1.44	1.01	1.30	1.40	2.78	2.06
P_2O_5	0.18	0.07	0.06	0.32	0.39	0.18	0.05	0.06	0.04	0.02
NiO	0.00	0.00	0.00	0.00	0.00	0.03	0.03	0.03	0.04	0.01
Cr_2O_3	0.00	0.00	0.00	0.00	0.00	0.07	0.10	0.10	0.10	0.03
SO_3	-0.05	-0.06	-0.06	-0.02	-0.03	-0.01	-0.02	-0.03	-0.05	-0.05
H_20-	0.10	0.09	0.09	0.13	0.11	0.14	0.13	0.11	0.16	0.13
LOI	1.17	0.53	0.30	0.46	0.26	0.67	0.00	0.00	0.58	0.77
Total	99.49	100.07	98.98	98.37	99.11	98.99	99.30	100.14	99.56	99.67

Table 4.2.1: Major element concentrations (wt. % oxide) obtained by XRF for samples collected from the Archean basement complex in the core of the Vredefort Dome.

Figures 4.2.1.1-8 show major element trends observed in the rocks from the core of the dome. The different lithologies are clearly distinguished on the binary diagrams. Of particular importance is the observation that the TTGs of the OGG and those of the ILG show very similar compositions and element trends. The ratio of silica to alumina plots as one would expect for a TTG suite with the trondjhemites plotting at the alumina-rich and slightly silica-depleted end of the trend line and exhibiting the highest Mg- and Fe-content

of the OGG samples. Potassium values are similar in the OGG and ILG trondjhemites, tonalites and granitoids, however, OGG samples do show a wider range of K_2O-content, with some samples exhibiting high degrees of potassium alteration (Fig. 4.2.1.8). The charnockites display lower Si- and K-content and higher Al-, Mg-, Fe-, Ca- and Na-content relative to the granitoids.

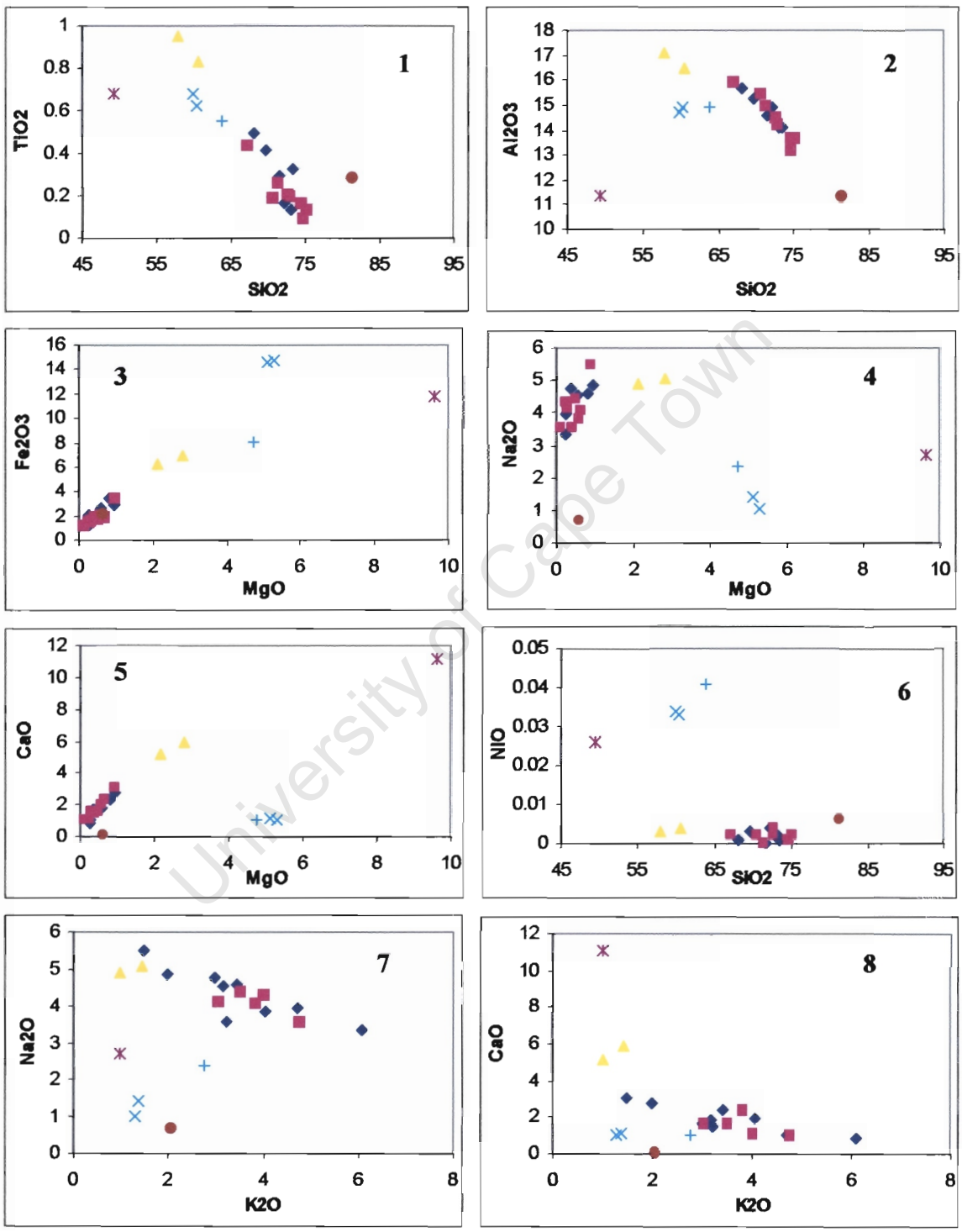

Figure 4.2.1.1-8: Binary diagrams illustrating bulk composition of samples analysed from the Vredefort core. ◆ OGG ■ ILG ▲ charnockites + SMZ migmatite x SMZ garnet restite ✳ mafic granulite ● VT623

The same twenty one samples were also analysed for their trace element compositions using ICP-MS. Samples were prepared by digesting 50mg of sample powder in closed

teflon beakers using HF and HNO_3 (for full procedure see "Analytical Techniques" for the ICP-MS facility on the webpage http://www.uct.ac.za/depts/geolsci), and analysed using the Perkin-Elmer/Sciex Elan 6000 ICP mass spectrometer in the Geochemistry Department, University of Cape Town. Instrument operating conditions are given in Table 4.2.2. The instrument was optimised to minimise the formation of oxides (CeO/Ce = 0.025) and doubly charged ions (Ba++/Ba+ = 0.028). The samples were analysed using 103Rh, 115In, 187Re and 209Bi as internal standards and calibration was done against a set of artificial standards made from synthetic multi-element standard solutions.

Nebuliser gas flow	0.9L/min
Main gas flow	~15L/min
Auxillary gas flow	~0.75L/min
ICP RF power	1075Watts
Autolens voltages :	
9Be	7.3V
59Co	8.0V
115In	8.7V
Instrument sensitivity for 103Rh	52178cps/ppb

Table 4.2.2: Instrument operating conditions for ICP-MS sample analysis.

The complete set of trace element data acquired is presented in Table 4.2.3. Chondrite-normalized Rare Earth Element (REE) data are plotted in Figures 4.2.4.1 & 2 and show similar ranges for the OGG and ILG granitoids to those of Hart *et al.* (1990). The OGG samples mostly display highly fractionated, smooth REE profiles as would be expected for Na-rich plutonic rocks (Ref.). However, sample 438, which is closest to the core-collar contact, displays a pronounced negative Eu anomaly and higher total concentrations for the HREEs compared to other samples from the OGG. Sample 431 also displays a small negative Eu anomaly, and has an overall higher REE concentration than the rest of the OGG samples analysed. This is contrary to what Hart *et al.* (1990) observed where samples closest to the Vredefort discontinuity show lower overall REE concentration relative to samples from higher up (closer to the core-collar contact) (Fig. 2.6.4). Sample 441 displays an entirely different REE pattern to the rest of the OGG samples, having relatively depleted LREE and enriched HREE concentrations, and displaying a positive Eu anomaly, thus being more MORB-like than the rest of the OGG samples. This sample shows the greatest amount of K-alteration in the sample-set, and the difference observed in its REE concentrations may well be associated with the increased alteration effects.

The ILG samples exhibit lower concentrations for all elements except Eu and Lu relative to the OGG samples (Figs. 4.2.2.1, 2). All the ILG samples exhibit a positive Eu anomaly, which may reflect the replacement of Ca^{2+} by Eu^{2+} in the mineral plagioclase or the retention of Eu in plagioclase as modelled by Taylor & McLennan (1985) for middle to lower crustal material. The two REE profiles for the charnockite samples are plotted in Figure 4.2.2.2 and have shallower slopes compared to the granitoids from both the OGG and ILG, however, they plot closer to the OGG field than the ILG field. Sample 436 displays a small negative Eu anomaly and 435 an even smaller depletion in Eu. The mafic granulite and garnet restite display even shallower REE profiles than the charnockites and also exhibit small negative Eu anomalies.

	OGG						ILG				
Sample	**438**	**441**	**443**	**437**	**432**	**431**	**433**	**428**	**429a**	**445**	**447**
Sc	1.48	0.84	0.87	1.20	1.30	1.37	0.29	1.12	0.49	0.85	0.60
V	6.83	4.93	5.28	10.72	15.17	17.32	5.10	9.54	4.45	8.15	5.66
Cr	2.72	6.02	2.28	3.59	11.02	9.62	7.49	7.03	3.27	2.20	3.64
Co	2.10	1.70	2.30	3.95	6.89	6.22	1.39	4.02	2.49	3.58	2.36
Ni	2.89	5.42	4.13	4.83	14.49	10.79	6.25	8.14	4.62	4.19	3.57
Cu	3.73	4.17	3.80	5.19	22.55	11.13	4.34	6.33	12.97	6.30	11.60
Rb	149.95	97.49	49.55	46.88	22.10	49.02	80.24	40.07	32.76	61.84	47.20
Sr	119.16	163.75	337.76	307.92	342.85	511.24	246.16	302.65	216.62	338.43	173.85
Y	11.62	6.02	2.35	3.00	2.74	4.67	0.67	1.53	0.47	1.07	0.88
Zr	167.62	120.51	54.43	72.85	57.36	93.62	75.92	126.80	57.44	59.60	104.46
Nb	17.14	4.54	2.17	3.55	3.29	5.07	0.44	1.57	0.90	2.18	0.67
Cs	1.00	0.31	0.29	0.22	0.13	0.21	0.10	0.05	0.04	0.13	0.10
Ba	564.68	910.02	670.77	719.28	569.01	1275.27	779.07	1120.65	465.93	721.84	570.03
La	40.20	3.31	24.94	30.65	45.84	50.08	11.28	42.56	9.78	10.57	12.63
Ce	89.27	6.92	43.58	67.09	86.18	104.73	17.14	79.17	17.94	17.50	23.13
Pr	7.56	0.78	4.68	6.64	8.40	10.23	1.44	7.49	1.50	1.58	2.11
Nd	24.38	3.10	15.77	22.17	27.14	33.96	4.25	23.78	4.74	5.25	6.94
Sm	3.80	0.81	2.35	2.82	2.96	4.48	0.46	2.58	0.56	0.77	0.89
Eu	0.50	0.44	0.70	0.67	0.68	0.91	0.82	0.72	0.46	0.67	0.51
Gd	2.65	0.90	1.39	1.51	1.60	2.42	0.24	1.15	0.28	0.45	0.44
Tb	0.40	0.17	0.15	0.17	0.18	0.27	0.03	0.11	0.03	0.05	0.05
Dy	2.15	1.05	0.60	0.72	0.72	1.19	0.12	0.40	0.11	0.23	0.19
Ho	0.41	0.22	0.09	0.12	0.12	0.19	0.02	0.06	0.02	0.04	0.03
Er	1.13	0.64	0.20	0.27	0.26	0.44	0.07	0.14	0.05	0.09	0.09
Tm	0.15	0.08	0.02	0.03	0.03	0.05	0.01	0.02	0.01	0.01	0.01
Yb	0.98	0.52	0.13	0.19	0.16	0.28	0.10	0.12	0.06	0.07	0.12
Lu	0.14	0.08	0.02	0.03	0.02	0.04	0.02	0.02	0.01	0.01	0.02
Hf	4.43	3.44	1.38	1.91	1.37	2.00	2.46	2.97	1.71	1.40	2.83
Ta	0.94	0.13	0.05	0.12	0.05	0.09	0.04	0.02	0.03	0.05	0.02
Pb	11.00	14.58	13.39	9.15	9.44	12.30	11.22	10.06	8.98	7.48	6.68
Th	7.45	0.42	5.77	5.39	5.01	5.42	0.82	6.40	0.69	0.15	1.22
U	0.84	0.25	0.13	0.12	0.08	0.11	0.22	0.15	0.11	0.07	0.14
Zr/Hf	37.84	35.01	39.30	38.06	41.77	46.71	30.91	42.71	33.54	42.64	36.91
La/Yb	41.10	6.36	193.23	159.57	294.98	180.87	114.88	347.07	173.26	160.00	105.98
Th/U	8.83	1.67	42.77	45.58	66.52	49.61	3.73	41.80	6.36	2.34	8.62

Table 4.2.3: Trace element content (ppm) for Archean basement complex samples collected from the core of the Vredefort dome.

						ILG				
Sample	450	461	457	435	436		456a	456b	HM6	VT623
Sc	3.32	2.03	1.00	7.63	15.26	34.09	24.18	21.24	14.56	6.88
V	15.66	6.48	6.42	43.75	52.20	91.48	74.27	67.08	52.32	27.34
Cr	24.06	8.74	7.35	11.58	13.12	241.99	356.67	331.70	351.82	87.90
Co	6.12	3.31	2.09	18.73	21.26	56.39	37.14	33.40	30.74	13.77
Ni	11.37	9.40	7.69	28.87	29.73	208.64	268.62	268.04	293.60	44.06
Cu	11.79	14.84	6.52	91.64	26.76	32.97	30.41	42.30	29.75	18.15
Rb	26.22	72.74	62.95	8.65	26.35	23.94	62.33	55.61	89.51	75.75
Sr	392.86	292.65	219.65	466.93	371.97	276.81	105.93	120.30	241.30	49.13
Y	4.20	3.24	1.91	10.20	15.08	21.32	33.47	29.20	23.97	9.52
Zr	90.41	81.02	88.47	62.36	41.06	44.33	189.31	129.40	144.85	84.85
Nb	7.01	6.08	4.33	11.67	13.33	6.12	12.44	11.13	11.29	5.86
Cs	0.12	0.20	0.08	0.08	0.15	0.19	1.27	0.98	1.21	2.18
Ba	469.43	407.18	529.18	312.38	314.53	92.43	222.52	227.87	451.23	309.69
La	35.99	21.27	21.71	31.43	33.57	20.44	35.67	35.18	31.84	24.69
Ce	67.19	38.11	41.01	80.55	82.87	51.68	73.65	71.76	64.51	48.05
Pr	6.89	3.97	4.03	8.23	9.40	7.09	8.51	8.18	7.10	5.34
Nd	23.48	13.26	13.55	30.26	37.15	29.88	32.05	31.18	24.71	18.76
Sm	3.37	2.26	2.00	4.47	6.79	6.47	6.16	6.06	4.08	3.22
Eu	1.04	0.62	0.62	1.13	1.11	1.69	1.11	1.27	1.17	0.44
Gd	2.08	1.45	1.05	3.25	4.81	5.38	5.74	5.33	3.27	2.26
Tb	0.23	0.18	0.11	0.43	0.65	0.78	1.00	0.85	0.58	0.33
Dy	0.96	0.74	0.44	2.19	3.30	4.08	5.99	5.14	3.74	1.78
Ho	0.15	0.12	0.07	0.40	0.58	0.75	1.21	1.04	0.82	0.34
Er	0.36	0.28	0.15	1.04	1.49	1.98	3.48	3.02	2.54	0.96
Tm	0.04	0.03	0.02	0.14	0.19	0.27	0.49	0.43	0.38	0.14
Yb	0.26	0.21	0.12	0.84	1.10	1.68	3.19	2.83	2.61	0.91
Lu	0.04	0.03	0.02	0.12	0.15	0.24	0.48	0.42	0.40	0.13
Hf	2.01	2.30	2.35	1.44	1.02	1.30	4.95	3.43	4.03	2.23
Ta	0.14	0.16	0.09	0.37	0.43	0.43	0.67	0.62	0.57	3.49
Pb	10.32	15.39	14.83	6.95	7.74	14.05	7.97	8.08	11.60	9.97
Th	5.37	14.74	4.63	0.32	0.31	0.54	9.62	8.34	5.77	5.51
U	0.20	0.33	0.21	0.09	0.06	0.18	1.37	1.15	0.44	3.11
Zr/Hf	44.96	35.19	37.62	43.43	40.36	34.23	38.21	37.71	35.92	37.98
La/Yb	137.02	101.61	183.01	37.31	30.64	12.17	11.18	12.43	12.21	27.20
Th/U	27.14	44.62	21.55	3.46	4.79	3.04	7.01	7.25	13.17	1.77

Table 4.2.3 (cont.): Trace element content (ppm) for Archean basement complex samples collected from the core of the Vredefort dome.

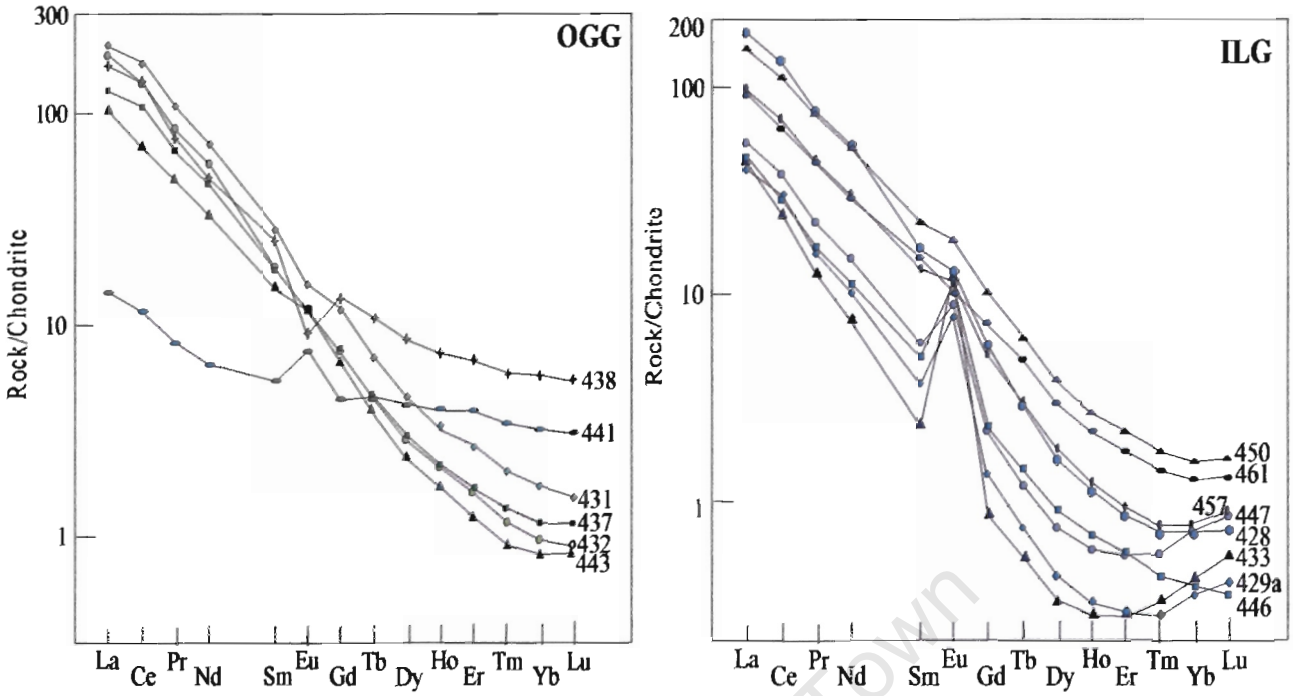

Figure 4.2.2.1: Chondrite-normalised Rare Earth Element (REE) plots for TTG samples from the OGG and ILG.

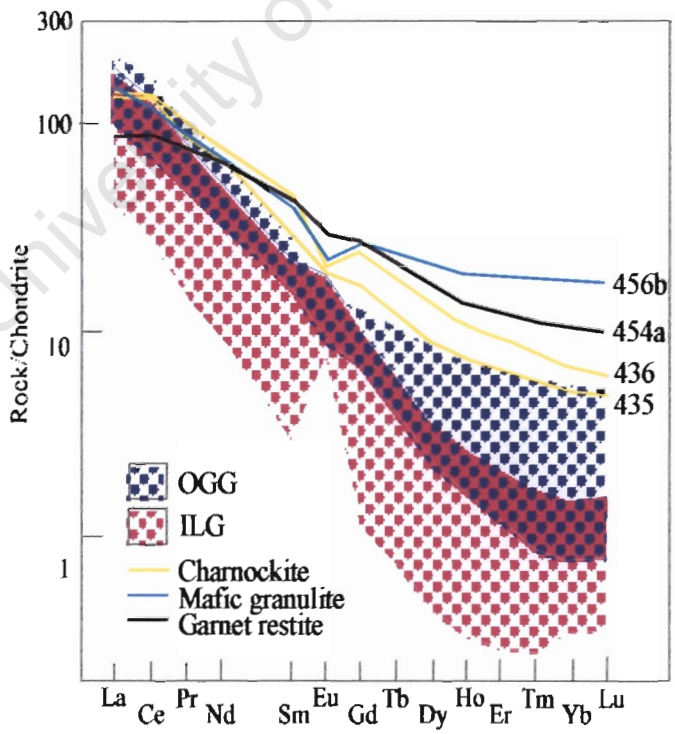

Figure 4.2.2.2: REE plots for the xenolithic supracrustals and charnockites found within the ILG, in relation to the OGG and ILG REE fields.

Figures 4.2.3.1 & 2 display various major and trace element concentrations as a function of distance from the core-collar contact for the Archean basement complex samples. These profiles were plotted for comparison with the data of Hart *et al.* (1990) which are presented in Figures 2.6.2 & 3. The results from this study were obtained for single samples along the traverse taken, whereas the data of Hart *et al.* (1990) were averaged concentrations and the profiles were smoothed using a triple point averaging procedure. Despite the different approaches taken in producing the profiles of this study, the results are still comparable and as shown in Figures 4.2.3.1 & 2, do not concur with those produced by Hart *et al.* (1990), which show distinct differences in major and trace element concentrations for the OGG and ILG. In the profiles of this study, only granitic and trondjhemitic to tonalitic samples have been included in the profile curve, whilst concentrations of the charnockites and mafic and metapelitic granulites of the ILG have been plotted but not included in the profiles. Naturally, the latter rocks have significantly different major and trace element signatures, and will therefore distort the geochemical profile of the granitoids in which they are found, thus not allowing for a direct comparison of the granitoids from the two granitoid terranes. From the profiles of this study it is apparent that the geochemistry of the charnockites are anything but "indistinguishable" from the ILG granites and that, in relation to the ILG granites they are enriched in Al, Fe, Mg, Ca, Ti, P, Co and Sr and depleted in Si, K, Hf, Zr and Ba. It is also obvious that should the mafic xenoliths within the ILG have been included in the profiles they would have distorted them to produce profiles comparatively similar to those of Hart *et al.* (1990).

If we consider the trondjhemitic to tonalitic granitoids in isolation, we see that the OGG and ILG are in fact fairly similar, but that the OGG in general contain greater amounts of K which complies with their greater biotite content compared to the leucogranites of the ILG. The OGG profiles correlate well with that observed by Hart *et al.* (1990) and suggest a trend towards slightly more basic compositions closer to the centre of the structure, with decreased Si- and K-content and increased Al-, Na-, Ca-, Mg-, Fe- and Ti-content observed in the direction of the OGG/ILG transition zone. Trace element profiles are consistent with these major element trends with U, Th, Rb, Cs, Hf and Zr decreasing and Sr, Ba and Co increasing in concentration towards the Vredefort discontinuity. Resultant K/U and Th/U ratios thus increase towards the transition zone, in agreement with the data of Hart *et al.* (1981), however, the averages of these ratios are even higher than those obtained by Hart *et al.* (1990). Therefore, the OGG does, indeed, appear to display a bimodal character between the upper 3-4km and the lower 3km. The profiles of the ILG are difficult to make comment on because the majority of the samples analysed are found in the vicinity of the transition zone and sample 450, which exhibits a REE pattern intermediate between those of the OGG and the ILG, distorts the profiles which would otherwise plot as relatively flat curves. Although it is notable that the ILG profiles do not continue any of the trends observed in the OGG, we know that the two terranes are compositionally similar, are of the same age and have experienced similar tectonic histories (Hart *et al.*, 1999 ; Lana *et al.*, 2003 ; Flowers, 2003).

Major and trace element concentrations observed in the mafic xenoliths from within the ILG are, as expected, enriched in Mg, Fe, Ni and Co and depleted in Si, K, Na, Ca, Rb, Sr and Ba in comparison to the granites. Bulk rock compositions obtained for the five samples analysed in this study are plotted on a Turner AFM diagram with Stevens *et al.* (1997), Gibson (2002) and Stepto (1990) data on it (Fig. 4.2.4). This illustrates their similarity to the samples analysed by Stevens *et al.* (1997) and Gibson (2002) and substantiates no

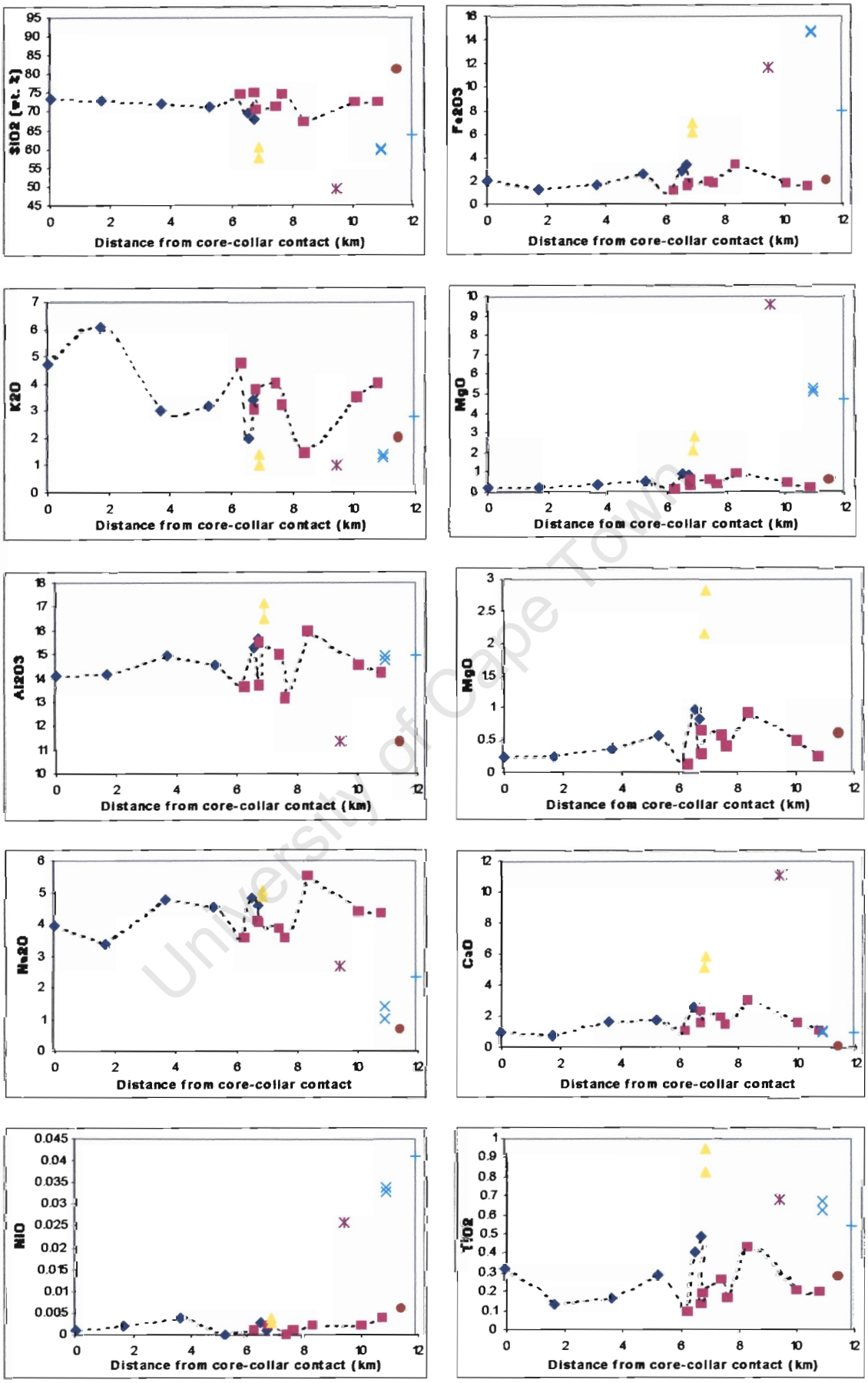

Figure 4.2.3.1: Major element profiles (plotted as weight % oxide) across the core of the Vredefort dome, where ◆ OGG ■ ILG ▲ charnockites + SMZ migmatite x SMZ garnet restite ✳ mafic granulite ● VT623

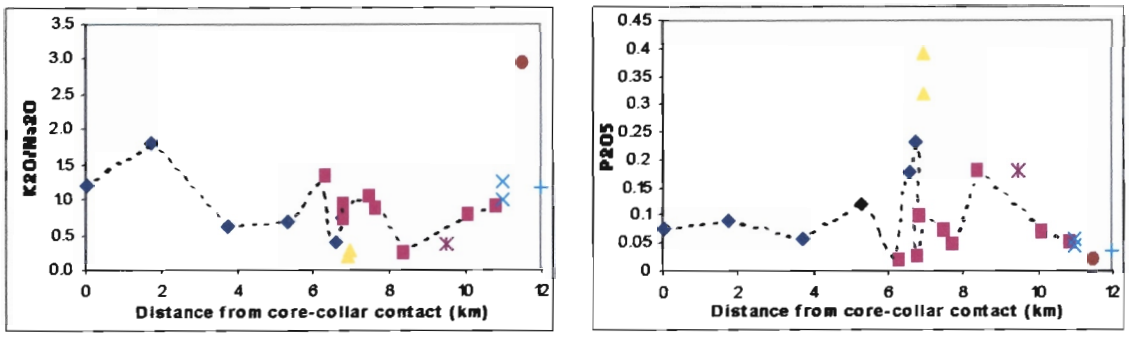

Figure 4.2.3.1a (cont.): Major element profiles (plotted as weight % oxide) across the core of the Vredefort dome, where ◆ OGG ■ ILG ▲ charnockites + SMZ migmatite x SMZ garnet restite ✳ mafic granulite ● VT623

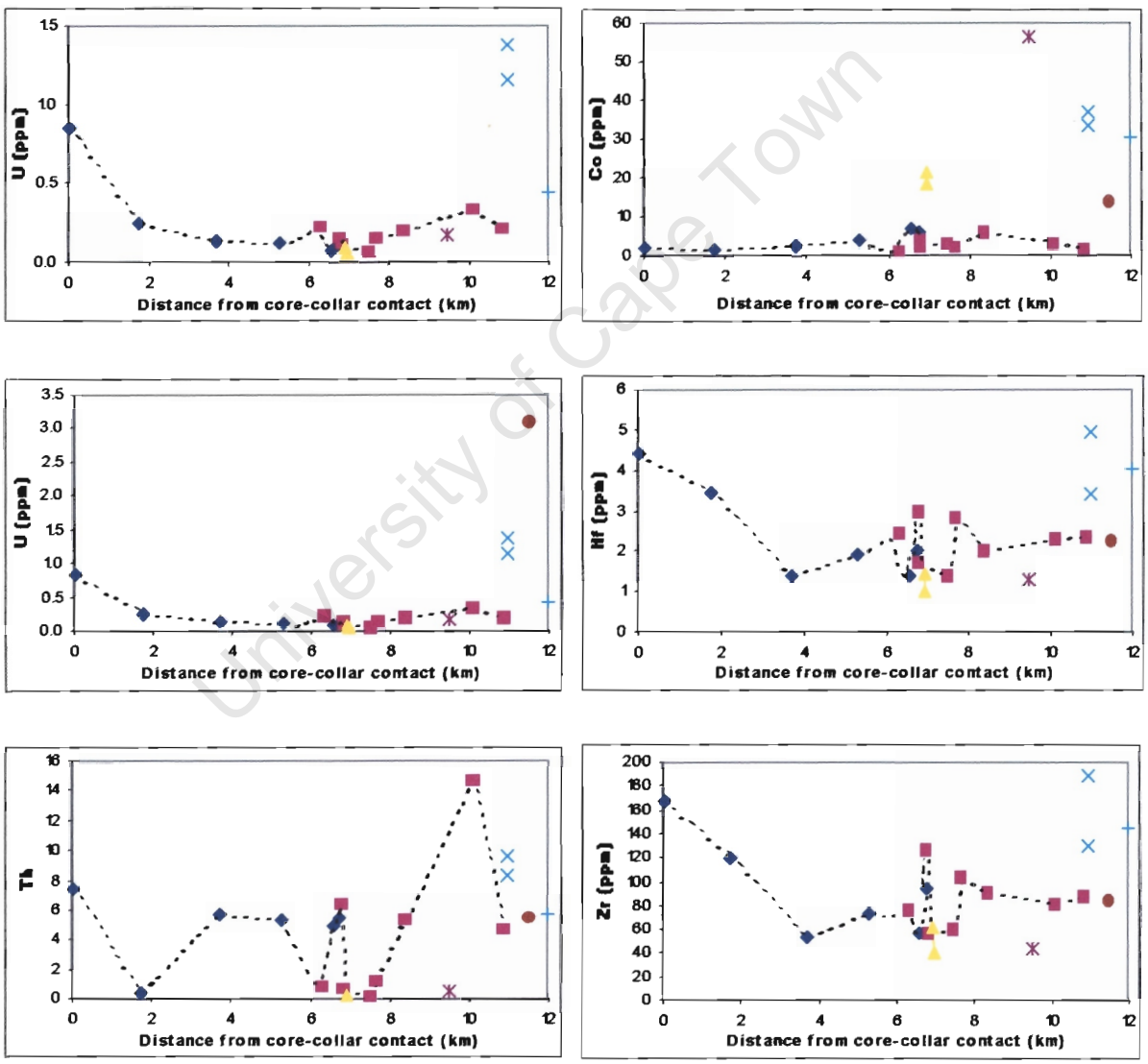

Figure 4.2.3.2: Trace element profiles (plotted as ppm) across the core of the Vredefort dome, where ◆ OGG ■ ILG ▲ charnockites + SMZ migmatite x SMZ garnet restite ✳ mafic granulite ● VT623

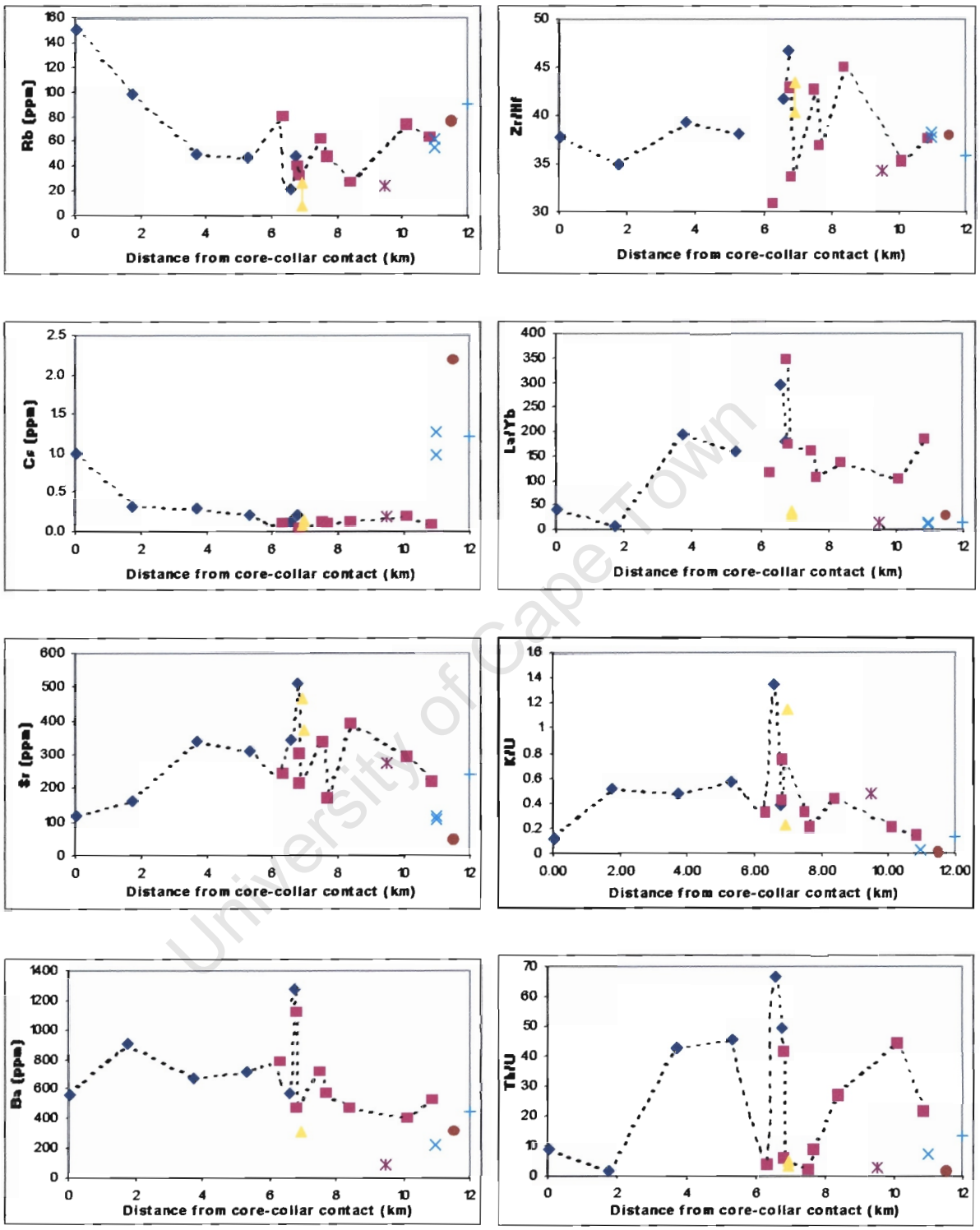

Figure 4.2.3.2 (cont.) : Trace element profiles (plotted as ppm, except K/U which plots weight %/ppm)) across the core of the Vredefort dome, where ◆ OGG ■ ILG ▲ charnockites + SMZ migmatite x SMZ garnet restite ✳ mafic granulite ● VT623

further action having been taken to present more data on these rocks. Sample 545a, which was initially thought to be a mafic granulite, is shown to in fact be a mafic-rich migmatite.

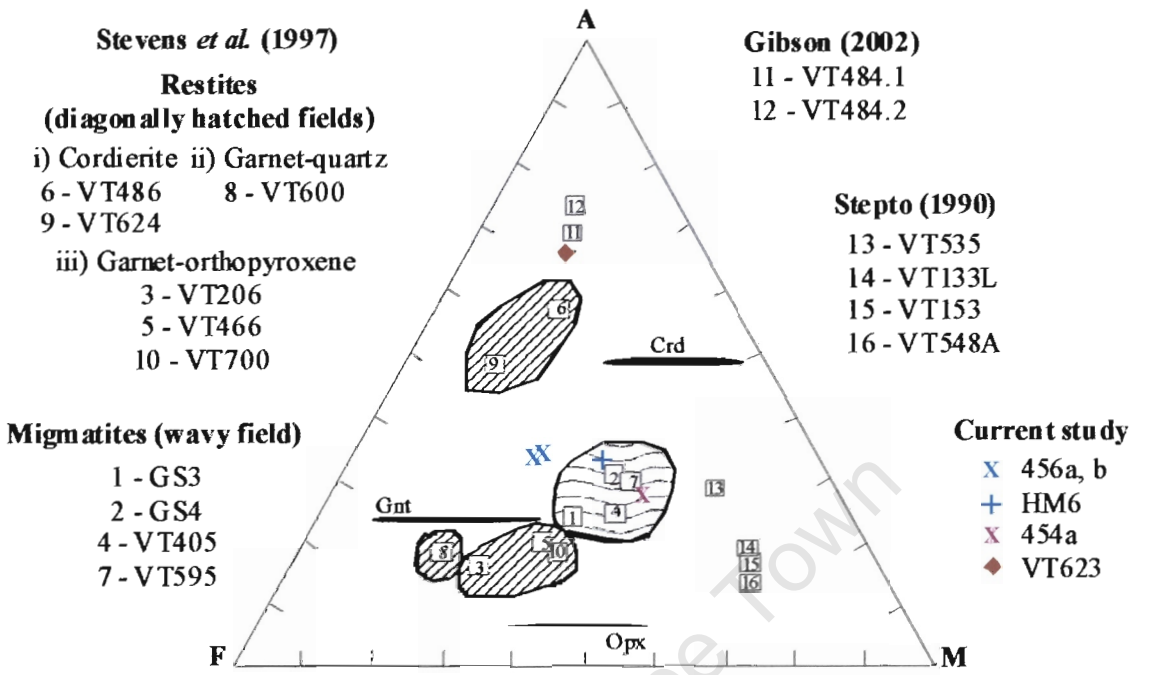

Figure 4.2.4: AFM projection from Qtz, Plag and Ksp for the metamorphic assemblages of the xenolithic metapelitic units from within the ILG (after Stevens *et al.*, 1997 and Gibson, 2002).

CHAPTER 5
METAMORPHISM

5.1 THE COLLAR ROCKS

The metamorphism displayed in the collar rocks shall be discussed in order of increasing grade, with samples displaying more complex metamorphic assemblages being considered individually. Each of the samples studied is first considered in terms of its metamorphic assemblage, which provides pressure-temperature constraints for the metamorphism according to their positions as plotted on relevant petrogenetic grids as defined by the key prograde reactions identified. Second, thermobarometric calculations using mineral compositions of the key metamorphic minerals are applied and the results compared with the petrogenetic P-T estimates.

A number of well-constrained P-T petrogenetic grids are available for pelites in the system K_2O-FeO-MgO-Al_2O_3-SiO_2-H_2O (KFMASH) (Harte & Hudson, 1979; Holland & Powell, 1990; Dymoke & Sandiford, 1992). Since it has been ascertained that the samples in this study correlate well with those analysed by Gibson *et al.* (1995), their peak metamorphic assemblages will also be considered in terms of the Dymoke & Sandiford (1992) grid used by Gibson *et al.* (1995) to constrain pressures and temperatures of formation, although Figure 5.1.1 also includes lower temperature reactions which define the peak metamorphic assemblages of the lower grade rocks in this study.

Sample 411 represents the lowest grade of metamorphism observed in the sample set, having attained mid-greenschist grades of metamorphism, as evidenced by its metamorphic assemblage Qtz + Ms + Chl ± Bt. The presence of small amounts of biotite indicates that this rock reached temperatures and pressures bordering on those required for the biotite-in prograde reaction, known to occur in the region of 420°C ± 20°C at 4.0 kbar (Harte & Hudson, 1979), probably by the reaction:

$$Ms + Chl \rightarrow Bt + Ms + Qtz + H_2O \quad (1)$$

In the ferruginous meta-shale, sample V25, garnet and amphibole are the main metamorphic minerals. Since it is a more basic rock than the metapelites amphibole is observed in place of biotite. From mineral composition data, the amphibole phases have been identified as gedrite and alumino-tschermakitic hornblende. Although no cordierite was identified in this sample, gedrite is likely to have formed by reaction involving chlorite + quartz (± plagioclase), imparting a temperature constraint of greater than 550°C at pressures greater than 2.0 kbar according to the PT diagram of Akella & Winkler (1996) (Fig. 5.1.1). Such a lower P-T constraint is corroborated by the presence of hornblende rather than an amphibole such as actinolite, since the reaction albite + chlorite + epidote + actinolite → hornblende + plagioclase has been found to occur experimentally at 550°C at 2.0 kbar (Deer *et al.*, 1996).

Sample V25 also provides us with information on the timing of peak metamorphism relative to the shock event and a period of fluid influx during which a silica-rich vein was formed. In Figs. 5.1.2.1 & 2 it is evident that pseudotachylite cross-cuts both the main metamorphic assemblage and the quartz vein, which itself has been shown to engulf parts of the host rock and truncate the fabric of the main metamorphic assemblage (Fig. 3.2.7).

The vein also exhibits extensive quartz recrystallisation and planar deformation features typical of that seen in the basement gneisses, which is considered a deformation feature associated with the shock event (Fig. 5.1.2.3). Therefore, the peak metamorphic event predates both a phase of fluid influx and the 2.03 Ga impact event during which pseudotachylite was formed, and the period of fluid influx also predates the impact event.

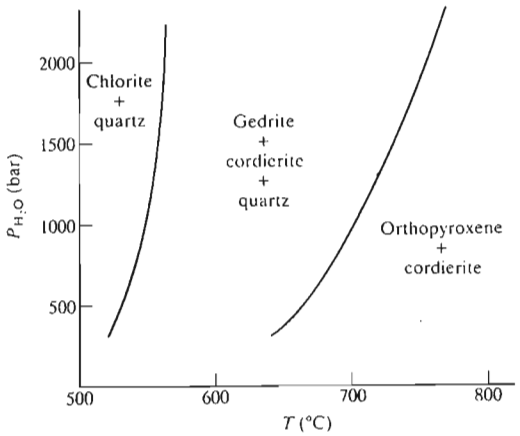

Figure 5.1.1: PT diagram showing an approximate stability field for gedrite + cordierite + quartz in a low pressure environment (from Akella & Winkler, 1996).

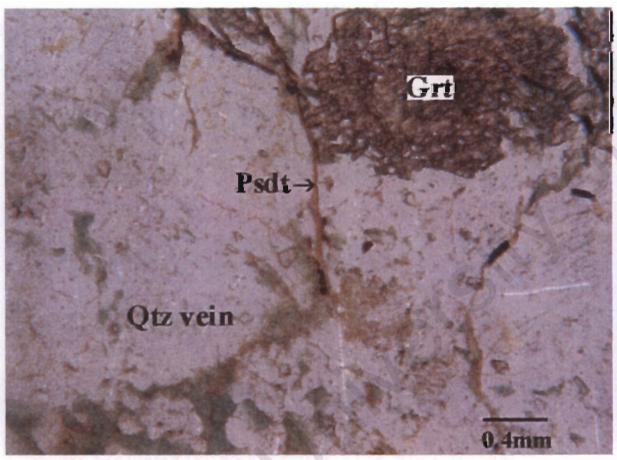

Figure 5.1.2.1: Pseudotachylite cross-cutting both garnet and the leucosome in sample V25.

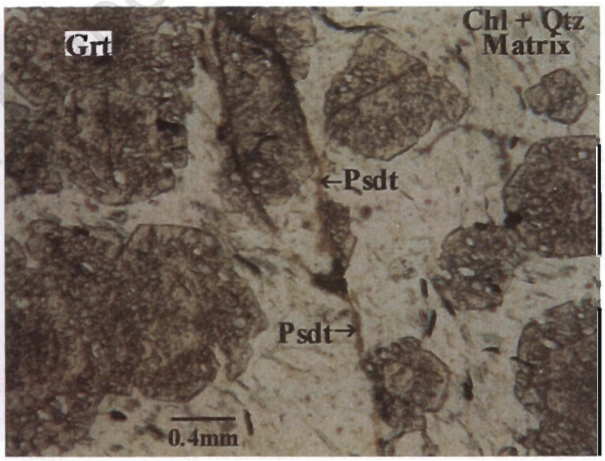

Figure 5.1.2.2: Pseudotachylite cross-cutting and displacing garnet within sample V25.

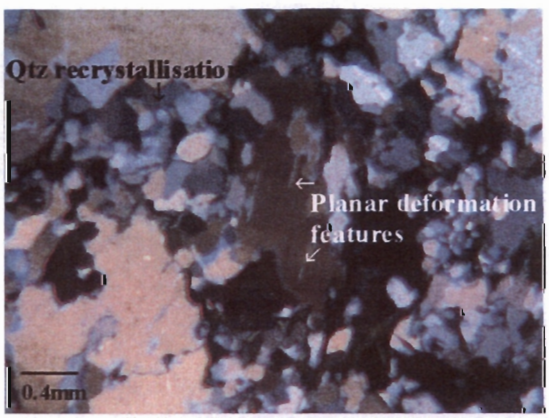

Figure 5.1.2.3: Photograph taken in cross polarised light illustrating the shock deformation features preserved in quartz from the quartz vein in sample V25.

Samples 424, 426 and V3 exhibit upper greenschist grades of metamorphism defined by their peak metamorphic assemblages of Qtz + Bt + Grt. In these samples, muscovite is absent indicating that the reaction,

$$Chl + Ms \rightarrow Grt + Bt + Qtz + H_2O \quad (2)$$

probably consumed all muscovite initially present in the rock. The relationship between chlorite and biotite is prograde with biotite replacing chlorite. Reaction (2) is well constrained (Thompson, 1976) and provides evidence of equilibration within the P-T field constrained at the lower limit by the presence of almandiferous garnet which is produced at temperatures greater than 500°C ± 30°C, and at the upper limit to temperatures less than ~550°C by the absence of staurolite which we would expect to form through reaction between Chl + Grt at temperatures in excess of this (Fig. 5.1.3).

The peak metamorphic assemblage of sample V19 is defined by poorly formed and intricately associated staurolite and andalusite, plus biotite. Although the relationship between andalusite and staurolite is not clear, this assemblage is comparable to the Fe-rich pelites observed by Gibson & Wallmach (1995), for which a positive P-T slope is depicted in Fig. 4.3.3. This assemblage is likely to have formed via the reaction:

$$Chl + Ms \leftrightarrow St + Bt + Qtz + H_2O \quad (3)$$

followed by reaction of staurolite to andalusite with increasing temperatures, by the reaction Chl + St → And + Bt. The minuscule amount of both chlorite and muscovite in this assemblage indicates that temperatures obtained must have been in excess of ~540°C at 3-4 kbar for a long enough period of time for one of the reactants to have been completely consumed, and that the remaining chlorite is retrograde. The presence of staurolite as part of the peak metamorphic assemblage implies that temperatures and pressures of formation must have exceeded 540°C and 3 kbar, since staurolite is not stable below these values. The lack of cordierite in this sample suggests that temperatures did not exceed 560°C at 3 kbar or 575°C at 4 kbar (Fig. 5.1.3).

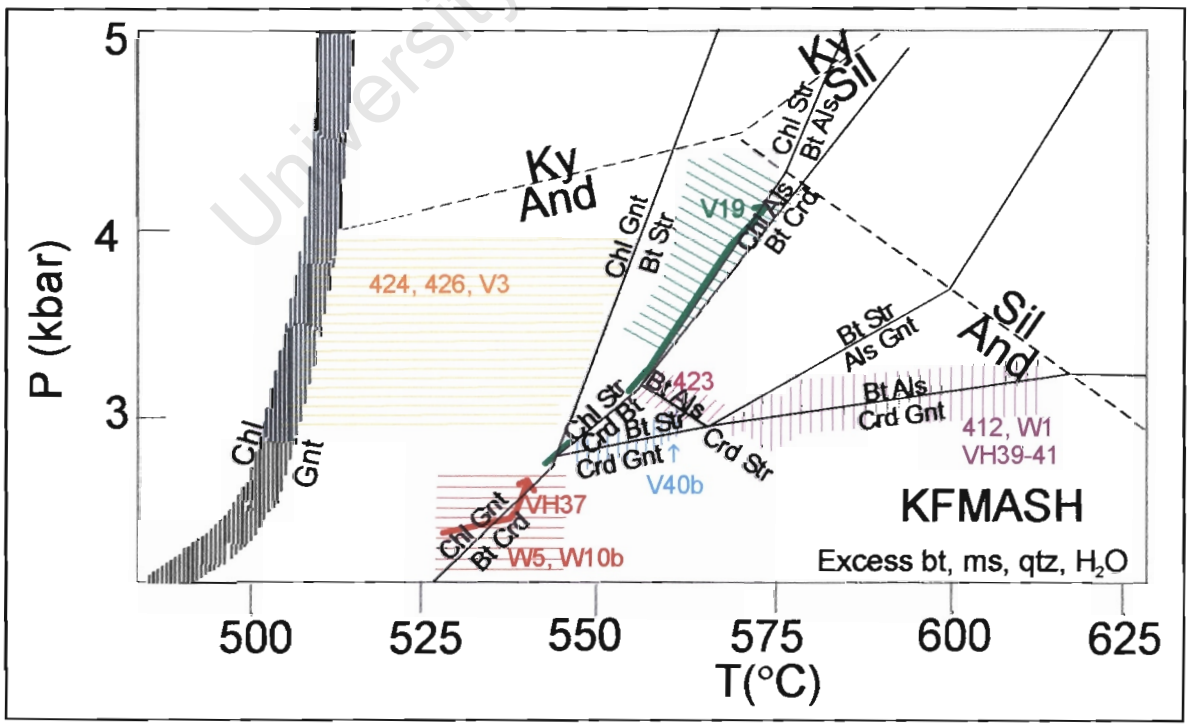

Figure 5.1.3: Petrogenetic grid calculated for garnet, staurolite, cordierite, aluminosilicate and chlorite reactions in the presence of excess biotite, muscovite, quartz and fluid (from Dymoke & Sandiford, 1992). The shaded areas indicate expected stability fields for the samples from this study, according to the peak metamorphic mineral assemblages they display.

In Samples VH37, W5 and W10b the metamorphic assemblages contain cordierite, muscovite, biotite and garnet, where garnet and biotite appear to have grown simultaneously whilst cordierite appears to have grown at the expense of both of these (Figs. 5.1.4.1 & 2). This suggests growth via the reaction Chl + Grt + Bt = Crd + Bt + Ms, which provides a pressure, temperature estimate of 525-545°C at 2-3 kbar when plotted on the Dymoke & Sandiford (1992) KFMASH grid (Fig. 5.1.3) and correlates well with the M1b metamorphic assemblages of Gibson & Wallmach (1995). VH37 is likely to have formed at the lower-end of this field in consideration of the small amount of cordierite observed in it, whereas W10b is more likely to have equilibrated at the upper-end of the field since it contains abundant cordierite and muscovite.

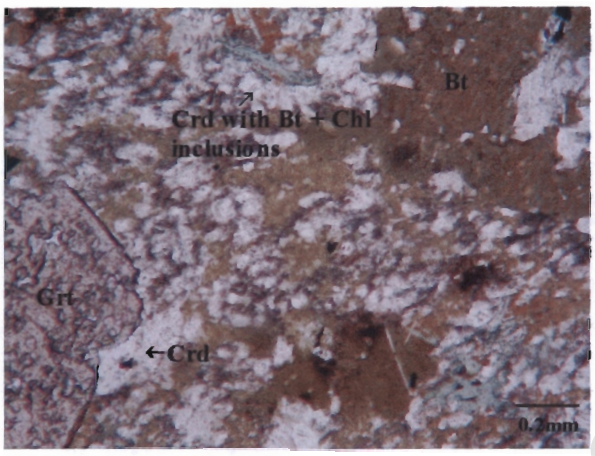

Figure 5.1.4.1: Sample VH37, note the textural relationship between cordierite and both garnet and biotite, in both cases cordierite appears to be consuming them.

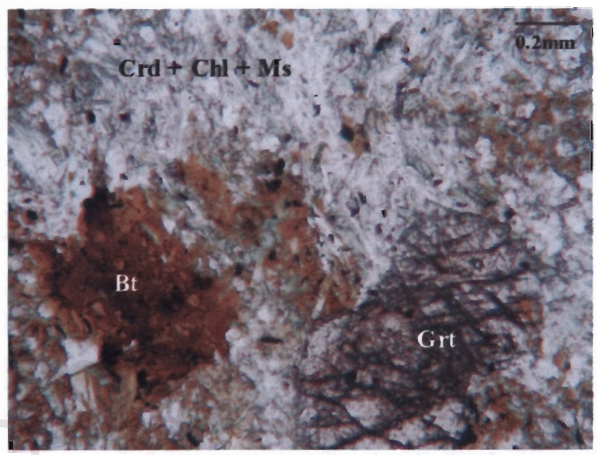

Figure 5.1.4.2: Sample W10b, biotite and garnet enclosed within cordierite, which is rich in muscovite and chlorite.

Related to the above assemblages are those found in samples 412, W1 and VH39-41. Due to the presence of prograde andalusite in the latter samples, they will have equilibrated at higher grade conditions than those experienced by the samples lacking andalusite. The observation of andalusite and biotite growing within cordierite grains suggests that these rocks equilibrated in the region of P-T conditions which support the reaction, Crd + Ms (+ Grt) = And + Bt (Fig. 5.1.3). The upper limits for both pressure and temperature are constrained by the fact that andalusite is the aluminous phase present and not sillimanite, and are constrained to less than 620°C at less than 4 kbar. The presence of andalusite also implies a lower limit of 3 kbar pressure, whilst the lack of staurolite as the product of Crd + Ms implies that temperatures were in excess of 560°C. As for sample V25, samples W1 and VH41 provide evidence that the peak metamorphic event preceded the shock event, in the form of pseudotachylite veins which cross-cut and displace garnet and biotite grains (Fig. 5.1.5.1). However, the majority of cordierite observed in these samples displays similar characteristics to M1b cordierite of Gibson & Wallmach (1995) (Crd poikiloblasts overgrowing peak assemblage, associated with fine-grained biotite aggregates), and is observed to overgrow pseudotachylite (Figs. 5.1.5.2 & 3).

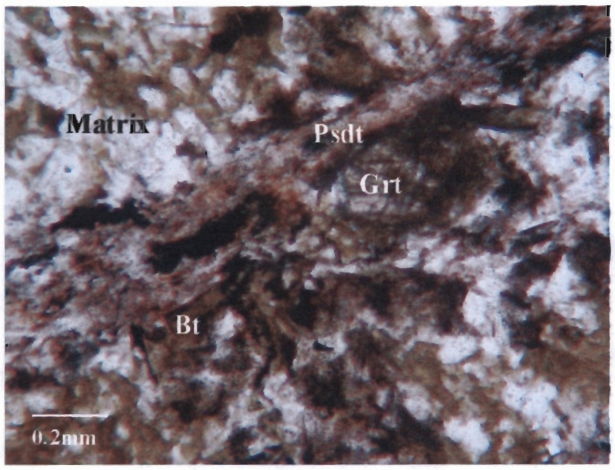

Figure 5.1.5.1: Pseudotachylite cross-cutting garnet, biotite and the matrix assemblage of sample VH41.

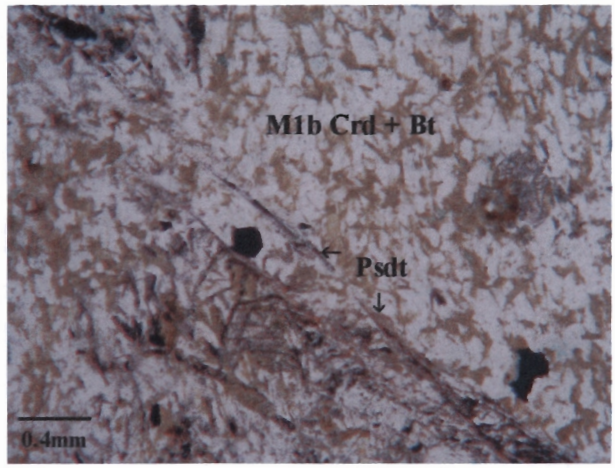

Figure 5.1.5.2: M1b cordierite overgrowing pseudotachylite in sample W1

The peak metamorphic assemblage of Sample 423 includes biotite, cordierite, andalusite, and staurolite. This assemblage is likely to have stabilized in the pink shaded area on the petrogenetic grid of Dymoke & Sandiford (1992) since in places all the phases appear to have grown simultaneously, probably by the reaction of muscovite and chlorite:

$$Chl + Ms + Qtz \rightarrow Crd + Str$$
$$Chl + Ms + Qtz \rightarrow And + Bt$$

The reaction of Chl + Ms to produce cordierite is evidenced by the large number of chlorite and muscovite inclusions in cordierite. The P-T field over which both such reactions could have been operating simultaneously is very small: 550-570°C at pressures greater than 3 kbar. However, the retrograde reaction And + Bt = Crd + Str appears to have been operative at some later stage since both staurolite and cordierite are observed growing between andalusite and biotite grains (Fig. 5.1.6.1), in other places cordierite has completely pseudomorphed andalusite (Fig. 5.1.6.2 & 3) and poorly formed staurolite is seen in the rims of such relict andalusite grains (Fig. 3.2.21). This sample, therefore, provides evidence of the polymetamorphism experienced by these rocks, with minerals of the peak metamorphic event still present (large porphyroblasts of andalusite and biotite), but exhibiting retrograde textures and overgrown by a later prograde assemblage (Crd).

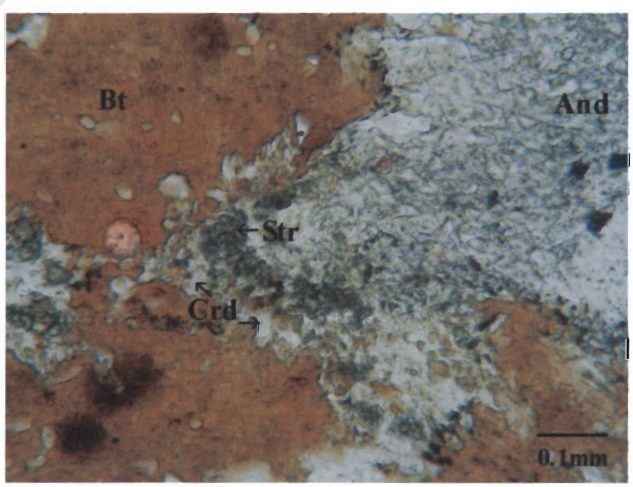

Figure 5.1.6.1: Enlarged portion of Fig. 3.2.19, illustrating the presence of cordierite and staurolite beginning to form where biotite and andalusite were previously in contact.

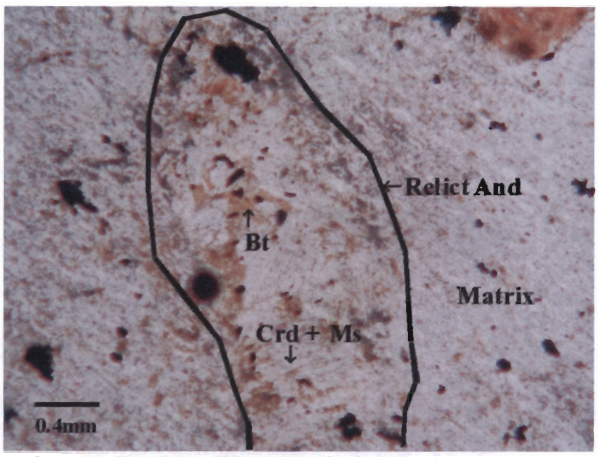

Figure 5.1.6.2: Plane polarised photomicrograph displaying a relict andalusite grain which has been pseudomorphed by cordierite + muscovite in sample 423. Small grains of staurolite are not observed in this grain, but are present in other similar grains (see Fig. 3.2.21).

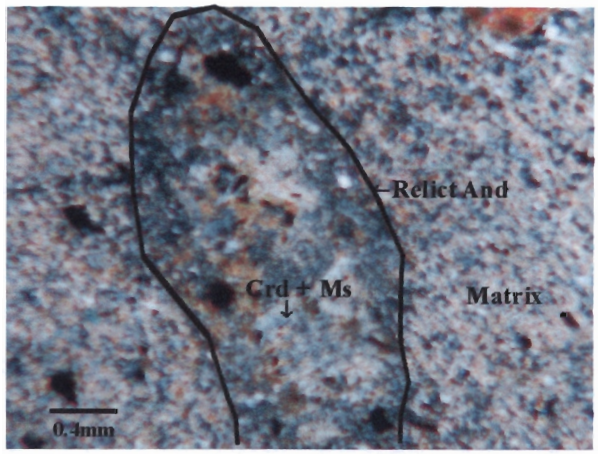

Figure 5.1.6.3: Cross polarised photomicrograph displaying a relict andalusite grain which has been pseudomorphed by cordierite + muscovite in sample 423.

The peak metamorphic assemblage observed in sample V40b suggests that this rock equilibrated in the area of the Dymoke and Sandiford (1992) P-T grid defined by the area surrounding reaction line Bt + Str = Crd + Grt. In sample V40b we observe areas where all four of the phases which define the peak metamorphic assemblage appear to have grown simultaneously (Fig. 3.2.23). We also observe an intricate relationship between staurolite, cordierite, muscovite and chlorite in a small portion of the sample, suggesting that the reaction Ms + Chl → Crd + Bt + St may have produced the peak metamorphic minerals. Due to the shallow slope of the reaction line Bt + Str = Crd + Grt up temperature only a small change in temperature could induce the consumption of biotite + staurolite in producing cordierite + garnet. The peak metamorphic assemblage described above is cross-cut by pseudotachylite (Fig. 5.1.7.1). Cordierite is also observed in a different form where it surrounds staurolite in the vicinity of biotite, into which it grows producing embayments (Fig. 5.1.7.2, Fig. 3.2.24). This type of cordierite is part of the later prograde metamorphic assemblage (M1b, after Gibson & Wallmach, 1995) which is post-impact as evidenced by pseudotachylite being truncated by it in this sample (Fig. 5.1.7.1 & 3).

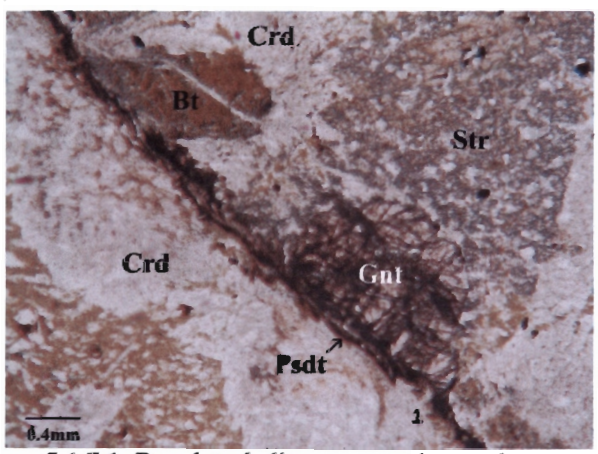

Figure 5.1.7.1: Pseudotachylite cross-cutting peak metamorphic minerals; garnet, biotite & staurolite in sample V40b. Cordierite is of the M1b type, seen to replacing biotite and to be overgrowing pseudotachylite at 1.

In light of the estimated P-T fields derived for the various metamorphic assemblages from the position of key reactions on the Dymoke & Sandiford (1992) petrogenetic grid, we will now consider the thermometric calculations of temperatures at which the minerals equilibrated. Mineral composition data acquired for garnet, chlorite, biotite and cordierite are applied to relevant geothermometers to provide P-T constraints on the environment under which these metamorphic minerals equilibrated.

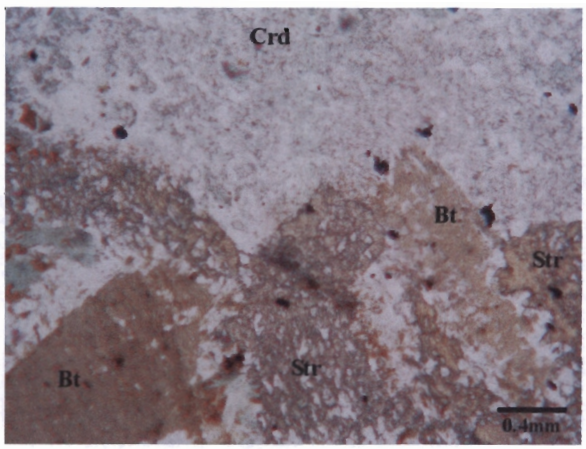

Figure 5.1.7.2: Cordierite replacing biotite and staurolite in sample V40b, see how cordierite overgrows the other minerals and creates embayments in the minerals it is replacing.

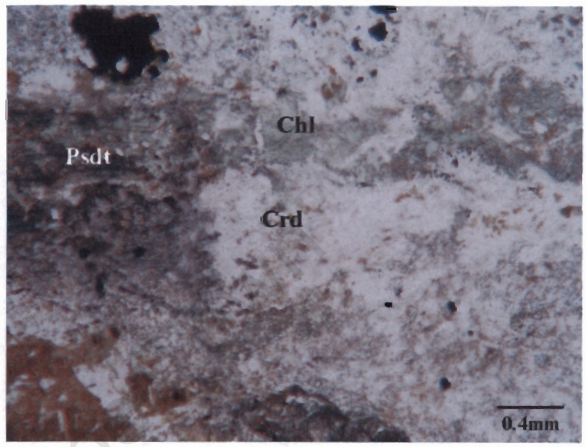

Figure 5.1.7.3: Cordierite seen to be overgrowing pseudotachylite in sample V40b.

Table 5.1.1 displays temperatures calculated using the Ferry & Spear (1978) garnet-biotite geothermometer at 4.0 kbar for samples 412, VH40, W5 and W10b. In samples 412 and W5 temperatures calculated using garnet core compositions are lower than for those using rim compositions, thus we know that garnet grew during prograde heating and it is likely that the rims experienced a retrograde Fe-Mg exchange with biotite. In sample 412 garnet and biotite analysed from within a cordierite grain produce temperatures similar to those obtained for rim compositions of garnets within the matrix, which suggests that the peak metamorphic minerals in this sample (garnet and biotite) have experienced retrograde re-equilibration with M1b cordierite and Fe-Mg exchange with minerals of the matrix. In sample VH40 the opposite trend is observed, this suggests that garnet observed within cordierite has experienced retrograde Fe-Mg exchange with cordierite, but that garnet found within the matrix has been less susceptible to the effects of retrogression and maintained their peak compositions. Sample W10b exhibits both scenarios. From previous studies (Gibson & Wallmach, 1995; Gibson, 1997), we know that the peak metamorphic assemblages for these rocks were formed under pressure conditions in the range 3.0-4.0 kbar at temperatures approximately 100°C higher than the temperatures calculated here. This suggests that the garnets and biotites analysed in this study have experienced retrograde re-equilibration most likely associated with the growth of the M1b (Gibson & Wallmach, 1995) assemblage.

Sample	Fe	Mg	Mg/Fe		Fe	Mg	Mg/Fe	Kd	ln Kd	T(K)	T(°C)
412											
Gnt 1.4 (core)	5.136	0.362	0.070	**Bt 4.2**	3.079	1.662	0.540	0.131	-2.036	751	478
Gnt 1.2 (rim)	4.971	0.364	0.073	**Bt 4.2**	3.079	1.662	0.540	0.136	-1.998	761	488
Gnt 2.4	5.009	0.293	0.058	**Bt 2.2**	3.085	1.337	0.433	0.135	-2.003	760	487
Gnt 2.4	5.009	0.293	0.058	**Bt 3.3**	3.139	1.397	0.445	0.131	-2.029	752	479
Gnt 4.3 (core)	4.718	0.302	0.064	**Bt 4.2**	3.079	1.662	0.540	0.119	-2.132	726	453
Gnt 4.1 (rim)	5.200	0.382	0.073	**Bt 4.2**	3.079	1.662	0.540	0.136	-1.994	762	489
VH40											
Gnt 1	4.390	0.356	0.081	**Bt 1.1**	2.655	1.949	0.734	0.110	-2.203	708	435
Gnt 4.2 (core)	4.398	0.392	0.089	**Bt 4.2**	2.644	1.960	0.741	0.120	-2.118	729	456
Gnt 4.5 (rim)	4.427	0.335	0.076	**Bt 4.2**	2.644	1.960	0.741	0.102	-2.282	690	417
Gnt 5.3 (core)	4.346	0.374	0.086	**Bt 4.2**	2.644	1.960	0.741	0.116	-2.153	720	447
Gnt 5.4 (rim)	4.584	0.323	0.070	**Bt 4.2**	2.644	1.960	0.741	0.095	-2.353	674	401
W5											
Gnt 1a.2 (core)	4.357	0.330	0.076	**Bt 1.4**	2.884	1.670	0.579	0.131	-2.034	751	478
Gnt 1a.1 (rim)	4.673	0.393	0.084	**Bt 1.4**	2.884	1.670	0.579	0.145	-1.929	780	507
Gnt 1b.1 (rim)	4.632	0.394	0.085	**Bt 1.4**	2.884	1.670	0.579	0.147	-1.918	783	510
Gnt 2a.1 (rim)	4.622	0.462	0.100	**Bt 2.5**	2.965	1.667	0.562	0.178	-1.727	843	570
Gnt 2b	4.611	0.383	0.083	**Bt 2.5**	2.965	1.667	0.562	0.148	-1.912	785	512
Gnt 3a.2 (core)	4.235	0.356	0.084	**Bt 3.2**	2.923	1.666	0.570	0.147	-1.914	785	512
Gnt 3a.1 (rim)	4.769	0.412	0.086	**Bt 3.2**	2.923	1.666	0.570	0.152	-1.887	793	520
Gnt 3b	4.735	0.377	0.080	**Bt 3.2**	2.923	1.666	0.570	0.140	-1.968	769	496
W10b											
Gnt 2b (core)	4.649	0.283	0.061	**Bt 2.2**	2.913	1.528	0.525	0.116	-2.154	720	447
Gnt 2b (rim)	4.738	0.316	0.067	**Bt 2.2**	2.913	1.528	0.525	0.127	-2.062	744	471
Gnt 3 (core)	4.412	0.322	0.073	**Bt 3.2**	2.892	1.527	0.528	0.138	-1.979	766	493
Gnt 3 (rim)	4.640	0.318	0.069	**Bt 3.2**	2.892	1.527	0.528	0.130	-2.042	749	476

Table 4.3.1: Temperatures calculated for peak metamorphic assemblage equilibration at 4.0 kbar using the Ferry and Spear (1978) garnet-biotite geothermometer where $\ln K_d = -2109/T(K) + 0.782$ and $K_d = (Mg/Fe)_{grt}/(Mg/Fe)_{bt}$.

In Table 5.1.2 the garnet-chlorite geothermometer of Dickenson & Hewitt (1986) is used to calculate temperatures for samples 412, VH40, V25, W5 and W10b at 4.0kbar. In samples 412, W5 and V25 the same trend is observed for temperatures calculated using garnet core and rim compositions for garnets in the matrix, as for garnet-biotite thermometry with rim compositions giving higher temperatures. However, in sample 412 temperatures calculated for garnet and chlorite found as inclusions within cordierite are lower (444-449°C) than for those found in the matrix (448-472°C) (Table 5.1.2). This suggests that chlorite and garnet found within cordierite experienced a retrograde re-equilibration with the host cordierite. In sample V25 garnet and chlorite found within a quartz vein show a slightly lower temperature than for garnet rim compositions in the bulk rock, which suggests they experienced chemical re-equilibration with the infiltrating Si-rich fluid. Trends in the garnet-chlorite thermometry of samples VH40 and W10b are similar to temperatures obtained from garnet-biotite thermometry, only ~20°C lower. All temperatures obtained from garnet-chlorite calculations are ~20° lower than for temperatures calculated from garnet-biotite thermometry and ~100°C lower than for that of the peak metamorphic assemblages, as calculated by Gibson & Wallmach (1995). This suggests that all chlorite analysed is retrograde.

Sample	Fe	Mg	Mg/Fe		Fe	Mg	Mg/Fe	Kd	ln Kd	T(K)	T(°C)
412											
Gnt 1.8 (core)	5.136	0.362	0.070	**Chl 4.3**	5.341	3.482	0.652	0.108	-2.225	733	460
Gnt 1.5 (rim)	4.667	0.336	0.072	**Chl 4.3**	5.341	3.482	0.652	0.110	-2.203	739	466
Gnt 2.4	5.009	0.293	0.058	**Chl 2.1**	5.640	3.166	0.561	0.104	-2.261	722	449
Gnt 2.4	5.009	0.293	0.058	**Chl 3.3**	5.475	3.131	0.572	0.102	-2.280	717	444
Gnt 4.3 (core)	4.843	0.328	0.068	**Chl 4.3**	5.341	3.482	0.652	0.104	-2.264	721	448
Gnt 4.1 (rim)	5.200	0.382	0.073	**Chl 4.3**	5.341	3.482	0.652	0.113	-2.183	745	472
VH40											
Gnt 1	4.390	0.356	0.081	**Chl 2.2**	4.700	4.200	0.894	0.091	-2.400	684	411
Gnt 4.3 (core)	4.398	0.392	0.089	**Chl 2.2**	4.700	4.200	0.894	0.100	-2.305	709	436
Gnt 4.6 (rim)	4.446	0.350	0.079	**Chl 2.2**	4.700	4.200	0.894	0.088	-2.429	677	404
Gnt 5.4 (core)	4.346	0.374	0.086	**Chl 5..2**	4.760	4.229	0.888	0.097	-2.334	701	428
Gnt 5.6 (rim)	4.584	0.323	0.070	**Chl 5..2**	4.760	4.229	0.888	0.079	-2.534	651	378
V25											
Gnt 1.4	4.543	0.723	0.159	**Chl 2.2**	3.991	4.970	1.245	0.128	-2.057	786	513
Gnt 3.3 (core)	4.307	0.553	0.128	**Chl 3.2**	3.548	5.038	1.420	0.090	-2.403	683	410
Gnt 3.5 (rim)	4.414	0.857	0.194	**Chl 3.2**	3.548	5.038	1.420	0.137	-1.990	809	536
Gnt 4.4 (core)	4.272	0.379	0.089	**Chl 4.1**	3.695	5.286	1.431	0.062	-2.780	598	325
Gnt 4.1 (rim)	4.587	0.668	0.146	**Chl 4.1**	3.695	5.286	1.431	0.102	-2.285	715	442
Gnt 5.2 (core)	4.278	0.455	0.106	**Chl 5.2**	3.623	5.414	1.494	0.071	-2.643	627	354
Gnt 5.1 (rim)	4.498	0.915	0.203	**Chl 5.2**	3.623	5.414	1.494	0.136	-1.994	808	535
W5											
Gnt 1a.2 (core)	4.357	0.330	0.076	**Chl1.1**	5.054	3.713	0.735	0.103	-2.272	719	446
Gnt 1a.1 (rim)	4.673	0.393	0.084	**Chl1.1**	5.054	3.713	0.735	0.114	-2.167	750	477
Gnt 1b.3 (rim)	4.632	0.394	0.085	**Chl1.1**	5.054	3.713	0.735	0.116	-2.156	753	480
W10b											
Gnt 2b (core)	4.649	0.283	0.061	**Chl 2.2**	5.369	3.428	0.638	0.095	-2.350	697	424
Gnt 2b (rim)	4.738	0.316	0.067	**Chl 2.2**	5.369	3.428	0.638	0.104	-2.259	723	450
Gnt 3 (core)	4.412	0.322	0.073	**Chl 1.2**	5.481	3.334	0.608	0.120	-2.120	765	492
Gnt 3 (rim)	4.640	0.318	0.069	**Chl 1.2**	5.481	3.334	0.608	0.113	-2.183	745	472

Table 5.1.2: Temperatures calculated for metamorphic assemblages euilibrated at 4.0kbar using the Dickenson and Hewitt (1986) garnet-chlorite geothermometer, where ln K_d = -1815/T(K)-0.253 and K_d = $(Mg/Fe)_{gnt}/(Mg/Fe)_{chl}$.

Temperatures calculated from the garnet-cordierite geothermometer of Perchuk & Lavrent'eva (1981) (487-561°C) (Table 5.1.3) for samples 412 and VH40 indicate that in both cases the temperatures obtained from garnet-biotite and garnet-chlorite thermometry are 20-50°C lower than that obtained for prograde cordierite. This suggests that biotite and garnet experienced retrogression prior to the formation of M1b cordierite and that chlorite was formed as a product of such retrogression associated with cooling and that each of these minerals then experienced further retrogression during the formation of M1b cordierite.

Sample	Mg	Fe	Mg/Fe		Mg	Fe	Mg/Fe	Kd	ln Kd	T(K)	T(°C)
412											
Gnt1.4 (core)	0.362	5.136	0.070	**Crd3.1**	0.951	1.027	0.926	13.144	2.576	809	536
Gnt1.4 (core)	0.362	5.136	0.070	**Crd3.2**	0.939	1.017	0.923	13.102	2.573	810	537
Gnt1.8 (rim)	0.336	4.667	0.072	**Crd3.1**	0.951	1.027	0.926	12.868	2.555	814	541
Gnt1.8 (rim)	0.336	4.667	0.072	**Crd3.2**	0.939	1.017	0.923	12.827	2.552	815	542
Gnt2.4	0.293	5.009	0.058	**Crd2**	0.946	1.063	0.890	15.207	2.722	780	507
Gnt2.4	0.293	5.009	0.058	**Crd2.1**	0.916	1.030	0.889	15.206	2.722	780	507
Gnt4.3 (core)	0.328	4.843	0.068	**Crd3.1**	0.951	1.027	0.926	13.678	2.616	801	528
Gnt4.3 (core)	0.328	4.843	0.068	**Crd3.2**	0.939	1.017	0.923	13.636	2.613	802	529
Gnt4.1 (rim)	0.382	5.2	0.073	**Crd3.1**	0.951	1.027	0.926	12.611	2.535	818	545
Gnt4.1 (rim)	0.382	5.2	0.073	**Crd3.2**	0.939	1.017	0.923	12.571	2.531	819	546
VH40											
Gnt1	0.356	4.39	0.081	**Crd3.1**	1.035	0.916	1.130	13.937	2.635	797	524
Gnt1	0.356	4.39	0.081	**Crd3.2**	1.017	0.972	1.047	12.910	2.558	813	540
Gnt1	0.356	4.39	0.081	**Crd3.3**	1.023	0.860	1.189	14.664	2.685	787	514
Gnt4.3 (core)	0.392	4.398	0.089	**Crd3.1**	1.035	0.916	1.130	12.680	2.540	817	544
Gnt4.3 (core)	0.392	4.398	0.089	**Crd3.2**	1.017	0.972	1.047	11.746	2.464	834	561
Gnt4.3 (core)	0.392	4.398	0.089	**Crd3.3**	1.023	0.860	1.189	13.342	2.591	806	533
Gnt4.6 (rim)	0.35	4.446	0.079	**Crd3.1**	1.035	0.916	1.130	14.357	2.664	791	518
Gnt4.6 (rim)	0.35	4.446	0.079	**Crd3.2**	1.017	0.972	1.047	13.299	2.588	807	534
Gnt4.6 (rim)	0.35	4.446	0.079	**Crd3.3**	1.023	0.860	1.189	15.106	2.715	781	508
Gnt5.4 (core)	0.374	4.346	0.086	**Crd3.1**	1.035	0.916	1.130	13.133	2.575	810	537
Gnt5.4 (core)	0.374	4.346	0.086	**Crd3.2**	1.017	0.972	1.047	12.166	2.499	826	553
Gnt5.4 (core)	0.374	4.346	0.086	**Crd3.3**	1.023	0.860	1.189	13.819	2.626	799	526
Gnt5.6 (rim)	0.323	4.584	0.070	**Crd3.1**	1.035	0.916	1.130	16.040	2.775	770	497
Gnt5.6 (rim)	0.323	4.584	0.070	**Crd3.2**	1.017	0.972	1.047	14.858	2.699	785	512
Gnt5.6 (rim)	0.323	4.584	0.070	**Crd3.3**	1.023	0.860	1.189	16.877	2.826	760	487

Table 5.1.3: Temperatures calculated for metamorphic assemblages equilibrated at 4.0kbar using the Perchuk & Lavrent'eva (1981) garnet-cordierite thermometer, where RT ln K_d = 1000/T – 0.41155 and $K_d = (Mg/Fe)_{Crd}/(Mg/Fe)_{Grt}$.

The results of P-T constraints calculated both from placement of samples on the petrogenetic grid of Dymoke & Sandiford (1992) according to their peak metamorphic assemblages identified through petrographic analysis, and from calculation using geothermometers based on their metamorphic mineral compositions, are summarised in Table 5.1.4.

Since all of the temperatures calculated from thermometry provide estimates lower than we expect for the peak metamorphic assemblages, it is clear that all garnet and biotite have experienced re-equilibration and retrogression associated with the younger post-shock metamorphism. All chlorite grains analysed are retrograde and are likely to have grown during M1b since they are mostly observed replacing kink-banded biotite. Cordierite is the major mineral identified within the M1b assemblage providing temperatures in the range 500-545°C for the post-shock metamorphism, which correlates well with temperatures calculated by Gibson & Wallmach (1995) for this assemblage (500-525°C).

Sample	Peak Metamorphic assemblage	P-T estimate according to position on (D&S) petrogenetic grid	T estimate from geothermometry calculations	Reference
411	Qtz + Ms + Chl + Bt	3.5kbar, <420°C		Bt-in melting curve
424/426 V3	Grt + Bt + Qtz	3.5kbar, >420°C		Grt stability
VH37	Grt + Bt + Crd + Chl	2.5 – 3.0 kbar, 525-545°C		
W5	Grt + Bt + Crd + Chl	2.5 – 3.0 kbar, 525-545°C	4.0 kbar, 493-567°C 4.0 kbar, 477-480°C	Grt-Bt (F&S, 1978) Grt-Chl (D&H, 1986)
W10b	Grt + Bt + Crd + Chl	2.5 – 3.0 kbar, 525-545°C	4.0 kbar, 445-490°C 4.0 kbar, 424-491°C	Grt-Bt (F&S, 1978) Grt-Chl (D&H, 1986)
422	Ep + Act + Grt			
V25	Qtz + Chl + Grt ± Hbl	* 2.0 kbar, >550°C	4.0 kbar, 442-536°C	Grt-Chl (D&H, 1986)
VH40/ VH39/ VH41	Grt + Crd + Bt + And	3.0-4.0 kbar, 570-620°C	4.0 kbar, 433-454°C 4.0 kbar, 411-436°C 4.0 kbar,487-561°C	Grt-Bt (F&S, 1978) Grt-Chl (D&H, 1986) Grt-Crd (P&L, 1981)
V19	Qtz + Bt + And + Str	3.0-4.0 kbar, 540-560°C		
423	Qtz + Chl + Bt + And + Str + Crd	3.0 kbar, 540-560°C		
V40b	Qtz + Chl + Bt + Grt + Str + Crd	3.0 kbar, 540-560°C		
412	Grt + Crd + Bt + And	3.0-4.0 kbar, 570-620°C	4.0 kbar, 480-486°C 4.0 kbar, 465-472°C 4.0 kbar, 506-546°C	Grt-Bt (F&S, 1978) Grt-Chl (D&H, 1986) Grt-Crd (P&L, 1981)
W1	Grt + Crd + Bt + And	3.0-4.0 kbar, 570-620°C		

Table 5.1.4: Summary of metamorphic assemblage P-T conditions as derived from petrogenetic grids and thermobarometry calculations, for samples from the collar of the Vredefort dome. * From Akella & Winkler (1996) P-T grid.

5.2 THE ARCHEAN BASEMENT COMPLEX ROCKS

The metamorphism of the Archean basement complex has largely been ascertained from the metamorphic textures and features displayed in the metapelitic granulites, due to the fact that igneous rocks such as granitoids, trondjhemites and tonalites don't reflect metamorphic changes in their constituent minerals which are formed from melts and are relatively stable at high pressures and temperatures. The gneisses do, however, exhibit shock deformation features which allow us to assume they have been exposed to, and altered by some of the metamorphic events which have been recorded by the metapelites, detailed by Stevens *et al.* (1997a) and Gibson (2002). The three-stage metamorphic history Stevens *et al.* (1997a) identified include an M1 peak metamorphic event estimated to have equilibrated at temperatures in excess of 900°C at approximately 5.0 kbar, a younger high-grade M2 retrograde event, likely to have been produced at temperatures in the region of 650°C and at similar pressures to the M1 event, and lastly a post-shock M3 event constrained to a P-T field of formation in the range 680-<900°C at 2.5 kbar. Gibson (2002) have since suggested that the M2 and M3 assemblages of Stevens *et al.* (1997a) are in fact a static metamorphic overprint of the M1 assemblage associated with rapid isobaric cooling followed by shock heating and exhumation during the 2.02 Ga impact event. They estimate maximum temperatures associated with the almost instantaneous heating and exhumation of the structure to be in the region of 900°C in the centre of the structure, and 775 ± 50°C at ~6 km from the centre.

CHAPTER 6
OXYGEN ISOTOPE DATA

6.1 INTRODUCTION

In nature various elements occur as a number of isotopes, which means that the atoms of such an element will all have the same number of protons but may have differing numbers of neutrons. In the case of oxygen, three isotopes have been identified, namely ^{16}O, ^{17}O and ^{18}O. These isotopes are considered to be stable because they do not exhibit radioactive decay at a detectable level. The relative abundances of these isotopes as observed in nature are 99.763%, 0.0375% and 0.1995%, respectively (Anders & Grevesse, 1989). Due to their slight physical and chemical differences, the isotopes partition differently into various phases. The latter phenomenon is termed isotope fractionation and, as a consequence of this process and the relative abundances of the oxygen isotopes, the ratio $^{18}O/^{16}O$ is important from a geological perspective.

Due to the fact that it easier to measure relative differences in isotopic ratios, rather than absolute abundances, standards of accurately known isotope ratios are used as references for stable isotope measurements. This means that the ratio of $^{18}O/^{16}O$ in the sample is measured relative to $^{18}O/^{16}O$ of the standard, which is much more accurate than trying to measure an absolute ratio for the sample. Therefore, stable isotope ratios are expressed using delta (δ) notation (Urey, 1947):

$$\delta_{(sample)} = [(R_{sample} - R_{standard})/R_{standard}] \times 1000,$$

where R = the measured isotope ratio, in this case $^{18}O/^{16}O$. δ values are given in per mil units ($^{o}/_{oo}$), which is equivalent to parts per thousand.

The internationally agreed-upon standards used for the oxygen isotope system are Standard Mean Ocean Water (SMOW) (Craig, 1961) and Pee Dee Belemnite (PDB) (O'Neil, 1986). SMOW has historically been used in igneous and metamorphic rock systems, and PDB for carbonate sedimentary rocks. In the laboratory we measure the isotope ratio of the sample relative to an arbitrary reference gas, for which we know the value of its ratio relative to SMOW. Therefore, by running this reference gas standard during the same run as samples, we can calculate the sample delta value relative to SMOW.

The broadly systematic variations displayed in the isotopic compositions of igneous, sedimentary and metamorphic rocks provide insight into their origin and temperature of oxygen isotope equilibration. $^{18}O/^{16}O$ ratios (given in δ notation) are well constrained for a variety of the most common crustal materials and the bulk mantle (Fig. 6.1.1) (Faure, 1986; Hoefs, 1997). Therefore, any perturbations of such ratios indicate that the rock has been exposed to processes capable of initiating further isotope fractionation during its history. The most important processes which give rise to isotope fractionation include equilibrium exchange reactions, processes which involve the continual loss or addition of one phase from or into a system, and kinetic processes (Faure, 1986). Equilibrium exchange reactions involve the distribution of isotopes of a certain element between two or more phases without a net chemical reaction taking place. For such reactions an isotope fractionation factor can be defined as (Friedman & O'Neil, 1977):

$$\alpha_{(X\text{-}Y)} = (^{18}O/^{16}O)_X / (^{18}O/^{16}O)_Y$$

Temperature is a fundamentally important factor in the control of fractionations due to its inverse relationship with the fractionation factor such that (O'Neil, 1986):

$$\ln \alpha \propto 1/T^2$$

As a result of isotopic fractionations being strongly dependant on temperature, the measured differences in stable isotope values between two coexisting minerals can be used to constrain temperatures at which isotope exchange and mineral equilibration probably occurred, providing us with isotope thermometers. The approximation useful for thermometry is:

$$\delta_x - \delta_y = \Delta_{x\text{-}y} = 1000.\ln \alpha_{x\text{-}y},$$

provided $\Delta x\text{-}y < 10‰$. Lists of useful mineral fractionations are given by Chiba *et al.* (1989) and Friedman & O'Neil (1977). Most fractionation curves are expressed as:

$$1000.\ln \alpha_{x\text{-}y} = A(10^6 T^{-2}) + B$$

where A & B are constants.

Therefore, the difference in δ values for two coexisting mineral phases which equilibrated oxygen with a common reservoir is a function of the temperature of equilibration, assuming they did, indeed, reach equilibrium.

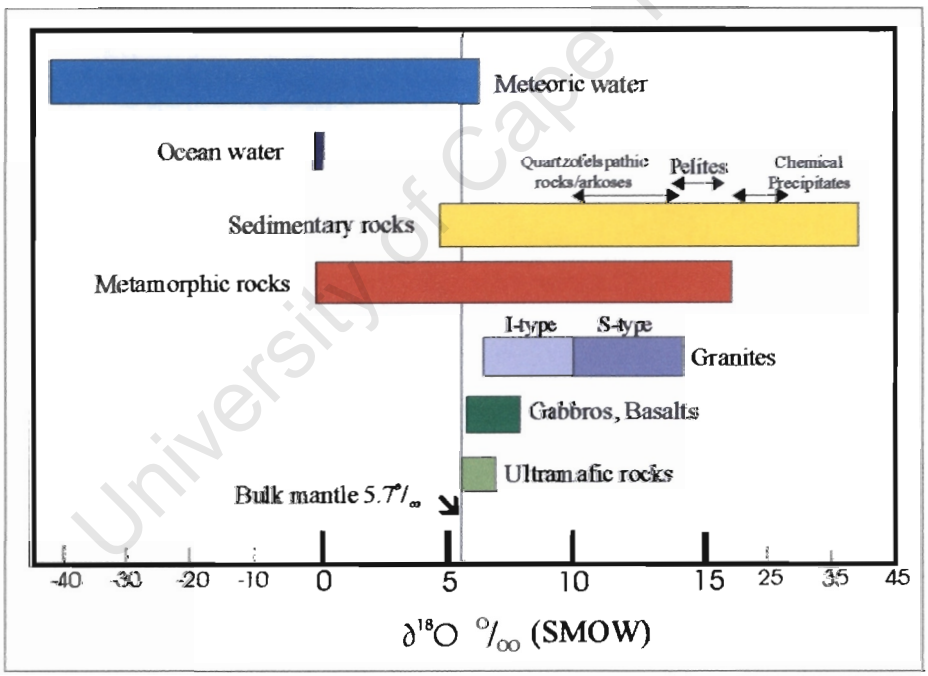

Figure 6.1: Oxygen Isotope values for common geological materials (after Faure, 1986 and Hoefs, 1997).

Processes which involve the loss or addition of phases to/from a system are extremely important for a range of geological processes, especially metamorphism. In the context of this study it is a fundamental consideration because of the pervasive influence of fluids on stable isotope values. Fluid-rock interaction is typically accompanied by isotopic resetting of the rock (Clayton, 1981). Therefore, stable isotope geochemistry can provide useful information about the fluid-rock dynamics in metamorphic settings. Fluids involved in metamorphism can be either externally or internally derived from the rock system under investigation. For open system environments, where crustal fluids interact with the rocks, stable isotope data can provide information such as a probable fluid source, the mode of

fluid flow (either pervasive or channeled) and whether fluid flow occurred under equilibrium or disequilibrium conditions (Faure, 1986). In pelitic rocks, interaction with an external fluid source will often result in the depletion of the oxygen isotope character of the rock, due to the fact that most crustal fluids typically have lower $\delta^{18}O$ values ($\leq$10-12‰) than pelitic rocks (10-30‰) (Hoefs, 1987). Since fractionation factors must be small to initiate $\delta^{18}O$ depletion, it only occurs at high temperatures, thus the stable isotope resetting must occur under hydrothermal conditions. However, the initial fluid must also have a low $\delta^{18}O$ value to facilitate the depletion and is thus more likely to be meteoric rather than magmatic (Sheppard, 1981).

Stable isotope shifts are also observed as a function of fluid-rock interaction, where the fluids are internally derived from, for instance, devolatilization reactions and dehydration reactions during metamorphism . In metapelitic rocks, water is typically liberated through the breakdown of hydrous minerals during prograde metamorphism. Devolatilization reactions result in a positive volume change and, because of the small porosities observed in metamorphic rocks, the fluids derived from the devolitilization reactions are commonly expelled from the rock system. Such fluid loss will be accompanied by a change in $\delta^{18}O$ values of the rock, i.e., an increase or decrease in the $^{18}O/^{16}O$ ratio, and can occur either after oxygen equilibration with the rock as a single pulse or continuously during devolitilization (Valley, 1996). In metapelitic rocks the fluid lost during dehydration can generally be assumed to be pure H_2O and, therefore, the changes in $\delta^{18}O$ will be very small (Valley, 1996). According to Valley (1996), the most important aspect of the resetting of oxygen isotopes during dehydration is the fact that the $\alpha^{18}O_{(fluid\text{-}rock)}$ value is dependent on temperature and in fact changes sign with increasing temperature. This is a function of water being depleted in $\delta^{18}O$ relative to metapelitic bulk compositions at temperatures <400-500°C, but being relatively enriched in $\delta^{18}O$ at temperatures greater than this. Therefore, at lower temperatures, dehydration reactions will result in an increase in whole-rock $\delta^{18}O$ values, but at temperatures above ~500°C they will produce depleted oxygen isotope resettings. Thus, when considering the stable isotope character of metamorphic rocks it is imperative to do so in collaboration with their metamorphic histories because resetting associated with one metamorphic event may indeed cancel out with that of a later or subsequent event.

6.2 METHOD

Oxygen isotope ratios were determined using the silicate isotope line in the Department of Geological Sciences, University of Cape Town, on 10mg of whole rock powder for each sample. The samples were dried overnight prior to loading and were then degassed at 200°C before reacting with ClF_3 to 550°C in Nickel tubes, in order to release the oxygen from the silicates present. The process involved is the same as that for extraction using Bromine pentaflourine (Clayton *et al.*, 1972). Thereafter, the liberated oxygen was passed over a hot carbon rod and converted to CO_2. Ten samples were loaded for every run, of which two were the internal standards of MQ (Murchison Line quartz vein). The raw values of MQ are used to directly recalculate the sample values relative to SMOW, assuming the value of MQ to be 10.10. During the period of sample analysis, the average raw value of MQ was typically 0.1-0.3 ‰ higher than the accepted value relative to SMOW, and therefore all data were corrected such that the MQ for each run equals 10.10. The CO_2 gas collected from each sample was analysed using the dual inlet gas-source

spectrometer (MAT252) in the Archaeology Department, University of Cape Town. Data are reported in the standard δ notation relative to SMOW.

Mineral separates were hand picked under the microscope from sample crushes which had been sieved to separate out the ~2mm grain fractions. The ~95% pure mineral separates were then crushed to a powder using an opal pestle and mortar, in acetone. These were then allowed to dry out overnight before being run through the silicate isotope line in the same manner as described for the whole rock samples.

6.3 THE COLLAR ROCKS

Whole rock oxygen isotope data obtained for samples from the collar of the Vredefort dome are presented in Table 6.3.1. In the collar samples all $\delta^{18}O$ values, except for sample W1, are depleted relative to values obtained for Witwatersrand quartzites (8-10 ‰ from Harris & Watkins, 1990) and what one would expect for metabasic and metapelitic assemblages to display (9-12 ‰) (Faure, 1986) (Fig. 6.1). The majority of the samples exhibit a depletion in the order of 2-4 ‰, ranging from 6-8 ‰, however, samples V34 and 426 display extremely low $\delta^{18}O$ values of 1.3 and 4.61 ‰, respectively. This indicates that the collar rocks have exchanged oxygen with significant quantities of fluid having a relatively low $\delta^{18}O$ value, i.e. meteoric rather than magmatic water.

Sample	Rock type	$\delta^{18}O$ (‰)
VH23	Dominion Gp metalava	6.7
CB1	Lower Witwatersrand Gp metamorphosed BIF	9.8
V35	Government Reef fine-banded oxide-bearing metashale	8.4
V34	Metamorphosed BIF	1.3
424	Government Reef metashale	6.6
426	Government Reef metashale	4.6
421	Government Reef hornfels	6.8
420	Government Reef actinolite hornfels	6.6
422	Government Reef epidotite	6.8
V40b	Government Reef metapelite	6.9
V25	Hospital Hill garnet-chlorite schist	7.2
V19	Government Reef metashale	7.1
412	Hospital Hill metapelite	7.0
423	Hospital Hill metashale	7.9
V3	Hospital Hill garnet-biotite hornfels	6.4
411	Johannesburg Gp metalava	7.8
VH37	Hospital Hill garnet-biotite-cordierite hornfels	8.0
VH39	Hospital Hill garnet-cordierite hornfels	8.2
VH40	Hospital Hill biotite-cordierite hornfels	8.4
VH41	Hospital Hill cordierite hornfels	7.8
K12d	Government Reef biotite-cordierite hornfels	8.6
W1	Hospital Hill metapelite	11.3
W5	Hospital Hill garnet-biotite-cordierite hornfels	7.0
W10b	Hospital Hill garnet-biotite-cordierite hornfels	8.5
W18	Hospital Hill metashale	7.7
W19	Hospital Hill metashale	7.1

Table 6.3.1: Whole rock $\delta^{18}O$ values obtained for the collar rocks of the Vredefort dome.

Since we are dealing with metamorphic rocks, we know they have been exposed to metamorphic fluids produced as a result of dehydration reactions. We are also aware that these rocks have been exposed to the heat and shock effects associated with the impact event, to M1b metamorphism which followed the impact event and the heat liberated from igneous bodies which have intruded into the collar (and associated hydrothermal fluids). Thus, we are aware that they have been exposed to numerous events during which significant fluid-rock interaction may have occurred. From the plot of $\delta^{18}O$ vs. grade of metamorphism (Fig. 6.3.1) we see there is little variation across the main dataset, however, rocks displaying the highest grades of metamorphism show slightly less depletion in $\delta^{18}O$ values compared to rocks displaying lower grades of metamorphism. This would suggest that the oxygen isotope resetting is not associated with metamorphic fluids liberated from these rocks due to dehydration reactions, since we would then expect the most highly metamorphosed rocks to exhibit the greatest depletion in $\delta^{18}O$ values.

$\delta^{18}O$ values have also been plotted as a function of distance from the closest of the large igneous bodies which intruded into the collar rocks, namely the Schurwedraai alkali complex and as a function of distance from the nearest dolerite sills to each sample (Figs. 6.3.2 & 3). None of these plots indicate a general relationship between the $\delta^{18}O$ values of the samples in relation to their distance from these igneous bodies, except for the two samples which display extremely depleted $\delta^{18}O$ values, namely V34 and 426, which are located within 100m of two different igneous intrusions. This suggests that the effect of heat or fluids associated with the igneous intrusions may in fact have affected the oxygen isotope values of rocks on a very local scale, by depleting their oxygen isotope ratio prior to the regional scale event which will have depleted them even further. However, rocks as close as 200m to igneous bodies (samples V19 and 422) do not exhibit such drastic depletions, therefore, factors such as rock porosity and structurally controlled channeled fluid flow should be investigated as possible causes for the randomly large depletions observed.

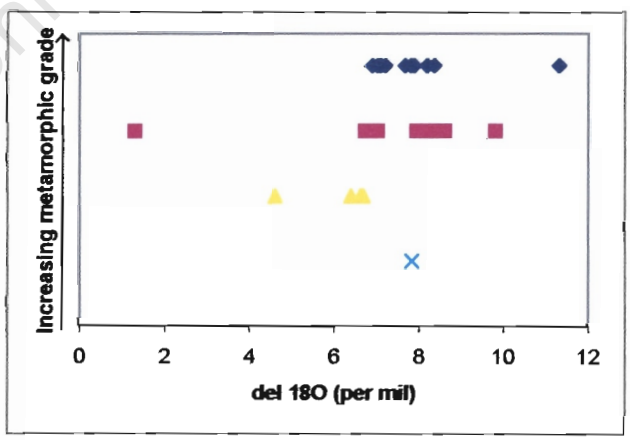

Figure 6.3.1: $\delta^{18}O$ values obtained for the collar samples vs. metamorphic grade displayed by these rocks. ◆ Amphibolite ■ Lower amphibolite ▲ Upper greenschist x Lower greenschist

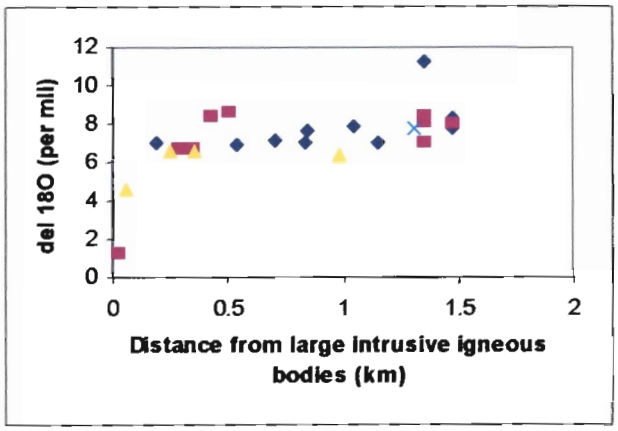

Figure 6.3.2: $\delta^{18}O$ values obtained for the collar samples vs. distance from large intrusive igneous bodies ◆ Amphibolite ■ Lower amphibolite ▲ Upper greenschist x Lower greenschist

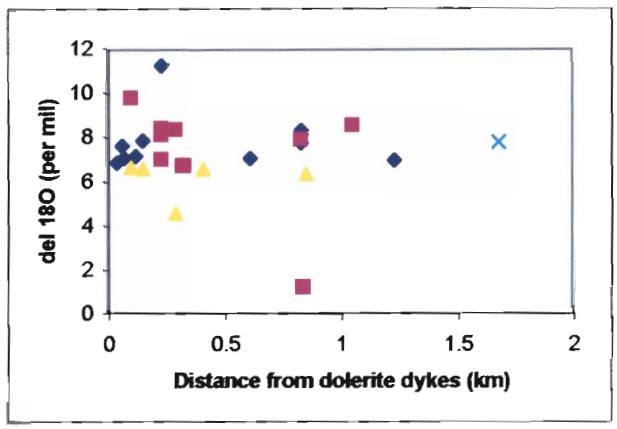

Figure 6.3.3: $\delta^{18}O$ values obtained for the collar samples vs. distance from dolerite sills ◆ Amphibolite ■ Lower amphibolite ▲ Upper greenschist x Lower greenschist

Finally, a plot of $\delta^{18}O$ as a function of distance from the core-collar contact (Fig. 6.3.4) also provides no conclusive evidence concerning the origin of the source responsible for the oxygen isotope resetting observed in the collar rocks. The pervasive nature of the resetting suggests that it is most likely the result of a regional scale event. However, due to the observation of some very highly depleted $\delta^{18}O$ values (V34, 426) and some minimally depleted values (W1), one should not discard the possibility that these rocks have experienced multiple episodes of fluid interaction which have reset their initial $\delta^{18}O$ values progressively to the point that one can no longer discern any single influencing factor on the observed depletion.

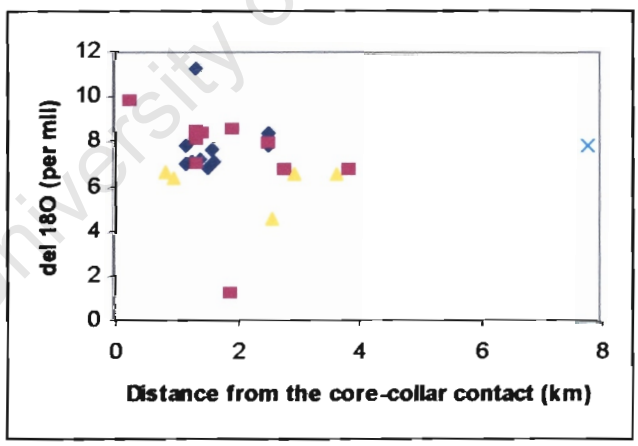

Figure 6.3.4: $\delta^{18}O$ values obtained for the collar samples vs. distance from the core-collar contact ◆ Amphibolite ■ Lower amphibolite ▲ Upper greenschist x Lower greenschist

Low grade metapelitic rocks from the SE quadrant of the dome were analysed in an effort to gain stable isotope data for comparison with metapelitic units analysed both from within the NW quadrant of the dome and the Witwatersrand Basin. They exhibit an even greater depletion in their $\delta^{18}O$ values (Table 6.3.2) in comparison to the collar rocks in the NW quadrant. This suggests that the rocks of the Witwatersrand Basin may have experienced a regional scale event resulting in the depletion of their oxygen isotope values prior to the impact event (since metapelitic units in the basement do not exhibit such depletions) or

that the more highly metamorphosed rocks closer to the centre of the structure may have been less permeable to post-impact fluids.

Sample	$\delta^{18}O$(‰)
QM107	4.5
QM110	4.3
QM132	4.4
QM135	3.4
QM137	6.0
QM140	5.0
QM145	5.8

Table 6.3.2: Table of whole rock $\delta^{18}O$ values obtained for the West Rand Group samples provided by Preston (1998) from the SE quadrant of the Vredefort structure.

6.4 THE ARCHEAN BASEMENT COMPLEX ROCKS

In the Archean basement complex in the core of the dome oxygen isotope data largely reflect values typical of I-type granites in both the OGG and ILG terranes (Table 6.4.1). $\delta^{18}O$ values for OGG rocks range from 8.4-11.5‰, with a mean of 8.9 ± 0.1‰ and ILG tonalites exhibit $\delta^{18}O$ values in the range 8.2-10.8 ‰ with a mean of 9.0 ± 0.1‰. The charnockites also plot in these ranges having $\delta^{18}O$ values of 8.5, 8.7 and 8.3‰ for the samples 435, 436 and 448a, respectively. Figure 6.4.1 plots whole rock data as a function of distance from the core-collar contact. From this plot it is obvious that there is very little difference in the range of $\delta^{18}O$ values for the OGG and ILG rocks, with the majority of $\delta^{18}O$ values plotting in the range 8.5-9.5 ‰, and that there is no or little observed variation across the OGG-ILG transition zone.

Sample	Rock type	$\delta^{18}O$ (‰)
438	OGG	9.3
439	OGG	11.5
440	OGG	9.2
441	OGG	8.8
442	OGG	9.7
443	OGG	8.6
444	OGG	8.4
437	OGG	11.1
434	OGG	9.2
433	ILG	9.5
432	OGG	8.9
430	Dolerite	6.8
431	OGG	8.8
428	ILG	8.8
429	ILG	9.0
435	ILG charnockite	8.5
436	ILG charnockite	8.7

Sample	Rock type	$\delta^{18}O$ (‰)
445	ILG	10.8
446	ILG	8.6
447	ILG	9.2
448	ILG	8.3
449	ILG	8.2
450	ILG	8.4
451	ILG	8.7
452	ILG	9.6
454b	ILG	8.7
455a	ILG	8.5
455b	ILG	9.3
461	ILG	10.2
460	ILG	8.9
459	ILG	9.1
458	ILG	8.9
457	ILG	9.3
456c	ILG	9.6

Table 6.4.1: Whole rock $\delta^{18}O$ values for the Archean basement complex rocks from the core of the Vredefort dome.

The oxygen isotope data plotted as a function of their Si-content (Fig. 6.4.2) do not support the observation of the section under study providing a section of fractionally differentiated crust from upper crustal levels in the OGG to mid-crustal levels in the ILG. This has been shown for other crustal sections (Chivas *et al.*, 1982) where an increase in $\delta^{18}O$ correlates with an increase in Silica content for more differentiated crust.

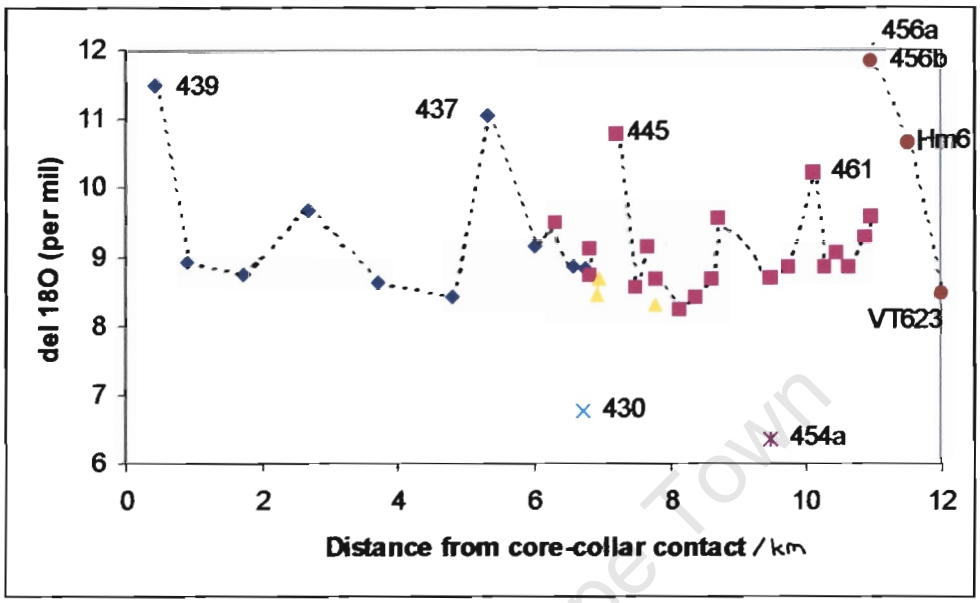

Figure 6.4.1: Plot of $\delta^{18}O$ vs. distance from the core-collar contact for samples from the core of the Vredefort dome ◆ OGG ■ ILG ▲ charnockites x dolerite ✳ mafic granulite ● metapelitic restites and migmatites.

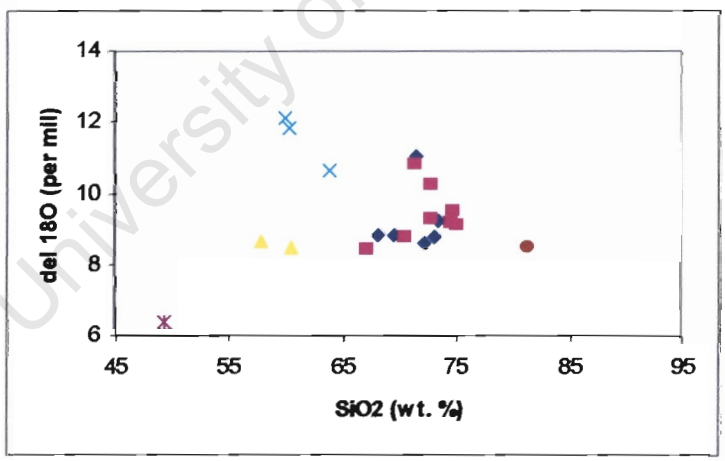

Figure 6.4.2: Plot of $\delta^{18}O$ vs. SiO2 for samples from the core of the Vredefort dome ◆ OGG ■ ILG ▲ charnockites x dolerite ✳ mafic granulite ● metapelitic restites and migmatites.

The mafic granulite 454a has a $\delta^{18}O$ value of 6.4 ‰ which can be expected due to its increased mafic content relative to the trondhjemites and tonalites of the OGG and ILG. The restites and metapelitic migmatites plot in the range 10.2-12.1 ‰ (Table 6.4.2) with the restites being at the upper end of this range of $\delta^{18}O$ values. As for the basement rocks in which they occur, these metapelitic units display $\delta^{18}O$ values typically expected for such lithologies (Faure, 1986).

Sample	Rock type	$\delta^{18}O$ (‰)
456a	Garnet restite	12.1
456b	Garnet restite	11.9
VH14	Garnet restite	11.5
VT652	Garnet restite	12.1
VT654	Garnet restite	10.2
HM3	Granitoid restite	11.5
HM6	Garnet restite	10.7

Sample	Rock type	$\delta^{18}O$ (‰)
HM7	Garnet restite	10.5
HM14	Granitoid restite	10.6
HM16	Grt restite+granitoid restite + leucosome	10.7
H5	Garnet restite	10.2
HM10	Mafic granulite	9.9
454a	Mafic granulite	6.4
VT623	Cordierite restite	8.5

Table 6.4.2: Table of whole rock $\delta^{18}O$ values for the granulite-grade xenoliths found within the ILG terrane.

The mineral separate data acquired (Table 6.4.3) for selected core samples are plotted in Figure 6.4.3. The values for the feldspar minerals are mostly depleted relative to the quartz values in each sample, other than 441. This can be expected even for rocks in which the minerals have equilibrated their oxygen isotopes because of the greater susceptibility of feldspars to exchange their oxygen isotopes. From this plot it is obvious that not all the mineral pairs have equilibrated their oxygen isotopes (namely samples 441, 443, 437, 432, 431, 429). Table 6.4.4 provides temperature estimates for samples in which the minerals appear to have equilibrated. Temperatures of equilibration which are plausible for the granitoids, in respect of temperatures obtained by Stevens *et al.* (1997a) for the metapelitic units, range from 619->1000°C, however the majority of the temperature estimates lie in the range 619-820°C. As for the whole rock data, the highest temperatures observed from mineral separate data, occur in the region of the OGG/ILG transition zone (943-1020°C) (Fig. 6.4.4).

Sample	$\delta^{18}O$qtz	$\delta^{18}O$fls	$\delta^{18}O$pyx	$\delta^{18}O$bt	$\delta^{18}O$hbd	$\delta^{18}O$gnt
438	9.7	8.1				
441	9.0	9.8				
443	9.5	9.2				
437	9.0	8.9				
433	9.8	8.6				
432	9.7	9.4				
431	9.2	9.0		5.0		
428	9.7	8.5				
429	9.2	9.1				
435	10.7	8.9	7.9			
436	9.8	8.6	7.5			
445	9.7	8.7				
447	9.8	9.0				
450	9.8	8.7				
461	10.7	8.9				
457	9.6	8.6				
454a		6.9	9.3		7.1	
456a	12.9					11.3
HM6	12.3					11.8
VT623	8.7					

Table 6.4.3 : Table of mineral separate $\delta^{18}O$ values for selected samples from the basement. All values in per mil units.

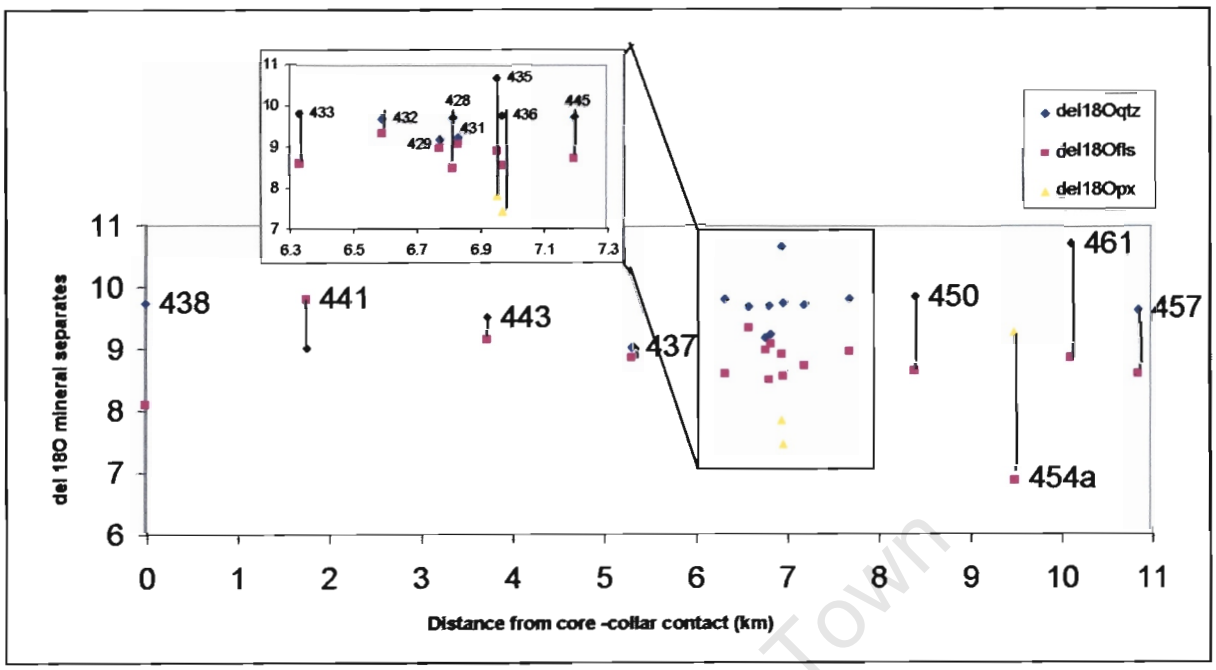

Figure 6.4.3: Graph illustrating mineral separate $\delta^{18}O$ values for samples from the core of the Vredefort dome.

Sample	$\delta^{18}O$ Qtz(‰)	$\delta^{18}O$ Fsp(‰)	$\Delta_{(Qtz-Fsp)}$	T(K)	T(°C)
438	9.7	8.1	1.6	943	650
433	9.8	8.6	1.2	1099	806
428	9.7	8.5	1.2	1103	810
435	10.7	8.9	1.8	912	619
436	9.8	8.6	1.2	1108	815
445	9.7	8.7	1.0	1216	943
447	9.8	9.0	0.8	1313	1020
450	9.8	8.7	1.1	1113	820
461	10.7	8.9	1.8	897	624
457	9.6	8.6	1.0	1186	893
Sample	**$\delta^{18}O$ Qtz(‰)**	**$\delta^{18}O$ Opx(‰)**	**$\Delta_{(Qtz-Pyx)}$**	**T(K)**	**T(°C)**
435	10.7	7.9	2.8	989	696
436	9.8	7.5	2.3	1098	805
Sample	**$\delta^{18}O$ Qtz(‰)**	**$\delta^{18}O$ Grt(‰)**	**$\Delta_{(Qtz-Gros)}$**	**T(K)**	**T(°C)**
456a	12.9	11.3	1.6	1376	1103

Table 6.4.4: Temperature estimates as calculated using oxygen isotope geothermometers for mineral pair fractionations. Equations used : $\Delta_{(Qtz-An50)} = 1.45\times 10^6/T^2$, $\Delta_{(Qtz-Pyx)} = 2.75\times10^6/T^2$ (Zheng, 1992) and $\Delta_{(Qtz-Gros)}=3.03\times10^6/T^2$ (Matthews, 1994).

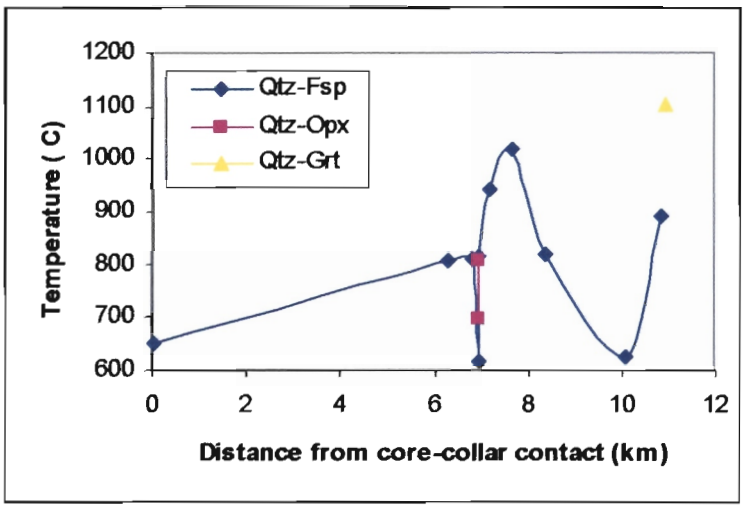

Figure 6.4.4: Diagram illustrating the variation in temperature (as obtained from mineral separate oxygen isotope data) with increasing distance from the core-collar contact (0 km).

CHAPTER 7
DISCUSSION AND CONCLUSIONS

The peak metamorphic assemblages observed in the collar rock samples of this study correlate well with previous work done by Gibson & Wallmach (1995) and provide a peak metamorphic P-T estimate ranging from 550-620°C at 3.5-4.5 kbar (obtained from petrographic analysis and phase stability). The timing of peak metamorphism in the collar has been identified as pre-impact based on the observation of pseudotachylite cross-cutting the peak metamorphic assemblages in numerous of the samples studied and has been linked to a syn-Bushveld Complex age of ~2.06 Ga (Gibson *et al.*, 1998). The M1b metamorphic assemblage described by Gibson & Wallmach (1995), dominated by poikiloblastic cordierite which overgrows the peak metamorphic assemblages and pseudotachylite, is also observed in the samples analysed in this study. Thermometric calculations applied to garnet, biotite, chlorite and cordierite provide a temperature estimate of 480-530 ± 10°C at 4.0 kbar for the post-shock metamorphism.

In the core of the dome, metamorphism of the metapelitic granulites found within the ILG has been well documented by Stevens *et al.* (1997) and Gibson (2002) and the samples collected in this study provide confirmation of their petrographic observations. Thus, we have a good constraint of temperatures in excess of 900°C (at approximately 5.0 kbar) for the Archean age, peak metamorphic assemblage observed in these rocks (M1), followed by a younger isobaric metamorphic event constrained to approximately 650°C (M2), and lastly, a low pressure, post-shock metamorphic event (M3) constrained to >900°C at the centre of the dome (locally may have exceeded 1350°C) and 775 ± 50°C at approximately 6km from the centre (Gibson, 2002). Temperatures obtained from mineral separate oxygen isotope data from the TTG gneisses in the core fall within a similar bracket, between 650->900°C, to temperatures obtained for the post-shock metamorphism. This suggests that the final oxygen isotope resetting was indeed related to fluids associated with the impact event.

From temperatures obtained using $\delta^{18}O$ mineral separate data it is notable that the highest temperatures recorded in the core are in the vicinity of the OGG-ILG transition zone (800-1000°C) and decrease in both directions away from this to temperatures in the 600-800°C range. Thus, although we don't observe any major disruption of the whole rock $\delta^{18}O$ values across the transition zone and there is no structural evidence of it being a discontinuity (Lana *et al.*, 2003), the mineral separate data indicate it was an area of increased heat and fluid flow during and after impact. The increased abundance of pseudotachylite in this area supports the latter conclusion.

The peak metamorphism observed in the core of the dome correlates well with the conclusion that these rocks were buried to a depth of 17-20 km at 3.1 Ga (Stevens *et al.*, 1997b ; Hart *et al.*, 1999). The post-shock metamorphism in both the core and the collar, M3 and M1b, respectively, equate well with rapid heating and exhumation of deep level crust by central uplift and rim collapse during impact cratering, with the heat for metamorphism being derived from non-adiabatic decay of the shock wave (Gibson, 2002; Melosh & Ivanov, 1999; Ivanov & Deutsch, 1999). The lateral and vertical temperature gradient associated with this heat source may provide an explanation for the radial increase in metamorphism towards the centre of the structure. Gibson (2002) discusses modelling of the thermal effects of impact on the Vredefort structure in terms of 2-D hydrocode modelling presented for large impact craters (Melosh & Ivanov, 1999; Ivanov & Deutsch,

1999; Pierazzo *et al.*, 1997). They conclude that evidence from granulites and granofelses in the inner 5-10 km of the central uplift of the dome support the predicted 'strong lateral thermal' gradient over this area that can be expected immediately after impact.

The oxygen isotope data acquired suggests that the rocks in the collar have been exposed to significant fluid/rock interaction (Fig. 7.1). The observed depletion in $\delta^{18}O$ values appears not to be linked to metamorphic fluids released from the rocks during prograde dehydration reactions, nor their proximity to igneous intrusions within the collar or dolerite dykes. Therefore, the current oxygen isotope signature is likely to be an overprint of any resettings which may have occurred during the peak metamorphic event or associated with contact metamorphism (and associated fluids) due to the intrusion of igneous bodies into the collar rocks prior to impact. However, the isotopic resetting observed in the collar appears to be regionally homogenous and related to some pervasive fluid/rock interaction in which the fluid had a greater affinity for the larger ^{18}O isotope. This indicates that the interacting fluid is likely to have been meteoric in nature with a low enough $\delta^{18}O$ value to initiate the depletion of oxygen isotopes to as low as 1 per mil in the collar rocks. In consideration of the polymetamorphic history of these rocks, it is likely that they have experienced multiple stages of oxygen isotope resetting prior to the impact event, but that fluid flow associated with impact has largely overprinted any earlier resettings.

The observation that rocks exhibiting the lowest grades of metamorphism from the SW quadrant of the dome have the most depleted $\delta^{18}O$ values indicates that the final oxygen isotope resetting is indeed not related to the degree of metamorphism experienced. In fact, such drastic depletions in rocks which have experienced greenschist grade metamorphism support the influx of massive amounts of meteoric fluids in order to facilitate the removal of ^{18}O.

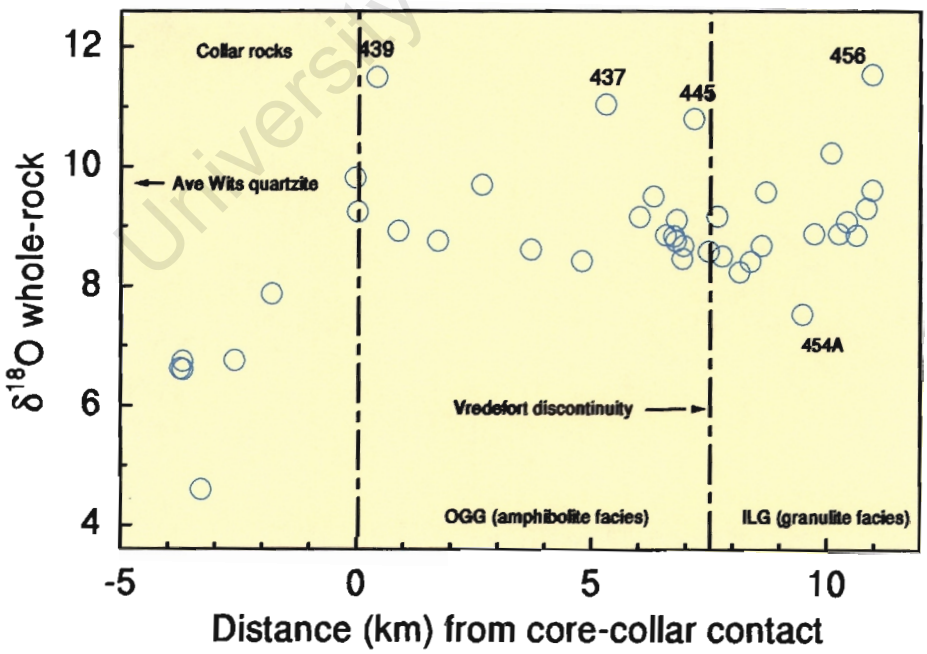

Figure 7.1: Plot of whole rock $\delta^{18}O$ values across the collar and the core of the Vredefort dome, illustrating the depleted nature of the samples from the collar and the contrasting comparatively unreset values for the core samples.

In the core of the structure $\delta^{18}O$ values do not appear to be reset. The trondjhemitic and tonalitic OGG and ILG samples display values typically observed for I-type granites and the metapelitic units display values one would expect for such lithologies. However, these rocks have also been subject to a polyphase tectonic history and are, therefore, most likely to have experienced multiple stages of oxygen isotope resettings associated with the major metamorphic events. In the case of the granulite-grade metapelitic units found within the ILG, minuscule depletions in $\delta^{18}O$ values due to prograde dehydration reactions may have been cancelled out and possibly surpassed by enrichment in the heavier ^{18}O isotope as related melt (with a greater affinity for the smaller ^{16}O isotope) was removed from the system (as suggested by Stevens *et al.*, 1997a). Elevated $\delta^{18}O$ values from the peak metamorphic times may then have been depleted proportionally to the collar rock metapelites resulting in the current, apparently undepleted, $\delta^{18}O$ values observed in these granulites. In the case of the TTG gneisses, their $\delta^{18}O$ values are sufficiently lower than metapelitic units to not be as susceptible to exchanging oxygen isotopes with a meteoric fluid, however, they may also have experienced some earlier resetting which elevated their oxygen 18 content, which was the depleted during the impact event.

Another consideration in terms of the observation that rocks at the centre of the dome exhibit little deviation in their oxygen isotope signatures from what is expected of such rocks compared to the large depletions observed in the collar rocks (specifically in the greenschists form the SW quadrant of the dome), is the permeability of the rocks through which the fluids flowed. If we consider that the rocks at the centre of the dome are mostly igneous rocks and that they experienced high degrees of recrystallization, it is likely that they were less permeable to hydrothermal meteoric fluids associated with the impact than the collar metapelites.

In conclusion, the $\delta^{18}O$ data from this study suggest that the rocks in both the core and the collar of the Vredefort dome have experienced (different) multiple stages of resettings prior to the impact event predominantly related to the peak metamorphism observed in each. However, both have experienced a similar final resetting associated with meteoric fluids under hydrothermal conditions which were activated during and after impact. Larger depletions in the collar rocks may be a result of their different pre-impact oxygen isotope history or due to them being more permeable than the rocks in the core.

The origin of such a fluid has yet to be considered. Temperatures obtained for the post-impact metamorphism from petrographic analysis, stable oxygen isotopes and fluid inclusion studies agree well. However, it seems doubtful that the CO_2-rich fluid inclusions associated with impact (type 1, Fricke *et al.*, 1990) could possibly represent the fluid associated with the oxygen isotope resettings if it is indeed meteoric in nature as concluded here. One would expect some component of the meteoric fluid to have become entrapped within the re-activated fluid inclusions thus dissolving and diminishing their CO_2 content. A stable isotope study, including $\delta^{18}O$, δD and $\delta^{13}C$, of the fluid inclusions would thus prove useful in the context of resolving this problem.

Finally, once greater inroads have been made into the structural dynamics, temperature gradients and potential effects a melt sheet may have had in the Vredefort impact structure, it is likely that the related fluid flow mechanics and regimes may be more easily constrained.

REFERENCE LIST

Akaogi M. and Navrotsky A. 1984 The quartz-coesite-stishovite transformations: new calorimetric measurements and calculations of phase diagrams. Physics of the Earth and planetary interiors V36, 124-134.

Akella and Winkler 1996 Cordierite phase stability at low pressures. Contrib. Min. Petr. V12, 1-12.

Albat H. M. and Mayer J. J. 1989 Megascopic planar shock fractures in the Vredefort Structure; a potential time marker? Tectonophysics 162, 265-276.

Alexopoulus J.S., Grieve R.A.F. and Robertson P.B. 1988 Microscopic lamellar deformation features in quartz: Discriminative characteristics of shock-generated varieties. Geology 16 796-799.

Allsopp H.L., Fitch F.J., Miller J.A. and Reimold W.U. 1991 $^{40}Ar/^{39}Ar$ stepheating age determinations relevant to formation of the Vredefort Dome, South Africa. SA J. of Sc. V87, 431-442.

Anders E. and Grevesse N. 1989 Abundances of the elements: Meteoritic and solar. Geochim. Cosmochim. Acta V53, 197-214.

Antoine L.A.G., Nicolayson L.O. and Nicol S.L. 1990 Processed and enhanced gravity and magnetic images over the Vredefort structure and their interpretation. Tectonophysics V171, 63-74.

Atherton M.P. 1977 Metamorphism of the Dalradian rocks of Scotland. Scottish Journal of Geology 13, 331-370.

Bayly B. 1989 The Vredefort structure: estimates of energy for some internal sources and processes. Tectonophysics V171, 153-167.

Beukes N. J. 1983 Palaeoenvironmental setting of iron-formations in the depositional basin of the Transvaal Supergroup, South Africa. In: Mineral deposits of Southern Africa Author(s): Anhaeusser, C. R. [editor]; Maske, S. [editor] Publisher: Geol. Soc. S. Afr. : Johannesburg, South Africa pp.131-209.

Bisschoff A.A. 1962 The pseudotachylite of the Vredefort Dome. Trans. Geol. Soc. SA V65, 207-225.

Bisschoff A.A. 1969 The petrology of the igneous and metamorphic rocks in the Vredefort Dome and the adjoining part of the Potchefstroom syncline. D. Sc. Thesis, Univ. Pretoria.

Bisschoff A.A. 1972a Tholeitic intrusions in the Vredefort Dome. Trans. Geol. Soc. S. Afr. 75, 23-30.

Bisschoff A.A. 1972b Dioritic rocks of the Vredefort Dome. Trans. Geol. Soc. S. Afr. 75, 31-45.

Bisschoff A.A. 1982 Thermal metamorphism in the Vredefort Dome. Trans. Geol. Soc. SA V85, 43-57.

Bisschoff A.A. 1988 The history and origin of the Vredefort Dome. SA J. of Sc. V84, 413-417.

Bisschoff A.A. 2000 Mapping of the Vredefort Dome. 62nd Ann. Met. Soc., Johannesburg, Meteoritics Planet. Sci 34 (suppl.), A11-A12

Brandl G. and Reimold W.U. 1988 The structural setting and deformation associated with pseudotachylite occurrences in the Palak Shear Belt and Sand River gneiss, Northern Transvaal. Tectonophysics V171, 201-220.

Brink M. 1986 Tektoniese en stratigrafiese ontwikkeling van die Witwatersrand Supergroep en verwante gesteentes in die gebied noord en oos van Klerksdorp. PhD thesis, Rand Afrikaans University, 317pp.

Bucher W.H. 1965 The largest so-called meteorite scars in 3 continents as demonstrably ties to major terrestrial structures. Annals of the NY Acad. Of Sc. V123, 897-903.

Carter N.L. 1968 Basal quartz deformation lamellae - a criterion for recognition of impactites. American Journal of Science, v. 263, pp. 786-806.

Chiba H., Chako T., Clayton R.N. and Goldsmith J.R. 1989 Oxygen Isotope fractionations involving diopside, forsterite, magnetite and calcite: application to geothermometry. Geochim. Cosmochim. Acta. 53, 2985-2995.

Chinner G.A. 1965 The kyanite isograd in Glen Clova, Angus. Mineralogy magazine 34, 132-143.

Chinner G.A. 1967 Chloritoid and the isochemical character of Barrow's zone. Journal of Petrology 8, 268-282.

Chivas A.R., Andrew A.S., Sinha A.K. and O'Neil J.R. 1982 Geochemistry of a Pliocene-Pleistocene oceanic arc pluton complex, Guadalcanal. Nature V300, 139-143.

Claisse F. 1989 Automated sample preparation for analysis of geological materials. In: Ahmedali S.T. (ed.) X-ray flourescence analysis in the geological sciences: Advances in methodology. Geol. Assn. Canada: Short course 7, 39-54.

Clayton R.N. 1981 Isotopic thermometry. In Newton R.C., Navrotsky A. and Wood B.J. (eds.), Thermodynamics of minerals and melts. Springer-Verlag, New York, 85-109.

Clayton R.N., O'Neil J.R. and Mayeda T.K. 1972 Oxygen isotope exchange between quartz and water. Journal of Geophysical Research 77, 3057-3067

Cloete M., Hart R.J., Schmid H.K., Drury M, Demanet C.M. and Sankar K.V. 1999 Characterization of magnetite particles in shocked quartz by means of electron- and magnetic force microscopy: Vredefort, South Africa. Contrib. Mineral. Petrol. 137, 232-245.

Colliston W.P., Reimold W.U. and Robertson A.S. 1987 A preliminary report on a detailed structural, geochemical and isotopic study of the Broodkop migmatite Complex, SE Vredefort Dome (working paper). Contrib. to Int. Worksh. on Cryptoexpl. & Catastr. In: the Geol. Rec., Parys July '87 Section C3 22p., BTI Geophys. Univ. Witwatersrand, Jhb.

Colliston W.P. 1989 Structural studies on the Vredefort Dome: Implications for a compressive tectonic origin. The structural geology of the West Rand and West Wits Line. Joint conf. Tect. Div. & W. Tvl. Branch Geol. Soc. S. Afr., Braamfontein pp.40-43.

Colliston W.P. 1990 A model of compressional tectonics for the origin of the Vredefort structure. Tectonophysics V171, 115-118.

Colliston W.P. and Reimold W.U. 1992 Structural review of the Vredefort Dome. Sudbury 92 Conference, Lunar Planet.Inst.Contr. No. 790., pp.16-17.

Corner B. and Wilshire W.A. 1989 Structure of the Wits Basin derived from aeromagnetic and gravity data. Proc. Expl. '87, Geol. Surv. Canada Spec. V3, pp. 532-546.

Corner B., Durrheim R.J. and Nicholaysen L.O. 1990 Relationships between the Vredefort structure and the Witwatersrand basin within the tectonic framework of the Kaapvaal craton as interpreted from regional gravity and aeromagnetic data. In: L.O. Nicholaysen and W.U. Reimold (eds.) Cryptoexplosions and Catastrophes in the Geological Record, with a Special Focus on the Vredefort Structure. Tectonophysics, 171., pp.19-61.

Craig H. 1961 Standard for reporting concentrations of deuterium and oxygen-18 in natural waters. Science V133, 1833-1834.

Daly R.A. 1947 The Vredefort ring structure of South Africa. J. Geol. V67, 496-506.

Deer W.A., Howie R.A. and Zussman J. (eds.) 1992 The rock-forming minerals 2nd edition.

Dickenson M.P. and Hewitt D. 1986 A garnet-chlorite geothermometer. Geol. Soc. Am. Abstracts with Programs 18 584.

Dietz R.S. 1960 Meteorite impact suggested by shatter cones in rock. Science V131, 1781-1784.

Dietz R.S. 1961 Vredefort ring structure: meteorite impact scar? J. Geol. V69, 499-516.

Drennen G.R., Meyer F.M., Robb L.J., Armstrong R.A. and De Bruiyn H. 1990 The nature of the Archean basement in the hinterland of the Wits Basin: II. A crustal profile west of the Welkom Goldfield and comparisons with the Vredefort crustal profile. SA J. of Geo. V93(1), 41-53.

Dressler, B. O. 1984 Effects of the Sudbury event on the footwall rocks of Sudbury Structure In: Program with Abstracts - Geological Association of Canada; Mineralogical Association of Canada; Canadian Geophysical Union, Joint Annual Meeting, Vol. 9, pp.58

Durrheim R.J. and Mooney W.D. 1991 Archean and Proterozoic crustal evolution; evidence from crustal seismology. Geology (Boulder), 19(6): 606-609.

Du Toit A.L. 1954 The Geology of South Africa. Olivier & Boyd, Edinburgh & London 3rd Ed. 611pp.

Dymoke P. and Sandiford M. 1992 Phase relationships in Buchan facies series pelitic assemblages: calculations with application to andalusite-staurolite paragenesis in the Mount Lofty Ranges, South Australia. Contrib. Min. & Petr. V110, 121-132.

Engelbrecht C.J., Baumbach G.W.S., Mathysen J.L. and Fletcher P. 1986 The West Wits Line. In Anhaeusser C R & Maske S (eds.). Mineral deposits of southern Africa, 1. Geol. Soc.S.Afr., 599-648.

Faure G. 1986 Principles of Isotope Geochemistry. John Wiley & Sons, New York, 464 p.

Ferry J.F. and Spear F.S. 1978 Experimental calibration of the partitioning of Fe and Mg between biotite and garnet. Contrib. Min. & Petr. V66, 113-117

Fletcher P. and Reimold W.U. 1989 Some notes and speculations on the pseudotachylites in the Witwatersrand Basin and Vredefort Dome, South Africa. SA J. Geol. V92, 223-234.

Flowers R.M. 2000 The Vredefort Discontinuity as a primary crustal boundary: Implications for Kaapvaal lithosperic structure, Vredefort impact structure, South Africa. Geol. Soc. Am. Summit 2000, Reno. Abstracts with Programs 32, p. A-164.

French B.M. and Nielsen R.L. 1990 Vredefort Bronzite granophyre: chemical evidence for origin as a meteorite impact melt. Tectonophysics V171, 119-138.

Fricke A., Medenbach O. and Schreyer W. 1990 Fluid inclusions, planar elements and pseudotachylites in the basement rocks of the Vredefort structure, South Africa. Tectonophysics V171, 169-183.

Friedman I. and O'Neil J.R. 1977 Compilation of stable isotope fractionation factors of geochemical interest. In: M. Fleischer (ed.), Data of Geochemistry, U.S. Geological Survey Professional Paper 440-KK, 6th Ed., Reston, VA.

Frimmel H.E. 1994 Metamorphism of Witwatersrand Goldfields. Exploration and mining geology 3, 357-370.

Gibson R.L. 1993 When is a hornfels not a hornfels? Metapelitic rocks from the Lower Wits Supergroup, Vredefort Dome, South Africa. S. Afr. J. Geol. 96, 42-48.

Gibson R.L. and Wallmach T. 1995a Low pressure-high temperature metamorphism in the Vredefort Dome, South Africa: anticlockwise pressure-temperature path followed by rapid decompression. Geol. J. V30, 319-331.

Gibson R.L. and Wallmach T. 1995b Metamorphism in the Witwatersrand basin: A perspective from the Vredefort Dome. EGRU Info. Circ. V288, 30. Wits Univ.

Gibson R.L., Armstrong R.A. & Reimold W.U. 1997 The age and thermal evolution of the Vredefort impact structure: a single-grain U-Pb zircon study. Geochim. Cosmochim. Acta 61, 1531-1540.

Gibson R.L. and Stevens G. 1998 Regional metamorphism due to anorogenic intracratonic magmatism. In Treloar, P.J., and O'Brien, P.J., eds., What drives metamorphism and metamorphic reactions? Special Publications: Geological Society, London, v. 138, p. 121-135.

Gibson R.L., Reimold W.U. and Stevens G. 1998 Thermal-metamorphic signature of an impact event in the Vredefort dome, South Africa. Geology, v. 26, p. 787-790.

Gibson R.L. and Reimold W.U. 1999 The significance of the Vredefort dome for the thermal and structural evolution of the Witwatersrand basin, South Africa. Mineralogy and Petrology, v. 66, p. 5-23.

Gibson R.L., Reimold W.U., Phillips D. and Layer P.W. 2000 $^{40}Ar/^{39}Ar$ constraints on the age of metamorphism in the Witwatersrand Supergroup, Vredefort dome (South Africa). SA J. of Geol. V103, 175-190.

Gibson R.L. 2002 Impact-induced melting of Archean granulites in the Vredefort Dome, South Africa. I: anatexis of metapelitic granulites. J. Metamorphic Geol. V20, 57-70.

Green R.W. and Chetty 1990 Seismic refraction studies in the basement of the Vredefort structure. Tectonophysics V171, 105-113.

Greive R.A.F., Coderre J.M., Robertson P.B. and Alexopoulos J. 1990 Microscopic planar deformation features in quartz of the Vredefort structure: Anomalous but still suggestive of an impact origin. Tectonophysics V171, 185-200.

Hall A.L. and Molengraaf G.A.F. 1925 The Vredefort mountain land in the Southern Transvaal and Northern Orange Freestate. Verh.Kon. Akad. Wetensch. V24, 183.

Hargraves R.B. 1961 Shatter cones in the rocks of the Vredefort Ring. Trans. Geol. Soc. SA V64, 147-161.

Harris C. and Watkins R.T. 1990 Fluid interaction in the Witwatersrand goldfields: oxygen isotope geochemistry of Ventersdorp-age dolerite intrusions. SA J. Geol. V93 (4), 611-615.

Hart R.J., Nicolayson L.O. and Gale N.H. 1981 Radioelement concentrations in the deep profile through Precambrian basement of the Vredefort structure. J. Geophys. Res. V86 No. B11, 10639-10652.

Hart R.J. and Andreoli M.A.G. 1986 A geological traverse of the Vredefort structure: The natural equivalent of a 15km borehole into the Archean Kaapvaal Craton, South Africa. GeoCongress '86 22nd Bienn. Cong.,Geol. Soc S. Afr., Jhb. Pp. 823-826.

Hart R.J., Andreoli M.A.G., Tredoux M. and de Wit M.J. 1990a Geochemistry across an exposed section of Archean crust at Vredefort, South Africa: with implications for mid-crustal discontinuities. Chem. Geol. V82, 21-50.

Hart R.J., Andreoli M.A.G., Smith C.B., Otter M.L. and Durrheim R. 1990b Ultramafic rocks at the centre of the Vredefort structure, South Africa: Possible exposure of the upper mantle? Chem. Geol. V83, 233-248.

Hart R.J., Andreoli M.A.G., Reimold W.U. and Tredoux M. 1991 Aspects of the dynamic and thermal metamorphic history of the Vredefort cryptoexplosion structure: implications for its origin. Tectonophysics V192, 313-331.

Hart R.J., Moser D. and Andreoli M.A.G. 1999 Archean age for the granulite facies metamorphism near the centre of the Vredefort structure. S. Afr. J. Geol., 27, 1091-1094.

Hart R.J., Hargraves R.B., Andreoli M.A.G., Tredoux M. and Cloete M. 1995 The magnetic anomaly near the centre of the Vredefort structure: Implications for impact-related magnetic signatures. Centenial GeoCongress '95 Jhb, Geol. Soc. S. Afr., 559-561.

Hart R.J., Connell S.H., Cloete M., Mare L., Drury M. and Tredoux M. 2000 "Super-magnetic" rocks generated by shock metamorphism from the centre of the Vredefort impact structure, South Africa. SA J. Geol. V103, 151-155.

Harte B. and Hudson N.F.C. 1979 Pelite facies series and the temperatures and pressures of Dalradian metamorphism in E Scotland. In: Harris A.L., Holland C.H. and Keake B.A. (eds.) The Caledonides of the British Isles – Reviewed. Geol. Soc. London and Academic Press, Edinburgh, 323-337.

Henkel H. and Reimold W.U. 1996a Integrated geophysical modelling of the Vredefort impact structure, Witwatersrand Basin, South Africa (abstract). Lunar and Planetary Science, v. XXVII, pp. 527-528.

Henkel H. and Reimold W.U. 1996b Integrated gravity and magnetic modelling of the Vredefort impact structure - reinterpretation of the Witwatersrand Basin as the erosional remnant of an impact basin. EGRU Int. Circ., v. 299.

Henkel H. and Reimold W.U. 1998 Integrated geophysical modelling of a giant, complex impact structure: anatomy of the Vredefort Structure, South Africa. Tectonophysics, 287(1-4) 1-20.

Hoefs J. 1987 Stable Isotope Geochemistry. Third edition, Springer-Verlag, Berlin, 241 p.

Holland M.J., Stanistreet I.G. and McCarthy, T.S. 1990 Tectonic control on the deposition of the Turfontein subgroup around the Vredefort Dome. SA J. of Geol. V93 (1), 158-168.

Holland T.J.B. and Powell R. 1990 An enlarged and updated internally consistent thermodynamic dataset with uncertainties and correlations: the system K_2O-Na_2O-CaO-MgO-MnO-FeO-Al_2O_3-TiO_2-SiO_2-H_2-O_2. J. Metam. Geol. V8, 89-124.

Ivanov B.A. and Deutsch A. 1999 Sudbury impact event: cratering mechanics and thermal history. In: Large meteorite Impacts and Planetary evolution II Special paper 339. Dressler B.O. and Sharpton V.L. (eds.), pp. 389-397. Geol. Soc.Am.

Kamo S.L., Reimold W.U., Krogh T.E. and Colliston W.P. 1996 A 2.023Ga age for the Vredefort impact event and a first report of shock metamorphosed zircons in pseudotachylite breccias and Granophyre. Earth & Pl. Sc. Letters 144, 369-387.

Kenkmann T., Hornemann U. and Stoffler D. 2000 Experimental generation of shock-induced pseudotachylites along lithological interfaces. Meteoritics and Planetary Sc. V35 (#6) 1275-1291.

Killick A.M. and Reimold W.U. 1990 Review of the pseudotachylites in and around the Vredefort Dome, South Africa. SA J. of Geol. V93 (2), 350-365.

Killick A.M. and Roering C. 1998 An estimate of the physical conditions of pseudotachylite formation in the West Rand Goldfield, Witwatersrand Basin, South Africa. Tectonophysics, v. 284, pp. 247-259.

Kretz R. 1983 Symbols for rock-forming minerals. American Mineralogist 68, 277-279.

Koeberl C., Reimold W.U. and Shirey S.B. 1996 Re-Os isotope and geochemical study of the Vredefort Granophyre: Clues to the origin of the Vredefort structure, South Africa. Geology, v. 24, pp. 913-916.

Lana C., Gibson R.L., Kisters A.F.M. & Reimold W.U. 2003 Archean crustal structure of the Kaapvaal craton, South Africa – evidence from the Vredefort dome. Earth & Pl. Sc. Letters 206, 133-144.

Leroux H., Reimold W.U. and Doukhan J. 1994 A TEM investigation of shock metamorphism in quartz from the Vredefort Dome, South Africa. Tectonophysics V230, 223-239.

Lilly P.A. 1980 Faulting mechanics in the collar rock of the Vredefort ring structure. Tectonophysics, August 01, Vol. 67, Issue 1-2, pp.45-60.

Magluoghlin J.F. and Spray J.G. 1992 Frictional melting processes and products in geological materials: Introduction (to this special volume) and discussion. Tectonophysics V204, 197-204.

Manton W.I. 1965 The orientation and origin of shatter cones in the Vredefort ring. Geol. Problems in Lunar Research, New York Acad. Of Sci. Annals 123, 1017-1049.

Maree B.D. 1944 The Vredefort structure as revealed by gravimetric survey. Trans. Geol. Soc. SA V47, 183-197.

Maree B.D. 1945 Discussion of the Vredefort structure as revealed by a gravimetric survey. Proc. Geol. Surv. S. Afr. 48, 91-82.

Martini J.E.J. 1978 Coesite and stishovite in the Vredefort Dome, South Africa. Nature V272, 715-717.

Martini J.E.J. 1991 The nature, distribution and genesis of the coesite and stishovite associated with pseudotachylite of the Vredefort Dome, South Africa. Earth & Pl. Sci. Letters V103, 285-300.

Martini J.E.J. 1992 The metamorphic history of the Vredefort Dome at approximately 2.0 Ga as revealed by coesite-stishovite-bearing pseudotachylites. J. met. Geol. V10, 517-527.

Matthews A. and Beckinsale R.D. 1979 Oxygen isotope equilibration systematics between quartz and water: American Mineralogist, v. 64, no. 1-2, p. 232-240.

McCarthy T.S., Charlesworth E.G. and Stanistreet I.G. 1986 Post Transvaal structural features of the Northern portion of the Witwatersrand basin. Trans. Geol. Soc. SA V89, 311-324.

McCarthy T.S., Stanistreet I.G. and Robb L.J. 1990 Geological studies related to the origin of the Witwatersrand basin and its mineralization – an introduction and a strategy for research and exploration. SA J. Geol. V93, 1-4.

McHone J.F., Nieman R.A., Lewis C.F. and Yates A.M. 1989 Stishovite at Cretaceous-Tertiary boundary, Raton, New Mexico. Science, 243, 1182-1184.

Melosh H.J. and Ivanov B.A. 1999 Impact crater collapse. Annual reviews Earth and Pl. Science V27, 385-415.

Menuge J.F. 1982 Nd isotopic studies in crust-mantle evolution: The Proterozoic of southern Norway and the Archean of southern Africa. Phd thesis (unpubl.), Univ. of Cambridge.

Merkle R.K.W. and Wallmach T. 1997 Ultramafic rocks in the centre of the Vredefort structure (South Africa): geochemical affinity to Bushveld rocks. Chemical Geology 143, 43-64.

Minnitt R.C.A. and Reimold W.U. 1994 The geology of the Greenlands Greenstone Complex and selected granitoid terranes in the south eastern quadrant of the Vredefort Dome. EGRU, Univ. of the Wits. Info. Circ. 281, 46pp.

Moser D.E. 1997 Dating the shock wave and thermal imprint of the giant Vredefort impact, South Africa. Geology, v. 25, pp. 7-10.

Moser D.E., Flowers R.M. and Hart R.J. 2001 Birth of the Kaapvaal tectosphere 3.08 billion years ago. Science V291, 465-468.

Nel L.T. 1927 The geology of the country around Vredefort. Geol. Surv. of SA Spec. Publ.6, Government printer, Pretoria, Union of SA.

Nicolayson L.O. 1972 North American cryptoexplosion structures: Interpreted as diapirs which obtain release from strong lateral confinement. Geol. Soc. Am. Mem. V132, 605-620.

Nicolayson L.O. 1989 The Vredefort structure: an introduction and a guide to recent literature. Tectonophysics V171, 1-6.

Nicolayson L.O. and Ferguson J. 1990 Cryptoexplosion structures, shock deformation and siderophile concentration related to explosive venting of fluids associated with alkaline ultramafic magmas. Tectonophysics V171, 303-335.

Nicolaysen L.O. and Reimold W.U. 1987 Shatter cones revisited. Contr. to Int. Workshop on Cryptoexpl. and Catastr. in the Geol. Rec., Parys, Section N2, 8p. BPI Geophysics Univ. of the Witwatersrand.

Nicolaysen L.O. and Reimold W.U. 1999 Vredefort shatter cones revisited. Journal of Geophysical Research, B, Solid Earth and Planets 104, 4911-4930.

O'Neil J.R., Reimold W.U. and Nicolayson L.O. 1987 Reconnaissance determinations of oxygen and hydrogen isotopic compositions of selected rocks from the Wits basin and the Vredefort structure, South Africa.

O'Neil J.R. 1986 Theoretical and experimental aspects of isotope fractionation. In Stable isotopes in high temperature geological processes. Valley J.W., Taylor Jr. H.P. and O'Neil J.R. eds. Mineralogical Society of America, Washington D.C.: 1-40.

Perchuk L.L. and Lavrent'eva I.V. 1981 Experimental investigation of exchange equilibria in the system cordierite-garnet-biotite. In: Kinetics and Equilibrium in mineral reactions. Saxena S.K. (ed.) Springer-Verlag, New York, 199-240.

Phillips G.N., Zhou T. and Powell R. 1997 Metamorphic temperature variations among Witwatersrand goldfields: evidence from the pyrophyllite-chloritoid-chlorite mineral assemblage. S. Afr. J. Geol., v. 100, pp. 393-404.

Pierazzo E., Vickery A.M. and Melosh H.J. 1997 A reevaluation of impact melt production. Icarus V27, 408-423.

Preston R. 1998 Metamorphism and alteration of the West Rand Group shales from distal portions of the Witwatersrand basin: Consequences for a basin wide model. B.Sc. Hons. Thesis (unpubl.), Univ. of the Wits., JHB, 25pp.

Reimold W.U. and Reid A.M. 1987 New facts on the Bronzite Granophyre from the Vredefort structure and implications for the genesis of this enigmatic rock type. International Workshop on Cryptoexplosion and Catastrophe in the Geol. Rec., v. Section R1, p. 9p.

Reimold W.U. 1988 Shock experiments with preheated Wits quartzite and the Vredefort microdeformation controversy. Lunar Planet. Sci. XIX, Lunar & Planet. Inst. Houston, 970-971.

Reimold W.U. and Miller R. 1989 The Roter Kamm impact crater, SWA/Namibia. Proceedings Lunar and Planetary Science Conference 19th, pp. 711-732.

Reimold W.U., Horsch H. and Durrheim R.J. 1990 The 'Bronzite' Granophyre from the Vredefort structure – a detailed analytical study and reflections on the genesis of one of Vredeforts enigmas. Proceedings of the 20th Lunar & PL. Sc. Conf., 433-450.

Reimold W.U. 1990 The controversial microdeformations in quartz from the Vredefort structure, South Africa – a discussion. SA J. of Geol. V93 (4), 645-663.

Reimold W.U. 1991 The geochemistry of pseudotachylite from the Vredefort Dome, South Africa. Neues J. Miner Abh. V162 (2), 151-184.

Reimold W.U. 1993a A review of the geology of and deformation related to the Vredefort structure, South Africa. J. of Geo.l Ed. V41, 106-117.

Reimold W.U. 1993b Further debate on the origin of the Sudbury structure: is it relevant to the Vredefort Dome and the Bushveld Complex? SA J. of Sc. V89, 546-552.

Reimold W.U. and Colliston W.P. 1994 Pseudotachylites of the Vredefort Dome and the surrounding Wits basin, South Africa. Geol. Soc. Of Am. Special paper 293.

Reimold W.U. 1995 Impact cratering - a review, with special reference to the economic importance of impact structures and the southern African impact crater record. Earth, Moon and Planets, v. 70, pp. 21-45.

Reimold W.U. 1996 Geology and evolution of the Vredefort impact structure, South Africa. J. of Afr. Earth Sc. V23 (2), 125-162.

Reimold W.U., Gibson R.L. and Layer P.W. 1996 Further ^{40}Ar-^{39}Ar stepheating data of fault rocks and metamorphic minerals from the Vredefort Dome and Witwatersrand Basin (abstract). Lunar and Planetary Science, v. XXVII, pp. 1067-1068.

Roering C., Barton J.M. and de la R. Winter H. 1990 The Vredefort structure: A perspective with regard to new tectonic data from adjoining terranes. Tectonophysics V171, 7-22.

Schenk P.E. (ed.) 1983 Regional Trends in the Geology of the Appalachian-Caledonian-Hercynian-Mauritanide Orogen.

Schreyer W. 1983 Metamorphism and fluid inclusions in the basement of the Vredefort dome, South Africa: guidelines to the origin of the structure. J. of Petrol. V24, 26-47.

Schreyer W. and Abraham K. 1978 Symplectic cordierite-orthopyroxene-garnet assemblages as products of contact metamorphism of pre-existing basement granulites in the Vredefort structure, South Africa, and their relationship to pseudotachylite. Contib. Min. Petr. 68, 53-62.

Shand S.J. 1916 The pseudotachylite of Parijs (O.F.S.) and its relation to 'trap-shotten' gneiss and 'flinty crush rock'. Quaterly J. of Geol. Soc. of london V72, 198-221.

Sheppard S.M.F. 1981 Stable isotope geochemistry in fluids. In: Rickard D.T. and Wickman F.E. (eds.) Chemistry and geochemistry of solutions at high temperatures and pressures. Phys. Chem. Earth 13/14, 419-445.

Simpson C. 1978 The Structure of the Rim Synclinorium of the Vredefort Dome. Trans. geol. Soc. S. Afr., 81, 115-121.

Simpson C. 1981 Occurrence and orientation of shatter cones in Pretoria Group quartzites in the collar of the Vredefort Dome: Impact origin precluded. J. Geophys. Res., 86, 10701-10706.

Slawson W.F. 1976 Vredefort core: a cross section of the upper crust? Geochim. Cosmochim. Acta V40, 117-121.

Spray J.G., Kelley S. P. and Reimold W. U. 1995 Laser probe argon-40/argon-39 dating of coesite- and stishovite-bearing pseudotachylites and the age of the Vredefort impact event. Meteoritics, 30, 335-343.

Spray J.G. 1998 Pseudotachylite type area: Vredefort. Fault Rocks and Fault Mechanisms. In Snoke A.W., Tullis J. and Todd V.R. (eds.), Fault-related rocks: A photographic atlas, Princeton University Press, Princeton, NJ, USA, p.75-79.

Stepto D. 1979 A geological and geophysical study of the central portion of the Vredefort dome structure. Ph.D. thesis, Wits Univ.

Stepto D. 1990 The geology and gravity field in the central core of the Vredefort structure. Tectonophysics V171, 75-103.

Stevens G., Gibson R.L. and Droop G.T.R. 1996 Polyphase granulite metamorphism in the Vredefort Dome: A window into the deep Kaapvaal Craton at 2.06Ga. EGRU Info. Circ. V297, 27. Wits Univ.

Stevens G., Gibson R.L. and Droop G.T.R. 1997 Mid-crustal granulite facies metamorphism in the Central Kaapvaal craton: The Bushveld Complex connection. Precamb. Res. V82, 113-132.

Sutton J. and Watson J. 1951 Varying trends in the metamorphism of dolerites. Geol. Mag., 88, 25-35.

Taylor S.R. and McLennan S.M. 1985 The continental crust: its composition and evolution. Blackwell, Oxford.

Therriault A.M., Reimold W.U. and Reid A.M. 1996 Field relations and petrography of the Vredefort granophyre. S. Afr. J. Geol. 99 1-21.

Therriault A.M., Grieve R.A.F. and Reimold W.U. 1997 Original size of the Vredefort Structure: Implications for the geological evolution of the Witwatersrand Basin. Meteoritics & Planetary Science, v. 32, pp. 71-77.

Thompson A.B. 1976 Mineral reactions in pelitic rocks: II Calculation of some P-T-X (Fe-Mg) phase relations. Am. J. Science V276, 425-454.

Thompson L.M. and Spray J.G. 1996 Pseudotachylite petrogenesis: constraints from the Sudbury impact structure. Contributions to Mineralogy and Petrology 125, 359-374.

Tredoux M., Hart R. J., Carlson R. W. and Shirey S. B. 1999 Ultramafic rocks at the centre of the Vredefort structure: Further evidence for the crust on edge model. Geology, v. 27, p. 923–926.

Trieloff M., Reimold W.U., Kunz J., Boer R.H. and Jessberger E.K. 1994 $^{40}Ar/^{39}Ar$ thermochronology of pseudotachylites at the Ventersdorp Contact Reef, Wits Basin, South Africa. S. Afr. J. Geol. 97 #3 Spec. issue VCR revisited, 365-384.

Turner A.K. 1992 Application of 3-D geoscientific mapping and modelling systems to hydro-geological studies. In: A. K. Turner (ed.), Three Dimensional Modelling with Geoscientific Information Systems, Series C: Mathematical and Physical Sciences, Volume 354. Kluwer Academic Publishers, Dordrecht, pp. 327-364.

Tucker R.F. and Viljoen R.P. 1986 The geology of the West Rand Goldfield, with special reference to the southern limb. In Anhaeusser C R, Maske S (Eds.) - Mineral Deposits of Southern Africa, v 1, pp 649-688.

Tweedie E.B. 1986 The Evander Goldfield. In Anhaeusser C. & Maske S. (Eds.). Mineral deposits of southern Africa, 1. Geol.Soc.S.Afr., 705-730.

Urey H.C. 1947 The thermodynamic properties of isotopic substances. Journal Chemical Society V1947, 562-581.

Valley J.W., Taylor H.P. and O'Neil J.R. 1986 Stable isotopes and high temperature geological processes. Reviews in Mineralogy, Mineral. Soc. Amer. No. 16.

Walraven F., Armstrong R.A. and Kruger F.J. 1990 A chronostratigraphic framework for the north-central Kaapvaal Craton, the Bushveld Complex and the Vredefort structure. Tectonophysics V171, 23-48.

Walraven F. and Hattingh E. 1993 Geochronology of the Nebo granite, Bushveld Complex. SA J. Geol. V96, 31-42.

Winter de la R. 1986 Cratonic foreland model of the Wits basin development in a continental back-arc plate tectonic setting. GeoCong. '86, Jhb. Bienn.Cong., Geol. Soc. S. Afr., 75-80.

Zartman R.E. and Wasserburg G.J. 1969 The isotopic composition of lead in K-feldspars from some 1.0Ba old North American igneous rocks. Geochim. Cosmochim. Acta V33, 901-942.

Zheng Y. F. 1993 Calculation of oxygen isotope fractionation in anhydrous silicate minerals: Geochim. Cosmochim. Acta, v. 57, no. 5, p. 1079-1091.